

# **Glaciohydrology of Himalaya-Karakoram: Functioning of glacierized catchments in Monsoon and Alpine climatic regimes**

**Ph.D. Thesis**

*by*

**Smriti Srivastava**



**Department of Civil Engineering  
Indian Institute of Technology Indore**

**December 2021**

# **Glaciohydrology of Himalaya-Karakoram: Functioning of glacierized catchments in Monsoon and Alpine climatic regimes**

**A Thesis**

*Submitted in partial fulfillment of the  
requirements for the award of the degree  
of*

**Doctor of Philosophy**

*by*

**Smriti Srivastava**



**Department of Civil Engineering  
Indian Institute of Technology Indore**

**December 2021**



## INDIAN INSTITUTE OF TECHNOLOGY INDORE

### CANDIDATE'S DECLARATION

I hereby certify that the work which is being presented in the thesis entitled "Glaciohydrology of Himalaya-Karakoram: Functioning of glacierized catchments in Monsoon and Alpine climatic regimes" in the partial fulfillment of the requirements for the award of the degree of **Doctor of Philosophy** and submitted in the **Department of Civil Engineering, Indian Institute of Technology Indore**, is an authentic record of my own work carried out during the time period from July 2019 to December 2021 under the supervision of Dr. Mohd. Farooq Azam, Assistant Professor, Discipline of Civil Engineering, Indian Institute of Technology Indore.

The matter presented in this thesis has not been submitted by me for the award of any other degree of this or any other institute.

*Smriti* 29-12-2021

Signature of the Student  
(**Smriti Srivastava**)

-----  
-----  
This is to certify that the above statement made by the candidate is correct to the best of my knowledge.

*Mohd. Farooq Azam* 29/12/2021

Signature of Thesis Supervisor  
(**Dr. Mohd. Farooq Azam**)

-----  
-----  
**Smriti Srivastava** has successfully given his Ph.D. Oral Examination held on .

Signature of Chairperson (OEB)

Signature of External Examiner

Signature of Thesis Supervisor

Date:

Date:

Date:

Signature of PSPC Member #1

Signature of PSPC Member #2

Signature of Convener,  
DPGC

Date:

Date:

Date:

Signature of Head of Discipline

Date:

-----  
-----



*Dedicated to my beloved  
parents*



## ABSTRACT

The Himalaya-Karakoram (HK) region is one of the most heavily glacierized and vulnerable mountainous regions on earth that supplies a significant amount of water to the Indus, Ganga, and Brahmaputra River basins. The field-based studies are limited in the HK hence remote sensing and glaciohydrological modelling provide an alternative solution to investigate the glacier mass balance and runoff evolution under changing climate. In the present thesis, a detailed review about the glaciohydrology of the HK region is developed that discusses the present status and recent advancements in the HK cryosphere, and highlights the critical knowledge gaps that severely affect the modelled contributions of different runoff components. Further, two highly glacierized Himalayan catchments —Dokriani Bamak (DBG) in the monsoon regime and Chhota Shigri (CSG) in the Alpine regime—were selected for the detailed glacier-runoff-climate investigations since 1950 using remote sensing methods, Temperature-index (T-index) glaciohydrological, and glacier-wide mass and Surface Energy Balance (SEB) models. T-index mass balance modelling on DBG and CSG showed decadal positive mass balances over 1950–1980s followed by a limited wastage over 1980–2000, and an accelerated mass wastage post-2000, in agreement with satellite-derived limited areal and snout changes up to 1990s, and then accelerated rates post-2000. In line, glacier-wide mass and SEB modelling also suggest a moderate mass wastage on both the glaciers since 1979 that is dominantly controlled by net shortwave radiation followed by longwave net radiation, latent and sensible heat flux. The long-term glaciohydrological modelling on both DBG and CSG catchments suggests that the higher catchment-wide runoffs correspond to more negative mass balances, and *vice versa*, that contrasts with the previously suggested mass balance-runoff relationship on DBG catchment. Detailed analysis also indicates that the hydrology of the DBG catchment in the monsoon regime is mainly dominated by the summer precipitation, while in CSG catchment in the Alpine regime, the hydrology is mainly controlled by the glacier-wide annual mass balance.

## LIST OF PUBLICATIONS

### A. Publications from Ph.D. thesis work:

1. **Smriti Srivastava**, Purushottam Kumar Garg and Mohd. Farooq Azam, Seven decades of dimensional and mass balance changes on Dokriani Bamak and Chhota Shigri glaciers, Indian Himalaya using satellite data and modelling. *Journal of Indian Society of Remote Sensing* (2021). (Impact Factor: 1.56)
2. Mohd. Farooq Azam and **Smriti Srivastava**, Mass balance and runoff modeling of partially debris-covered Dokriani Glacier in monsoon-dominated Himalaya using ERA5 data since 1979. *Journal of Hydrology*. 590, 125432 (2020). (Impact Factor: 5.72)
3. Mohd. Farooq Azam, Jeffrey S. Kargel, Joseph M. Shea, Santosh Nepal, Umesh K. Haritashya, **Smriti Srivastava**, Fabien Maussion, Nuzhat Qazi, Pierre Chevallier, A. P. Dimri, Anil V. Kulkarni, J. Graham Cogley, Isa M. Bahuguna, Glaciohydrology of the Himalaya-Karakoram. *SCIENCE* (2021). (Impact Factor: 47.73)

### B. Articles under review:

1. **Smriti Srivastava** and Mohd. Farooq Azam, Functioning of glacierized catchments in Monsoon and Alpine regimes of Himalaya, *Journal of Hydrology* (Impact Factor: 5.72)
2. **Smriti Srivastava** and Mohd. Farooq Azam, Mass-, and energy-balance modelling of Dokriani Bamak and Chhota Shigri glaciers in Himalaya since 1979, *Journal of Glaciology* (Impact Factor: 3.12)

### C. Other publication during PhD thesis:

1. Mohd. Farooq Azam, Patrick Wagnon, Christian Vincent, A.L. Ramanathan, Naveen Kumar, **Smriti Srivastava**, J.G. Pottakkal and Pierre Chevallier, Snow and ice melt contributions in a highly glacierized catchment of Chhota Shigri Glacier (India) over the last five decades. *Journal of Hydrology*, 574, pp.760-773 (2019). (Impact Factor: 5.72)

## **D. List of Conferences, Workshops and Schools:**

- 1. Smriti Srivastava** and Mohd. Farooq Azam, American Geophysical Union (AGU) 2021, 13-17 December, 2021 (eLightning presentation)
- 2. Smriti Srivastava** and Mohd. Farooq Azam, European Geosciences Union (EGU) 2021, 19-30 April 2021 (PiCO presentation)
- 3. Smriti Srivastava** and Mohd. Farooq Azam, International Conference of Himalayan Cryosphere (ICHC), 19-23 October 2020, (Oral presentation)
- 4. Smriti Srivastava** and Mohd. Farooq Azam, UKIERI-DST sponsored partnership development workshop on **Water SEcurity Assessment of Indian Rivers oriGinating from Himalayas “WEIGH”**, 7-11 September 2020 (Oral Presentation)
- 5. Mohd. Farooq Azam and Smriti Srivastava**, European Geosciences Union (EGU) 2020, 4-8 May 2021 (Poster presentation)

## **ACKNOWLEDGEMENTS**

First of all I would like to thank God almighty for blessing my life with wonderful people and providing me the opportunity to be a part of IIT Indore, which helped me a lot to grow personally and professionally.

A profound sense of gratitude binds me to my guide Dr. Mohd. Farooq Azam, who has been a tremendous mentor for me. I would like to thank him for encouraging my research and for allowing me to grow as a researcher. His advice on both research as well as on my career have been invaluable. Being under his guidance has made me strive to do more. The passion and commitment he put into my research is exceptionally commendable.

My PhD research work is funded by DST-INSPIRE and SAC-ISRO project. A deep acknowledgment to the sponsoring agencies for their financial support.

I am grateful to Dr. Neelima Satyam and Dr. Guru Prakash for their worthy comments, suggestions and kind support during the completion of my research work.

I would also like to extend my sincere thanks to the Civil Engineering Department for all the support at the institute for the administrative purposes.

I express my deep sense of gratitude to Dr. Purushottam Kumar Garg for his scientific guidance. His energy and passion towards research has always motivated me.

My thanks also goes to Dr. Munir Ahmad Nayak, NIT Srinagar, for his precious support and advice during the course of my work.

A special thanks to my close friends Rosa, Parul and Saniya for all their support and encouragement during my hard times. I am also thankful to Arif, Sachin and Himanshu for all their cooperation and support in the lab at IIT Indore and during the field visit.

I am deeply indebted to my parents for always letting me to follow my passion. Their unconditional support and love throughout my life supported me a lot. Thanks to my sister and brother-in-law for their constant support, love and care.

Finally, I am thankful to all who directly and indirectly contributed, helped and supported me.

# TABLE OF CONTENTS

<b>ABSTRACT</b> .....	I
<b>LIST OF PUBLICATIONS</b> .....	II
<b>ACKNOWLEDGEMENTS</b> .....	IIV
<b>LIST OF FIGURES</b> .....	X
<b>LIST OF TABLES</b> .....	XVIII
<b>ACRONYMS</b> .....	XX
<b>Chapter 1</b> .....	1
<b>Introduction</b> .....	1
1.1 Importance of HK glaciers .....	2
1.2 HK climate .....	2
1.2.1 Temperature changes .....	3
1.2.2 Precipitation changes .....	3
1.3 Hydrological regimes in the HK region .....	4
1.4 Methods for glacier surface mass balance estimation .....	5
1.4.1 Glaciological method .....	6
1.4.2 Geodetic method .....	6
1.4.3 Modelling approaches .....	7
1.4.3.1 Temperature-index models .....	8
1.4.3.2 Surface Energy balance models .....	8
1.5 Methods for estimating glacier runoff .....	9
1.5.1 Direct discharge measurement .....	9
1.5.2 Hydrological balance approach .....	10
1.5.3 Hydrological models .....	10
1.6 Limitations and research gaps .....	11
1.7 Objectives of the thesis .....	11
1.8 Organization of the thesis .....	12
<b>Chapter 2</b> .....	14
<b>Literature review</b> .....	14
2.1 Introduction .....	14
2.2 Glacier changes in HK region .....	15

2.2.1	Glacier snout fluctuations and areal changes .....	15
2.2.2	Mass balance changes .....	17
2.2.2.1	Mass balance changes at glacier scale .....	17
2.2.2.2	Mass balance changes at regional scale .....	18
2.3	Temperature-index mass balance modelling of HK glaciers .....	18
2.4	Energy-balance modelling of HK glaciers .....	19
2.5	Hydrological modelling of HK glaciers .....	21
2.5.1	Present status of Hydrological modelling .....	21
2.5.2	Challenges in Glaciohydrological modelling .....	24
2.5.2.1	Glacier Area/Volume .....	24
2.5.2.2	Precipitation distribution .....	25
2.5.2.3	Permafrost thaw .....	25
2.5.2.4	Black carbon and dust .....	26
2.5.2.5	Sublimation .....	26
2.5.2.6	Debris cover .....	27
2.5.2.7	Glacier Dynamics .....	27
<b>Chapter 3</b>	.....	<b>30</b>
<b>Long-term dimensional and mass balance changes on Dokriani Bamak and Chhota Shigri glaciers using satellite data and modelling</b>	.....	<b>30</b>
3.1	Introduction .....	30
3.2	Study Area .....	32
3.3	Data and methods .....	33
3.3.1	Data Used .....	33
3.3.1.1	Satellite data .....	33
3.3.1.2	Meteorological data and bias-correction since 1950 .....	34
3.4	Methodology .....	36
3.4.1	Glacier area and snowline altitude changes .....	36
3.4.2	Mass-balance model .....	37
3.4.3	Model Parameters .....	40
3.4.4	Model calibration and validation .....	41
3.4.5	Uncertainty estimation .....	42
3.5	Results .....	43
3.5.1	Glacier retreat and area loss .....	43
3.5.2	Annual and seasonal glacier-wide mass balances .....	45

3.6 Discussion.....	48
3.6.1 Fragmentation of western tributary glacier of Chhota Shigri Glacier.....	48
3.6.2 Decadal mass balances and climatic drivers .....	49
3.6.3 Linkages between glacier dimensional changes and mass balances.....	52
3.6.3.1 Snout retreat and areal changes.....	53
3.6.3.2 Dynamic changes .....	55
3.7 Conclusions.....	56
<b>Chapter 4 .....</b>	<b>58</b>
<b>Glacier-wide mass, and energy balances of Dokriani Bamak and Chhota Shigri glaciers using energy balance approach .....</b>	<b>58</b>
4.1 Introduction.....	58
4.2 Site description, available field measurements and climate data.....	61
4.2.1 Study area: Dokriani Bamak and Chhota Shigri glaciers.....	61
4.2.2 Available field data .....	64
4.2.3 Climate data and bias correction.....	64
4.3 Methods .....	65
4.3.1 Mass-, and energy-balance model.....	65
4.3.2 Accumulation terms .....	65
4.3.3 Ablation terms.....	66
4.3.4 Computation of surface temperature.....	66
4.3.5 Computation of turbulent heat fluxes.....	67
4.3.6 Computation of conductive heat flux and wetness parameter for debris surface.....	68
4.3.7 Computation of mass balance .....	69
4.3.8 Model Parameters .....	71
4.3.9 Model Calibration .....	72
4.3.10 Model Validation .....	73
4.3.11 Uncertainty estimation.....	74
4.4 Results.....	76
4.4.1 Meteorological conditions and seasonal characteristics .....	76
4.4.2 Glacier-wide annual and seasonal mass balances .....	79
4.4.3 Seasonal and annual glacier-wide surface energy balance .....	81
4.4.4 Altitudinal distribution of mean annual mass balance and SEB .....	83
4.4.5 Glacier-wide sublimation.....	87

4.4.6 Relative mass wastage from snow, clean ice and debris-covered ice .....	88
4.5 Discussion .....	89
4.5.1 SEB in ablation and accumulation zones .....	89
4.5.2 Major drivers for glacier mass balances.....	91
4.5.3 Annual glacier-wide mass balance sensitivity .....	93
4.6 Conclusions.....	94
<b>Chapter 5 .....</b>	<b>97</b>
<b>Glaciohydrological modelling of Dokriani Bamak Glacier .....</b>	<b>97</b>
5.1 Introduction.....	97
5.2 Study Area, climatic settings and previous studies .....	99
5.3 Data and methods.....	102
5.3.1 Climate data and bias corrections .....	102
5.3.2 Model set-up .....	104
5.3.3 Model parameters.....	107
5.3.4 Model calibration .....	110
5.3.5 Model validation .....	113
5.3.6 Model sensitivity and uncertainty estimation .....	116
5.4 Results.....	119
5.4.1 Annual and seasonal glacier-wide mass balances.....	119
5.4.2 Equilibrium-line altitude and accumulation area ratio.....	119
5.4.3 Annual and seasonal catchment-wide runoff .....	122
5.5 Discussion.....	125
5.5.1 Spatial distribution of debris-cover, altitudinal mass balances and gradients .....	125
5.5.2 Decadal mass balances, runoffs and climatic drivers.....	128
5.5.3 Near-balanced conditions preceding 2000 .....	129
5.5.4 Mass balance and runoff sensitivity .....	131
5.5.5 Model equifinality.....	132
5.6 Conclusions.....	133
<b>Chapter 6 .....</b>	<b>136</b>
<b>Glacier mass balance-runoff relationship in Monsoon and Alpine regimes of Himalayan catchments .....</b>	<b>136</b>
6.1 Introduction.....	136

6.2 Climate, study area and existing data .....	138
6.2.1 Climate and climatic regimes.....	138
6.2.2 Study area .....	139
6.2.3 MB and runoff data.....	141
6.3 Methods .....	144
6.3.1 Climate data and bias correction.....	144
6.3.2 Glacio-hydrological model .....	144
6.3.3 Model parameters and extrapolation of climate data .....	148
6.3.4 Model calibration and validation .....	149
6.3.5 Uncertainty estimation .....	151
6.3.6 Glacier MB-runoff relationship: concept.....	154
6.4 Results.....	155
6.4.1 Glacier-wide MBs and annual mass turn over .....	155
6.4.2 Catchment-wide runoffs.....	157
6.4.3 Glacier-wide MB and catchment-wide runoff patterns.....	157
6.5 Discussion.....	160
6.5.1 Glacier MB-runoff relationship in Himalaya: short-term historical data.	160
6.5.2 Glacier MB-runoff relationship in studied reference catchments: long-term modelled data.....	163
6.5.3 Glacier buffer system: glacier-degraded runoff .....	166
6.5.4 Hydrological years: daily mean glacier-wide MBs and catchment-wide runoffs.....	168
6.6 Conclusions.....	171
<b>Chapter 7 .....</b>	<b>173</b>
<b>Conclusions and scope of future work .....</b>	<b>173</b>
7.1 Conclusions.....	173
7.2 Future scope of work .....	176
<b>REFERENCES.....</b>	<b>179</b>

## LIST OF FIGURES

**Figure 1.1:** Map of Himalaya-Karakoram (HK) region showing the location of three major river basins. Glacier boundary (blue colour) is from GAMDAM glacier inventory and basin boundaries are from (Bajracharya and Shrestha, 2011). (Here, KK= Karakoram, WH = western Himalaya, CH = central Himalaya, EH = eastern Himalaya)

**Figure 1.2:** Panel (A) and (B) show annual temperature and precipitation extracted from ERA5 (<https://cds.climate.copernicus.eu/>) over 1979-2019. (Here, KK= Karakoram, WH = western Himalaya, CH = central Himalaya, EH = eastern Himalaya)

**Figure 1.3:** The three major glaciohydrological regimes of HK.

**Figure 1.4:** Energy balance fluxes at the glacier surface.

**Figure 2.1:** Annual glacier-wide mass balances using glaciological method over HK.

**Figure 2.2:** Annual glacier-wide mass balances using T-index modelling over HK.

**Figure 2.3:** Geographic location of studies discussed in Table 2.2. The Melt contribution is the sum of snow and glacier melts while the other contribution is the sum of rain and base flow (Table 2.2). HK region is divided into four sub-regions, *i.e.* Karakoram (KK), western Himalaya (WH), central Himalaya (CH), and eastern Himalaya (EH) (Bolch et al., 2012), the basin boundaries (IB, GB and BB) are from (Bajracharya and Shrestha, 2011).

**Figure 3.1:** Location of (A) Dokriani Bamak Glacier (yellow outline) on sentinel-2 MSI sensor imagery of 28 October 2020 and (B) Chhota Shigri Glacier (yellow outline) on sentinel-2 MSI sensor imagery of 21 September 2020 in the Himalaya

**Figure 3.2:** Mass-balance model:  $T$  and  $P$  is daily temperature and precipitation,  $L_R$  is temperature lapse rate,  $P_G$  is precipitation gradient,  $T_M$  is threshold temperature for melt and  $T_P$  is threshold temperature for precipitation.

**Figure 3.3:** Model calibration and validation: Scatter plots are showing the correlations between modelled and field-observed mass balances for (A1)

Dokriani Bamak Glacier over 1993-2000 and (B1) Chhota Shigri Glacier over 2004-2019 and between modelled and satellite-derived snow line altitudes (SLA) for Dokriani Bamak and Chhota Shigri glaciers, respectively (B1 and B2) over 1992 to 2017.

**Figure 3.4:** Snout changes of (A) Dokriani Bamak Glacier between 1968 to 2020 and (B) Chhota Shigri Glacier between 1971 to 2020 (Background image is from Sentinel-2/MSI sensor 28 October 2020 and 21 September 2020 respectively on panel A and B)

**Figure 3.5:** Annual mass balances (AMB; positive = blue bars and negative = orange bars), winter mass balances (WMB) with purple lines and summer mass balances (SMB) with green lines for (A) Dokriani Bamak Glacier and (B) Chhota Shigri Glacier over 1950-2020 are shown. The annual mass balance uncertainty is shown with grey lines.

**Figure 3.6:** (A) and (B) shows Chhota Shigri Glacier boundaries for year 2009 and 2020 respectively, and (C) and (D) shows field photographs of tributary glacier of Chhota Shigri Glacier from September 2016 and September 2018, respectively.

**Figure 3.7:** Mean summer, winter and annual mass balances (MBs) for all the seven decades (1950-2020) (Black thick lines). Red thick line represents the mean decadal summer temperature ( $^{\circ}\text{C}$ ) and green thick and dotted lines represents mean decadal summer and winter precipitation sums (mm) at (A) Dokriani Bamak Glacier and (B) Chhota Shigri Glacier respectively.

**Figure 4.1:** (A) The state boundary of Himanchal Pradesh and Uttarakhand along with locations of Dokriani Bamak and Chhota Shigri glaciers, (B) DBG (red outline) on Google earth imagery (CNES-Airbus) of 10 July 2017, (C) CSG (red outline) on Google earth imagery (CNES-Airbus) of 10 April 2017.

**Figure 4.2:** Mass-, and energy-balance model structure.  $T_a$  is air temperature,  $P$  is precipitation,  $RH$  is relative humidity,  $WS$  is wind speed,  $SW$  and  $LW$  are the shortwave and longwave radiations,  $L_R$  is the temperature lapse rate,  $P_G$  is precipitation gradient,  $T_M$  is threshold temperature for melt,  $T_P$  is threshold temperature for precipitation,  $\alpha_s$  is the albedo of snow,  $\alpha_i$  is the albedo of ice, and  $\alpha_d$  is the albedo of debris cover.

**Figure 4.3:** Model calibration: the modelled (green) and field-observed (violet)  $B_a$  on DBG over 1992-2014 (a), and CSG over 2003-2019 (b). Insets in both the panels show the correlations between modelled and field-observed mass balances.

**Figure 4.4:** Model validation: the modelled and field-observed mean  $b_a$  over 2009-2013 for DBG (a) and over 2002-2013 for CSG (b). Orange and blue bars show the 50-m hypsometry of debris-covered and clean glacier; orange and blue stars show the field-observed mean  $b_a$  for the debris-covered and clean glacier; orange and blue lines show the modelled mean  $b_a$  for the debris-covered and clean glacier.

**Figure 4.5:** Glacier-wide mean monthly values of  $T_a$  (red dots),  $T_s$  (brown dots),  $RH$  (green triangles),  $WS$  (blue circles),  $P$  (grey bars),  $SWI$  (orange bars) and  $LWI$  (violet bars) at (a) DBG base camp (3774 m a.s.l) and (b) CSG high camp (4863 m a.s.l), respectively from bias-corrected ERA5 data over 1979-2020.  $SWI$  and  $LWI$  are at point scale while all other parameters are at glacier-wide scale.

**Figure 4.6:** Annual mass balances (black squares), winter mass balances (green bars), and summer mass balances (grey bars) over 1979-2020 on (a) DBG and (b) CSG, respectively. The uncertainties of annual mass balances are shown.

**Figure 4.7:** Box-whisker plots of mean daily SEB components calculated from all available data from 1979-2020 and classified into seasons, post-monsoon, winter, pre-monsoon, and summer-monsoon. The boundaries of each box cover the 25<sup>th</sup> to the 75<sup>th</sup> percentile of each distribution, while the middle line of the box shows the median value. Box-whisker in (a - e) shows the values for DBG and (f - j) CSG, respectively.

**Figure 4.8:** Distribution of modelled mean altitudinal mass balances and mean SEB components for 1979-2020 period of (a) DBG and (b) CSG, respectively. Glaciers' maps not to scale.

**Figure 4.9:** Monthly mean glacier-wide  $T_a$  (orange dots),  $RH$  (brown triangles),  $WS$  (blue stars), sublimation (blue-green bars) on (a) DBG and (b) CSG.

**Figure 4.10:** Relative mass wastage contribution from snow (dark blue color), clean ice (green color), and debris-covered ice (orange color) on (a) DBG and (b) CSG.

**Figure 4.11:** SEB in ablation and accumulation zones of (a) DBG and (b) CSG.

**Figure 4.12:** The panel (a) and (b) shows a graphical representation of correlations with 1% (0.01)  $p$  significance values among the inter-annual variability of mass balance, energy fluxes and its meteorological drivers during 1979-2020 for DBG and CSG, respectively (red color shows negative while blue color shows positive correlation values). WMB and SMB are winter and summer mass balances.

**Figure 5.1:** Location of the study area. (a) panel a show the state boundary of Uttarakhand, (b) locations of Tela camp, base camp and advance base camp, in Dokriani Glacier catchment, and (c) location map of Dokriani Glacier catchment (red outline) and the glacier area (yellow line) on imagery from Google Earth (CNES/Airbus) of 10 July 2017. The locations of surrounding mountain peaks Jaonli, DKD I and II are also shown on the map.

**Figure 5.2:** The hypsography (50-meter altitudinal ranges) for Dokriani Glacier catchment. Symbology: grey, blue and orange bars represent the catchment area, glacier area and debris-covered glacier area. The glacier area-altitude distribution is estimated in the present study using the high-resolution google earth image (CNES/Airbus) on 10 July 2017.

**Figure 5.3:** (a) Mean monthly cycle of temperature and precipitation obtained from daily data from ERA5 bias-corrected series over 1979-2018. Mean monthly cycles of temperature, relative humidity and precipitation observed at Dokriani Glacier base camp from available studies (Thayyen et al., 2005; Verma et al., 2018) are also shown, (b) Series of annual mean temperature (blue dots) and annual precipitation sums (blue bars) from bias-corrected ERA5 data set (1979-2018).

**Figure 5.4:** Glacio-hydrological model structure.  $T_p$ ,  $P_G$ ,  $T_{LR}$ ,  $T_M$ ,  $DDF_{S,I,D}$  are the threshold temperature for snow/rain limit, altitudinal precipitation gradient, temperature lapse rates, threshold temperature for melt, degree day factor

(*DDF*) for snow, ice and debris-covered ice, respectively. The details about all input parameters are given in Table 5.2.

**Figure 5.5:** Monthly temperature lapse rates ( $T_{LRs}$ ) in Dokriani Glacier catchment estimated between Tela Camp (TC, 2540 m a.s.l.), Base Camp (BC, 3763 m a.s.l.) and Advance Base Camp (ABC, 4364 m a.s.l.) from all available studies. The black dots are the mean monthly  $T_{LRs}$  estimated from Thayyen and Dimri (2018) and Yadav et al. (2019), error bars show the  $1\sigma$  values (standard deviation). The dotted line shows the standard environmental lapse rate value of 6.49 °C/km.

**Figure 5.6:** Scatter plot between mass balances and runoffs RMSEs (root mean square errors) estimated through model calibration (section 3.4). Grey dots show the total model runs and red dot shows the selected model run.

**Figure 5.7:** Model Calibration, (a) the modelled and field-observed mass balances and (b) the modelled and field-observed mean monthly runoffs. The inset in panel (a) shows the correlation between modelled and observed annual mass balances.

**Figure 5.8:** Validation of modelled snow Line Altitudes (SLAs) with the satellite-derived SLAs for 28 days between 1992 and 2017. The red line indicates a perfect agreement between modelled and satellite-derived SLAs.

**Figure 5.9:** (a) Annual (black bars), winter (green bars) and summer (orange bars) glacier-wide mass balances for Dokriani Glacier over the modelled period of 1979–2018. The uncertainties on annual, winter and summer glacier-wide mass balances are also shown. The horizontal dotted line represents the zero MB, (b) equilibrium line altitude as a function of annual-glacier wide mass balances, and (c) accumulation area ratio as a function of annual-glacier wide mass balance.

**Figure 5.10:** Mean monthly hydrographs of total runoff and different hydrologic components (snow melt, ice melt, and rainfall-induced runoff) for the whole year. The envelopes on hydrographs represent the parametric uncertainties.

**Figure 5.11:** Box-Whisker plot of modelled mean annual mass balances (m w.e.  $a^{-1}$ ) calculated for 50m intervals (1979-2018) for Dokriani Glacier. The

boundaries of each box indicate the upper and lower quartiles, while the middle line of the box shows the median value. Whisker ends indicate the maximum and minimum values excluding outliers (shown as green plus sign). Orange and light blue bars represent the fraction of debris-covered and clean ice area for each 50m altitudinal range below 5000 m a.s.l. while orange and light blue dots represent the mass balance fractions from debris-covered and clean ice area from each 50m altitudinal range below 5000 m a.s.l. The mean altitudinal mass balance gradients for debris-covered ablation area (<5000 m a.s.l.), clean ablation area (5000-5500 m a.s.l.) and accumulation area (5500-6600 m a.s.l.) are shown in black, blue and red lines.

**Figure 5.12:** Distribution of modelled mean altitudinal mass balances for 1979-2018 period over the whole glacier. Dotted lines show the contours at 50 m difference.

**Figure 5.13:** The cumulative mass balance curves for Mera (central Himalaya, Nepal) over 1961-2007 (Shea et al., 2015b), Chhota Shigri (western Himalaya, India) over 1969-2016 (Azam et al., 2019) and Dokriani glaciers for 1979-2018 (present study). The grey shaded area between 1989-1997 shows the near-balanced state for Dokriani Glacier.

**Figure 5.14:** Contour maps showing the RMSE for mass balance (panel a) and runoff (pane b) for ranges of threshold melt temperature and precipitation gradient used in model calibration (section 3.4).

**Figure 6.1:** Location of eight glacierized catchments where glacier-wide MB and catchment-wide runoff measurements are available in the Himalaya (Table 6.1). Glacier cover (white polygons) is from RGIv6 ([https://www.glims.org/RGI/rgi60\\_dl.html](https://www.glims.org/RGI/rgi60_dl.html)). The green lines represent the rivers in different basins.

**Figure 6.2:** Location of Dokriani Bamak Glacier (DBG) (A) and Chhota Shigri Glacier (CSG) (B) catchments in the Himalaya. Red and green polygons show the boundary of glaciers and catchments, respectively and insets show the 50-m hypsometry for debris cover (orange bars), clean glacier (green bars) and total catchment area (yellow bars) in both the catchments.

**Figure 6.3:** MB-runoff model structure.  $T$ ,  $P$ ,  $T_P$ ,  $T_{LR}$ ,  $T_M$ ,  $P_G$  and  $DDF_{S,I,D}$  are the temperature, precipitation, threshold temperature for snow/rain limit, temperature lapse rates, threshold temperature for melt, altitudinal precipitation gradient and degree day factor (DDF) for snow, ice and debris-covered ice, respectively.

**Figure 6.4:** Model Calibration: Modelled and field-observed glacier-wide mass balances for DBG (A1) and CSG (B1); Modelled and field-observed catchment-wide runoffs for DBG (A2) and CSG (B2) and Model validation: Modelled and satellite derived SLAs for DBG (A3) and CSG (B3) ; Modelled and field-observed catchment-wide runoffs for DBG (A4) and CSG (B4).

**Figure 6.5:** Annual (black shaded bars), winter (green dots) and summer (orange dots) glacier-wide MBs and annual catchment-wide runoffs on (A) DBG in Monsoon regime and (B) CSG in Alpine regime over 1950-2020. Error bars are showing MBs and runoff uncertainties.

**Figure 6.6:** Mean monthly hydrographs of total runoff and different hydrologic components (snow melt, ice melt and rainfall runoff) for (A) DBG and (B) CSG catchment. Pie charts in inset show the rain on glacierized area, rain on un-glacierized area, snow melt on glacier, snow melt on un-glacierized area and glacier ice melt.

**Figure 6.7:** Relationship between annual glacier-wide MB and mean daily summer runoff at catchment outlet (Table 6.1) for eight glaciers' catchments in the Himalaya. DBG, Shaune Garang, Gara, Neh Nar and Hamtah glaciers (panels A-E) showed higher catchment-wide runoff associated with less negative glacier-wide MBs while Tipra Bank, Dunagiri and CSG (F-H) showed higher catchment-wide runoff with more negative glacier-wide MBs. However, the MB-runoff relationship is significant only on CSG ( $p < 0.05$ ). 'A' stands for alpine and 'M' stands for monsoon catchment regime.

**Figure 6.8:** Relationship between annual glacier-wide MB and annual mean glacier-wide runoff for DBG (A) and SCG (B) catchments.

**Figure 6.9:** Correlation matrix for DBG (A) and CSG (B) catchments. Large circles correspond to strong correlations while smaller circles represent weaker correlations. The color scale indicates the sort of correlation (1 denotes

completely positive correlation, dark blue, and  $-1$  denotes completely negative correlation, dark red). Only significant correlations are shown ( $P < 0.05$ ). AMB, SMB and WMB = Annual, summer and winter glacier-wide MBs; GLQ, NGQ and CTQ = Glacier runoff, non-glacier runoff and catchment runoff; AnnP, WinP and SumP = Annual, winter and summer precipitation sums, and AnnT, WinT and SumT = Annual, winter and summer mean temperatures.

**Figure 6.10:** Relationship between annual glacier-wide MB and mean daily catchment-wide runoffs on Dokriani (DBG) (A) and Chhota Shigri (CSG) (B) catchments. Glacier-degraded runoff % contribution to total catchment-wide runoff is also shown.

**Figure 6.11:** Panel (A) shows glacier-wide daily mass balances and (B) shows catchment-wide daily runoffs for Dokriani (DBG) and Chhota Shigri (CSG). Hydrological year is defined between 1<sup>st</sup> October to 30 September of next year.

## LIST OF TABLES

**Table 2.1:** SEB studies over HK glaciers.

**Table 2.2:** Some of the studies with % estimates of different hydrologic components of river runoff in the HK region. Studies were selected to keep the representations from meso-watershed scale to the basin scale studies and to show the most common methods used (water balance, hydrograph separation, T-index, SEB, ablation model). Total melt is estimated by combining glacier and snow melts from each study. In each basin, the studies are arranged from a larger to smaller scale.

**Table 3.1:** List of satellite data used in the present study. Dokriani Bamak Glacier = DBG, Chhota Shigri Glacier = CSG.

**Table 3.2:** List of model parameters, sensitivity and uncertainty ranges for Dokriani Bamak Glacier and Chhota Shigri Glacier.

**Table 3.3:** Changes in various glacier and climatological parameters during the study. DBG = Dokriani Bamak Glacier, Chhota Shigri Glacier = CSG.

**Table 3.4:** Decadal mass balances (MB, m w.e./y) and meteorological parameters on Dokriani Bamak and Chhota Shigri glaciers (winter (WMB, m w.e./y) and summer (SMB, m w.e./y) mass balances, precipitation sum (P, mm), winter precipitation sum (WinP, mm), summer precipitation sum (SumP, mm), temperature (T, °C), winter temperature (WinT, °C), summer temperature (SumT; °C)

**Table 4.1:** Abbreviation, unit and value of parameters used in this study.

**Table 4.2:** List of geographical and topographical characteristics of DBG and CSG.

**Table 4.3:** List of model parameters, sensitivity and uncertainty ranges for DBG and CSG.

**Table 4.4:** Mean seasonal and annual  $T_a$ ,  $T_s$ ,  $RH$ ,  $WS$ ,  $SWI$ ,  $LWI$  and  $P$  using bias-corrected ERA5 data over 1979-2020.

**Table 4.5:** Mean seasonal and annual glacier-wide SEB components ( $W m^{-2}$ ) on DBG and CSG.

**Table 4.6:** Mean seasonal and annual SEB components ( $\text{W m}^{-2}$ ) over ablation and accumulation zone of DBG and CSG.

**Table 5.1:** Topographical characteristics of Dokriani Glacier catchment.

**Table 5.2:** List of the model parameters, range of parameters used to estimate the uncertainties (section 3.6), and mass balance and runoff sensitivity for unit change in each parameter estimated in section 5.5.4.

**Table 5.3:** Modelled mean glacier-wide mass balance, equilibrium line altitude (ELA), accumulation area ratio (AAR) and runoff are discussed in section 5.4. The modelled mean mass balance gradients are estimated separately for debris-covered ablation area (<5000 m a.s.l.), clean ablation area (5000-5500 m a.s.l.) and accumulation area (5500-6600 m a.s.l.) (section 5.3.1) Mean Meteorological conditions are calculated from bias-corrected ERA5 dataset available over 1979-2018 and extracted at Base Camp (section 5.3.1).

**Table 5.4:** Mean annual (AMB), summer (SMB) and winter (WMB) glacier-wide mass balances ( $\text{m w.e. a}^{-1}$ ) for demarcated periods I (1979-1988), II (1989-1997), III (1998-2006), IV (2007-2018) and for the whole 39-year period over 1979-2018 with their corresponding catchment-wide snow-melt runoff, ice-melt runoff, rainfall runoff, and total runoff. All hydrologic components are in  $\text{m}^3 \text{s}^{-1}$ . The values in brackets show the runoff contribution of each hydrologic component in % with respect to total runoff. Mean temperature ( $^{\circ}\text{C a}^{-1}$ ) and precipitation ( $\text{mm w.e. a}^{-1}$ ) anomalies are also shown for each period.

**Table 6.1:** Characteristics of eight glacierized catchments in the Himalaya where glacier-wide annual MB and catchment-wide runoff data are available.

**Table 6.2:** Details of the model parameters, input data, calibration, and validation. Details can be found in Azam et al. (2014b; 2019) and Azam and Srivastava, (2020).

**Table 6.3:** List of model parameters and uncertainty ranges for DBG and CSG catchments.

**Table 6.4:** Annual and seasonal glacier-wide MBs ( $\text{m w.e. a}^{-1}$ ) for periods I (1951-1975), II (1976-2000) and III (2001-2020) with their corresponding total catchment-wide runoffs ( $10^6 \text{ m}^3 \text{ a}^{-1}$ ).

## ACRONYMS

Himalaya-Karakoram	HK
Surface Energy Balance	SEB
Temperature Index	T-index
Karakoram	KK
Western Himalaya	WH
Central Himalaya	CH
Eastern Himalaya	EH
Survey of India	SOI
Geological Survey of India	GSI
Dokriani Bamak Glacier	DBG
Chhota Shigri Glacier	CSG
Global Land Ice Measurements from Space	GLIMS
Digital Elevation Model	DEM
Degree Day Factor	DDF
Annual Mass Balance	AMB
Summer Mass Balance	SMB
Winter Mass Balance	WMB
Mass Balance	MB
Equilibrium line altitude	ELA
Accumulation area ratio	AAR
Automatic Weather Station	AWS
Base Camp	BC
Root Mean Square Error	RMSE
Indian Summer Monsoon	ISM
Western Disturbances	WDs
Snow Line Altitude	SLA

# Chapter 1

## Introduction

The Himalaya-Karakoram (HK) often known as the Third Pole or Water Tower of Asia is stretching east to west over 2500 km with a total glacierized area of  $\sim 42,000 \text{ km}^2$  and more than 39000 glaciers (Azam et al., 2021) (Fig. 1.1). The snow and ice reserves impact the billion-plus population by regulating the flow of HK rivers: river systems *i.e.* Indus, Ganga and Brahmaputra (Fig. 1.1). The HK glaciers are losing mass over the last 5-6 decades (Azam et al., 2018) with a heterogeneous pattern along with the Himalayan range and near-steady state over the Karakoram (Brun et al., 2017; Shean et al., 2020). These glacier changes directly impact river runoff (Immerzeel et al., 2020; Lutz et al., 2014), and reductions in glacier volumes contribute to sea-level rise (Zemp et al., 2019).

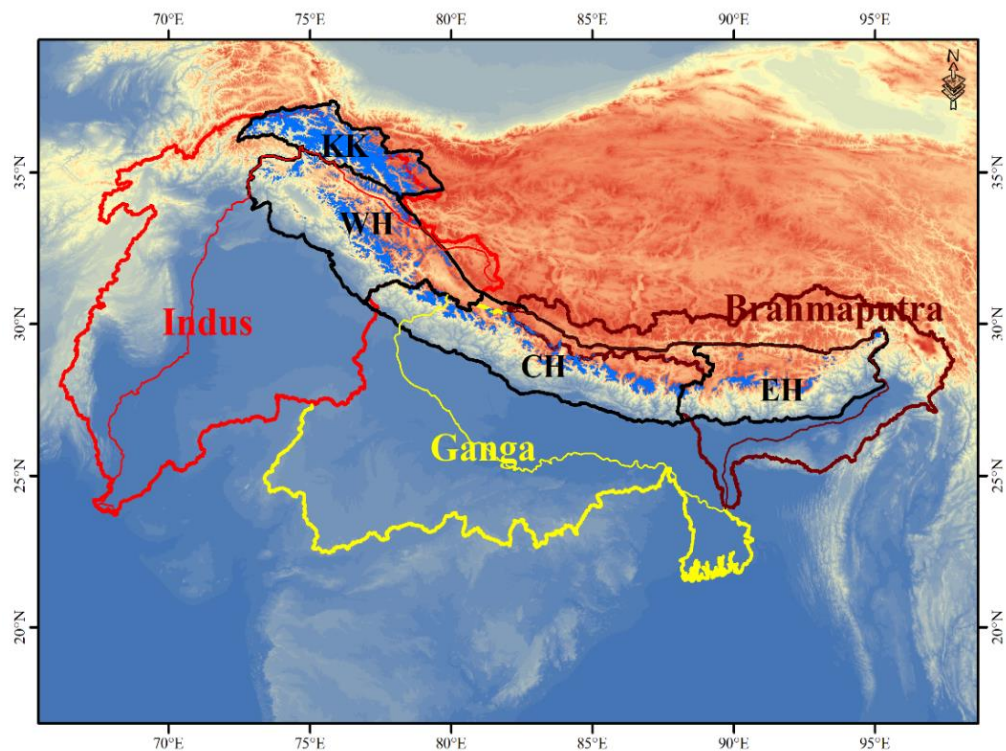


**Figure 1.1:** Map of Himalaya-Karakoram (HK) region showing the location of three major river basins. Glacier boundary (blue colour) is from GAMDAM glacier inventory and basin boundaries are from (Bajracharya and Shrestha,

2011). (Here, KK= Karakoram, WH = western Himalaya, CH = central Himalaya, EH = eastern Himalaya)

## **1.1 Importance of HK glaciers**

With the increasing population and industrialization, the demand for fresh water is increasing worldwide. The available snow and ice over the HK region are an essential source of fresh water (Immerzeel et al., 2010). HK river basins cover an area of 2.75 million km<sup>2</sup> and have the largest irrigated area (~577,000 km<sup>2</sup>), 5 megacities (Delhi, Dhaka, Karachi, Kolkata and Lahore) with populations greater than 94 million, and the world's largest installed hydropower capacity (26,432 MW) (Azam et al., 2021). A large population residing downstream depends on the rivers originating from the HK basins as they are considered as the most melt-water dependent river systems on the earth (Schaner et al., 2012). Heterogeneous mass balance response of the HK glaciers suggests that the impact of a changing climate on melt runoff generation depends on the geographic location, changes in local, regional, and global climate, and a range of interactive effects that include orographic forcing, spatial variability, and debris cover (Azam et al., 2018). Glacier changes are also linked with potential hazards such as glacial lake outburst floods and landslides (Bhambri et al., 2020; Fujita et al., 2013). Therefore, there is a need for integrated and continuous monitoring of the HK glaciers.

## **1.2 HK climate**

The HK climate is influenced by two synoptic circulation systems, i.e. Indian Summer Monsoon (ISM) and Indian Winter monsoon (IWM) (Dimri et al., 2015; Schiemann et al., 2008). The ISM originates from the Indian Ocean and propagates northward, producing the bulk of annual precipitation over the Indian sub-continent, particularly over the southern rim of the Himalaya during summers. Conversely, the IWM originates over the Mediterranean Sea/West Atlantic Ocean and brings precipitation, mainly in solid form, to the high-altitude Mountains during winters. The Inter Tropical Convergence Zone (ITCZ) regulates these circulation systems (Bookhagen and Burbank, 2010).

### **1.2.1 Temperature changes**

More than a billion people are partly dependent on HK river basins that raises a serious concern about the impact of climate change on the HK glaciers. Due to the scarcity of high-altitude meteorological stations in the HK region, a better understanding of climatic variables is missing. However, the studies based on low-elevation observations reveal rising temperatures over the past five decades (Hock et al., 2019; Nepal and Shrestha, 2015). Based on ERA5 data over 1979-2019, the mean annual temperatures are higher over Indo-Gangetic plains and south slopes of the HK region compared to elevated north slopes of the HK region (Fig. 1.2A). The temperature trends over the HK region show warming over the whole HK indicating accelerated mass loss in the recent decades (Banerjee and Azam, 2016; Krishnan et al., 2019).

### **1.2.2 Precipitation changes**

The changes in temperature are projected to cause changes in precipitation patterns. The physical factors influencing precipitation are far more complex to understand and result in wide variations in precipitation trends over different regions. The precipitation patterns have not shown any significant trend over the HK (Doblas-Reyes et al., 2021). The notable decreasing trend in the annual precipitation has been reported by several studies in the western Himalaya (Bhutiyan et al., 2010; Dimri and Dash, 2012). Contrary, an increasing trend in winter precipitation has been reported in the upper Indus basin. The steep regional orography plays a dominant role in the formation of precipitation rather than large scale circulation (Dimri, 2004; Fowler and Archer, 2005). Based on ERA5, the mean annual precipitation is highest over the eastern Himalaya (~2850 mm w.e.) and lowest over the Karakoram (~600 mm w.e.) of the HK region (Fig. 1.2).

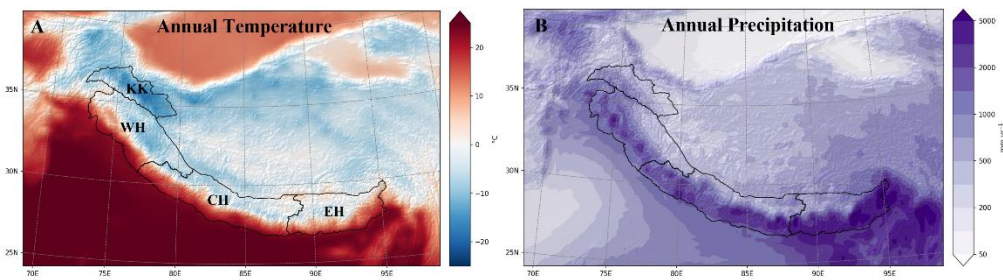


**Figure 1.2:** Panel A and B show annual temperature and precipitation extracted from ERA5 (<https://cds.climate.copernicus.eu/>) over 1979-2019. (Here, KK= Karakoram, WH = western Himalaya, CH = central Himalaya, EH = eastern Himalaya)

### 1.3 Hydrological regimes in the HK region

The glaciers of the HK region are exposed to different glaciohydrological regimes because of their different geographical extent and regional orography and climate. Based on spatial and temporal distribution of precipitation and runoff, the HK region is characterized in three major glacio-hydrological regimes: (1) Himalayan catchments, (2) Alpine catchments, and (3) Cold-arid catchments (Thayyen and Gergan, 2010). In the Himalayan catchments (central and eastern Himalaya), major precipitation comes from ISM during summer (Fig. 1.2A), which delivers rain at lower altitudes and snow over high altitudes (Bookhagen and Burbank, 2010). Glacier meltwater also contributes to the river runoff during this period of high annual flows produced by the ISM (Lutz et al., 2014). In these catchments, periods of summertime ablation coincide with snow accumulation; hence, the glaciers therein are characterized as ‘summer-accumulation type glaciers’. Alpine catchments (western Himalaya and Karakoram) receive more uniform precipitation over the hydrological year with two slight peaks in Feb-March and July-August (Fig. 1.3). However, major snow accumulation occurs during winters due to IWM; hence, the glaciers therein are characterized as ‘winter-accumulation type glaciers’. This accumulated snow is melted in summer months and produces distinct accumulation and ablation periods (Azam et al., 2014a). Though average precipitation in the Karakoram is only  $\sim 600$  mm w.e.  $a^{-1}$ , around 83% of annual

precipitation falls as snow due to the higher altitudes and lower temperatures (Fig. 1.2). The western Himalaya represents a transition area receiving a moderate amount of annual precipitation (~1075 mm w.e.), with a majority of snow accumulation during IWM (Dimri et al., 2015) and smaller and sporadic snowfall events during the summer ablation period (Azam et al., 2016). However, in Cold-arid catchments of the Ladakh mountain range (northwest mountain range of western Himalaya) both ISM and IWM are weak, leading to very low amounts of annual precipitation. Glacier and snow melt is thus a major source of water during summers (Thayyen and Gergan, 2010).

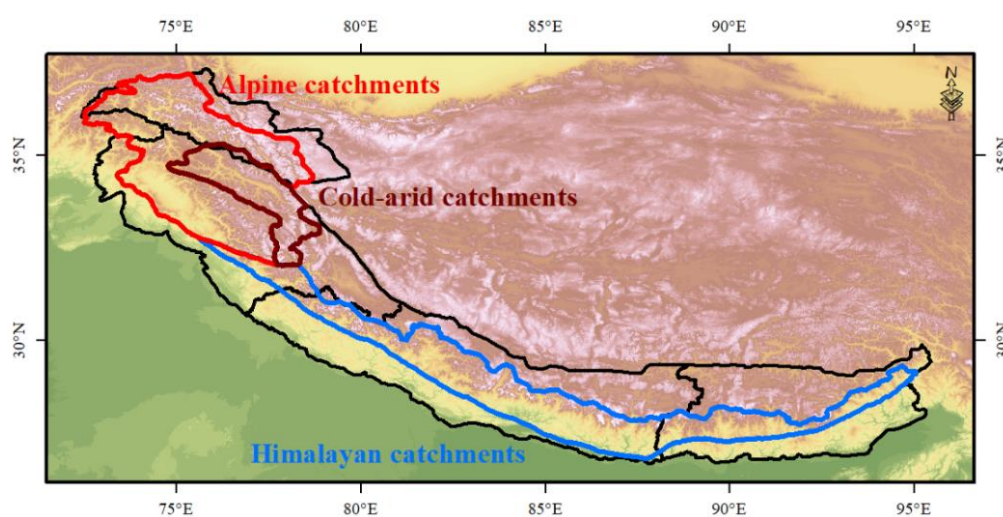


**Figure 1.3:** The three major glaciohydrological regimes of HK.

#### **1.4 Methods for glacier surface mass balance estimation**

Glacier mass balance is defined as the difference between accumulation and ablation (Cuffey and Paterson, 2010). If the ablation is equal to accumulation, then the glacier is in a balanced state. If the mass balance is positive or negative, the glacier is advancing or retreating. The changes in glacier mass balance provide crucial information about climate change, water resources and sea-level rise (Zemp et al., 2019). Further, glacier mass balance is a direct signal of glacier's health, reflecting the changing climate. There are several methods for glacier mass balance estimation including in-situ, remote sensing or modelling approaches.

### 1.4.1 Glaciological method

The glaciological method is the method that uses field measurements to estimate the glacier mass balance at annual or seasonal scale (Kaser et al., 2003). Point-scale measurements for ablation using stakes in the ablation zone and accumulation using coring or snow pits in the accumulation zone are performed on some selected sites on the glacier surface (Østrem and Brugman, 1966). The glacier-wide mass balance is calculated by interpolating these point-scale ablation and accumulation measurements over the corresponding altitudinal areas as given in equation 1.1:

$$B_a = \frac{\sum A_n b_n}{A} \quad (1.1)$$

Where  $B_a$  is the glacier-wide mass balance (m w.e.),  $b_n$  is the altitudinal mass balance (m w.e.),  $A_n$  is the altitudinal area of the glacier ( $m^2$ ) and  $A$  is the total glacier area ( $m^2$ ). This method necessitates huge manpower and is very difficult over the rough terrain of the HK region; therefore, generally, small glaciers have been chosen for this method that raises a question on the representativeness of these glaciers at a regional scale (Vincent et al., 2013). Though having large uncertainties, this approach provides the most specific information on the spatial variation of mass balance magnitudes (Azam et al., 2012; Kaser et al., 2003; Wagnon et al., 2021).

### 1.4.2 Geodetic method

In the geodetic method, the volume change is estimated by differencing the surface elevations at glacier-scale or regional-scale (having large glacierized area) using Digital Elevation Models (DEMs) obtained at two different time periods, generally at 5-10 years gap (Bolch et al., 2011; Racoviteanu et al., 2009). This volume change is then converted into mass change using the surface density of different parts of the glacier (Huss, 2013). This method is now widely used to estimate elevation changes and hence mass balance of glaciers throughout the world (Berthier et al., 2007; Gardelle et al., 2013; Zemp et al., 2019). Unlike the glaciological method, geodetic method does not offer yearly

and seasonal glacier surface mass balance variations, required for understanding the glacier-climate relationship. Besides providing a mean mass balance over 5-10 years period, geodetic estimates can also be used to cross check the glaciological mass balances, as later often being affected with systematic biases (Azam et al., 2016; Wagnon et al., 2021; Zemp et al., 2013).

### **1.4.3 Modelling approaches**

The direct glaciological measurements of mass balance provide insights about individual glacier ice volume changes at a seasonal or annual scales (Zemp et al., 2015). However, extrapolating these glacial observations, made over a few glaciers, to worldwide glacier mass balance estimates can lead to significant uncertainties (Braithwaite et al., 2006; Huss and Hock, 2018; Zemp and Marzeion, 2021). Glacier mass balance modelling provides an alternative solution to extrapolate these glacier-scale, in-situ observations temporally and spatially, to regional scale. These models can be categorized as (i) based on empirical relationship between melt and air temperature called as Temperature-index (T-index) or degree-day models (Hock, 2003; Martinec et al., 1995) and (ii) based on detailed energy fluxes called as surface energy balance (SEB) models (Azam et al., 2014a; Wagnon et al., 1999). The T-index models are simple and require very limited input data. Conversely, the SEB models are physically based and complex hence require a lot of input parameters. Unfortunately, due to the scarcity of in-situ measurements at high altitudes of the HK region the applications of SEB models are very scarce (Azam et al., 2014a). This forces the use of simplified T-index models for mass balance simulations as they depend on temperature and precipitation data (Azam et al., 2014b; Kumar et al., 2020; Shea et al., 2015). The T-index models have been found to perform as good as SEB models because temperature shows a high correlation with various other components of the SEB model (Hock, 2005). These two models are discussed below in detail.

### 1.4.3.1 Temperature-index models

T-index models are based on the relationship of melt and air temperature, expressed as positive temperature sums (Hock, 2003). The basic equation for this model is as given in equation 1.2:

$$M = DDF * T \quad (1.2)$$

Where  $M$  (mm) is the amount of ice or snow melt,  $T$  ( $^{\circ}\text{C}$ ) is the positive air temperatures and  $DDF$  ( $\text{mm d}^{-1} \text{ }^{\circ}\text{C}^{-1}$ ) is the degree-day factor.

### 1.4.3.2 Surface Energy balance models

SEB models are based on complex energy balance equations (Hock, 2005) and provide detailed results, but require a lot of extensive input datasets. The major contribution to glacier ablation comes from the surface melt (Azam et al., 2014a; Favier et al., 2004; Litt et al., 2019), calculated using the net energy flux available at the surface. The simplified equation of surface energy balance model is (Fujita and Ageta, 2000; Fujita and Sakai, 2014; Fujita et al., 2011):

$$Q = (1 - \alpha_{s,i,d}) SWI + LWI - \varepsilon\sigma(T_s + 273.15)^4 + H + L + R \quad (1.3)$$

Where  $Q$  is the net surface energy budget ( $\text{Wm}^{-2}$ ),  $\alpha_{s,i,d}$  is the albedo of snow ( $\alpha_s$ ), ice ( $\alpha_i$ ) and debris surface ( $\alpha_d$ ),  $\varepsilon$  is emissivity (dimensionless) and considered 1, and  $\sigma$  is the Stefan Boltzmann constant =  $5.67 \times 10^{-8} \text{ W m}^{-2} \text{ K}^{-4}$ ,  $T_s$  is the surface temperature ( $^{\circ}\text{C}$ ).  $H$ ,  $LE$  and  $R$  are the turbulent sensible heat, latent heat and rain fluxes ( $\text{W m}^{-2}$ ), respectively. Fig. 1.4 is the systematic representation of different processes which are accounted for on the glacier surface.

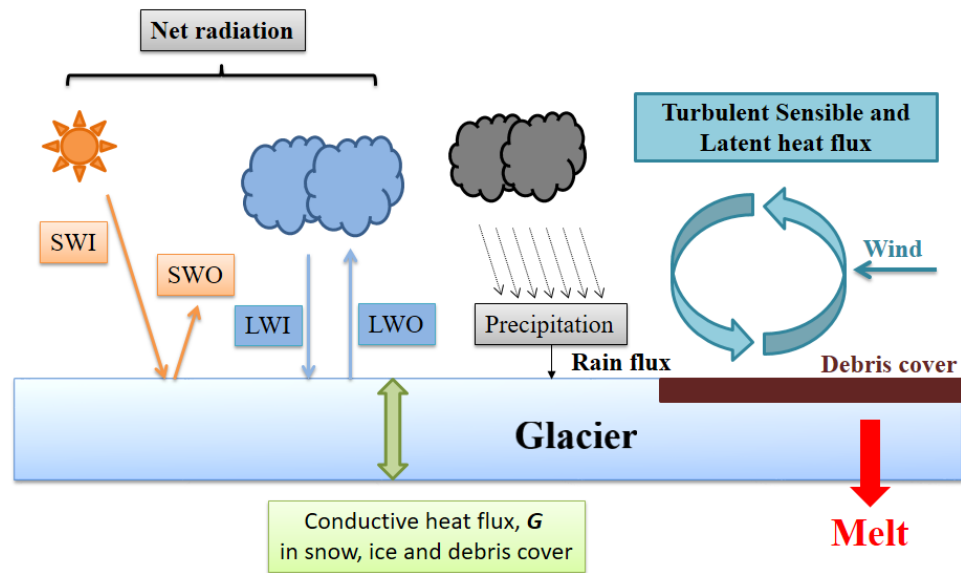


**Figure 1.4:** Energy balance fluxes at the glacier surface.

## 1.5 Methods for estimating glacier runoff

A range of methods with varying complexities have been developed to estimate the runoff composition of the HK rivers. These methods include empirical relationships between precipitation and runoff (Kraaijenbrink et al., 2017; Pritchard, 2019), water balance approaches (Singh and Jain, 2002; Singh et al., 1997), ice ablation models (Racoviteanu et al., 2013), hydrograph separation methods (Mukhopadhyay and Khan, 2014; Mukhopadhyay and Khan, 2015), snow-melt modeling (Bookhagen and Burbank, 2010; Immerzeel et al., 2010; Tahir et al., 2016; Tahir et al., 2011), isotope tracer methods (Boral and Sen, 2020; Jeelani et al., 2017; Maurya et al., 2011), the glaciological method (Brun et al., 2017) and semi-distributed/distributed glaciohydrological models (Armstrong et al., 2019; Bocchiola et al., 2011; Eeckman et al., 2019; Immerzeel et al., 2013; Immerzeel et al., 2010; Jeelani et al., 2012; Lutz et al., 2014; Nepal and Shrestha, 2015; Ragetti et al., 2015). Direct discharge measurement, hydrological balance approach and hydrological models are further discussed in details below.

### 1.5.1 Direct discharge measurement

Direct discharge measurement is the simplest and least data intensive method for assessing glacier contribution to the total watershed discharge by taking

measurements immediately downstream of the glacier tongue (Gascoin et al., 2011; Thayyen and Gergan, 2010). In this approach, it is assumed that all the water coming to the glacier tongue is from glacier parts and all the glacial melt water is measured at the first stream gauge within the watershed (Frenierre and Mark, 2014). However, direct discharge measurements are often performed some distance downstream the glacier snout (Thayyen and Gergan, 2010) that induces a lot of uncertainty by bringing large non-glacierized parts into account. Direct discharge measurements are often made using velocity-area method that requires channel width, stream velocity and water flow depth at vertical cross section (Hersch, 1993). The mean stream velocity and cross-sectional area give the total discharge passing through the cross section, known as discharge site.

### **1.5.2 Hydrological balance approach**

The hydrological balancing approach is a straightforward method based on mass conservation in the water cycle. The basic hydrological mass balance equation is given as:

$$Q = P + \Delta G - G_w - E \quad (1.4)$$

Where  $Q$  is the total discharge,  $P$  is the precipitation,  $\Delta G$  is the glacier storage change,  $G_w$  is the groundwater flux and  $E$  is the net evapotranspiration (Mark and Seltzer, 2003). This equation can be further simplified if evapotranspiration and groundwater flux are neglected.

### **1.5.3 Hydrological models**

It is not possible to estimate the glacier melt contribution to total river runoff through field-based methods. Hydrological modelling is the most widely used method for calculating the contribution of the glacier melt water to total river runoff. These models combine glaciological, meteorological and hydrological data to improve the understanding of hydrological processes (Verbunt et al., 2003). In general, there are two main categories of hydrological models (1) physically-based models that require a lot of input data and thus limited to smaller watersheds from where in-situ data is available (2) conceptual models are based on past hydro-climatic conditions and simulate hydrology of the

watershed using statistical relationships (Hagg et al., 2011). The latter approach simplifies input data requirement and can be applied to those watersheds where data availability is limited. But these conceptual models are more prone to the problem of equifinality (Hagg et al., 2011) where different combinations of model parameters can produce the same output with inducing a significant source of uncertainty in the modelled hydrologic components (Beven, 2006).

## **1.6 Limitations and research gaps**

In-situ glaciohydrological studies in the HK are available for a few glacierized catchments for short period of time. Most of the glaciohydrological models have been applied at either covering the whole HK or large basins that generally use very limited data for model calibration and validation hence the modelled mass balances and runoffs carry large uncertainties. The catchment-scale long-term glacier-wide mass balance and runoffs reconstructions are limited in the HK due to limited in-situ glaciohydrological data, mainly because of inaccessibility and rugged terrain over the HK. The glacier-climate relationship in different climatic regions is also poorly understood in the HK region. Further, the relationship between glacier mass balance and runoff is not yet understood in the HK due to data scarcity. Therefore, the present situation necessitates an understanding of the present and past behaviour of a few selected glacierized catchments from different climatic regimes where ample amount of in-situ data is available.

## **1.7 Objectives of the thesis**

Keeping the research gaps mentioned above in mind, two representative glacierized catchments, one from the Monsoon-dominated regime 'Dokriani Bamak Glacier catchment' and other from the Alpine regime 'Chhota Shigri Glacier catchment' have been selected for the present study. These catchments are selected mainly because of their different climatic regimes (Monsoon vs. Alpine) and the availability of in-situ observations.

The main motive of this study is to reconstruct long-term dimensional changes, glacier mass balances and catchment runoffs for the selected 11 glacierized

catchments, and to understand the glacier-climate relationship in the Monsoon and Alpine regimes. The following objectives have been framed in this research work:

- Status of glaciohydrology in the Himalaya-Karakoram.
- Long-term dimensional and mass balance changes on Dokriani Bamak and Chhota Shigri glaciers using satellite data and modelling.
- Glacier-wide mass, and energy balances of Dokriani Bamak and Chhota Shigri glaciers using energy balance approach.
- Glaciohydrological modelling of Dokriani Bamak Glacier.
- Glacier mass balance-runoff relationship in Monsoon and Alpine regimes of Himalayan catchments.

## **1.8 Organization of the thesis**

The thesis is organized as follows to address all the above-mentioned objectives.

**Chapter 1** presents a brief about the HK glaciers, climate, hydrological regimes, and different methods for estimating glacier mass balance and runoff. This chapter highlights the research gaps and defines the objectives.

**Chapter 2** describes the status of the glacier snout and area changes, and glaciohydrology of the HK. It includes a comprehensive review of all the available studies, advancements and challenges, and the sources of various uncertainties which have been overlooked in the past glaciohydrological studies.

**Chapter 3** presents dimensional and mass balance changes of Dokriani Bamak and Chhota Shigri glaciers over the last seven decades using satellite data and modelling. Dimensional (glacier area and snout position) changes were investigated using satellite data from Corona (1968-1971), Landsat TM/ETM+ (1993-2010) and Sentinel-MSI (2020) along with limited field checks. Besides, the annual and seasonal glacier-wide mass balances on both the glaciers were reconstructed applying a simple T-index model forced with bias-corrected ERA5 data over 1950-2020. The models were calibrated/validated through extensive in-situ data.

**Chapter 4** discusses a mass-, and energy-balance model used to compute the glacier-wide mass balances on Dokriani Bamak and Chhota Shigri glaciers using bias-corrected ERA5 data over 1979-2020. The model is calibrated using available in-situ glacier-wide annual mass balances and validated against in-situ mean altitudinal mass balances on both the glaciers.

**Chapter 5** reconstructs the glacier-wide mass balance and catchment-wide runoff over 1979-2018 for the Dokriani Glacier catchment in Garhwal Himalaya (India) using a simplified T-index glaciohydrological model. The model was forced with daily air temperature and precipitation fields from bias-corrected ERA5 reanalysis products. The model was calibrated using 6 years of observed annual glacier-wide mass balances (1993-1995 and 1998-2000) and observed summer mean monthly runoff (1994, 1998-2000) data. Model validation was done using satellite-derived snow line altitudes and field-observed runoff (1997-1998).

**Chapter 6** discusses the long-term relationships between glacier-wide annual mass balances and catchment-wide runoffs on the selected reference catchments—Dokriani Bamak Glacier and Chhota Shigri Glacier—in the Himalaya using the long-term output from a simplified T-index glaciohydrological model since 1950. Further, the available short-term, in-situ glacier mass balance and runoff data have also been exploited to understand the mass balance-runoff relationship in eight glacierized catchments of the Himalaya.

**Chapter 7** is the conclusion of the work that has been presented in the thesis and a small description of the future scope of this work that can be carried out for further development in this field.

## Chapter 2

### Literature review

#### 2.1 Introduction

The Himalayan–Karakoram (HK) region in South Asia, often called the water tower of Asia or the Third Pole (Immerzeel et al., 2020), is one of the most heavily glacierized mountain regions on Earth (Bolch et al., 2019). Glaciers in the HK mountain ranges exhibit a range of responses to the changing climate (Azam et al., 2018; Gardelle et al., 2013). In general, Himalayan glaciers have been retreating and losing mass since the end of the Little Ice Age (~1850), similar to other mountain ranges (Bolch et al., 2012; Bolch et al., 2019; Brun et al., 2017). Conversely, the Karakoram glaciers showed a mean balanced state at least since 1970s (Azam et al., 2018; Bolch et al., 2019). This heterogeneous mass wastage of HK glaciers suggests that the impact of a changing climate on melt runoff generation depends on the geographic location, changes in local, regional, and global climate, and a range of interactive effects that include orographic forcing, spatial variability, and debris cover. The dynamic storage of water in the HK cryosphere regulates the runoff into regional river systems (primarily Indus, Ganges and Brahmaputra basins), by releasing water generally in April through October— primarily snow melt in April through June, and glacier melt in June through October. Basin runoff is the sum of snow melt, glacier melt, rainfall run-off and base flow from groundwater recharge (Lutz et al., 2014), minus evaporation and evapotranspiration. In addition, storage and release from glacial lakes and reservoirs can modulate basin flow. Permafrost, which covers a substantial fraction of the HK region (Gruber et al., 2017), controls surface water–groundwater interactions and is significant for water and ice storage but is currently not represented in hydrological models. The presence of snow, glacier and permafrost within each of these basins changes the spatio-temporal river runoff characteristics from what would occur with only rainfall-runoff and base flow. Thus, cryospheric change has direct impacts on runoff (Immerzeel et al., 2020; Lutz et al., 2014), and reductions in glacier volumes

contribute to sea level rise (Gardner et al., 2013; Zemp et al., 2019). The subsequent sections of this chapter discuss the areal and mass changes in glaciers and, status of runoff estimates over the HK.

## **2.2 Glacier changes in HK region**

The glacier fluctuation is the filtered and delayed response of climate forcing (Oerlemans, 2005; Sakai and Fujita, 2017); therefore, deriving the climate signal from glacier fluctuations is difficult (Zemp et al., 2008). Conversely, glacier mass balance is the direct and un-delayed response to climatic conditions (Singh et al., 2018). Here, a detailed compilation of studies is made in order to understand the glacier retreat, area loss and mass balance changes over the HK.

### **2.2.1 Glacier snout fluctuations and areal changes**

Before satellite images, glacier snout fluctuations and areal changes were carried out using topographical maps and aerial photographs. The plane table survey and heavy theodolites were used to survey the HK glaciers in the early 19<sup>th</sup> century (Godwin-Austen, 1864). Survey of India (SOI) and Geological Survey of India (GSI) started producing topographical maps at various resolutions for many glaciers using plane table, terrestrial photogrammetry and aerial images mixed with field images since 20<sup>th</sup> century (Survey of India, 2005). These topographical maps are not in public domain and some of these maps contain errors (Bhambri and Bolch, 2009). As a result, the uncertainties of mapped glacier outlines are obscure. Starting in the 1960s, satellites have delivered images of glacierized areas around the globe. Comparison of the latest satellite-based images with old maps and photographs allowed researchers to quantify the glacier snout fluctuations or area changes. Some revised studies using the satellite data (Chand and Sharma, 2015; Nainwal et al., 2016) indicated an overestimation of area shrinkage and snout retreat compared to the previous studies. The majority of the Himalayan glaciers have been retreating, with rates ranging regionally and from glacier to glacier, since the mid-nineteenth century, whereas the snouts of the Karakoram glaciers have been

retreating, stable, or advancing (Azam et al., 2018; Bolch et al., 2012; Cogley, 2011). The length change varies greatly across the Himalaya, ranging from 60 to 88 metres every year (Kulkarni et al., 2021). Furthermore, glaciers in the Karakoram region have exhibited just a slight length change ( $1.37 \pm 22.8$  metres per year), indicating a mean stable condition (Azam et al., 2018).

The majority of glacier area change studies were conducted at a basin-wide scale, with only a few individual glacier scale (Azam et al., 2018). Along the Himalayan range, shrinkage is quite common over the HK region in last 5-6 decades with huge variation from  $-0.07 \text{ \% a}^{-1}$  for Kimoshung Glacier over 1974-2015 to  $-1.38 \text{ \% a}^{-1}$  for Ganju La Glacier over 2004-14 (Azam et al., 2018). Since the mid-nineteenth century, however, glaciers in the Karakoram Range have shown a minor areal decrease or steady state (Azam et al., 2018). Over the period 1965-2005, glaciers in the Khumbu Valley ( $92 \text{ km}^2$ ) showed a  $-0.12 \text{ \% a}^{-1}$  decrement in glacier area (Bolch et al., 2008). Salerno et al. (2008) found a similar decline rate of  $-0.14$  over a  $404 \text{ km}^2$  glacierized area in the same region from 1956 to 1990 using historical maps. The differences in these estimations can be attributed to varying glacierized area extents because of challenges in mapping debris-covered glaciers, varied observation times, methodology, data used and related uncertainties.

In the HK, increasing supraglacial debris-covered area was caused by shrinking clean-ice areas (Nuimura et al., 2012; Scherler et al., 2011; Thakuri et al., 2014). Multiple observation periods in studies demonstrated specific trends in area shrinkage rates from different parts of the HK. Over the last 5-6 decades, steady trends in the eastern Himalaya (Racoviteanu et al., 2015), accelerated shrinkage in the central Himalaya (Bolch et al., 2008; Thakuri et al., 2014), and decreasing shrinkage in the western Himalaya's Zaskar and Ravi basins (Chand and Sharma, 2015; Schmidt and Nüsser, 2012) have been observed.

## 2.2.2 Mass balance changes

### 2.2.2.1 Mass balance changes at glacier scale

There has been a significant increase in the number of field mass-balance studies related in the HK region, but still these studies are scarce compared to the vast HK region. Glacier mass balances were estimated using glaciological, gravimetric, geodetic and hydrological balance approaches. The glaciological mass balance studies are highly significant in remote areas where the glacier-climate relationship is still not well understood. The first glaciological mass balance study was started on Gara Glacier in September 1974 by GSI (Raina et al., 1977). Susequently, GSI and some other institutes/organisations started working on several other glaciers in different regions of the HK. Presently, the glaciological mass balance measurements are available for around 27 glaciers over the HK (Fig. 2.1). These estimates are available for short and discontinuous time periods (Azam et al., 2018). The mean annual mass balance estimate of the HK glaciers showed a negative trend since 1975 (Fig. 2.1).

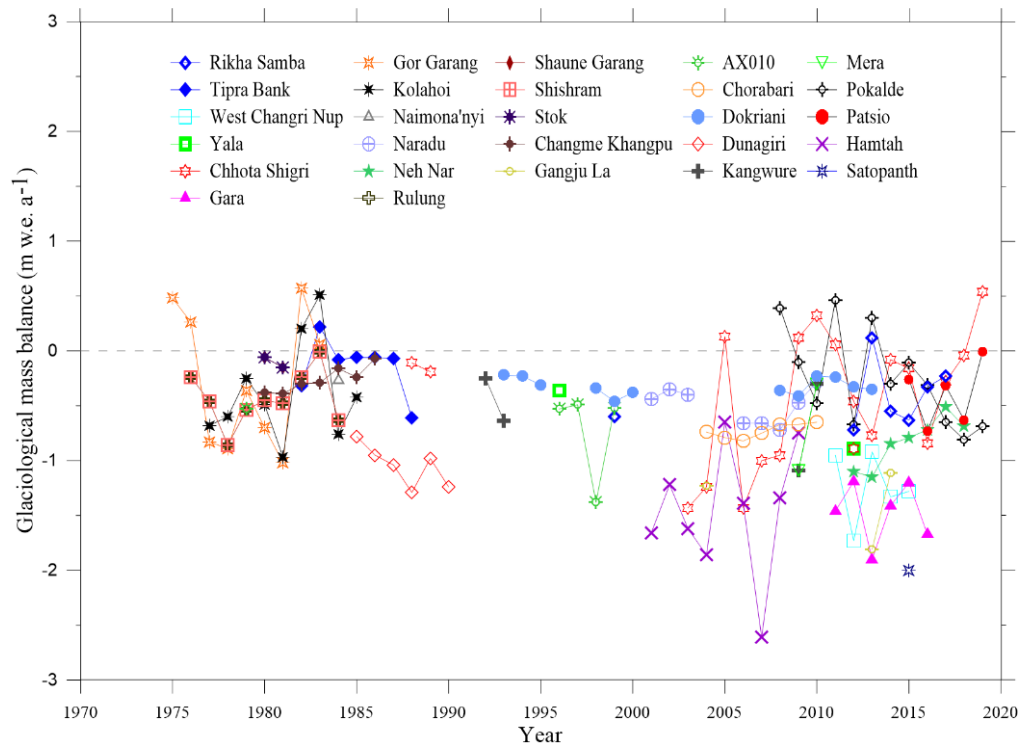


**Figure 2.1:** Annual glacier-wide mass balances using glaciological method over the HK.

### **2.2.2.2 Mass balance changes at regional scale**

In recent decade since 2000, with rapid advancement in the satellite images, several studies have been undertaken to calculate the mass balance changes over the HK. Bolch et al. (2011) estimated a mass balance of  $-0.32 \pm 0.08$  m w.e  $a^{-1}$  over 1970-2002 and  $-0.79 \pm 0.52$  m w.e  $a^{-1}$  over 2002-2007 for Khumbu region. Another study, over the Khumbu region stated a mean mass balance of  $-0.45 \pm 0.60$  m w.e  $a^{-1}$  over 2000-2008 (Nuimura et al., 2012). Gardelle et al., 2013 showed largest mass wastage in the western Himalayas ( $-0.45 \pm 0.13$  m w.e  $a^{-1}$ ), moderate mass loss in the central and eastern Himalayas ( $-0.22 \pm 0.12$  m w.e  $a^{-1}$  to  $-0.33 \pm 0.14$  m w.e  $a^{-1}$ ) and mass gain in Karakoram east and west regions ( $+0.11 \pm 0.14$  m w.e  $a^{-1}$  and  $+0.09 \pm 0.18$  m w.e  $a^{-1}$ ). Another regional study, suggested that moderate mass loss has been observed over the Himalayan range with values ranging from  $-0.42 \pm 0.20$  m w.e  $a^{-1}$  in Bhutan to  $-0.33 \pm 0.20$  m w.e  $a^{-1}$  in the east Nepal region between 2000-2016 obtained using time series of digital elevation models derived from satellite stereo imagery (Brun et al., 2017). One of the most recent studies estimated total High Mountain Asia (HMA) glacier mass balance as  $-0.19 \pm 0.03$  m w.e  $a^{-1}$  between 2000-2018, suggesting relatively large mass loss with some spatial variability (Shean et al., 2020).

### **2.3 Temperature-index mass balance modelling of HK glaciers**

T-index melt modelling is the most common approach for mass balance computation as it includes only air temperature and precipitation as an input data (Hock, 2003). Despite of being in simplest category, their performance is relatively good. Most of the widely used hydrological models such as HBV (Bergström, 1976), SRM (Martinec et al., 1995), UBC (Quick and Pipes, 1977), HYMET (Tangborn, 1984), SHE (Bøggild et al., 1999), SPHY (Terink et al., 2015) use T-index models. These models are based on assumed relationship between melt and air temperature along with degree day factors (Fig. 2.2).

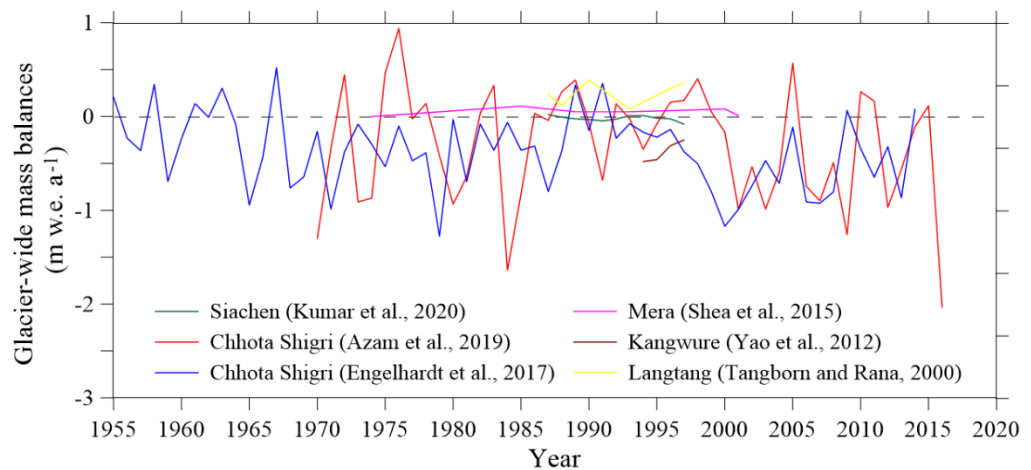


**Figure 2.2:** Annual glacier-wide mass balances using T-index modelling over HK.

## 2.4 Energy-balance modelling of HK glaciers

The glacier surface energy balance (SEB) can be used to understand the physical basis of glacier-climate relationships. In SEB modelling, the energy for melt is mainly supplied by net radiation flux, followed by turbulent fluxes (Hock, 2005). A limited number of SEB studies are available, the majority of them being from the Nepal's central Himalaya, most of them are at point scale and only for short period of time (Rounce et al., 2015; Steiner et al., 2018; Acharya and Kayastha, 2019; Litt et al., 2019; Matthews et al., 2020; Steiner et al., 2021). In Indian Himalaya, a few studies have been performed both at point-scale and glacier-wide scale (Table 2.1). Singh et al. (2020) conducted an SEB experiment on a moraine surface with ephemeral snow cover near the Pindari Glacier in Uttarakhand using two-year data from a weather station. Recent study, estimated glacier-wide surface energy balances over eight selected glaciers in Chandra Basin using remote sensing data (Patel et al., 2021) (Table 2.1).

**Table 2.1:** SEB studies over HK glaciers

Glacier	Elevation (m)	Region	Period	R ( $W m^{-2}$ )	H ( $W m^{-2}$ )	LE ( $W m^{-2}$ )	Reference
Baltoro	3490-8610	Karakoram	25 June – 31 Aug 2004	102	10	-14	Collier et al. 2013
Chandra basin	4000-6400	Western Himalaya	October 2013 – Sep 2019	77	16	-11	Patel et al. 2021
Chhota Shigri	4863	Western Himalaya	8 Jul – 5 Sep 2013	187	31	11	Azam et al. (2014a)
Dhundi	4670	Western Himalaya	13 Jan – 12 Apr 2005	83	3	-1	Datt et al. (2008)
Ganglass, Ladakh	3050	Western Himalaya	1 Sep 2015 – 31 Aug 2017	29	14	13	Wani et al. (2020)
Ganja La	4727	Central Himalaya	5 March – 25 May 2018	42	14	-8	Stigter et al. (2021)
Yala	5090	Central Himalaya	9 February – 26 May 2018	30	25	-25	Steiner et al. (2018) Stigter et al. (2021)
Camp II, Everest	6464	Mt. Everest, Central Himalaya	24 Jun – 31 Oct 2019	20	3	-8	Matthews et al. (2020)
South Col, Everest	7945	Mt. Everest, Central Himalaya	22 May – 31 Oct 2019	16	11	-25	Matthews et al. (2020)
AX010	5080	Central Himalaya	25 May – 25 Sep 1978	55	8	3	Kayastha et al. (1999)
Pindari	3750	Central Himalaya	13 Jun 2016 – 30 Jan 2018	76	-10	2	Singh et al. (2019)
East Rongbuk	6523	Central Himalaya	1 May – 22 July 2005	41	12	-20	Liu et al. (2021)
Naimona'nyi	5950	Central Himalaya	Oct 2010 – Sept 2018	8	12	-16	Zhu et al. (2021)

## **2.5 Hydrological modelling of HK glaciers**

### **2.5.1 Present status of Hydrological modelling**

Glacio-hydrological modeling—a representation of the hydrological cycle at glacier/river basin scale—is widely used to understand the relative contribution of different runoff components to total river runoff. Unlike most of the other methods (Table 2.2), modeling allows all major runoff components to be computed separately. Several glacio-hydrological studies, covering meso-watershed (<100 km<sup>2</sup>) to meso-basin scale (>200,000 km<sup>2</sup>), have been carried out to understand the river runoff composition and analyze the temporal variations of different runoff components (Table 2.2).

In-situ glacio-hydro-meteorological data from high altitudes are very limited in the HK region (Eeckman et al., 2019; Mandal et al., 2020; Shea et al., 2015a); therefore, glaciohydrological studies frequently use T-index models, in which snow and ice melt is a function of temperature above the freezing point and a specified melt factor. T-index approaches have been applied widely since temperatures can be estimated from regional climate models, reanalysis products, or nearby meteorological stations. However, these simplifications may not be reliable, and T-index parameters may not be transferrable between sites or seasons (Litt et al., 2019).

In water balance approaches (Singh and Jain, 2002; Singh et al., 1997), a combined contribution of snow and glacier runoff is estimated from the difference between basin-wide precipitation and runoff at basin outlet; therefore, partitioning of snow and ice melt is not possible. Similarly, the ablation method—based on mass balance gradients, assuming zero gradient at equilibrium line altitude on the glacier—estimates the combined runoff from snow and ice (Racoviteanu et al., 2013). In contrast, the hydrograph separation method can quantify baseflow, snow melt and glacial melt, separately (Mukhopadhyay and Khan, 2014; Mukhopadhyay and Khan, 2015). Detailed process-based studies that include relevant cryospheric processes such as glacier dynamics, avalanching, refreezing, and debris cover effects are available

only at meso- to macro-watershed scales (Brown et al., 2014; Fujita and Sakai, 2014; Lutz et al., 2016; Ragettli et al., 2015).

The varying climatic settings and observed heterogeneous glacier mass balances across the HK region are likely to differentially impact HK rivers. Total runoff at a given point is a combination of upstream snow and ice melt, overland runoff, shallow or deep groundwater inputs, and direct precipitation to lakes and rivers. These inputs vary both spatially and temporally but provide a starting point for identifying hydrological regimes in the HK region. This review also considers the glacier cover (GC, extracted from the corresponding studies), the time period, and the basin domain reported in each study (Table 2.2).

The definitions of ‘glacier melt’ and ‘snow melt’ vary between studies (Frenierre and Mark, 2014; Hock, 2005; Immerzeel et al., 2009; Lutz et al., 2014; Nepal and Shrestha, 2015). To provide a meaningful comparison between studies, the overall melt runoff (glacier + snow melt) and the other runoff (rainfall-runoff + base flow) were extracted from published data (Fig. 2.3; Table 2.2). Subsurface flow paths and groundwater dynamics play important roles in mountain hydrology (Andermann et al., 2012; Lutz et al., 2014), especially in the mid-elevations of the HK region (Scott et al., 2019), yet base flow computations are only occasionally integrated in the HK hydrological modeling (Table 2.2).

In the upper Indus basin (5% – 9% GC), between 62% and 72% of the total river runoff is composed of snow and ice melt (Fowler and Archer, 2005; Lutz et al., 2014; Maussion et al., 2014). However, estimates of total runoff contributions from ice melt (21% – 40%) and snow melt (22% – 49%) vary between studies (Fowler and Archer, 2005; Lutz et al., 2014), likely due to the modeling approach, definition of ‘glacier melt’, the spatial domain, and the time period considered for each study (Table 2.2). Similarly, river runoff in the Hunza (Karakoram, 20% GC), Shigar (Karakoram, 31% GC) and Baltoro basins (Karakoram, 48% GC) were largely composed of snow and ice melt (60 – 92%; Table 2.2). A simple water balance approach suggested a combined melt runoff of 41% – 59% in the Chenab (24% GC) and Sutlej (20% GC) basins (western

Himalaya) over 1982-1992 and 1986-1996, respectively (Singh and Jain, 2002; Singh et al., 1997). A T-index model study focused on a watershed with 45% GC in the Chandra basin (western Himalaya) estimated the melt runoff up to 80% over 1969-2016 (Azam et al., 2019). In general, glacier melt dominated in the Karakoram, while snow melt contributed more than glacier melt to the annual runoffs in the western Himalayan (Table 2.2, Mukhopadhyay and Khan, 2015).

In the upper Ganges basin (5% GC), combined snow and ice melt represented 20% of total runoff, with rainfall and base flow contributions of 66% and 14%, respectively, over 1998-2007 (Lutz et al., 2014). In the Dudh Koshi basin (14% GC, Everest region in central Himalaya), melt runoff was estimated as 34% (5% glacier and 29% snow melts) over 1986-1997 with a T-index model (Nepal et al., 2014). However, upstream in the same basin (43% GC), the melt runoff was 87%, with a very high glacier melt contribution of 46% over 2012-2015 using a SEB model (Mimeau et al., 2019). Hydrological investigations in the Brahmaputra basin are scarce, but in the upper Brahmaputra Basin (3% GC), melt runoff was 25% (9% glacier and 16% snow melts) and river runoff was also dominated by other runoff of 75% (rainfall-runoff = 59% and base flow = 16%) (Lutz et al., 2014).

The Langtang watershed (Ganges basin, central Himalaya) is well studied using different models and provides an opportunity to compare results from different studies. Large differences in runoff composition, with melt runoff varying from 33 to 92% for almost the same watershed outlet, were observed from different studies (Fig. 2.2 and Table 2.2). This inconsistency could be due in part to different time periods, model structures, or glacier coverage (34% - 46%) of the various studies. Changes in the location which the melt water estimations are derived, different definitions of glacier and snow melt, and the equifinality issue in applied models may also be a factor in the discrepancies, but the fact remains that the differences are large and this highlights the difficulty in comparing individual studies. A more detailed investigation is required to explain such large differences. Unfortunately, most of the available studies cannot be compared/cross-checked because they are the only studies

available in their respective regions. Further, some of the studies end during the 1990s (Table 2.2), and comparing them with recent studies is somewhat questionable, especially given the accelerating wastage of HK glaciers in many regions.

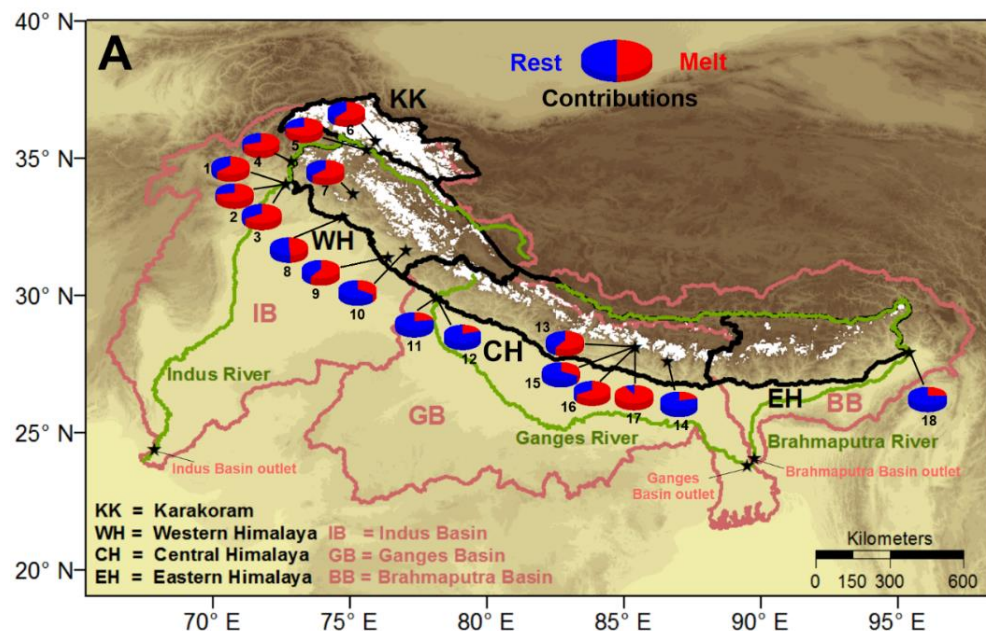


**Figure 2.3:** Geographic location of studies discussed in Table 2.2. The Melt contribution is the sum of snow and glacier melts while the other contribution is the sum of rain and base flow (Table 2.2). HK region is divided into four sub-regions, *i.e.* Karakoram (KK), western Himalaya (WH), central Himalaya (CH), and eastern Himalaya (EH) (Bolch et al., 2012), the basin boundaries (IB, GB and BB) are from (Bajracharya and Shrestha, 2011).

## 2.5.2 Challenges in Glaciohydrological modelling

In this section, the major challenges associated with glaciohydrological modelling are highlighted with a main focus on glacier area/volume, precipitation distribution, permafrost thaw, sublimation, black carbon, debris cover over glaciers and glacier dynamics.

### 2.5.2.1 Glacier Area/Volume

Accurate glacier area, volume, and quantified uncertainties are prerequisites for glacio-hydrological studies, but published records vary widely. For example, HK glacierized area estimates range from 36,800 to 50,800 km<sup>2</sup> (Bolch et al., 2012; Dong et al., 2019; Cogley, 2011; RGI Consortium, 2017). This issue is

also evident in the basin area. For instance, in the Indus basin, the estimated basin area (at Besham Qila) shows large differences ranging from 164,000 to 266,000 km<sup>2</sup> in the published literature (Khan et al., 2014). These differences are primarily due to different geographical demarcation of the mountain ranges, different maps and satellite images used, different methodologies (manual or semi-automatic methods of delineation), inclusion or not of steep avalanche walls, difficulty in identifying debris-covered parts of glaciers and cloud cover and cast shadows in satellite imagery hampering glacier delineation.

The estimated ice volumes by Frey et al. (2014) vary from 2950 to 4740 km<sup>3</sup> for the HK region based on the Bolch et al. (2012) glacier inventory. This wide range indicates the need for improvements in ice volume models and stresses the requirement of largely unavailable in-situ glacier ice thickness calibration/validation data (Azam et al., 2012; Vincent et al., 2016).

### **2.5.2.2 Precipitation distribution**

Most meteorological stations in the HK region are installed in valley bottoms, far away from the glacier (Azam et al., 2018; Shea et al., 2015a; Pellicciotti et al., 2012). As a result, many studies use bias-corrected gridded precipitation data (remote sensing and interpolated rain gauge data) that is incapable of capturing spatial (3-D) variation and magnitude of mountain precipitation (Immerzeel et al., 2015; Andermann et al., 2012; Misra et al., 2020; Palazzi et al., 2013; Rasmussen et al., 2012). Underestimation/overestimation in precipitation amounts due to flawed gradients can produce a considerable bias in the modelled runoff.

### **2.5.2.3 Permafrost thaw**

The impacts of permafrost thaw on the hydrological cycle remain unknown and understudied in the region. With a warming climate, volume changes in subsurface ice stored in permafrost can affect local water balances (Devkota and Gyawali, 2015; Biskaborn et al., 2019; Wang et al., 2019b). However, permafrost mass balance studies are now as deficient as glacier mass balance studies were half a century ago. Based on a surface temperature model (Gruber,

2012), the best estimate for the total permafrost area is 1,003,000 km<sup>2</sup> for the Himalaya-Karakoram-Hindu Kush region (HKH, including the Tibetan Plateau), which is 16 times more than the HKH glacierized area (Gruber et al., 2017), highlighting the urgency for involving permafrost in hydrological modeling of the HK rivers.

#### **2.5.2.4 Black carbon and dust**

Recently, several studies have quantified the BC/dust-induced additional melting of snow and glaciers in the HK. A shallow firn/ice core extracted from Mera Glacier (6376 m a.s.l.) in the central Himalaya was used to quantify changes in surface snow albedo over time and the potential melting caused by BC and dust (Ginot et al., 2014). When comparing the melting rates computed with a mass-SEB model at the same site, BC accelerated melting by ~16%. In comparison, the contribution of dust and BC was responsible for a maximum of 26% of surface melting between November 2009 and October 2010. Radiative transfer changes within the snowpack due to a reduction in albedo led to accelerated melting of the snowpack in the Khumbu valley, central Himalaya (Jacobi et al., 2015). As a result, the number of melting days of the winter snowpack lengthened from 3 to 10 days and 17 to 27 days during the three winter seasons between 2009 and 2012 in the presence of 100 ppb and 300 ppb BC, respectively, compared to clean snow. Such detailed studies are clustered around Mt. Everest, central Himalaya (Gertler et al., 2016); the radiative forcings of BC and dust in other parts of the HK region are unknown. Nevertheless, available findings are enough to reveal the critically important role of BC and dust deposition on snow and glacier melt via decreasing surface albedo and to highlight the need for their proper representation in glacio-hydrological models developed for HK water resources assessment.

#### **2.5.2.5 Sublimation**

Besides melting, glacier and snow surfaces also lose a significant amount of mass through sublimation (Azam et al., 2014b; Datt et al., 2008). On Chhota Shigri Glacier in the western Himalaya, which is influenced by both ISM and IWM, sublimation was ~2% of total mass loss over 2012-2013 (Azam et al.,

2014). Another study computed the sublimation on Yala Glacier in ISM-dominated central Himalaya and concluded that 21% of annual precipitation was lost through sublimation (Stigter et al., 2018). These studies advocate that the sublimation amounts have a high spatial variability and a strong dependence on regional climate and local meteorology, and can be a vital share of the mass wastage from glaciers and snow cover, especially in the dry conditions of the north-west parts of the HK (Karakoram, western Himalaya and even in the central Himalaya due to strong winds (Litt et al., 2019; Huintjes et al., 2015).

#### **2.5.2.6 Debris cover**

With T-indexed melt models, a single melt factor for ice underneath debris (which is typically less than the ice melt factor), has been used for debris-covered surfaces irrespective of the high spatial variability of debris cover along the HK region (Lutz et al., 2014; Azam et al., 2014a; Shea et al., 2015). A recent debris-cover inventory suggests more debris concentration over the Karakoram and southern slopes of the Himalaya (Mukhopadhyay and Khan, 2014). One study reconstructed spatial fields of debris thickness for the upper Langtang catchment using data from an unmanned aerial vehicle (UAV) and did SEB modeling (Ragetti et al., 2015). Thermal-band remote sensing data were used to estimate the debris thickness (Mihalcea et al., 2008; Garg et al., 2017), but these were questioned due to the long revisit time of satellite that restricts data on diurnal temperature changes (Kraaijenbrink et al., 2018). Some studies combining thermal-band satellite data with SEB models estimated the debris-thickness distribution in the HK region (Schauwecker et al., 2015), yet again stressing the need for extensive field data.

#### **2.5.2.7 Glacier Dynamics**

In glacio-hydrological modeling, glacier dynamics are often oversimplified or even neglected entirely, leading to inaccurate glacier melt contribution to total river discharge in the long-term (Immerzeel et al., 2015; Gantayat et al., 2017; Soncini et al., 2015). Simple glacier retreat models ( $\Delta h$ -parametrization) have been incorporated in micro- to meso-basin scale hydrological models (Lutz et al., 2014; Rounce et al., 2020a; Rees and Collins, 2006). Such models require

initial ice thickness and surface elevation inputs and can be developed with minimum data using glacier surface maps from different years or simplified calibration (Huss et al., 2010). Assuming basal sliding as a principal process for glacier dynamics, some studies have incorporated Weertman's sliding law in nano-basin scale hydrological models (Immerzeel et al., 2013). These elementary methods may be reasonable to represent the glacier dynamics at the basin-scale glacio-hydrological model, but essentially do not involve the principle of glacier flow (a combination of basal sliding and internal deformation) (Cuffey and Paterson, 2010), and found to have biases at glacier scale (Banerjee et al., 2020).

**Table 2.2:** Some of the studies with % estimates of different hydrologic components of river runoff in the HK region. Studies were selected to keep the representations from meso-watershed scale to the basin scale studies and to show the most common methods used (water balance, hydrograph separation, T-index, SEB, ablation model). Total melt is estimated by combining glacier and snow melts from each study. In each basin, the studies are arranged from a larger to smaller scale. (KK= Karakoram, WH = western Himalaya, CH = central Himalaya, EH = eastern Himalaya, # = study scale is adopted from Khan et al. (2001); HM = hydrological model, TI = temperature index, HS = hydrograph separation method, WB = water balance, SEB = surface energy balance, AM = ablation model, P = precipitation,  $\alpha$  = surface albedo, A = avalanche, D = debris cover, S = sublimation)

Basin/ sub-basin	Sub- region	Period	Basin area (km <sup>2</sup> )	Scale <sup>#</sup>	Glacierized area (%)	Method	Total melt (%)	Rest (%)	Glacier melt (%)	Snow melt (%)	Rainfall- runoff (%)	Base flow (%)	Reference	
<b>Indus</b>														
1.	Upper Indus	KK	1998-2007	200677	Meso basin	5	HM (TI)	62	38	40	22	27	11	Lutz et al., 2014
2.	Upper Indus	KK	2001-2005	200677	Meso basin	5	HM (TI)	72	28	32	40	28	-	Immerzeel et al., 2009
3.	Upper Indus	KK	1962-2010	172173	Meso basin	9	HS	70	30	21	49	30	-	Mukhopadhyay and Khan, 2014
4.	Sutlej	WH	1986-1996	22305	Micro basin	20	WB	59	41	59		41	-	Singh and Jain, 2002
5.	Chenab	WH	1982-1992	22200	Micro basin	24	WB	49	51	49		51	-	Singh et al., 1997
6.	Hunza	KK	2000-2010	13761	Micro basin	20	HM (TI)	92	8	47	45	8	-	Shrestha and Nepal, 2019
7.	Hunza	KK	2002-2004	13737	Micro basin	20	HM (SEB)	83	17	50	33	17	-	Shrestha et al., 2015
8.	Shigar	KK	1985-1997	7000	Nano basin	31	HM (TI)	72	28	33	40	28	-	Soncini et al., 2015
9.	Beas	WH	1990-2004	5278	Nano basin	15	WB	35	65	35		65	-	Kumar et al., 2007
10.	Baltoro	KK	1961-1990	1415	Nano basin	48	HM (TI)	60	40	39	22	4	36	Immerzeel et al., 2013
11.	Liddar	WH	1901-2010	653	Macro watershed	6	WB	62	38	2	60	38	-	Jeelani et al., 2012
12.	Chandra	WH	1969-2016	35	Meso watershed	45	HM (TI)	80	20	17	63	20	-	Azam et al., 2019
<b>Ganges</b>														
13.	Upper Ganges	CH	1998-2007	-	Meso basin	5	HM (TI)	20	80	12	9	66	14	Lutz et al., 2014
14.	Trishuli	CH	2007-2013	4603	Nano basin	14	HM (TI)	25	75	11	14	30	45	Kayastha et al., 2020
15.	Marsyangdi	CH	2004-2010	4062	Nano basin	13	HM (TI)	21	79	13	8	38	41	Kayastha et al., 2020
16.	Tamor	CH	2000-2010	3990	Nano basin	10	HM (TI)	16	84	7	9	39	45	Kayastha et al., 2020
17.	Dudh Koshi	CH	1986-1997	3712	Nano basin	14	HM (TI)	34	66	5	29	46	20	Nepal et al., 2014
18.	Din Gad	CH	1979-2018	16	Meso watershed	50	HM (TI)	56	44	22	34	44	-	Azam and Srivastava, 2020
19.	Langtang	CH	1961-1990	360	Macro watershed	46	HM (TI)	33	67	13	20	10	57	Immerzeel et al., 2013
20.	Langtang	CH	2003-2010	360	Macro watershed	44	HM (SEB)	92	8	62	30	8	-	Brown et al., 2014
21.	Langtang	CH	1988-2006	352	Macro watershed	44	AM	58	42	58		42	-	Racoviteanu et al., 2013
22.	Langtang	CH	2012-2013	350	Macro watershed	34	HM (SEB)	66	34	40	26	34	-	Ragettli et al., 2015
23.	Hinku	CH	1988-2006	158	Macro watershed	35	AM	21	79	21		79	-	Racoviteanu et al., 2013
24.	Upper Dudh Koshi	CH	2012-2015	146	Macro watershed	43	HM (SEB)	87	13	46	41	13	-	Mimeau et al., 2019
<b>Brahmaputra</b>														
25.	Upper Brahmaputra	EH	1998-2007	-	Meso basin	3	HM (TI)	25	75	16	9	59	16	Lutz et al., 2014

## Chapter 3

# Long-term dimensional and mass balance changes on Dokriani Bamak and Chhota Shigri glaciers using satellite data and modelling

### 3.1 Introduction

The majestic Himalayan Mountain Range —alias The Third Pole— holds a significant amount of frozen ice volume that regulates the headwaters of Indus, Ganga and Brahmaputra River basins, and partly cater to the water needs of more than a billion people (Azam et al., 2021). Due to climate change, the Himalayan Range witnessed the glaciers' shrinkage and wastage over the last 5 decades (Bhambri and Bolch, 2009; Azam et al., 2018; Bolch et al., 2019) with a heterogenous pattern along the Himalayan range (Kulkarni and Karyakarte, 2014; Brun et al., 2017; Shean et al., 2020). Glacier mass balance is a direct and the best indicator of climate change, while glacier retreat and shrinkage are filtered indicators (Vincent et al., 2018; Banerjee and Azam, 2016).

Due to availability of Survey of India topographic maps from 1960s, and rapid progress in satellite data acquisition and availability over the last five decades, several studies investigated the glacier snout and areal changes in the Himalayan Range (Bhambri and Bolch, 2009; Kulkarni et al., 2011; Bahuguna et al., 2014). Almost all studies stress that the Himalayan glaciers are retreating and shrinking with varying rates (Kulkarni and Karyakarte, 2014; Shukla et al., 2020) depending on the local microclimatic and topographic settings (Krishnan et al., 2019; Garg et al., 2017a; Mir et al., 2017). A systematic review, carefully excluding highly uncertain data, computed the unweighted mean area shrinkage rate of  $-0.36\%/y$  for 1960–2010 period using 60 data series, available at glacier- and regional-scale (Azam et al., 2018). Himalayan glaciers showed a regionally-varying but continuous shrinkage over 1960–2010, with slightly higher shrinkage over post-1980 period (Azam et al., 2018). The computed mean unweighted shrinkage rate of the Himalayan glaciers is less than the unweighted

mean shrinkage rate of  $-0.57\%/y$  calculated for the whole of High Mountain Asia (Cogley, 2016) over the same period. The general shrinkage of glaciers since 1960s is causing the fragmentation of large glaciers; consequently, the number of glaciers is increasing in the Himalaya (Kulkarni et al., 2007).

Over the recent years, tremendous progress has been made in satellite-based geodetic mass balance estimations at glacier as well as regional scale (Berthier et al., 2007; Vijay and Braun, 2016; 2018; Bandyopadhyay et al., 2019; Remya et al., 2020). Though these geodetic estimates unequivocally advocate glacier wastage in the Himalaya, but these estimates cannot be used to interpret the climate change at seasonal or annual scale (Vincent et al., 2018). The in-situ seasonal and annual glacier-wide mass balance observations, generally used to understand the glacier-climate processes, are extremely rare and available only on 26 glaciers for short time period (often  $<10$  years) in the Himalaya (Azam et al., 2018).

In data scarce regions such as the Himalaya, glacier mass-balance modelling provides an alternative solution to investigate the glacier-climate interactions (Azam et al., 2018; 2021). Modelling efforts have been made at regional/basin scale (Shea et al., 2015a; Tawde et al., 2017; Kumar et al., 2019) as well as at individual glacier scale (Azam et al., 2014b; Azam and Srivastava, 2020; Kumar et al., 2020; Soheb et al., 2020). Due to glacio-meteorological data scarcity in the Himalaya, often simplified Temperature-index (T-index) models have been developed (Azam et al., 2018). These models exploit the available field glacio-meteorological observations and reconstruct the glacier mass balance over the past several decades, depending on the length of the input data. A simplified T-index model application on Dokriani Bamak Glacier (central Himalaya) showed a mean wastage of  $-0.25 \pm 0.37$  m w.e./y over 1979-2018 (Azam and Srivastava, 2020). Using the same model, Chhota Shigri Glacier (western Himalaya) suggested a mean mass wastage of  $-0.30 \pm 0.36$  m w.e./y over 1969-2012 (Azam et al., 2014b).

In line with previous studies (Dobhal et al., 2004; Azam et al., 2014b; Azam and Srivastava, 2020), the present study utilizes the longest available

datasets to estimate snout retreat and areal changes (1968-2020) and mass balance reconstruction (1950-2020) for the Dokriani Bamak (central Himalaya) and Chhota Shigri (western Himalaya) glaciers to understand their long-term response to prevailing climatic conditions. Both the glaciers are reference glaciers and well-studied in the field, and provide the best datasets for mass balance modelling in the Himalaya (Azam, 2022; section 3.2). The objectives are set as follows: (i) estimation of snout retreat and areal changes on both the glaciers since 1960s using remote sensing data and (ii) understand the long-term mass balance patterns on both the glaciers since 1950s.

### **3.2 Study Area**

The Dokriani Bamak Glacier is located in ‘Din Gad Catchment’ (30°50’ N and 78°50’E), Bhagirathi Basin in the central Himalaya (Garhwal region, Uttarakhand, India). This catchment is guarded by three peaks; Jaonli (6632 m a.s.l.) on eastern side, Draupadi Ka Danda I (5716 m a.s.l.) on southern side and Draupadi Ka Danda II (5670 m a.s.l.) on western side. Dokriani Bamak Glacier is a valley glacier, ranging from 4050-6632 m a.s.l., with an area of 7.03 km<sup>2</sup> (Fig. 3.1). The lower ablation area (4050 to 4900 m a.s.l.) of the glacier tongue is covered with debris (0.90 km<sup>2</sup> ~13% of total glacier area). This glacier is among the most studied glaciers in the Himalaya for meteorology, areal changes, mass balances and hydrology (Thayyen et al., 2005; Dobhal et al., 2004; 2008; 2021; Pratap et al., 2015; Yadav et al., 2019; Azam and Srivastava, 2020).

Chhota Shigri Glacier (32°28’ N, 77°52’ E) is located in the Chandra Basin in the western Himalaya (Lahaul valley, Himachal Pradesh, India) (Fig. 3.1). Chhota Shigri Glacier catchment makes up a single proglacial stream and drains to the Chandra River, a tributary of the Indus River. The catchment is bounded by a cirque in south and a peak, Devachan (6263 m a.s.l.) in east (Fig. 3.1). Chhota Shigri Glacier covers an area of 15.5 km<sup>2</sup> (Azam et al., 2016), with only ~4% debris cover area over its lower tongue (Vincent et al., 2013). This glacier has extensively been studied for various aspects including mass

balances, dynamics, ice thickness, energy balance, and hydrology (Wagnon et al., 2007; Azam et al., 2012; 2014; 2016; 2019; Pandey and Venkataraman, 2013; Ramsankaran et al., 2018; Mandal et al., 2020; Haq et al., 2021).

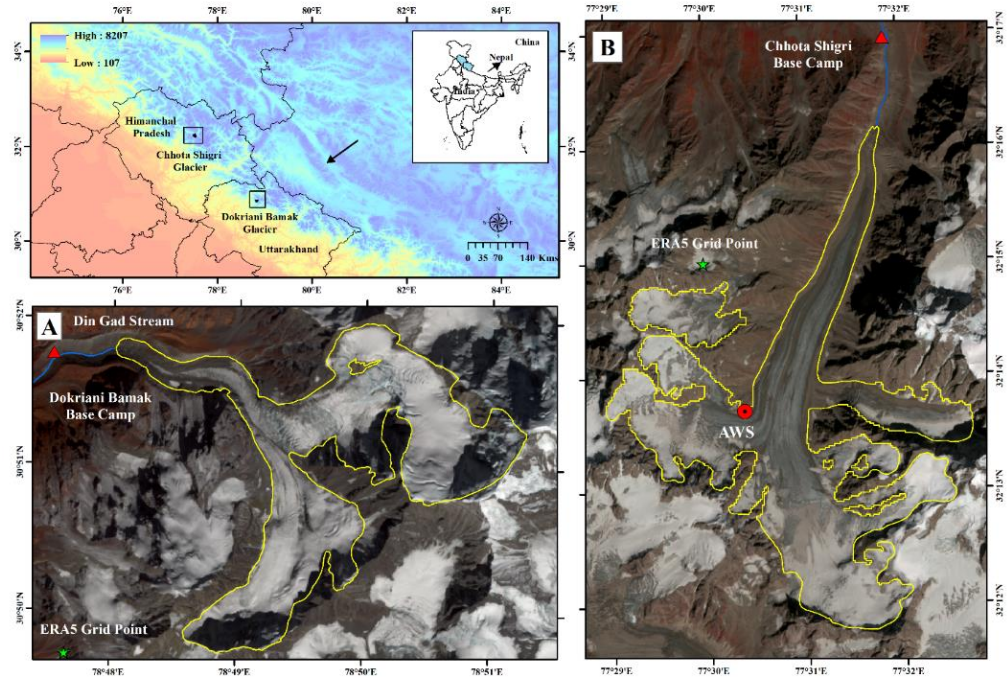


**Figure 3.1:** Location of (A) Dokriani Bamak Glacier (yellow outline) on sentinel-2 MSI sensor imagery of 28 October 2020 and (B) Chhota Shigri Glacier (yellow outline) on sentinel-2 MSI sensor imagery of 21 September 2020 in the Himalaya

### 3.3 Data and methods

#### 3.3.1 Data Used

##### 3.3.1.1 Satellite data

Present study utilizes high (<10 m) to medium (10-30 m) spatial resolution, multi-sensor and multi-temporal satellite data to assess the dimensional changes on Dokriani Bamak and Chhota Shigri glaciers between 1968 and 2020. The used data include Corona, Landsat (orthorectified L1T)-Thematic Mapper (TM), Enhanced Thematic Mapper Plus (ETM+), Operational Land Imager (OLI), and Sentinel-2 (orthorectified L1C) Multi-Spectral Instrument (MSI) images; acquired from the U.S. Geological Survey (USGS;

(<http://earthexplorer.usgs.gov>). Seasonal snow and cloud cover influence the suitability of satellite imagery for glacier mapping to a great extent (Burns and Nolin, 2014); therefore, post-monsoon cloud-free images were carefully selected for the study. The Shuttle Radar Topographic Mission (SRTM) Global Digital Elevation Model version-3 (GDEM-v3) was also downloaded from the USGS Earth Explorer site (<http://earthexplorer.usgs.gov>) and used here as an elevation reference. Complete details of satellite data used are given in Table 3.1.

For both the glaciers, respective 2000 ETM+ images were taken as a base and congruence among images was checked and ensured. The orthorectified Landsat and Sentinel images showed good congruence with the base images (Root Mean Square Error, RMSE, < 6 m). However, Corona images showed a large shift owing to their different acquisition geometry (Dashora et al., 2007; Bhambri et al., 2011). Hence, a projective transformation, followed by spline adjustment, was performed based on suitable reference points (mountain peaks, river confluences and first order streams) and SRTM DEM-v3 to rectify the Hexagon image taking 2000 ETM+ image as a base. This provides acceptable RMSEs (<1 pixel; 3 m). All the images were projected in the UTM coordinate system with datum WGS84.

### **3.3.1.2 Meteorological data and bias-correction since 1950**

Long-term ERA5 preliminary (1950-1978) and ERA5 (1979-2020) reanalysis data were downloaded at hourly scale and extracted to daily bias-corrected ERA5 data (temperature and precipitation) in order to reconstruct the mass balances for both Dokriani Bamak and Chhota Shigri glaciers over the period 1950-2020 (Copernicus Climate Change Service C3S, 2017). Daily temperature and precipitation were extracted for the nearest grids and bias corrected using the field data from earlier studies (Azam et al., 2016; Verma et al., 2018; Mandal et al., 2020). The details of bias corrections in ERA5 data for Dokriani Bamak Glacier can be found in Azam and Srivastava (2020). For Chhota Shigri Glacier the regression equation between daily air temperatures from raw ERA5 and

**Table 3.1:** List of satellite data used in the present study. Dokriani Bamak Glacier = DBG, Chhota Shigri Glacier = CSG.

Glacier	Satellite/Sensor	Image/Product ID	Date of requisition	Spatial resolution (m)	Coregistration error
DBG	Corona	DS1048-1134DF108_108	27 Sep 1968	~ 3	1.5
	Landsat-5/TM	LT51460391994273ISP00	30 Sep 1994	30	6
	Landsat-7/ETM+	LE71460392000218SGS00	5 Aug 2000	30	5
	Landsat-TM	LT51460382010269KHC00	26 Sep 2010	30	6
	Sentinel-2/MSI	L1C_T44RKV_A027944_20201028T052216	28 Oct 2020	10	5
CSG	Corona	DS1115-2282DF064_64	28 Sep 1971	~ 3	1.5
	Landsat-5/TM	LT51470381993277ISP00	4 Oct 1993	30	6
	Landsat-7/ETM+	LE71470382000241SGS00	28 Aug 2000	30	5
	Landsat-TM	LT51470382009225KHC00	13 Aug 2009	30	6
	Sentinel-2/MSI	L1C_T43SGR_A027415_20200921T053331	21 Sep 2020	10	5
DBG and CSG	SRTM DEM	-	Feb 2000	30	

Automatic Weather Station (AWS; Fig. 3.1) over 2009-2016 (Azam et al., 2016) was used to bias-correct the ERA5 data since 1950, while monthly scale factors, developed between precipitation series over 2012-2020 from raw-ERA5 and an automated rain/snow gauge (Geonor T-200B) installed at Chhota Shigri base camp (Fig. 3.1), were used to bias-correct the ERA5 precipitation series since 1950. The mean annual bias correction factor was estimated to be 1.10 with minimum and maximum mean monthly corrections of 0.56 in November and 2.01 in May.

### **3.4 Methodology**

#### **3.4.1 Glacier area and snowline altitude changes**

We followed the Global Land Ice Measurements from Space (GLIMS) guidelines (<http://www.glims.org/MapsAndDocs/guides.html>) to map the glacier outlines from the satellite images for both the glaciers. Manual interpretation was preferred to delineate the glacier outlines because, though laborious, it is one of the most accurate methods (Stokes et al., 2007; Pandey and Venkataraman, 2013; Garg et al., 2017b). The visual interpretation was aided by different combinations of false color composites such as SWIR-NIR-Green, NIR-SWIR-Red, and NIR-Red-Green etc. (Basnett et al., 2013). The proglacial morphology, ice wall shadows, presence of snow/ice, rough texture of the debris-covered part, flow patterns, breaks in surface slope and shape of the valley facilitated the precise delineation of glacier outlines (Stokes et al., 2007; Chand and Sharma, 2015; Shukla and Qadir, 2016). The ice divides were interpreted with the help of SRTM Digital Elevation Model (DEM). High resolution images from the Google Earth were used as additional sources to improve the glacier outlines. The uppermost boundary of the glacier was kept fixed, and the temporal glacier changes were estimated for the rest of the parts as no visible change could be identified in the upper accumulation region because of seasonal snow cover (Bhambri et al., 2011; Chand and Sharma, 2015; Racoviteanu et al., 2019). Finally, temporal glacier outlines were compared to estimate glacier area changes over time. Length changes were

calculated following the standard method wherein strips with an offset of 50 m are drawn parallel to the central flow line and the length change is calculated as an average of all the strips intersecting the glacier boundaries (Bhattacharya et al., 2016; Shukla and Qadir, 2016; Garg et al., 2017b).

### 3.4.2 Mass-balance model

The annual glacier-wide mass balances were reconstructed applying a simple glacier mass-balance model that includes an accumulation module and a T-index melt module. Daily temperature and precipitation data were used to force the model. This model had been applied in several previous studies (Azam et al., 2014; 2019; Azam and Srivastava, 2020). Here we provide the basic structure of the model and refer to the previous papers for more details.

At a given altitudinal range, the biased-corrected daily temperature  $T$  ( $^{\circ}\text{C}$ ) is extrapolated as:

$$T = T_{BC} + \Delta H \times L_R \quad (3.1)$$

Where  $T$  is the extrapolated temperature at different altitudinal bands,  $T_{BC}$  is the temperature at base camp ( $^{\circ}\text{C}$ ),  $\Delta H$  is the altitudinal difference between base camp and altitudinal band (m) and  $L_R$  is the temperature lapse rate ( $^{\circ}\text{C}/\text{m}$ ).  $T$  is extrapolated using mean monthly temperature lapse rates ( $L_{Rs}$ ) for Dokriani Bamak Glacier estimated in Azam and Srivastava (2020), while for Chhota Shigri Glacier estimated using field-temperature data recorded using automatic temperature sensors at Chhota Shigri Glacier base camp (3850 m a.s.l.) and AWS site (4863 m a.s.l.; Fig. 3.1) over three hydrological years from October 2016 to September 2019 (Mandal et al., 2020).

At a given altitudinal range, the biased-corrected daily precipitation  $P$  (mm w.e.  $\text{d}^{-1}$ ) is extrapolated as:

$$P = P_{BC} + \Delta H \times P_G \quad (3.2)$$

Where  $P$  is the extrapolated precipitation at different altitudinal bands,  $P_{BC}$  is the precipitation at base camp (mm w.e.  $\text{d}^{-1}$ ),  $\Delta H$  is the altitudinal

difference between base camp and altitudinal band (m) and  $P_G$  is the precipitation gradient (% increase per 1000 meter).

The daily snow accumulation  $S_{acc}$  (mm w.e. d<sup>-1</sup>) at each altitudinal range is computed by:

$$S_{acc} = \begin{cases} P: & \text{when } and T \leq T_P \\ 0: & \text{when } and T > T_P \end{cases} \quad (3.3)$$

Where  $P$  and  $T$  are daily precipitation (mm) and temperature (°C) respectively extrapolated at each altitudinal range and  $T_P$  is the threshold temperature (°C) for snow-rain.

The temperature-index module relates the amount of melt with positive air temperature sums (positive degree days) and a proportionality factor called degree-day factor ( $DDF$ ). At each altitudinal range, the daily melt  $M$  (mm w.e. d<sup>-1</sup>) is computed by:

$$M(S, I, D) = \begin{cases} DDF_{S,I,D} \cdot (T - T_M): & \text{when } and T > T_M \\ 0: & \text{when } and T \leq T_M \end{cases} \quad (3.4)$$

where,  $DDF$  denotes the degree-day factor (mm d<sup>-1</sup> °C<sup>-1</sup>), different for snow ( $S$ ), ice ( $I$ ) and debris-covered ice ( $D$ ) surfaces, and  $T$  is extrapolated daily mean air temperature (°C) at given altitudes and  $T_M$  is the threshold temperature (°C) for melt.

In this model, the extrapolated snow (eq. 3) over 50-m altitudinal ranges of the glacier is melted out using the corresponding  $DDF_s$ , when  $T > T_M$  for the corresponding 50-m altitudinal range (eq. 4). Thus, the dynamic storage of snow is maintained in the model. If  $T > T_M$  and all the accumulated snow is melted out, then ice melt starts depending on the surface whether it is debris-covered ice or clean ice.

Mean altitudinal mass balance for each 50-m altitudinal range ( $b_z$ , m w.e.) is estimated using the accumulation and the ablation terms as:

$$b_z = S_{acc} - M \quad (3.5)$$

where,  $S_{acc}$  (mm w.e. d<sup>-1</sup>) is daily snow accumulation and  $M$  (mm w.e. d<sup>-1</sup>) is the daily melt computed using equation 3.3 and 3.4, respectively.

Daily glacier-wide mass balances  $B_a$ , (m w.e.) is calculated using the mean altitudinal mass balances as:

$$B_a = \frac{\sum A_z b_z}{A} \quad (3.6)$$

Where  $A_z$  ( $m^2$ ) and  $b_z$  (m w.e.) are the 50-m altitudinal glacier area and mean mass balances, respectively, and  $A$  is the total glacier area ( $m^2$ ). Annual mass balances are calculated using daily mass balance values for the hydrological year from 1 November through 31 October of next year for the Dokriani Bamak Glacier (Dobhal et al., 2008) and hydrological year from 1 October through 30 September of next year for the Chhota Shigri Glacier (Wagnon et al., 2007). The overall structure of the model is given in Fig. 3.2.

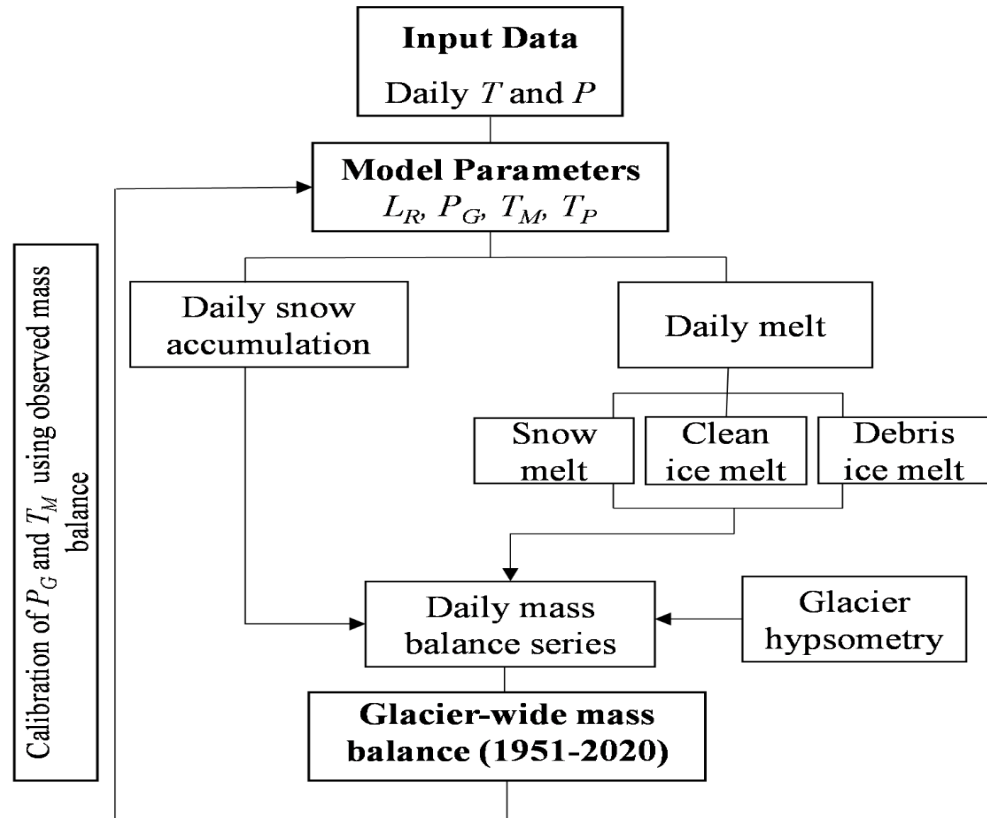


**Figure 3.2:** Mass-balance model:  $T$  and  $P$  is daily temperature and precipitation,  $L_R$  is temperature lapse rate,  $P_G$  is precipitation gradient,  $T_M$  is threshold temperature for melt and  $T_P$  is threshold temperature for precipitation.

### 3.4.3 Model Parameters

Air temperature ( $T$ ) plays an important role in mass-balance models as it helps in determining the distribution of snow and rain. The degree day factors ( $DDFs$ ) for both the glaciers were adopted from previous studies considering different values for snow, clean ice and debris-covered ice surfaces (Azam et al., 2019; Azam and Srivastava, 2020). The threshold temperature for precipitation ( $T_P$ ) were taken from Jennings et al. (2018) as  $0.7^\circ\text{C}$  and  $1.1^\circ\text{C}$  which correspond to 70-80% and 60-70% relative humidity percent ranges for Dokriani Bamak Glacier and Chhota Shigri Glacier, respectively, at which 90 to 100% precipitation was considered as snow. The mass-balance models are highly sensitive to  $T_M$ , nearly unexplored in the Himalayan glaciers (Engelhardt et al., 2017; Azam et al., 2019; Azam and Srivastava, 2020) and the precipitation distribution over the Himalayan region is spatially non-uniform due to valley-specific  $P_G$  (Immerzeel et al., 2015). Hence, in the present study, for Dokriani Bamak Glacier, the calibrated values of  $T_M$  and  $P_G$  were adopted from Azam and Srivastava (2020), while for Chhota Shigri Glacier these parameters were calibrated against the field-observed mass balances (Table 3.2).

**Table 3.2:** List of model parameters, sensitivity and uncertainty ranges for Dokriani Bamak Glacier and Chhota Shigri Glacier.

Parameters	Dokriani Bamak		Chhota Shigri	
	Model value	Uncertainty estimation range	Model value	Uncertainty estimation range
Altitudinal precipitation gradient ( $\% \text{ km}^{-1}$ ) *	80	72 to 88	89	80 to 98
Temperature Lapse rate ( $LR$ ) ( $^\circ\text{C km}^{-1}$ )	$T_{LR}$	$L_{R+1\sigma}$ to $L_{R-1\sigma}$	$T_{LR}$	$L_{R+1\sigma}$ to $L_{R-1\sigma}$
Threshold temperature for snow/rain ( $T_P$ ) ( $^\circ\text{C}$ )	0.70	0.63 to 0.77	1.10	0.99 to 1.21
Threshold temperature for melting ( $T_M$ ) ( $^\circ\text{C}$ ) *	-2.7	-3 to -2.40	-0.70	-0.77 to -0.63
DDF of snow ( $DDFs$ )	6.1	4.7 to 5	5.28	4.05 to 5.43
DDF of clean ice ( $DDF_I$ )	7.7	7.4 to 8	8.63	5.13 to 9.08
DDF of Debris covered ice ( $DDF_D$ )	4.8	5.7 to 6.4	3.34	-
Temperature ( $1^\circ\text{C}$ )	-	-	-	-
Precipitation (10%)	-	-	-	-

\*Calibrated parameters

### 3.4.4 Model calibration and validation

For model calibration, we have adopted similar parameters for Dokriani Bamak Glacier from Azam and Srivastava (2020). For Chhota Shigri Glacier, Monte Carlo simulations with 10000 parameter sets was performed where the parameters were varied over the plausible parameter's limits (Rounce et al., 2020b). The input parameters  $P_G$  was changed from 0 to 100%  $\text{km}^{-1}$  and  $T_M$  was changed from  $-4^\circ\text{C}$  to  $+4^\circ\text{C}$ . The run with minimum RMSE between modelled and field-observed annual mass balances were selected. The selected run showed an RMSE of 0.44 m w.e./y (2003-2019) between modelled and field-observed mass balances for Chhota Shigri Glacier (Fig. 3.3).

For the model validation, the snow line altitudes (SLAs) computed from mass-balance model were compared against satellite-derived SLAs from Landsat satellite images of the same days from 1992 to 2017. For Dokriani Bamak Glacier, we used satellite-derived SLAs from Azam and Srivastava (2020) and for Chhota Shigri Glacier from Chandrasekharan et al. (2018). The modelled SLAs showed good agreement with satellite-derived SLAs for both Dokriani Bamak Glacier ( $R^2 = 0.67$ ) and Chhota Shigri ( $R^2 = 0.54$ ) glaciers, with RMSEs of 157 and 153 m, respectively (Fig. 3.3).

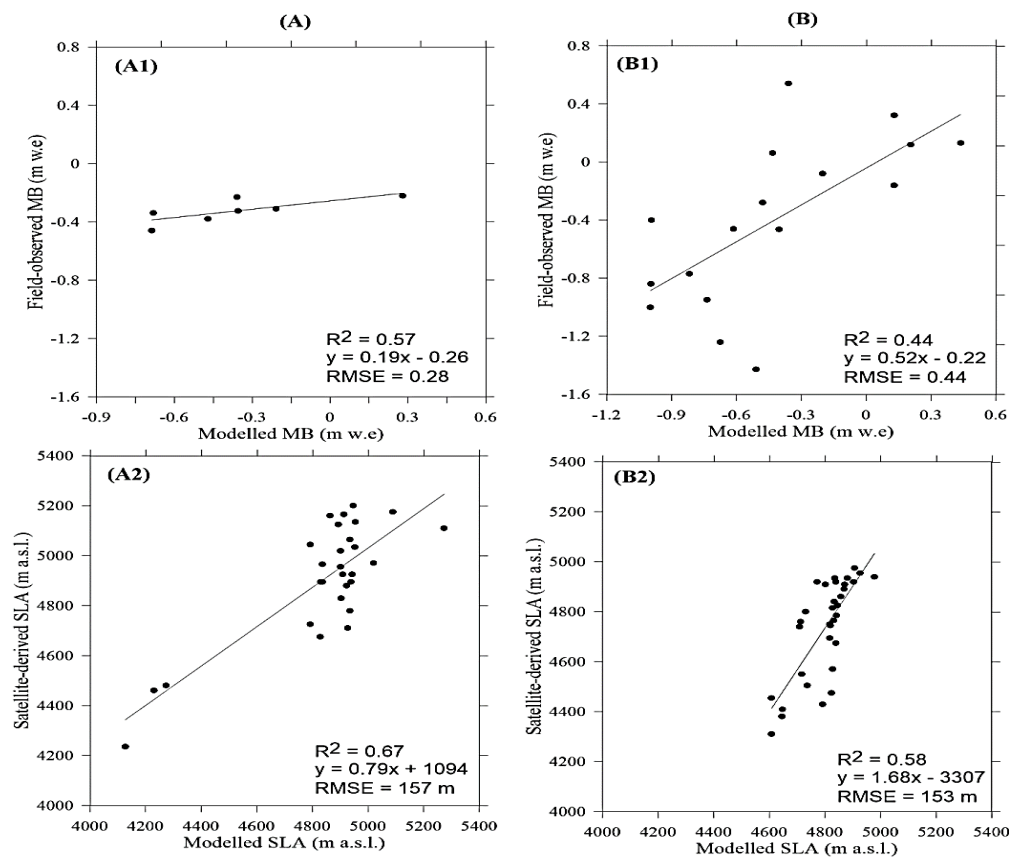


**Figure 3.3:** Model calibration and validation: Scatter plots are showing the correlations between modelled and field-observed mass balances for (A1) Dokriani Bamak Glacier over 1993-2000 and (B1) Chhota Shigri Glacier over 2004-2019 and between modelled and satellite-derived snow line altitudes (SLA) for Dokriani Bamak and Chhota Shigri glaciers, respectively (B1 and B2) over 1992 to 2017.

### 3.4.5 Uncertainty estimation

Quantification of uncertainties associated with monitored parameters is essential to substantiate the significance of results. Here, the uncertainties associated with glacier area estimations were quantified using buffer method (Granshaw and Fountain, 2006; Bolch et al., 2010; Chand and Sharma, 2015). The buffer size was chosen to be half of the estimated shift caused by misregistration as only one side can be affected by the shift (Bolch et al., 2010). The estimated area uncertainties ranged between 1.2 and 2.5% which are in line with previously reported values (Basnett et al., 2013; Chand and Sharma, 2015; Garg et al., 2017b). The uncertainties associated with the retreat estimations

were determined according to Hall et al. (2003) as the square root of sum of squares of temporal images added by coregistration error.

Uncertainties in reconstructed annual mass balances were calculated by re-running the model while adjusting the parameters one-by-one within a reasonable range of their calibrated values and keeping other model parameters unchanged. The uncertainties in  $L_R$  were taken as standard deviations of mean monthly values for both Dokriani Bamak and Chhota Shigri glaciers. The uncertainties in other parameters ( $P_G$ ,  $T_M$  and  $T_P$ ) are unknown hence these parameters varied with the range of  $\pm 10\%$  from their calibrated values (Ragetti et al., 2013; 2015) (Table 3.2). The total uncertainty in annual mass balance was calculated by summing up all parametric uncertainties applying the error propagation rule:

$$B_a = \sqrt{(\partial DDF_S)^2 + (\partial DDF_I)^2 + (\partial DDF_D)^2 + (\partial L_R)^2 + (\partial P_G)^2 + (\partial T_P)^2 + (\partial T_M)^2} \quad (3.7)$$

Where  $B_a$  is the glacier wide mass balances,  $DDF_{S,I,D}$  is the degree day factor for snow, ice and debris covered ice,  $L_R$  is the temperature lapse rate,  $P_G$  is the precipitation gradient, and  $T_P$  and  $T_M$  are the threshold temperature for precipitation and melting, respectively.

## 3.5 Results

### 3.5.1 Glacier retreat and area loss

Both Dokriani Bamak and Chhota Shigri glaciers showed deglaciation and retreat during the study period over 1968-2020. However, the rates were temporally heterogeneous. The total glacier area of the Dokriani Bamak Glacier decreased from  $7.07 \pm 0.1 \text{ km}^2$  in 1968 to  $6.91 \pm 0.1 \text{ km}^2$  in 2020, revealing a total deglaciation of  $2.22 \pm 1.54\%$  ( $0.04 \pm 0.03 \text{ \%}/\text{y}$ ) (Table 3.3). The terminus of glacier also retreated at an average rate of  $10.81 \pm 0.3 \text{ m}/\text{y}$  during 1968-2020.

To assess the temporal fluctuations, the total study period was divided into four time frames depending on the available images i.e. 1969-1994 (26 years), 1994-2000 (6 years), 2000-2010 (10 years) and 2010-2020 (10 years). Results show that, among studied time frames, Dokriani Bamak Glacier

deglaciated with the highest rate ( $0.09 \pm 0.2\%/y$ ) during recent decade (2010-2020) and minimum rate ( $0.02 \pm 0.1 \%/y$ ) over 1968-1993. Between 1994 and 2000, the deglaciation rate slightly increased than previous time frame to  $0.07 \pm 0.4 \%/y$  and subsequently decreased to  $0.03 \pm 0.2\%/y$  during 2000-2010 (Table 3.3). Snout retreat estimation show that the glacier retreated with a limited rate of  $3.69 \pm 1.3$  m/y between 1968 and 1994. However, during 1994-2000, the rate increased to  $17.83 \pm 8.1$  m/y. In the following time frame (2000-2010) the retreat rate decreased slightly to  $16.00 \pm 4.8$  m/y. Notably, in the recent decade (2010-2020), the glacier retreated with the highest rate of  $19.90 \pm 3.7$  m/y (Table 3.3).

The initial area of Chhota Shigri Glacier was  $15.64 \pm 0.19$  km<sup>2</sup> in 1971 which decreased to  $14.94 \pm 0.32$  km<sup>2</sup> exhibiting a total area loss of  $4.47 \pm 1.69\%$  ( $0.09 \pm 0.03 \%/y$ ). This total deglaciation is almost double than the Dokriani Bamak Glacier, which is mainly because of the detachment of left bank tributary of Chhota Shigri Glacier during 2010-2020, leading to vacation of a large area. However, the average terminus retreat on Chhota Shigri Glacier was almost negligible ( $3.45 \pm 0.3$  m/y) during 1971-2020 (Table 3.3). This is because of the local topography, terminus of Chhota Shigri Glacier is heavily debris covered and constrained between narrow and steep valley walls which cause deep shadow restricting its exposure to solar radiation for a limited time of the day (Wagnon et al., 2007).

The temporal assessment showed that the Chhota Shigri Glacier deglaciated with a minimum rate during 1971-1993 ( $0.01 \pm 0.1 \%/y$ ) and maximum during 2009-2020 ( $0.26 \pm 0.2 \%/y$ ). Comparatively higher deglaciation was observed during 1993-2000 ( $0.18 \pm 0.3 \%/y$ ) followed by a lower deglaciation rate during 2000-2009 ( $0.02 \pm 0.3\%/y$ ) (Table 3.3). The terminus retreat on the Chhota Shigri Glacier was very low and almost consistent among all the considered time frame (Table 3.3). Though magnitude differed only slightly, minimum ( $2.39 \pm 1.4$  m/y) and maximum ( $4.64 \pm 3.3$  m/y) retreat occurred during 1971-1993 and 2009-2020, respectively. The retreat was  $4.0 \pm 6.9$  m/y over 1993-2000 and  $3.89 \pm 5.4$  m/y over 2009-2020, showing a slight reduction (Table

3.3). Thus, the overall dimensional monitoring reveals that the deglaciation and retreat rates were greatly fluctuated on both the glaciers over decadal scale. The terminus of the Chhota Shigri Glacier was also monitored in the field between 2012 and 2015 using a Differential Global Positioning System (Topcon GB-1000) relative to a fixed reference point on firm rock at base camp (Fig. 3.4). Observations reveal a terminus retreat of 4 m/y during 2012-2015. Thus, the field measurements complement remotely-deduced retreat estimations and confirm a low magnitude of retreat on the Chhota Shigri Glacier.

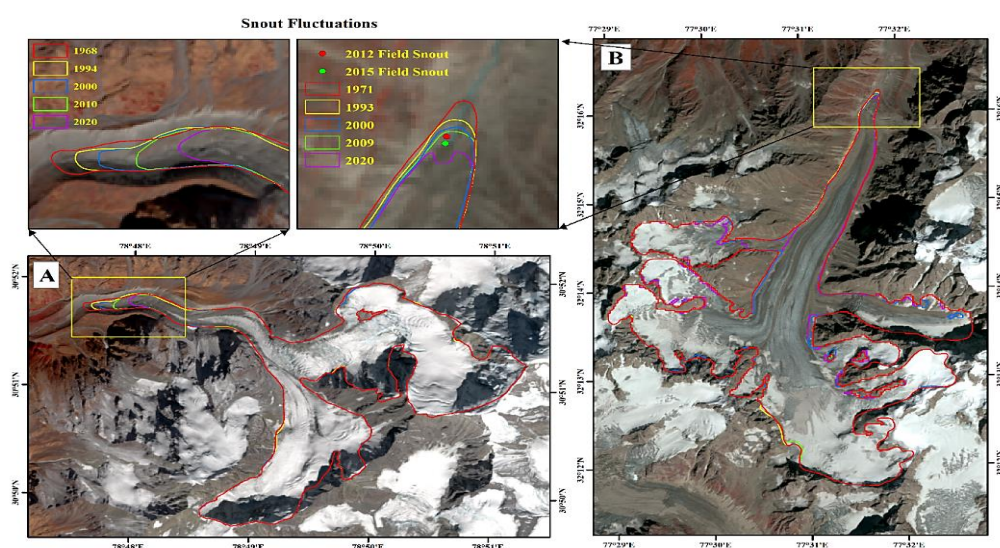


**Figure 3.4:** Snout changes of (A) Dokriani Bamak Glacier between 1968 to 2020 and (B) Chhota Shigri Glacier between 1971 to 2020 (Background image is from Sentinel-2/MSI sensor 28 October 2020 and 21 September 2020 respectively on panel A and B)

### 3.5.2 Annual and seasonal glacier-wide mass balances

The annual glacier-wide mass balance reconstruction was done on Dokriani Bamak Glacier over 1980-2018 and on Chhota Shigri Glacier over 1970-2016 in previous studies (Azam et al., 2019; Azam and Srivastava, 2020). In the present study, the reconstructions on both the glaciers were extended back in time up to 1950 in order to investigate the long-term mass balance patterns. These reconstructed mass balance series, over the last seven decades, are the longest in the Himalaya (Azam et al., 2018). The mean annual glacier-wide

**Table 3.3:** Changes in various glacier and climatological parameters during the study. DBG = Dokriani Bamak Glacier, Chhota Shigri Glacier = CSG.

Glacier	Parameter	Decadal time period				Total time period
		1968/71-1993/94	1993/94-2000	2000-2009/10	2009/10-2020	1968/71-2020
DBG	Area change (area loss) %/y	$0.02 \pm 0.1$	$0.07 \pm 0.4$	$0.03 \pm 0.2$	$0.09 \pm 0.2$	$0.04 \pm 0.03$
	Length change (retreat) m/y	$3.69 \pm 1.3$	$17.83 \pm 8.1$	$16.00 \pm 4.8$	$19.90 \pm 3.7$	$10.81 \pm 0.3$
CSG	Area change (area loss) %/y	$0.01 \pm 0.1$	$0.18 \pm 0.3$	$0.02 \pm 0.3$	$0.26 \pm 0.2$	$0.09 \pm 0.03$
	Length change (retreat) m/y	$2.39 \pm 1.4$	$4.0 \pm 6.9$	$3.89 \pm 5.4$	$4.64 \pm 3.3$	$3.45 \pm 0.3$

mass balances were computed to be  $-0.09 \pm 0.35$  m w.e./y and  $-0.12 \pm 0.28$  m w.e./y with cumulative mass wastage of  $-6.33$  m w.e. and  $-8.61$  m w.e. on Dokriani Bamak Glacier and Chhota Shigri Glacier over 1950-2020, respectively. The year 1974/75 and 1950/51 showed maximum annual mass balances of  $1.24 \pm 0.32$  m w.e. and  $1.03 \pm 0.20$  m w.e., while year 2015/16 and 2000/01 showed minimum annual mass balances of  $-0.95 \pm 0.40$  m w.e. and  $-1.23 \pm 0.33$  m w.e. for Dokriani Bamak and Chhota Shigri glacier, respectively (Fig. 3.5). The Dokriani Bamak Glacier showed positive annual mass balances for 28 years and negative for 42 years whereas Chhota Shigri Glacier showed 34 years positive annual mass balances and for 36 years negative mass balances over 1950-2020 (Fig. 3.5). Modelled seasonal mass balances ranged from 0.29 to 1.48 m w.e./y and 0.45 to 1.73 m w.e./y for winter, and  $-1.68$  to  $-0.12$  w.e./y and  $-1.98$  to  $-0.08$  w.e./y for summer on Dokriani Bamak and Chhota Shigri Glaciers, respectively (Fig. 3.5).

However, available estimates on Dokriani Bamak and Chhota Shigri glaciers from previous studies using in-situ, geodetic and modelling approaches over different time periods are in line with our reconstructed mass balances. The in-situ glaciological method showed moderate average mass wastage of  $-0.32$  m w.e. /y on the Dokriani Bamak Glacier over 1992-2013 with intermittent gaps (Dobhal et al., 2008; 2021). A recent study suggests a mass loss of  $-0.23 \pm 0.1$  m w.e./y using geodetic measurements for 1999-2014 (Garg et al., 2022). One study, using CORONA-SRTM DEMs, estimated the long-term near-stable state of Chhota Shigri Glacier with an average balance of  $-0.03 \pm 0.10$  m w.e./y between 1971 and 1999 (Mukherjee et al., 2018). Further, a moderate mass wastage of  $-0.24 \pm 0.10$  m w.e./y was estimated over 2000-2011 by differencing SRTM-CARTOSAT DEMs (Mukherjee et al., 2018). Another study, using enhanced T-index model, reconstructed the mass balance back in time and computed mean annual mass balance of  $-0.36 \pm 0.33$  m w.e./y during 1955-2014 (Engelhardt et al., 2017).

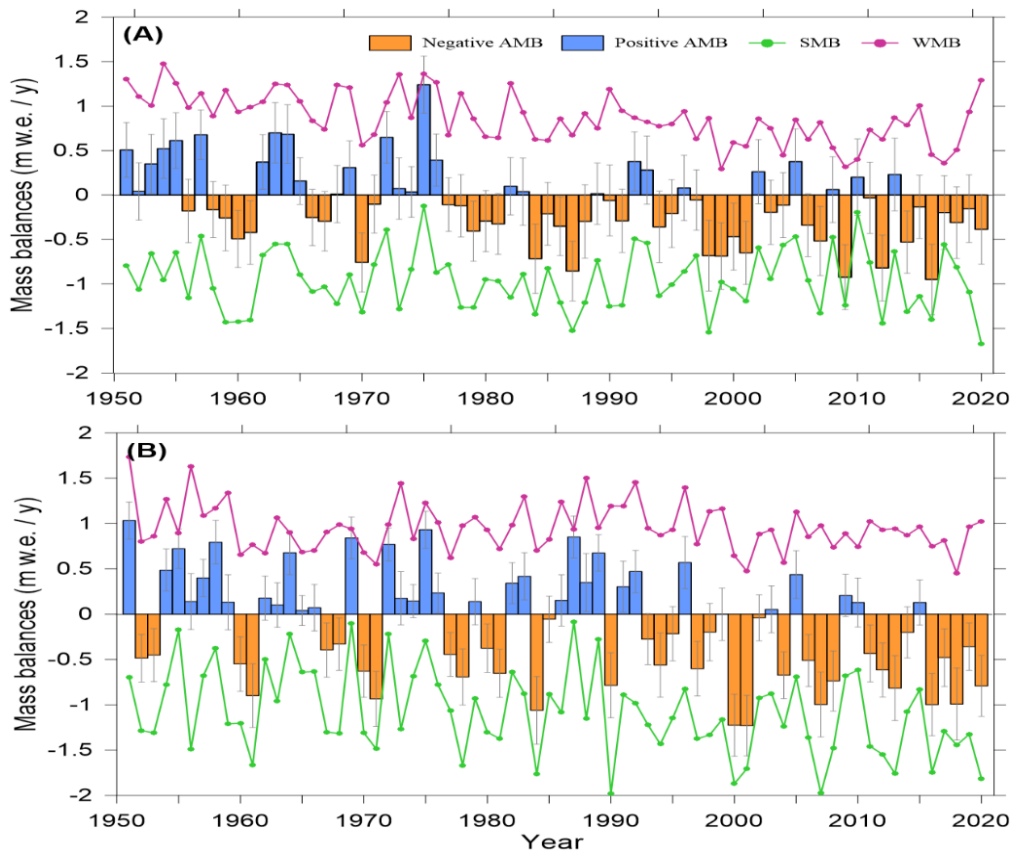


**Figure 3.5:** Annual mass balances (AMB; positive = blue bars and negative = orange bars), winter mass balances (WMB) with purple lines and summer mass balances (SMB) with green lines for (A) Dokriani Bamak Glacier and (B) Chhota Shigri Glacier over 1950-2020 are shown. The annual mass balance uncertainty is shown with grey lines.

### 3.6 Discussion

#### 3.6.1 Fragmentation of western tributary glacier of Chhota Shigri Glacier

During the study, a peculiar phenomenon was observed on the Chhota Shigri Glacier wherein its left bank tributary glacier got detached from the main trunk glacier during the decade of 2009-2020 (Fig. 3.6). Satellite image of 2009 clearly shows that the tributary glacier was connected through ice with the main trunk; however, in 2020 satellite image, detached tributary glacier and its separate snout are evident (Fig. 3.6B). The field photograph of September 2016 showed a clear visible snout of the fragmented tributary glacier (Fig. 3.6C). Another field photograph from September 2018 also showed a visible stream

channel coming from the fragmented tributary glacier (Fig 3.6D). Continuous observations during our annual field visits confirm that the fragmentation was started in summer 2012. Together with the climatic drivers (section 5.2), this fragmentation resulted in the highest deglaciation rate ( $0.26 \pm 0.2\%/y$ ) of Chhota Shigri Glacier during 2009-2020, among considered periods (Table 3.3). Notably, 2011-2020 is also the decade when the Chhota Shigri Glacier experienced the most negative average decadal mass balance ( $-0.56$  m w.e./y; Section 3.6.2) in its monitoring history. Continuous glacier mass loss, hence thinning, might have resulted in this fragmentation process. Also, the tributary glacier is resting upon a steep slope (mean slope:  $21^\circ$ ; having some areas with  $>50^\circ$ ) which likely exerts negative impact on its stability and possibly contributed to fragmentation. Previously, glacier fragmentation and resultant increase in number of glaciers have been reported by several studies in the different sub-regions of the Himalaya owing to mass loss (Kulkarni et al., 2007; Bhambri et al., 2011; Brahmabhatt et al., 2017; Dash and Sharma, 2019).

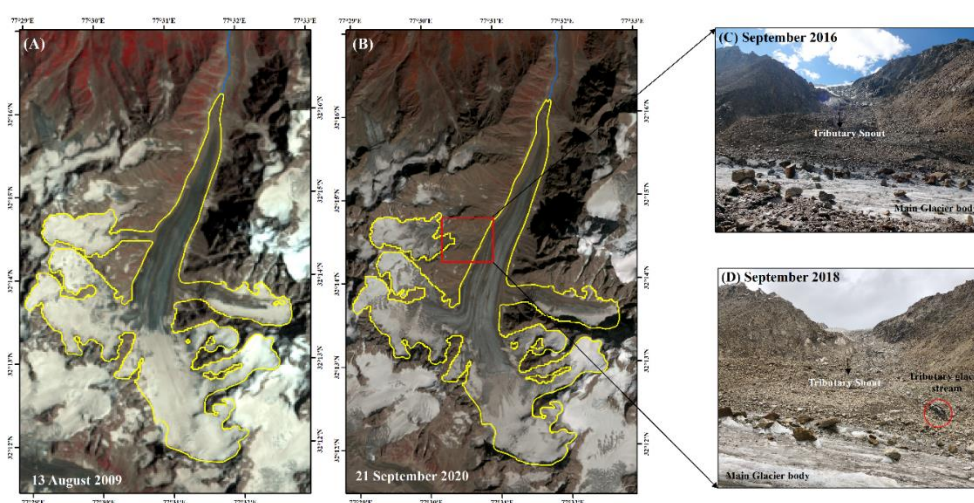


**Figure 3.6:** (A) and (B) shows Chhota Shigri Glacier boundaries for year 2009 and 2020 respectively, and (C) and (D) shows field photographs of tributary glacier of Chhota Shigri Glacier from September 2016 and September 2018, respectively.

### 3.6.2 Decadal mass balances and climatic drivers

A general wastage of the Himalayan glaciers is evident from most of the studies that generally cover the last five decades (Azam et al., 2018; Bolch et al., 2019).

In the present study, the modelled annual mass balances on Dokriani Bamak and Chhota Shigri glaciers have been analysed for decadal patterns over the last seven decades, the longest period in the Himalaya.

Over 1950s, 1960s, and 1970s, the mean decadal mass balances on Dokriani Bamak Glacier were positive with values of 0.16, 0.05 and 0.14 m w.e./y respectively, corresponding to lower summer mass balances and higher winter mass balances. On Chhota Shigri Glacier the mean decadal mass balance was positive over 1950s with a value of 0.22 m w.e./y due to highest winter mass balance (1.14 m w.e./y), and became nearly balanced over 1960s and 1970s with a value of  $-0.03$  and  $-0.01$  respectively, as glacier received lower precipitation in winter months which resulted in lower winter mass balances hence near-balanced state (Fig. 3.7; Table 3.4).

Over 1980s, the Dokriani Bamak Glacier started losing mass at moderate rate with a value of  $-0.27$  m w.e./y; conversely, Chhota Shigri Glacier still remained in near-balanced state in line with previous decades with a value of 0.02 m w.e./y (Table 3.4). The increased mass loss on Dokriani Bamak Glacier was mainly because of the highest decadal summer temperature that led to higher summer mass balances hence higher mass wastage. Conversely, on Chhota Shigri Glacier both the summer and winter mass balances were roughly equal that led to near-balanced state (Fig. 3.7; Table 3.4).

Over 1990s, both the Dokriani Bamak and Chhota Shigri glaciers showed slight mass wastage with values of  $-0.20$  m w.e./y and  $-0.17$  m w.e./y respectively, corresponding to moderate summer and winter mass balances (Fig. 3.7; Table 3.4). However, in some of the previous studies it has been discussed that these glaciers were in near-balanced state over the 1990s using different approaches such as dynamic, geodetic and modelling (Azam et al., 2012; Vincent et al., 2013; Azam et al., 2019; Azam and Srivastava, 2020). Given the uncertainty ranges in the available estimates, the reconstructed slight mass wastage on both the glaciers over 1990s is in agreement with previous studies.

Over 2000s, Dokriani Bamak Glacier showed slightly less mass wastage as compared to 1980s and 1990s. Though the precipitation amounts were almost

same, the summer temperature was slightly lower over 2000s that resulted in less summer mass balance hence less annual mass balances (Fig. 3.7; Table 3.4). Conversely, on Chhota Shigri Glacier, the mass wastage almost doubled over 2000s in comparison with 1990s due to higher summer mass balances (Fig. 3.7). Over the 2010s decade, both Dokriani Bamak and Chhota Shigri glaciers showed highest mass wastage with a value of  $-0.33$  m w.e./y and  $-0.56$  m w.e./y, respectively corresponding to lowest winter mass balances and highest summer mass balances (Fig. 3.7; Table 3.4). This accelerated mass wastage was much higher on Chhota Shigri Glacier mainly because the decadal summer temperature increased up to approximately  $1^{\circ}\text{C}$  that resulted in highest summer mass balance over this decade.

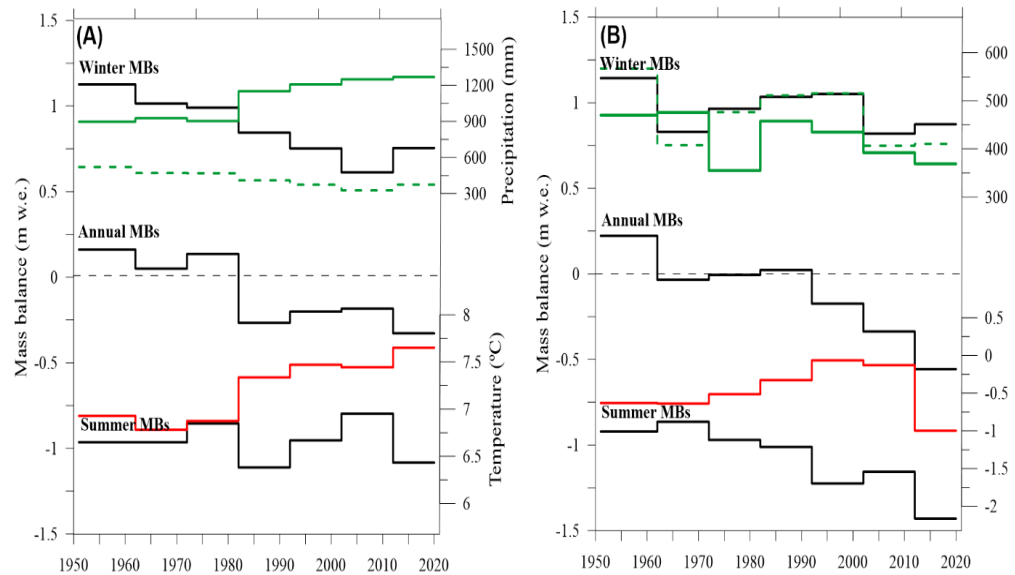


**Figure 3.7:** Mean summer, winter and annual mass balances (MBs) for all the seven decades (1950-2020) (Black thick lines). Red thick line represents the mean decadal summer temperature ( $^{\circ}\text{C}$ ) and green thick and dotted lines represents mean decadal summer and winter precipitation sums (mm) at (A) Dokriani Bamak Glacier and (B) Chhota Shigri Glacier respectively.

**Table 3.4:** Decadal mass balances (MB, m w.e./y) and meteorological parameters on Dokriani Bamak and Chhota Shigri glaciers (winter (WMB, m w.e./y) and summer (SMB, m w.e./y) mass balances, precipitation sum (P, mm), winter precipitation sum (WinP, mm), summer precipitation sum (SumP, mm), temperature (T, °C), winter temperature (WinT, °C), summer temperature (SumT; °C)

<b>Dokriani Bamak Glacier</b>									
<b>Period</b>	<b>AMB</b>	<b>WMB</b>	<b>SMB</b>	<b>P</b>	<b>WinP</b>	<b>SumP</b>	<b>T</b>	<b>WinT</b>	<b>SumT</b>
1951-1960	0.16	1.13	-0.96	1419	522	897	2.11	-2.71	6.93
1961-1970	0.05	1.01	-0.96	1398	470	927	2.09	-2.60	6.78
1971-1980	0.14	0.99	-0.85	1372	469	903	2.30	-2.28	6.88
1981-1990	-0.27	0.84	-1.11	1560	410	1151	2.91	-1.52	7.34
1991-2000	-0.20	0.75	-0.95	1581	373	1207	2.96	-1.55	7.47
2001-2010	-0.18	0.61	-0.80	1576	327	1250	3.42	-0.61	7.44
2011-2020	-0.33	0.75	-1.08	1643	374	1269	3.32	-1.01	7.65
1951-2020	-0.09	0.87	-0.96	1507	421	1086	2.73	-1.75	7.21
<b>Chhota Shigri Glacier</b>									
1951-1960	0.22	1.14	-0.92	1037	567	470	-6.38	-12.13	-0.63
1961-1970	-0.03	0.83	-0.86	883	408	476	-6.44	-12.24	-0.64
1971-1980	-0.01	0.96	-0.97	831	476	355	-6.29	-12.07	-0.51
1981-1990	0.02	1.03	-1.01	969	511	458	-5.97	-11.61	-0.33
1991-2000	-0.17	1.05	-1.22	950	515	435	-5.86	-11.65	-0.07
2001-2010	-0.34	0.82	-1.16	799	407	392	-5.53	-10.93	-0.13
2011-2020	-0.56	0.87	-1.43	801	411	369	-5.30	-9.91	-1.00
1951-2020	-0.12	0.96	-1.08	896	471	422	-5.97	-11.51	-0.47

### 3.6.3 Linkages between glacier dimensional changes and mass balances

Glacier growth and shrinkage is determined by its mass balance which, in turn, is a function of prevailing climatic conditions (Benn and Evans, 2010). Glaciers

tend to adjust their geometry in order to establish an equilibrium with the climate and ensuing mass balance regime. However, there is a significant time lag from a few years to centuries (depending on glacier size) between the changing mass balance and its corresponding adjustment in glacier area and snout position (Jóhannesson et al., 1989; Cuffey and Paterson, 2010; Mehta et al., 2014). In the present study, to minimize the influence of time lag, the mass balance-dimensional change assessment was carried out at the decadal scale.

### **3.6.3.1 Snout retreat and areal changes**

The mass balance of the Dokriani Bamak Glacier was in balance (0.02 m w.e./y) between 1950 and 1990 (Section 3.6.2). Consequently, the deglaciation ( $0.02 \pm 0.1\%/y$ ) and retreat ( $3.69 \pm 1.3$  m/y) were almost negligible during 1968-1994 (Table 3.3). A significantly positive mass balance (0.14 m w.e.) over 1971-1980 might have helped sustain glacier geometry over 1968-1994. As the mass balance became negative during 1991-2000 ( $-0.20$  m w.e./y), the glacier showed an increased deglaciation ( $0.07 \pm 0.4$  %/y) and retreat ( $17.83 \pm 8.1$  m/y) between 1994 and 2000 (Table 3.3). From 2000 to 2010, a comparatively less negative mass balance ( $-0.18$  m w.e./y) was observed than previous decade. Accordingly, deglaciation ( $0.03 \pm 0.2$  %/y) and retreat ( $16.00 \pm 4.8$  m/y) were also reduced slightly during this time period (2000-2010). Over 2010-2020 decade, Dokriani Bamak Glacier experienced the highest decadal wastage ( $-0.33$  m w.e./y) that resulted in highest deglaciation ( $0.09 \pm 0.2$  %/y) and retreat ( $19.90 \pm 3.7$  m/y).

It may be noted that a chain of interlinked processes is involved in dimensional adjustment of a glacier against a mass balance perturbation, particularly the terminus retreat. The terminus environment such as presence of ice-wall, debris cover, slope characteristics etc. exerts strong influence on the retreat rates (Garg et al., 2017b). On Dokriani Bamak Glacier, fluctuating yet consistently negative mass balances after 1980s (Sections 5.2) caused incredible surface thinning and gave rise to a wide supraglacial channel (Pratap et al., 2015). Recent field observations confirm that the supraglacial channel is

connected with the snout wall and promoting mechanical disintegration of ice blocks from the snout leading to a higher retreat (Pratap et al., 2015).

Chhota Shigri Glacier was in balanced conditions (0.05 m w.e./y; 1951-1990) till 1990s (Section 3.6.2). As a result, the deglaciation ( $0.01 \pm 0.1$  %/y) and retreat ( $2.39 \pm 1.4$  m/y) were also negligible during 1971-1993 (Table 3.3). The mass balance became slightly negative after 1991 ( $-0.17$  m w.e./y during 1991-2000), consequently an increase in deglaciation ( $0.18 \pm 0.3$  %/y) and retreat ( $4.0 \pm 6.9$  m/y) were observed over the 1990s. The mass balance became further negative to  $-0.34$  m w.e./y between 2001-2010. Surprisingly, despite the higher negative mass balance, a reduction in the rate of deglaciation ( $0.02 \pm 0.3$  %/y) as well as retreat ( $3.89 \pm 5.4$  m/y) was observed over 2000-2009 (Table 3.3). This is most probably because of the local topography around Chhota Shigri Glacier snout, which is bounded by steep valley walls and prone to have snow-rock avalanches during winters (Wagnon et al., 2007; Vincent et al., 2013). Such avalanches, often observed during early summer expeditions, might have provided extra blanket of snow-rock mixture over the snout region hence subdued deglaciation and retreat. Similar to the Dokriani Bamak, Chhota Shigri Glacier also experienced the most negative average decadal mass balance of  $-0.56$  m w.e./y during 2011-2020 (Table 3.3). In line, the deglaciation ( $0.26 \pm 0.2$  %/y) and retreat rates ( $4.64 \pm 3.3$  m/y) were also the highest during 2009-2020 among all monitored decades (Table 3.3).

Though the mass wastage patterns are similar on both the glaciers, Chhota Shigri Glacier showed consistently lower terminus retreat than that of the Dokriani Bamak Glacier. This is because of the topographic settings of Chhota Shigri Glacier snout. First, it is north-south oriented and bounded by steep valley walls that provide shading effect most of the day except for noon hours and protect lower ablation area for higher melting (Wagnon et al., 2007). Second, the terminus is heavily debris-covered, with debris thickness varying from a few centimetres to over a couple of meters that protects glacier for higher melting. The ablation stake data clearly showed the reduced mass wastage over debris-covered glacier compared to clean glacier (Wagnon et al., 2007; Azam

et al., 2016). Thus, the combined effect of shading and thick debris cover resulted in lower terminus retreat of the Chhota Shigri Glacier than Dokriani Bamak Glacier where the snout area is widely open and having a big supraglacial stream. The subdued deglaciation due to shading and heavy debris cover has been observed in several other studies (Reznichenko et al. 2010; Scherler et al. 2011; Sharma et al., 2016; Mir et al., 2017; Banerjee and Shankar, 2013).

### **3.6.3.2 Dynamic changes**

Glacier dynamics is a direct manifestation of glacier mass balance regime (Heid and Kääb, 2012; Dehecq et al., 2019). The velocity measurements on the Dokriani Bamak Glacier were available for 1993/94, 2000/01 and 2014/15 with reported velocities of  $22.14 \pm 3.9$  m/y,  $18.08 \pm 2.5$  m/y and  $10.53 \pm 2.4$  m/y, respectively (Shukla and Garg, 2020). These measurements revealed that owing to prevailing negative mass balance conditions since 1980s, a total velocity reduction (slowdown) of 41.7% (2%/y) occurred between 1993/94 and 2014/15. The rate of slowdown also increased from 2.6% during 1993/94-2000/01 to 3%/y during 2000/01-2014/15 (Shukla and Garg, 2020) which can be ascribed to a very high negative mass balance after 2010 (Section 3.6.2).

The field glacier velocity measurements on Chhota Shigri Glacier are available from 1987/88 and then post-2000 period (Azam et al., 2012). Several other studies estimated the surface velocities, mainly post-2000, using satellite data. The dynamic changes were negligible between 1987/88 and 2003/04 (Azam et al., 2012), confirming the lower modelled mass wastage over this period ( $-0.02$  m w.e./y; 1988-1999). Over the last two decades, available remote sensing studies (Tiwari et al., 2014; Patel et al., 2017; Garg et al., 2017a; Sahu and Gupta 2019), ubiquitously, observed a decrease in glacier surface velocities corresponding to rapid post-2000 deglaciation and retreat on Chhota Shigri Glacier (section 3.5.1). In agreement to the highest wastage over 2010-2020, the velocity decrease was also higher with a rate of 4-5%/y compared to velocity decrease of 2-4%/y over 2000s. The post-2000 glacier slowdown was also observed using field data. The surface velocity decreased by 25–42% in the

lower and middle ablation zone (below 4700m a.s.l.) since 2003 (Mandal et al., 2020). In general, the slowdown rate on Chhota Shigri Glacier was higher than the Dokriani Bamak Glacier that can be ascribed to its comparatively higher mass wastage ( $-0.36$  m w.e./y) than the Dokriani Bamak Glacier ( $-0.26$  m w.e./y) during post-2000 period. The observed slowdown likely alter the epiglacial morphology and can affect the spatial debris distribution on both the glaciers in future which will eventually influence the mass balances (Shroder et al., 2000; Garg et al., 2021).

### **3.7 Conclusions**

Due to harsh climatic conditions, the long-term in-situ glaciological observations are sparse in the Himalaya that hinders an in-depth understanding of glacier-climate relationship. In the present study, we have investigated Dokriani Bamak (central Himalaya) and Chhota Shigri (western Himalaya) glaciers for long-term dimensional and mass balance changes using satellite data and modelling.

Dokriani Bamak Glacier area decreased from  $7.07 \pm 0.1$  km<sup>2</sup> in 1968 to  $6.91 \pm 0.1$  km<sup>2</sup> in 2020 revealing a total deglaciation of  $2.22 \pm 1.54\%$  ( $0.04 \pm 0.03$  %/y) corresponding to a terminus retreat of  $10.81 \pm 0.3$  m/y. Whereas, Chhota Shigri Glacier area was  $15.64 \pm 0.19$  km<sup>2</sup> in 1971 which decreased to  $14.94 \pm 0.32$  km<sup>2</sup> exhibiting a total area loss of  $4.47 \pm 1.69\%$  ( $0.09 \pm 0.03$  %/y). The total deglaciation of Chhota Shigri Glacier was almost double than the Dokriani Bamak Glacier due to the detachment of a western tributary glacier of Chhota Shigri Glacier during 2010-2020, leading to vacation of a large area ( $1.17$  km<sup>2</sup>).

Over the last seven decades, Dokriani Bamak and Chhota Shigri glaciers showed almost similar and limited mass wastage with mean annual glacier-wide mass balance of  $-0.09 \pm 0.35$  m w.e./y and  $-0.12 \pm 0.28$  m w.e./y, respectively. Both the glaciers showed decadal positive mass balances over 1950-1980s, slight mass wastage over 1990s, and an accelerated mass wastage after 2000. The results revealed a significant impact of mass balance on deglaciation and

retreat of both the glaciers. The deglaciation and retreat rates were negligible upto 1990 when the glaciers were in almost balanced condition. However, over post-2000 period, particularly during 2011-2020, as the mass balance became more negative, both Dokriani Bamak and Chhota Shigri glaciers experienced accelerated deglaciation and retreat. The observations also revealed that the impact of mass balance is manifested through dimensional changes on or within the decadal time-scale. Further, though the mass wastage patterns were similar on both the glaciers, Chhota Shigri Glacier showed consistently lower terminus retreat than that of the Dokriani Bamak Glacier because of the topographic settings of its snout. The combined effect of shading and thick debris cover resulted in lower terminus retreat of the Chhota Shigri Glacier than Dokriani Bamak Glacier where the snout area is widely open and having a big supraglacial stream. The negative mass balance regime post-2000 period also led to significant reduction in glacier velocity on both the glaciers which, in turn, likely influence the debris growth rates and epi-glacial morphology.

## Chapter 4

# Glacier-wide mass, and energy balances of Dokriani Bamak and Chhota Shigri glaciers using energy balance approach

### 4.1 Introduction

Himalaya-Karakoram (HK) —also known as Third Pole— is among the most vulnerable water towers on Earth (Immerzeel et al., 2020). Glaciers in the HK region generate the headwaters of South Asian River systems including the Indus, Ganga, and Brahmaputra (Bolch et al., 2019). These river systems quench the water requirements for irrigation, hydropower and industrial needs of more than a billion people of the neighboring countries (Azam et al., 2021). Due to increasing temperatures and erratic precipitation patterns (Bolch et al., 2019; Hock et al., 2019; Krishnan et al., 2019), HK glaciers are at risk. Studies suggest a spatially heterogeneous glacier wastage in the High Mountain Asia (HMA) (Kääb et al., 2015; Brun et al., 2017; Shean et al., 2020) including the HK region (Azam et al., 2018). As a response to regional and global warming (Banerjee and Azam, 2016; Kraaijenbrink et al., 2017), Himalayan glaciers have been losing mass over the last 6-7 decades, similar to the glaciers worldwide (Azam et al., 2018). However, Karakoram glaciers have been in a near-balanced state since at least the 1970s (Bolch et al., 2017; Berthier and Brun, 2019), a phenomenon termed as ‘Karakoram Anomaly’ (Hewitt, 2005; Gardelle et al., 2012; Managave et al., 2020). Emerging evidence infers that the exceptional behavior of Karakoram glaciers might be linked with increasing local irrigation (de Kok et al., 2018) that results in increased snowfalls over the Karakoram range hence balanced mass budgets (Kumar et al., 2019). Nevertheless, our understanding of Karakoram Anomaly is under progress and needs further investigations (Farinotti et al., 2020).

Long-term  $B_a$  measurements are necessary to comprehend the climate change effects, especially in the inaccessible regions such as HK where high-

altitude meteorological measurements are sparse and our interpretation of the climate-glacier relationship is still limited (Shea et al., 2015a; Azam et al., 2018; Bolch et al., 2019). The classical glaciological method (Østrem and Brugman, 1991) is used to observe glacier mass changes at an annual or seasonal scale that can directly be interpreted as undelayed feedback to meteorological changes (Oerlemans, 2001).  $B_a$  measurements in the HK region are logistically challenging due to rugged topography, extreme climate and high expedition cost; consequently, measurements have been conducted on only 24 glaciers, covering only  $\sim 112 \text{ km}^2$  (out of a total glacierized area of  $\sim 40,000 \text{ km}^2$  in the HK) (Azam et al., 2018). Further,  $B_a$  measurements using the glaciological method are available for very short periods, generally  $< 10$  years, and cannot be used to understand climate change (Azam et al., 2018).

Accelerated progress in satellite data collection and processing, and open access to recently released stereo pairs from spy satellites have offered many geodetic mass change estimates at the glacier- as well as regional-scale over the last two decades (Brun et al., 2017; Vijay and Braun, 2018; Garg et al., 2019; Maurer et al., 2019; Berthier and Brun, 2019; Shean et al., 2020; Rashid and Majeed, 2020). An advantage of remote sensing tools is the large areal coverage but the geodetic estimates cannot be interpreted directly to comprehend changes in climate as they are available at a multiannual scale and provide an average response of glaciers over several years. Tree ring isotopic analysis, based has also been exploited to predict the glacier mass balances at regional scale over the HK region (Managave et al., 2012; Singh et al., 2021) but such predictions need to be tested at glacier-wide scale due to strong topographical and micrometeorological control on glacier mass balance.

In this situation, an alternative tool is to use glacier mass balance models to compute the long-term annual or seasonal  $B_a$ , and understand their climate change responses (Oerlemans et al., 1998; Vincent et al., 2004; Huss et al., 2008; Pellicciotti et al., 2008; Azam et al., 2014a). For long-term mass balance reconstructions, models exploit the available short-term in-situ mass balance and meteorological data together with long-term gridded meteorological and satellite data (Fujita et al., 2011; Azam et al., 2014a; Zhang et al., 2011; Sunako

et al., 2019). A few studies have already been performed mass balance reconstructions in the HK region at a glacier-wide scale (Brun et al., 2015; Kumar et al., 2016; Azam et al., 2019; Kumar et al., 2020; Azam and Srivastava, 2020) as well as region-wide scale (Shea et al., 2015b; Tawde et al., 2017; Kumar et al., 2019).

Brun et al. (2015) measured the seasonal changes of glacier surface albedo on CSG (Himachal Pradesh, India) and Mera (Khumbu Region, Nepal) glaciers using remote sensing data and reconstructed the  $B_a$  over 1999-2013 using a surface albedo model. A few studies developed a simplified temperature-index (T-index) model and reconstructed the long-term  $B_a$  on CSG and Shaune Garang (western Himalaya), DBG (central Himalaya) and Siachen (Karakoram) glaciers (Kumar et al., 2016; Engelhardt et al., 2017; Azam et al., 2019; Azam and Srivastava, 2020; Kumar et al., 2020) over the last 4-5 decades. Tawde et al. (2017) developed a model by combining a T-index model, accumulation-area ratio method and satellite-derived snowlines, and estimated a mean mass wastage of  $-0.61 \pm 0.46$  m w.e.  $a^{-1}$  for 146 glaciers over 1984-2012 in the Chandra Basin (western Himalaya). Shea et al. (2015b) used a more sophisticated T-index model including snow redistribution, avalanche contribution and glacier dynamics, and estimated a volume loss of  $-6.4 \pm 1.5$   $km^3$  for the Dudh Koshi Basin over 1961-2007.

Due to limited field-observed glacio-meteorological data, available studies often used the simplified T-index approach for the  $B_a$  reconstructions in the HK region. The application of surface energy balance (SEB)-based mass balance models —explaining the physical basis of glacier mass balance— have been applied on a few glaciers (Patel et al., 2021). In the present study, we applied a mass-, and energy-balance model to simulate the  $B_a$  on two climatically contrasting glaciers of DBG (central Himalaya) and CSG (western Himalaya), where relatively good field observations are available (Azam et al., 2018). The model is forced with long-term, bias-corrected meteorological ERA5 reanalysis data between 1979 and 2020. The major objectives are: (i) to reconstruct the long-term annual and seasonal  $B_a$  on DBG and CSG, (ii) to understand the  $B_a$  governing annual and seasonal energy fluxes on both the

glaciers, and (iii) to quantify the role of sublimation in mass wastage on both the glaciers. Further, the  $B_a$  sensitivities for different parameters of the model are also discussed.

## **4.2 Site description, available field measurements and climate data**

Table 4.1 summarises the abbreviations, values, units of all parameters used in this study.

### **4.2.1 Study area: Dokriani Bamak and Chhota Shigri glaciers**

DBG (30°51' N, 78°49' E) is in the Garhwal range of the central Himalaya (Fig. 4.1). It is a valley glacier with ~6 km length and an area of 7.03 km<sup>2</sup>, ranging from 4050-6632 m a.s.l. (Table 4.2) (Azam and Srivastava, 2020). DBG has a north-west orientation and is guarded by three peaks: Jaonli (6632 m a.s.l.) in the east, Draupadi Ka Danda I (5716 m a.s.l.) in the south, and Draupadi Ka Danda II (5670 m a.s.l.) in the west (Fig. 4.1). DBG terminus (4050-4900 m a.s.l.) is partially debris-covered (0.90 km<sup>2</sup>, ~13% of DBG area) (Fig. 4.1). The proglacial stream from DBG is called Din Gad that contributes to the Bhagirathi River of the Ganga River system. DBG has extensively been investigated for its meteorological conditions and mass balances (Dobhal et al., 2008; Yadav et al., 2019; Verma et al., 2018; Azam and Srivastava, 2020; Yadav et al., 2021; Dobhal et al., 2021; Garg et al., 2021a).

CSG (32°16' N, 77°34' E) is in the Lahaul-Spiti valley of the western Himalaya (Fig. 4.1). This is a valley glacier with a length of ~9 km and an area of 15.5 km<sup>2</sup>, ranging from 4070-5850 m a.s.l. (Table 4.2) (Azam et al., 2016). CSG has a mean orientation of north and upper accumulation area is bounded by valley ridges, Devachan peak being the highest (6250 m a.s.l.). The terminus of CSG (<4500 m a.s.l.) is covered with debris (~4% of CSG area) (Vincent et al., 2013). CSG drains through a proglacial stream to the Chandra River, a tributary of the Indus River system (Fig. 4.1). Since 2002, CSG is under continuous observations focusing on mass balances, SEB, ice thickness-volume-dynamics, and hydrology (Wagnon et al., 2007; Berthier et al., 2007;

**Table 4.1:** Abbreviation, unit and value of parameters used in this study.

Parameters	Symbol	Unit	Value
Air temperature	$T_a$	°C	-
Surface temperature	$T_s$	°C	-
Precipitation	$P$	mm	-
Wind speed	$WS$	$m s^{-1}$	-
Relative humidity	$RH$	%	-
Incoming shortwave radiation	$SWI$	$W m^{-2}$	-
Incoming longwave radiation	$LWI$	$W m^{-2}$	-
Outgoing shortwave radiation	$SWO$	$W m^{-2}$	-
Outgoing longwave radiation	$LWO$	$W m^{-2}$	-
Net shortwave radiation	$SWN$	$W m^{-2}$	-
Net longwave radiation	$LWN$	$W m^{-2}$	-
Net radiation	$R_n$	$W m^{-2}$	-
Sensible heat flux	$H$	$W m^{-2}$	-
Latent heat flux	$LE$	$W m^{-2}$	-
Rain Flux	$R$	$W m^{-2}$	-
Total energy available on surface	$Q$	$W m^{-2}$	-
Total energy available for melting	$Q_m$	$W m^{-2}$	-
Heat flux into the upper ice/snow layer	$H_{ice}$	$W m^{-2}$	-
Latent heat of evaporation	$l_e$	$J kg^{-1}$	$2.5 \times 10^6$
Latent heat of vaporization	$l_v$	$J kg^{-1}$	$2.864 \times 10^6$
Density of air	$\rho_a$	$kg m^{-3}$	-
Saturated specific humidity	$q(T_a), q(T_s)$	$kg kg^{-1}$	-
Bulk coefficient	$C$	dimensionless	0.002 (snow-ice), 0.005 (debris)
Heat transfer into the glacier	$H_g$	$W m^{-2}$	-
Specific heat of air	$c_a$	$J kg^{-1} K^{-1}$	1006
Specific heat of water	$c_w$	$J kg^{-1} K^{-1}$	4200
Specific gas constant for dry air	$R_{specific}$	$J kg^{-1} K^{-1}$	287.058
Saturation vapor pressure	$e^*$	dimensionless	-
Air pressure	$P$	k Pa	-
Density of water	$\rho_w$	$kg m^{-3}$	1000
Rainfall temperature	$T_r$	°C	-
Rainfall rate	$W$	$m s^{-1}$	-
Wetness parameter	$\tau_w$	dimensionless	1 (snow and ice)
Temperature of thermally active layer	$\theta$	°C	-
Albedo of snow	$\alpha_s$	dimensionless	-
Albedo of clean ice	$\alpha_i$	dimensionless	-
Albedo of debris-covered ice	$\alpha_d$	dimensionless	-
Brightness temperature	$T_b$	K	-
Debris-surface temperature	$T_{S(d)}$	°C	-
Conductive heat flux through the debris layer	$G_d$	$W m^{-2}$	-
Spectral Radiance	$L_\lambda$	$W sr^{-1} m^{-2}$	-
Temperature at the debris-ice interface	$T_i$	°C	-
Thermal resistance of the debris layer	$R_t$	$m^2 K W^{-1}$	-
Daily melt of ice beneath the debris layer	$M_d$	$mw.e. d^{-1}$	-
Length of the day	$t_{day}$	seconds	86400
Latent heat of fusion of ice	$l_m$	$J kg^{-1}$	$3.33 \times 10^5$
Glacier-wide mass balance	$B_a$	m w.e.	-
Altitudinal mass balance	$b_z$	m w.e.	-

Azam et al., 2012; Ramsankaran et al., 2018; Azam et al., 2019; Kumar et al., 2019; Mandal et al., 2020; Haq et al., 2021).

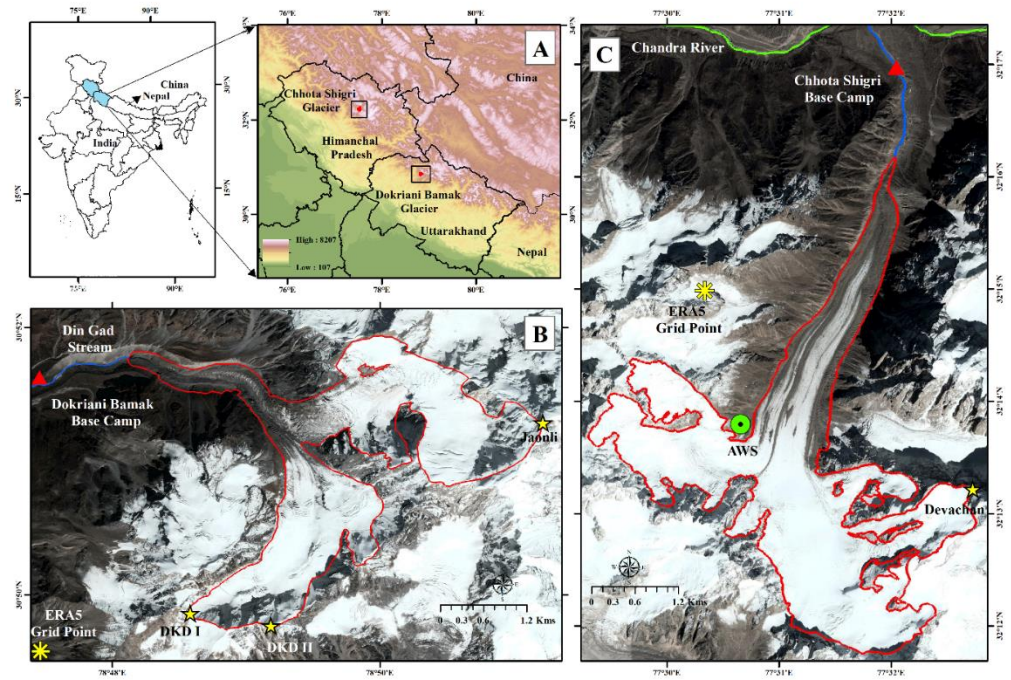


**Figure 4.1:** (A) The state boundary of Himanchal Pradesh and Uttarakhand along with locations of Dokriani Bamak and Chhota Shigri glaciers, (B) DBG (red outline) on Google earth imagery (CNES-Airbus) of 10 July 2017, (C) CSG (red outline) on Google earth imagery (CNES-Airbus) of 10 April 2017.

**Table 4.2:** List of geographical and topographical characteristics of DBG and CSG.

Glacier characteristics	Dokriani Bamak Glacier	Chhota Shigri Glacier
Area	7.03 km <sup>2</sup> (2017)	15.5 km <sup>2</sup> (2014)
Debris-covered area	0.94 km <sup>2</sup> (2017)	0.52 km <sup>2</sup> (2014)
Length	~5 km	~9 km
Terminus position	4050 m a.s.l. (2017)	4072 m a.s.l. (2015)
Orientation	north-west	north
Maximum elevation	6632 m a.s.l.	5830 m a.s.l.
Mean mass balance	-0.32 m w.e. (1992-2014)	-0.46 ± 0.40 m w.e. (2002-19)
Mean ELA*	5072 m a.s.l. (1992-2013)	5047 m a.s.l. (2002-19)
Mean AAR <sup>#</sup>	67% (1992-2013)	49% (2002-19)
Mean Accumulation area	4.72 km <sup>2</sup>	7.5 km <sup>2</sup>
Mean Ablation area	2.31 km <sup>2</sup>	8.0 km <sup>2</sup>

\*ELA = equilibrium line altitude. <sup>#</sup>AAR = accumulation area ratio

### 4.2.2 Available field data

DBG and CSG have extensively been studied hence different datasets are available from previous studies. On DBG Base Camp (BC, 3774 m a.s.l.) an automatic weather station (AWS) logged the data over 2011-2016 while on CSG an AWS, mounted on a side moraine close to high camp (HC, 4863 m a.s.l.), provided the meteorological data between 2009 and 2017. An automated precipitation gauge (Geonor T-200B) at CSG BC (3850 m a.s.l.) provided the data since 2012. The locations of AWSs and all-weather precipitation gauge are given in Fig. 4.1.  $B_a$  measurements on DBG were performed intermittently during 1992-2014 ( $-0.32$  m w.e.  $a^{-1}$ ; 1992-1995, 1996-2000 and 2007-2014) (Dobhal et al., 2008; 2021; Garg et al., 2021a) while CSG represents the longest continuous  $B_a$  series since 2002 ( $-0.46 \pm 0.40$  m w.e.  $a^{-1}$ ) in the Himalaya (Mandal et al., 2020).  $b_a$  is also available for 50-m bands over 2009-2013 for DBG (Pratap et al., 2015) and over 2002-2013 for CSG (Azam et al., 2016). Table S1 provides the logging details of meteorological data.

### 4.2.3 Climate data and bias correction

Daily reanalysis data from ERA5 was used to compute the surface energy fluxes and glacier-wide MBs on DBG and CSG. ERA5 data is available since 1979 at  $0.25^\circ \times 0.25^\circ$  resolution (Copernicus Climate Change Service C3S, 2017). The ERA5 data was found to outperform other available data sets over the Indian sub-continent (Mahto and Mishra, 2019), and it has already been used for mass- and energy-balance models in a few studies (Kumar et al., 2021; Stewart et al., 2021). Daily incoming shortwave and net radiation ( $SWI$  and  $SWN$ ), incoming longwave radiation ( $LWI$ ), wind speed ( $WS$ ), relative humidity ( $RH$ ), air temperature ( $T_a$ ) and precipitation ( $P$ ) were downloaded for the nearest grids at DBG and CSG (Fig. 4.1). The ERA5 raw data series for both the glaciers were bias-corrected using available in-situ meteorological data. The bias correction of  $T_a$  was done using a linear regression between mean monthly and daily raw ERA5 and in-situ  $T_a$  data for DBG and CSG, respectively. The bias correction of daily  $P$ ,  $WS$ ,  $RH$ ,  $SWI$ ,  $SWN$  and  $LWI$  were performed using monthly factors derived from monthly in-situ and ERA5 raw data on DBG and CSG. No in-situ

for LWI data was available from DBG hence no bias correction was given. All of the bias-corrected parameters showed a good coefficient of determination after the bias correction ( $R^2 > 0.90$ ).

## 4.3 Methods

### 4.3.1 Mass-, and energy-balance model

The mass-, and energy-balance model (Fig. 4.2) computes the SEB fluxes and  $b_a$  for each 50-m altitudinal range, and simulates snow accumulation, refreezing of rain/meltwater, surface melt, and sublimation/re-sublimation at daily time step using the long-term, bias-corrected daily ERA5 data between 1979 and 2020 (section 4.2.3).

### 4.3.2 Accumulation terms

Accumulation terms include solid precipitation and the refreezing of rain/melt water at the surface. At a given altitudinal range, the solid precipitation  $P$  (mm w.e.  $d^{-1}$ ) is computed as:

$$P = \begin{cases} P: & \text{when } T_a \leq T_P \\ 0: & \text{when } T_a > T_P \end{cases} \quad (4.1)$$

Where  $P$  and  $T_a$  represent daily precipitation (mm) and daily air temperature ( $^{\circ}C$ ), respectively extrapolated at each 50-m altitudinal range, and  $T_P$  represents the snow-rain threshold temperature ( $^{\circ}C$ ).

Refreezing of rain/melt water at each altitudinal range is computed using Oerlemans 2-m model (Oerlemans, 1992) in which the total energy available for melting ( $Q_m$ ) is determined by an exponential function of the temperature ( $\theta$ ) of the thermally active layer, considered equivalent to an upper 2-m thickness of glacier:

$$Q_m = Q \exp(\theta) \quad (4.2)$$

$$H_{ice} = Q - Q_m = Q [1 - \exp(\theta)] \quad (4.3)$$

$$c \frac{d\theta}{dt} = H_{ice} \quad \theta \leq 0 \quad (4.4)$$

Where,  $Q$  is the net surface energy budget ( $\text{W m}^{-2}$ ) and  $H_{ice}$  is the heat flux into the upper ice/snow layer. At the beginning of the mass balance modelling,  $\theta$  is set to the mean annual  $T_a$  and can only be changed at the beginning of ablation season by refreezing melt water given in equation 4.  $c$  is a constant that determines how rapidly the melted snow or ice fraction that runs off reaches 1, it was set to  $1 \text{ K}^{-1}$  (Oerlemans, 1992).

Sublimation/re-sublimation is calculated using the latent heat flux ( $LE$ ) (section 4.3.5 below) and the latent heat of vaporization ( $l_v$ ,  $2.864 \times 10^6 \text{ J kg}^{-1}$ ) as:

$$R_S = \frac{LE}{l_v} \quad (4.5)$$

### 4.3.3 Ablation terms

The major contribution to glacier ablation comes from the surface melt (Favier et al., 2004; Azam et al., 2014b; Litt et al., 2019) which is calculated using the net energy flux available at the surface. We used a simplified surface energy balance model:

$$Q = (1 - \alpha_{s,i,d}) SWI + LWI - \varepsilon\sigma(T_s + 273.15)^4 + H + L + R \quad (4.6)$$

Where  $\alpha_{s,i,d}$  is the albedo of snow ( $\alpha_s$ ), ice ( $\alpha_i$ ) and debris surface ( $\alpha_d$ ),  $\varepsilon$  is emissivity (dimensionless) and considered 1, and  $\sigma$  is the Stefan Boltzmann constant =  $5.67 \times 10^{-8} \text{ W m}^{-2} \text{ K}^{-4}$ ,  $T_s$  is the surface temperature ( $^{\circ}\text{C}$ ).  $H$ ,  $LE$  and  $R$  are the turbulent sensible heat, latent heat and rain fluxes ( $\text{W m}^{-2}$ ), respectively. Dynamic storage of snow over different altitudinal ranges was maintained using daily accumulation and ablation terms.

### 4.3.4 Computation of surface temperature

Surface temperature ( $T_s$ ) at each altitudinal range is computed following Fujita and Ageta (2000) as:

$$T_s = T_a + \frac{SWN + \varepsilon LWI - \varepsilon\sigma(T_a + 273.15)^4 - l_e \rho_a CWS(1 - RH)q(T_a) + H_g}{4\varepsilon\sigma(T_a + 273.15)^3 + \left(\frac{dq}{dT_a} l_e + c_a\right) \rho_a CWS} \quad (4.7)$$

Where,  $SWN$  is the net shortwave radiation ( $\text{W m}^{-2}$ ),  $l_e$  is the latent heat of evaporation of water ( $2.5 \times 10^6 \text{ J kg}^{-1}$ ),  $\rho_a$  is the density of air ( $\text{kg m}^{-3}$ ),  $C$  is

the bulk coefficient (0.002 for snow and clean ice and 0.005 for debris surfaces),  $q(T_a)$  is the saturated specific humidity,  $H_g$  is the heat transfer into the glacier ( $\text{W m}^{-2}$ ) (here, considered as zero) and  $c_a$  is the specific heat of the air ( $1006 \text{ J kg}^{-1} \text{ K}^{-1}$ ). We have considered all the positive surface temperatures which are coming from equation 4.7 as zero because the glacier starts melting if  $T_a$  exceeds  $0^\circ\text{C}$ .

$\rho_a$  is estimated using the gas equation, where  $P$  is the air pressure (Pa),  $R_{specific}$  is the specific gas constant for dry air ( $287.058 \text{ J kg}^{-1} \text{ K}^{-1}$ ):

$$\rho_a = \frac{P}{R_{specific} T_a} \quad (4.8)$$

$q(T_a)$  and  $[q(T_s)$  in next section (4.3.6)] at a temperature is calculated using the saturation vapor pressure ( $e^*$ ) at air and surface temperature, respectively and air pressure ( $P$ ) (k Pa):

$$q(T_{a,s}) = 0.622 * \frac{e^*}{P} \quad (4.9)$$

$$e^* = 0.611 \exp\left(\frac{17.3T_{a,s}}{T_{a,s}+237.2}\right) \quad (4.10)$$

### 4.3.5 Computation of turbulent heat fluxes

$H$ ,  $LE$  and  $R$  are computed using the simplified bulk method (Hay and Fitzharris, 1988):

$$H = c_a \rho_a CWS(T_a - T_s) \quad (4.11)$$

$$LE = l_e \rho_a CWS \tau_w [RHq(T_a) - q(T_s)] \quad (4.12)$$

$$R = c_w \rho_w w (T_r - T_s) \quad (4.13)$$

Where,  $c_w$  is the specific heat of water ( $4200 \text{ J kg}^{-1} \text{ K}^{-1}$ ),  $\rho_w$  is the density of water ( $\text{kg m}^{-3}$ ),  $T_r$  is the rainfall temperature (assumed equal to be  $T_a$ ),  $w$  is the rainfall rate ( $\text{m s}^{-1}$ ),  $\tau_w$  is the wetness parameter whose value is considered as 1 for snow and ice surfaces, but it varies over the debris-cover surface (section 4.3.6). In the present study we used the bulk method for the calculation

of energy fluxes which is known to give reasonable results even in katabatic winds conditions (Denby and Greuell, 2000).

### 4.3.6 Computation of conductive heat flux and wetness parameter for debris surface

The energy balance is defined for a debris surface as follows:

$$Q_d = (1 - \alpha_d)SWI + LWI - \varepsilon\sigma(T_{S(d)} + 273.15)^4 + H + LE - G_d \quad (4.14)$$

Where,  $Q_d$  is the net energy flux available at the debris surface ( $\text{W m}^{-2}$ ),  $\alpha_d$  is the albedo of the debris surface,  $T_{S(d)}$  is the debris-surface temperature ( $^{\circ}\text{C}$ ) and  $G_d$  is the conductive heat flux through the debris layer ( $\text{W m}^{-2}$ ).

The  $T_{S(d)}$  was calculated from brightness temperature ( $T_b$ ) as (Weng et al., 2004):

$$T_{S(d)} = \frac{T_b}{\left(1 + \left(\lambda X \frac{T_b}{c_2}\right)\right)} \quad (4.15)$$

The  $T_b$  (in K) was calculated following Boori et al. (2014):

$$T_b = \frac{K_2}{\ln\left(\frac{K_1}{L_\lambda} + 1\right)} \quad (4.16)$$

Where  $K_1$  (641.32) and  $K_2$  (1271.22) are constants derived from Planck's radiance function and  $L_\lambda$  is the spectral radiance ( $\text{W sr}^{-1} \text{m}^{-2}$ ).

$$L_\lambda = (DN - 1) X UCC \quad (4.17)$$

Where  $DN$  is estimated from an average of five sensors in the thermal infrared bands (TIR, bands 10-14) from two cloud-free images of ASTER level 3A1 data, which is an orthorectified product available from NASA space agency following Suzuki et al. (2007) and  $UCC$  is unit conversion factor ( $0.005225 \text{ W m}^{-2} \text{sr}^{-1} \mu\text{m}^{-1}$ ).

At the debris-covered glacier, only  $G_d$  reaches to the glacier ice through debris and was estimated by:

$$G_d = \frac{T_{S(d)} - T_i}{R_t} \quad (4.18)$$

Where,  $T_i$  (°C) is the temperature at the debris-ice interface, assumed to be at melting point (Fujita and Sakai, 2014) and  $R_t$  ( $\text{m}^2 \text{K W}^{-1}$ ) is the thermal resistance of the debris layer.

Assuming zero heat storage in the debris layer (*i.e.*  $Q_{(d)} = 0$ ),  $G_d$  is obtained from equations 4.14 and 4.18:

$$G_d = \frac{T_{s(d)}}{R_t} = (1 - \alpha_d)SWI + LWI - \varepsilon\sigma(T_{s(d)} + 273.15)^4 + H + LE \quad (4.19)$$

By neglecting  $H$  and  $LE$  (Suzuki et al., 2007) and incorporating all other parameters, equation 4.21 was solved for  $R_t$ .

Further, exploiting the  $R_t$  in equation 4.19, we have determined the  $T_{s(d)}$  by iterative calculation that satisfies equation 4.19 (Fujita and Sakai, 2014), incorporating turbulent sensible and latent heat fluxes, though initially these were neglected while calculating ( $R_t$ ).

The wetness parameter, mentioned in equation 4.12, was calculated incorporating the  $R_t$  derived from equation 4.19:

$$\tau_w = e^{-300R_t} \quad (4.20)$$

Thus, beneath the debris layer, the daily melt of ice ( $M_d$ ) is

$$M_d = t_{day} * G_d / l_m \quad (4.21)$$

Where,  $t_{day}$  denotes the length of the day *i.e.*, 86400 seconds and  $l_m$  denote latent heat of fusion of ice ( $3.33 \times 10^5 \text{ J kg}^{-1}$ ).

### 4.3.7 Computation of mass balance

The surface melt is calculated using the heat available for melting at different surfaces ( $Q_{(s,i,d)}$ ,  $\text{W m}^{-2}$ ). The net energy available at the surface is used to produce the melt when the  $T_s$  is above the threshold temperature for melt ( $T_M$ ) otherwise it is used to raise the  $T_s$  upto  $T_M$ :

$$M(s, i, d) = \begin{cases} 0: & \text{when } T_s \leq T_M \\ \frac{Q_{(s,i,d)}}{l_m}: & \text{when } T_s > T_M \end{cases} \quad (4.22)$$

$l_m$  is the latent heat of fusion ( $3.33 \times 10^5 \text{ J kg}^{-1}$ ) and  $Q_{(s,i,d)}$  is the amount of total energy available at the different surfaces.

$b_a$  for each 50-m altitudinal range (m w.e.) is estimated using the accumulation and the ablation terms as:

$$b_a = \frac{(P_S + R_F) - (M(s, i, d) - R_S)}{\rho_w} \quad (4.23)$$

Where  $\rho_w$  is the density of water ( $1000 \text{ kg m}^{-3}$ ).

$B_a$ , (m w.e.) is calculated using the mean  $b_a$  as:

$$B_a = \frac{\sum A_a b_a}{A} \quad (4.24)$$

Where  $A_a$  ( $\text{m}^2$ ) and  $b_a$  (m w.e.) are the 50-m altitudinal glacier area and mean mass balance, respectively, and  $A$  is the total glacier area ( $\text{m}^2$ ).  $B_a$  is calculated using daily values for the hydrological year from 1 November through 31 October of next year for the DBG (Dobhal et al., 2008) and hydrological year from 1 October through 30 September of next year for the CSG (Wagon et al., 2007). The overall structure of the model is given in Fig. 4.2.

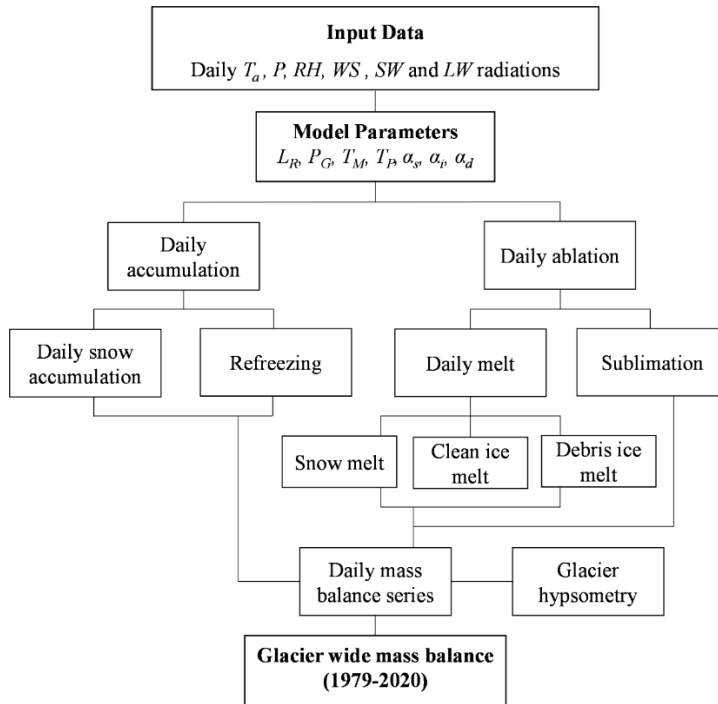


**Figure 4.2:** Mass-, and energy-balance model structure.  $T_a$  is air temperature,  $P$  is precipitation,  $RH$  is relative humidity,  $WS$  is wind speed,  $SW$  and  $LW$  are the shortwave and longwave radiations,  $L_R$  is the temperature lapse rate,  $P_G$  is precipitation gradient,  $T_M$  is threshold temperature for melt,  $T_P$  is threshold temperature for precipitation,  $\alpha_s$  is the albedo of snow,  $\alpha_i$  is the albedo of ice, and  $\alpha_d$  is the albedo of debris cover.

### 4.3.8 Model Parameters

In the mass-, and energy-balance model,  $T_a$  is among the most important parameters as it decides the precipitation phase (snowfall or rain) (Shea et al., 2015a; Hock, 2003). In this study we calculated the extrapolated values of  $T_a$  using the temperature lapse rates ( $T_{LR}$ ) developed using field observations (Azam and Srivastava, 2020; Azam et al., 2014a). Further, the  $T_p$  values were adopted from Jennings et al. (2018), where we used a  $T_p$  value of  $0.7^\circ$  and  $1.1^\circ$  C corresponding to 70-80% and 60-70%  $RH$  ranges for DBG and CSG, respectively, at which 90 to 100% precipitation was considered as snow. Both the  $T_a$  and  $T_p$  are critical parameters for mass-, and energy-balance modelling in a glacierized catchments as they decide the precipitation phases especially in the snow-rain transition zones (Shea et al., 2015a; Hock, 2003; Jennings et al., 2018).

The net solar radiation is crucial in the surface mass-, and energy-balance modeling, and the amount of insolation available for melt production largely depends on surface albedo (Azam et al., 2014b; Litt et al., 2019). Surface albedo values ( $\alpha_s$ ,  $\alpha_i$ ,  $\alpha_d$ ) have high spatiotemporal variability over the glaciers. Deposition of dust and black carbon aerosols together with progressive snow compaction makes albedo values very uncertain (Oerlemans and Knap, 1998b; Brock and Arnold, 2000). Moreover, the mass-, and energy-balance models are highly sensitive to surface albedo (Acharya and Kayastha, 2019; Stigter et al., 2021; Johnson and Rupper, 2020); therefore, surface albedo values ( $\alpha_s$ ,  $\alpha_i$ ,  $\alpha_d$ ) are calibrated in the present study using the plausible ranges available from Cuffey and Paterson (2010). Due to lack of understanding of surface albedo evolution (even with satellites) as well as to keep the model computationally simple, we have used static calibrated albedo values for snow, ice and debris

surfaces (Ragettli et al., 2013, 2015; Acharya and Kayastha; 2019). Energy-, and mass-balance models are also sensitive to  $T_M$ , often unknown in the HK (Engelhardt et al., 2017; Azam et al., 2019; Azam and Srivastava, 2020). Further, the distribution of precipitation over glaciers is one of the biggest challenges in glaciological modelling, and it is spatially non-uniform in the HK region due to valley-specific precipitation gradients ( $P_G$ ) (Immerzeel et al., 2015; Sakai et al., 2015; Maussion et al., 2014).  $T_M$ ,  $P_G$ ,  $\alpha_s$ ,  $\alpha_i$  and  $\alpha_d$  are highly sensitive parameters and least explored in the HK region and thus used for the calibration of the mass-, and energy- balance model in this study.

### 4.3.9 Model Calibration

For the calibration of the mass-, and energy-balance model, Monte Carlo simulations are performed with 10000 parameter sets where the parameters are varied over the plausible parameter's limits (Rounce et al., 2020b; Konz and Seibert, 2010).  $P_G$  is changed from 0 to 100%  $\text{km}^{-1}$ ,  $T_M$  from  $-3^\circ\text{C}$  to  $+3^\circ\text{C}$ ,  $\alpha_s$  from 0.45 to 0.85,  $\alpha_i$  from 0.35 to 0.55 and  $\alpha_d$  from 0.1 to 0.2 following Cuffey and Paterson (2010). The runs with minimum RMSE between modelled and field-observed  $B_a$  are selected for both the glaciers. The selected runs show an RMSE of  $0.21 \text{ m w.e. a}^{-1}$  (1992-2014) and  $0.32 \text{ m w.e. a}^{-1}$  (2002-2019) between modelled and field-observed  $B_a$  for DBG and CSG, respectively. The difference between the modelled and field-observed mean  $B_a$  are  $0.01$  and  $0.06 \text{ m w.e. a}^{-1}$  on DBG and CSG, respectively (Table 4.4; Fig. 4.3).

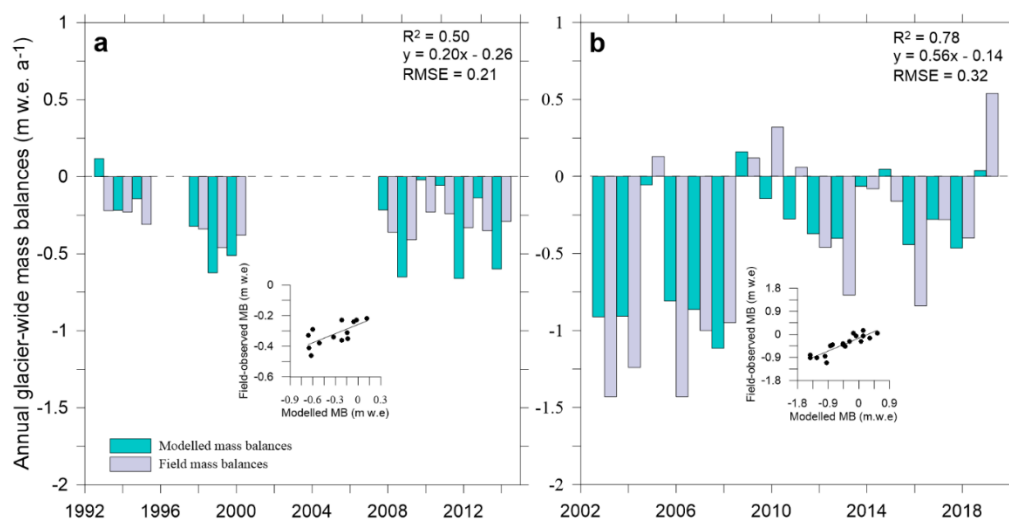


**Figure 4.3:** Model calibration: the modelled (green) and field-observed (violet)  $B_a$  on DBG over 1992-2014 (a), and CSG over 2003-2019 (b). Insets in both the panels show the correlations between modelled and field-observed mass balances.

#### 4.3.10 Model Validation

The model is validated against the field-observed mean  $b_a$  available for 50-m bands from 4050 to 4950 m a.s.l. over 2009-2013 for DBG and from 4250 to 5300 m a.s.l. over 2002-2013 for CSG (section 2.2). The agreement between modelled and field-observed  $b_a$  show a good agreement with  $R^2$  of 0.88 and 0.98 over clean ice on DBG and CSG, respectively (Fig. 4.4). On DBG, the agreement over debris cover is insignificant ( $R^2 = 0.06$ ) while CSG shows good agreement ( $R^2 = 0.76$ ) over debris-cover glacier. This is probably due to the strong spatial variability in debris distribution on DBG that accumulates towards the steep valley walls (Pratap et al., 2015), and results in heterogeneous melt, captured with ablation stakes but not in model. Even though the debris-cover area on DBG is small (~13%), we checked the mass balance sensitivity to debris cover (section 5.3). The present validation of the model against the observed  $b_a$  suggests that the model is robust enough to reconstruct the mass balances on both the glaciers.

A secondary validation is performed for  $T_s$ . The modelled  $T_s$  (section 3.1.3) are compared with the observed  $T_{S_0}$  derived from bias-corrected  $LWO$  at CSG AWS. A good agreement ( $R^2 = 0.95$ ; Fig. S14) between modelled and observed  $T_s$  indicates the robustness of surface temperature scheme. Unfortunately, the field-observed  $LWO$  data is not available for DBG.

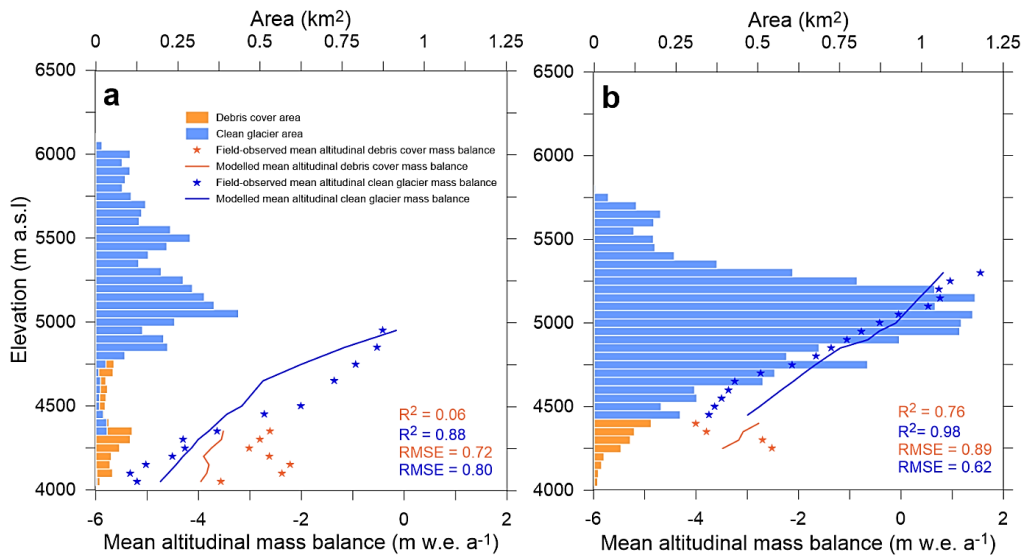


**Figure 4.4:** Model validation: the modelled and field-observed mean  $b_a$  over 2009-2013 for DBG (a) and over 2002-2013 for CSG (b). Orange and blue bars show the 50-m hypsometry of debris-covered and clean glacier; orange and blue stars show the field-observed mean  $b_a$  for the debris-covered and clean glacier; orange and blue lines show the modelled mean  $b_a$  for the debris-covered and clean glacier.

### 4.3.11 Uncertainty estimation

The model parameters are the key source of uncertainty in the modelled mass balances (Ragetti et al., 2013; Shea et al., 2015b). These uncertainties are calculated by re-running the model while adjusting the parameters one-by-one within a reasonable range of their calibrated values, and keeping other model parameters unchanged (Table 4.3). The uncertainties in  $T_{LR}$  are taken as standard deviations of mean monthly values for both DBG and CSG. The uncertainties in other parameters ( $\alpha_s$ ,  $\alpha_i$ ,  $\alpha_d$ ,  $P_G$ ,  $T_M$  and  $T_P$ ) are unknown hence these parameters are varied with the range of  $\pm 10\%$  from their calibrated values (Ragetti et al., 2013, 2015; Anslow et al., 2008).

The total uncertainty in  $B_a$  is calculated by summing up all parametric uncertainties applying the error propagation rule. The estimated mean uncertainties for  $B_a$  are  $0.32 \text{ m w.e. a}^{-1}$  and  $0.38 \text{ m w.e. a}^{-1}$  for DBG and CSG, respectively over 1979-2020. Among all the parameters, the highest uncertainty in  $B_a$  on both the glaciers is contributed by  $\alpha_s$  (Table 4.3). The parametric

**Table 4.3:** List of model parameters, sensitivity and uncertainty ranges for DBG and CSG.

Parameters	Dokriani Bamak Glacier				Chhota Shigri Glacier			
	Model value	Uncertainty estimation range	Sensitivity test range	Mass balance sensitivity (m w.e. a <sup>-1</sup> )	Model value	Uncertainty estimation range	Sensitivity test range	Mass balance sensitivity (m w.e. a <sup>-1</sup> )
Altitudinal precipitation gradient (% km <sup>-1</sup> ) *	36	33 to 40	33 to 40	0.08	73	66 to 81	66 to 81	0.06
Temperature Lapse rate ( $T_{LR}$ ) (°C km <sup>-1</sup> )	$T_{LR}^{\#}$	L <sub>R</sub> +1σ to L <sub>R</sub> -1σ	L <sub>R</sub> +1σ to L <sub>R</sub> -1σ	0.10	$T_{LR}^{\S}$	L <sub>R</sub> +1σ to L <sub>R</sub> -1σ	L <sub>R</sub> +1σ to L <sub>R</sub> -1σ	0.12
Threshold temperature for snow/rain ( $T_p$ ) (°C)	0.70	0.63 to 0.77	0.60 to 0.80	0.02	1.10	0.99 to 1.21	1 to 1.20	0.01
Threshold temperature for melting ( $T_M$ ) (°C) *	-1.90	-1.71 to -2.09	-1.71 to -2.09	0.01	-1.83	-1.65 to -2.01	-1.93 to -1.73	0.02
Albedo of snow ( $\alpha_s$ ) *	0.77	0.69 to 0.85	0.69 to 0.85	0.29	0.77	0.70 to 0.84	0.70 to 0.84	0.37
Albedo of clean ice ( $\alpha_i$ ) *	0.47	0.42 to 0.51	0.42 to 0.51	0.02	0.50	0.36 to 0.44	0.36 to 0.44	0.02
Albedo of Debris-covered ice ( $\alpha_d$ ) *	0.16	0.14 to 0.18	0.14 to 0.18	0.02	0.13	0.13 to 0.15	0.13 to 0.15	0.001
Temperature (1°C)	-	-	T+1 to T-1	-0.50	-	-	T+1 to T-1	-0.30
Precipitation (10%)	-	-	-10% to +10%	0.23	-	-	-10% to +10%	0.13

\*Calibrated parameters; #Monthly lapse rate; §Daily lapse rate

uncertainty in summer and winter mass balances are 0.38 and 0.01 m w.e a<sup>-1</sup> for DBG and 0.36 and 0.02 m w.e. a<sup>-1</sup> for CSG, respectively over 1979-2020.

In this study, a fixed glacier hypsometry was used on both the glaciers. For DBG, the hypsometry was manually delineated from high-resolution CNES-Airbus data from 10 July 2017 using a high-resolution Google Earth platform (Azam and Srivastava, 2020) while hypsometry for CSG was estimated using a Digital Elevation Model (DEM) developed using Pléiades stereo pair from 18 August 2014 (Azam et al., 2016). This fixed area assumption includes  $B_a$  uncertainties, but these were found to be insignificant comparing the total estimated uncertainty in  $B_a$  in previous studies using T-index models (Azam et al., 2019; Azam and Srivastava, 2020), hence ignored in this present study.

## 4.4 Results

### 4.4.1 Meteorological conditions and seasonal characteristics

The HK Mountain range is located in a sub-tropical climate zone with a large annual temperature amplitude resulting in clear summer and winter seasons. The climate of the HK is controlled by the Indian winter monsoon (IWM), embedding western disturbances, mainly during winters and the Indian summer monsoon (ISM) mainly during summer (Gadgil et al., 2003; Dimri et al., 2016). The influence of IWM decreases eastwards, conversely, ISM intensity decreases westwards along with the HK mountain range (Maussion et al., 2014). In-situ meteorological data from DBG and CSG are available for short periods (section 2.2); therefore, long-term, bias-corrected ERA5 data over 1979-2020 is exploited to understand the mean seasonal characteristics on both the glaciers.

Mean monthly cycles of  $T_a$  and  $RH$  on both the glaciers followed roughly similar trends, however,  $WS$  showed strong seasonality on DBG and moderate winds on CSG (Fig. 4.5). The amplitudes of mean monthly  $T_a$  and  $RH$  ( $T_{aDBG} = -7.2$  °C and  $RH_{DBG} = 46\%$  on DBG and  $T_{aCSG} = -6.1$ °C and  $RH_{CSG} = 47\%$  on CSG) were sufficiently large to characterize the different seasons. A humid, warm and less windy summer-monsoon from June through September

and a less humid, cold and windy winter season from December through March were demarcated on both the glaciers (Fig. 4.5). A pre-monsoon over April-May and a post-monsoon over October-November were also defined (Table 4.5). The same season demarcation was suggested on CSG by Azam and others (2014a) using 3-years of AWS data (Fig. 4.1).

The summer-monsoon was warmest ( $T_{aDBG} = -1.5$  °C,  $T_{aCSG} = 1.8$  °C), least windy ( $WS_{DG} = 3.6$  m s<sup>-1</sup>,  $WS_{CSG} = 4.8$  m s<sup>-1</sup>) and most humid ( $RH_{DBG} = 63\%$ ,  $RH_{CSG} = 61\%$ ) on both the glaciers (Table 4.5). Conversely, winter season was coldest, much below freezing point ( $T_{aDBG} = -12.7$  °C,  $T_{aCSG} = -13.5$  °C), and windiest ( $WS_{DBG} = 8.8$  m s<sup>-1</sup>,  $WS_{CSG} = 5.7$  m s<sup>-1</sup>) on both the glaciers. Pre-monsoon and post-monsoon showed the moderate conditions for  $T_a$ ,  $RH$  and  $WS$  (Table 4.4). Surface temperature ( $T_s$ ) was always negative on both the glaciers except for the summer-monsoon when it was close to 0 °C, showing the melting at the surface due to higher  $T_a$  of summer-monsoon (Table 4.4).

The mean monthly  $P$  cycles were remarkably different on both the glaciers (Fig. 4.5). ISM brought the major amount of annual  $P$  (74%) over DBG during the summer-monsoon, while IWM brought the major amount of annual  $P$  (53%) over CSG during the winter. Therefore, these glaciers can be considered as summer accumulation-type and winter accumulation-type glaciers, respectively. The mean annual  $P$  on DBG was almost double that of CSG (Table 4.3). Systematically,  $P$  amounts on DBG in all seasons were 1.5-2 times less than that of CSG except the summer-monsoon when  $P$  on DBG was 9 times compared to CSG (Table 4.4).

Despite the maximum solar angle in the summer-monsoon,  $SWI$  was maximum during pre-monsoon on both the glaciers ( $SWI_{DBG} = 298$  W m<sup>-2</sup>,  $SWI_{CSG} = 418$  W m<sup>-2</sup>) because monsoonal cloud cover impedes the  $SWI$  in the summer-monsoon (Litt et al., 2019; Azam et al., 2014b). However, this effect was much stronger on DBG due to strong monsoonal influence (Fig. 4.5). The reduced  $SWI$  ( $SWI_{DBG} = 294$  W m<sup>-2</sup>,  $SWI_{CSG} = 410$  W m<sup>-2</sup>) during the summer-monsoon were compensated by the highest  $LWI$  ( $LWI_{DBG} = 310$  W m<sup>-2</sup>,  $LWI_{CSG} = 272$  W m<sup>-2</sup>) on both the glaciers —mostly emitted from warm, dense summer-monsoonal clouds and surrounding valley walls. Post-monsoon and winter

exhibited quite similar conditions, receiving lower *SWI* and *LWI* because of decreasing solar angle,  $T_a$  and *RH* (Table 4.4).

**Table 4.4:** Mean seasonal and annual  $T_a$ ,  $T_s$ , *RH*, *WS*, *SWI*, *LWI* and *P* using bias-corrected ERA5 data over 1979-2020.

	Variable	Dokriani Bamak Glacier	Chhota Shigri Glacier
Post-monsoon (ON)	$T_a$ (°C)	-8.0	-7.8
	$T_s$ (°C)	-6.0	-11.6
	<i>RH</i> (%)	29	36
	<i>WS</i> (m s <sup>-1</sup> )	6.5	5.2
	<i>SWI</i> (W m <sup>-2</sup> )	218	305
	<i>LWI</i> (W m <sup>-2</sup> )	225	188
	<i>P</i> (mm w.e.)	36	47
Winter (DJFM)	$T_a$ (°C)	-12.7	-13.5
	$T_s$ (°C)	-14.4	-18.0
	<i>RH</i> (%)	40	37
	<i>WS</i> (m s <sup>-1</sup> )	8.8	5.7
	<i>SWI</i> (W m <sup>-2</sup> )	182	207
	<i>LWI</i> (W m <sup>-2</sup> )	210	184
	<i>P</i> (mm w.e.)	380	520
Pre-monsoon (AM)	$T_a$ (°C)	-7.1	-5.6
	$T_s$ (°C)	-4.6	-7.4
	<i>RH</i> (%)	44	49
	<i>WS</i> (m s <sup>-1</sup> )	5.9	5.2
	<i>SWI</i> (W m <sup>-2</sup> )	298	418
	<i>LWI</i> (W m <sup>-2</sup> )	248	214
	<i>P</i> (mm w.e.)	131	246
Summer-monsoon (JJAS)	$T_a$ (°C)	-1.5	1.8
	$T_s$ (°C)	-0.3	-0.6
	<i>RH</i> (%)	63	61
	<i>WS</i> (m s <sup>-1</sup> )	3.6	4.8
	<i>SWI</i> (W m <sup>-2</sup> )	294	410
	<i>LWI</i> (W m <sup>-2</sup> )	310	272
	<i>P</i> (mm w.e.)	1544	169
Annual (mean)	$T_a$ (°C)	-7.2	-6.1
	$T_s$ (°C)	-6.6	-9.3
	<i>RH</i> (%)	46	47
	<i>WS</i> (m s <sup>-1</sup> )	6.2	5.2
	<i>SWI</i> (W m <sup>-2</sup> )	245	326
	<i>LWI</i> (W m <sup>-2</sup> )	252	219
	<i>P</i> (mm w.e.)	2091	981

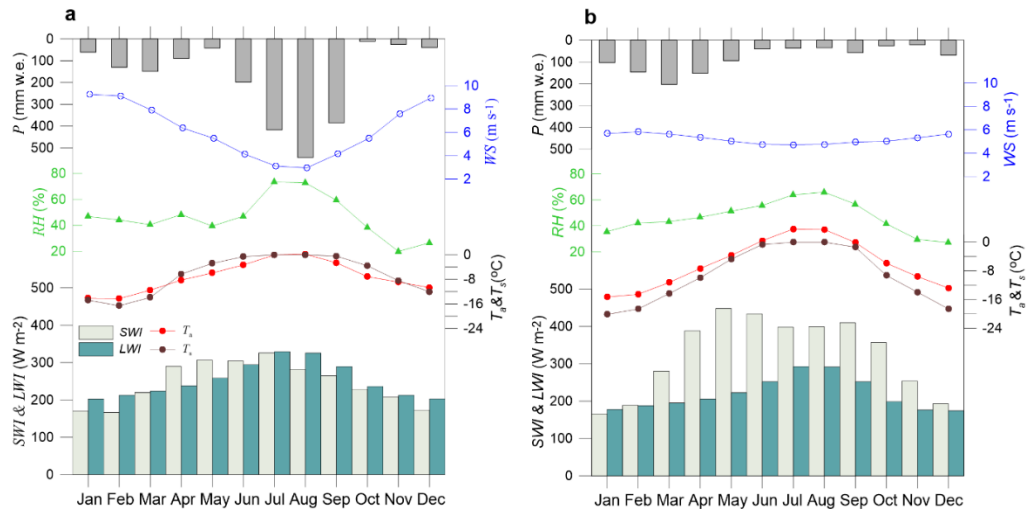


**Figure 4.5:** Glacier-wide mean monthly values of  $T_a$  (red dots),  $T_s$  (brown dots),  $RH$  (green triangles),  $WS$  (blue circles),  $P$  (grey bars),  $SWI$  (orange bars) and  $LWI$  (violet bars) at (a) DBG base camp (3774 m a.s.l) and (b) CSG high camp (4863 m a.s.l), respectively from bias-corrected ERA5 data over 1979-2020.  $SWI$  and  $LWI$  are at point scale while all other parameters are at glacier-wide scale.

#### 4.4.2 Glacier-wide annual and seasonal mass balances

The mass wastage was moderate, and similar, on both the glaciers with a mean wastage of  $-0.27 \pm 0.32$  m w.e.  $a^{-1}$  (equivalent cumulative mass wastage of  $-11.16 \pm 2.06$  m w.e.) on DBG and  $-0.31 \pm 0.38$  m w.e.  $a^{-1}$  (equivalent cumulative mass wastage of  $-12.61 \pm 2.67$  m w.e.) on CSG, over 1979-2020 (Fig. 4.6). The year 1982/83 and 1988/89 showed the maximum  $B_a$  of  $0.20 \pm 0.33$  m w.e. and  $0.42 \pm 0.23$  m w.e., while year 2000/01 showed the minimum  $B_a$  of  $-0.75 \pm 0.32$  m w.e. and  $-1.49 \pm 0.76$  m w.e. for DBG and CSG, respectively.  $B_a$  was negative for 35 and 27 years and positive for 6 and 14 years on DBG and CSG, respectively. Though the mass wastage on both the glaciers was almost the same, the mass turnover on CSG ( $1.27$  m w.e.  $a^{-1}$ ) was almost double that of DBG ( $0.92$  m w.e.  $a^{-1}$ ) (Fig. 4.6). This is because CSG is a winter accumulation-type glacier and receives a lot of accumulation during winter that is melted out during the summer-monsoon, while for DBG the accumulation and ablation seasons coincide during the summer-monsoon (section 4.1).

Modelled seasonal mass balances ranged from 0.07 to 0.69 m w.e. a<sup>-1</sup> and 0.17 to 0.72 m w.e. a<sup>-1</sup> for winter, and -1.00 to -0.16 and -1.69 to -0.06 w.e. a<sup>-1</sup> for summer on DBG and CSG, respectively. The mean summer and winter mass balances were  $-0.60 \pm 0.30$  and  $0.32 \pm 0.02$  m w.e. a<sup>-1</sup> on DBG and  $-0.79 \pm 0.36$  and  $0.48 \pm 0.02$  m w.e. a<sup>-1</sup> on CSG for the period 1979-2020, respectively.

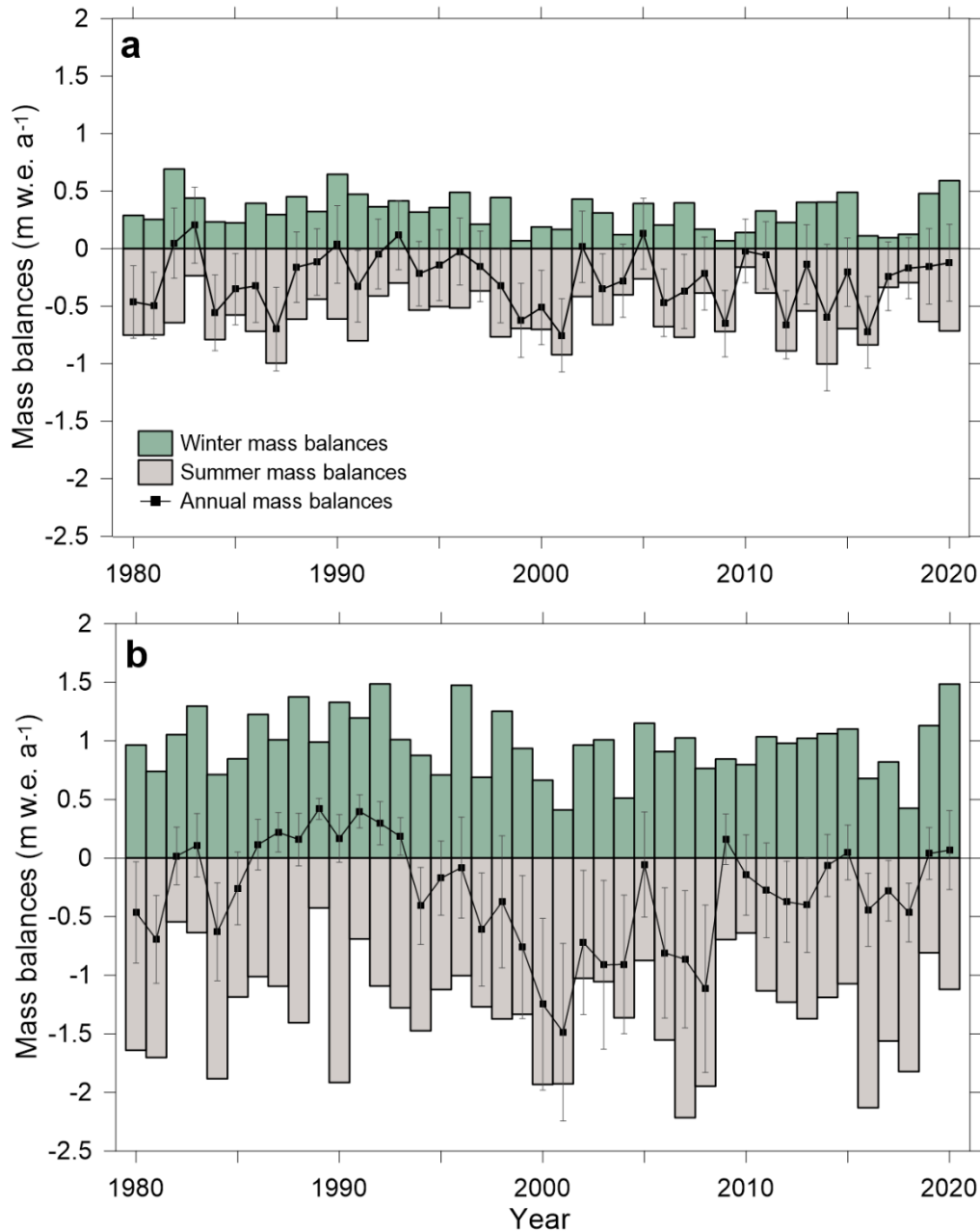


**Figure 4.6:** Annual mass balances (black squares), winter mass balances (green bars), and summer mass balances (grey bars) over 1979-2020 on (a) DBG and (b) CSG, respectively. The uncertainties of annual mass balances are shown.

#### 4.4.3 Seasonal and annual glacier-wide surface energy balance

SEB mainly depends on the seasons (Litt et al., 2019). In the summer-monsoon,  $SWN$  was highest with mean values of 100 and 125  $W m^{-2}$  on DBG and CSG, with high daily variability from 71 to 151  $W m^{-2}$  and 76 to 171  $W m^{-2}$ , respectively (Fig. 4.7).  $LWN$  was also maximum in the summer-monsoon on both the glaciers due to humid, warm and dense cloud cover conditions that result in high values of  $LWI$  (Table 4.5). Highest  $SWN$  and  $LWN$  resulted in the highest net radiation ( $R_n$ ) at the surface during the summer-monsoon with the mean seasonal values of 95 and 84  $W m^{-2}$  on DBG and CSG, respectively (Fig. 4.7, Table 4.6). Both the glaciers gained a small amount of energy through  $H$ . Conversely, a small amount of energy was released through  $LE$ —indicating some mass loss through sublimation (Table 4.6). The resulting energy,  $Q$ , was highest and positive during the summer-monsoon on both the glaciers mainly because of the highest values of both  $SWN$  and  $LWN$  (Table 4.4).

In winter,  $SWN$  was least with 42 and 37  $W m^{-2}$  values while  $LWN$  remained moderate with  $-45$  and  $-57$   $W m^{-2}$  values on DBG and CSG, respectively (Table 4.4). Winter  $SWN$  and  $LWN$  showed comparatively less variability on both the glaciers (Fig. 4.7). In winter, DBG and CSG released some energy ( $-3$  and  $-20$   $W m^{-2}$ , respectively) through  $R_n$  (Fig. 4.7). Similar to CSG, a recent study also found negative  $R_n$  during winter on 8 glaciers in the Chandra valley, including CSG (Patel et al., 2021). Due to the higher temperature gradient and strongest  $WS$  in winter (Table 4.4),  $H$  was maximum and provided 13 and 23  $W m^{-2}$  energy at the surface of DBG and CSG, respectively (Table 4.5).  $LE$  was moderately negative during winter showing moderate glacier-wide sublimation (Table 4.5). The net energy,  $Q$ , was also moderate but negative with  $-23$  and  $-16$   $W m^{-2}$  values, mainly due to the least values of winter  $SWN$  on both the glaciers (Table 4.5).

In pre-monsoon and post-monsoon,  $SWN$  values were moderate as 67 and 56  $W m^{-2}$  on DBG, and 87 and 61  $W m^{-2}$  on CSG, respectively (Table 4.5). Energy loss through  $LWN$  was highest in post-monsoon as compared to other seasons on both the glaciers (Fig. 4.7).  $R_n$  was positive in pre-monsoon while negative in post-monsoon (Table 4.6) due to most negative  $LWN$  values in post-

monsoon on both the glaciers. Both DBG and CSG gained more energy in the form of  $H$  in post-monsoon than pre-monsoon (Fig. 4.7). The most negative values of  $LE$  in pre-monsoon and post-monsoon (Table 4.5) indicate the maximum mass loss through sublimation during these seasons. The  $Q$  was least in both pre-monsoon and post-monsoon because of higher negative values of  $LWN$  and  $LE$ , and moderate values of  $SWN$  (Table 4.5).

**Table 4.5:** Mean seasonal and annual glacier-wide SEB components ( $W m^{-2}$ ) on DBG and CSG.

	Variable	Dokriani Bamak Glacier	Chhota Shigri Glacier
Post-monsoon (ON)	$SWN$	56	61
	$LWN$	-65	-78
	$R_n$	-8	-17
	$H$	6	21
	$LE$	-40	-30
	$Q$	-42	-26
Winter (DJFM)	$SWN$	42	37
	$LWN$	-45	-57
	$R_n$	-3	-20
	$H$	13	23
	$LE$	-33	-20
Pre-monsoon (AM)	$Q$	-23	-16
	$SWN$	67	87
	$LWN$	-47	-70
	$R_n$	19	17
	$H$	6	6
	$LE$	-43	-34
Summer- monsoon (JJAS)	$Q$	-20	-21
	$SWN$	100	125
	$LWN$	-4	-41
	$R_n$	95	84
	$H$	10	8
	$LE$	-21	-23
Annual (mean)	$Q$	84	70
	$SWN$	68	77
	$LWN$	-35	-57
	$R_n$	33	20
	$H$	9	15
	$LE$	-32	-25
	$Q$	10	10

Similar to previous studies in the HK region (Mölg et al., 2012; Azam et al., 2014b; Huintjes et al., 2015a; Huintjes et al., 2015b; Johnson and Rupper, 2020; Patel et al., 2021), annual glacier-wide *SWN* contributed the maximum amount of energy to the total SEB on DBG and CSG. Further, both the glaciers lost energy through *LWN* at  $-35$  and  $-57$   $\text{W m}^{-2}$ , respectively. *H* brought some energy throughout the year with 9 and 15  $\text{W m}^{-2}$  values on DBG and CSG (Table 4.5; Fig. 4.7). Patel and others (2021) also observed a similar mean annual value of *H* on 8 glaciers in the Chandra valley (Fig. 4.7). *LE* remained negative throughout the year on both the glaciers indicating mass loss through sublimation, in line with other glacier-wide SEB studies in the HK region (Huintjes et al., 2015a; Huintjes et al., 2015b; Patel et al., 2021). Annually, the highest *SWN* results in maximum  $R_n$  followed by *H* and *LE* on both the glaciers. Annual glacier-wide net energy,  $Q$ , was positive with a value of 10  $\text{W m}^{-2}$  on both DBG and CSG (Table 4.5), indicating net glacier-wide wastage (section 4.4.2).

#### **4.4.4 Altitudinal distribution of mean annual mass balance and SEB**

The mean 50-m  $b_a$  varied from  $-4.62$  to  $2.20$  m w.e. on DBG and  $-1.95$  to  $0.57$  m w.e. on CSG (Fig. 4.8). On DBG, the terminus area  $< 4950$  m a.s.l. showed less glacier wastage towards the valley walls compared to the middle of the glacier (Fig. 4.8). This is due to the distribution of debris cover on DBG which is thicker towards valley walls (Pratap et al., 2015). Similarly, the CSG terminus area  $< 4400$  m a.s.l. also showed less mass wastage (Fig. 4.8) due to thick debris cover (Vincent et al., 2013). Despite the lowest albedo of debris cover those results in the highest *SWN* over the debris-covered glacier with mean values of 188 and 141  $\text{W m}^{-2}$  on DBG and CSG, respectively, the melting was least because a thick debris cover protects glacier for higher melt (Vincent et al., 2016; Banerjee, 2017). Going up on the glacier, the  $b_a$  increased and become positive in the accumulation areas on both the glaciers (Fig. 4.8). The increase in  $b_a$  with altitude closely followed *SWN* that continuously reduced with altitude and achieved near-constant values of 56 and 59  $\text{W m}^{-2}$  at higher altitudes on

DBG (> 5250 m a.s.l.) and CSG (> 5050 m a.s.l) glaciers, respectively. This was probably because of the permanent snow cover in the accumulation area, having higher surface albedo values hence near-stable *SWN*. Glaciers lost some energy through *LWN* that was highly negative over lower reaches (< 4500 m a.s.l) compared to higher altitudes on both the glaciers (Fig. 4.8).  $R_n$  was higher over lower reaches (< 4850 m a.s.l), then showed a reduction between 4800 to 5500 m a.s.l and again increased slightly towards higher reaches (> 5500 m a.s.l) due to the highest *LWN* at higher reaches on both the glaciers (Fig. 4.8). DBG showed high and positive  $H$  values at lower altitudes (< 5250 m a.s.l) and slightly negative values at higher altitudes due to the negative air-surface temperature gradient ( $T_a - T_s$ ) while it remained positive over the whole CSG (Fig. 4.8). *LE*, generally more negative at higher altitudes, showed altitudinal mass loss through sublimation equivalent to  $-6$  to  $-42 \text{ W m}^{-2}$  on both DBG and CSG (Fig. 4.8). The resulting energy,  $Q$ , was positive at lower altitudes (< 5000 m a.s.l) and became negative at higher altitudes on both the glaciers (Fig. 4.8).

On the DBG terminus area (< 4950 m a.s.l.), all the SEB components showed different behavior towards valley walls as compared to the middle of the glacier because of thick debris cover towards valley walls (Fig. 4.8). Due to the low albedo of debris cover, *SWN* was highest that resulted in maximum  $R_n$  and  $Q$  over those areas (Fig. 4.8).  $H$  was slightly negative over debris-covered area compared to positive values at the middle of the glacier while *LE* was slightly less negative over debris-covered area compared to more negative values at the middle of the glacier. This is due to the higher  $T_s$  than  $T_a$  over the debris-covered area due to the unavailability of snow or ice cover during mainly the summer-monsoon (Fig. 4.8).

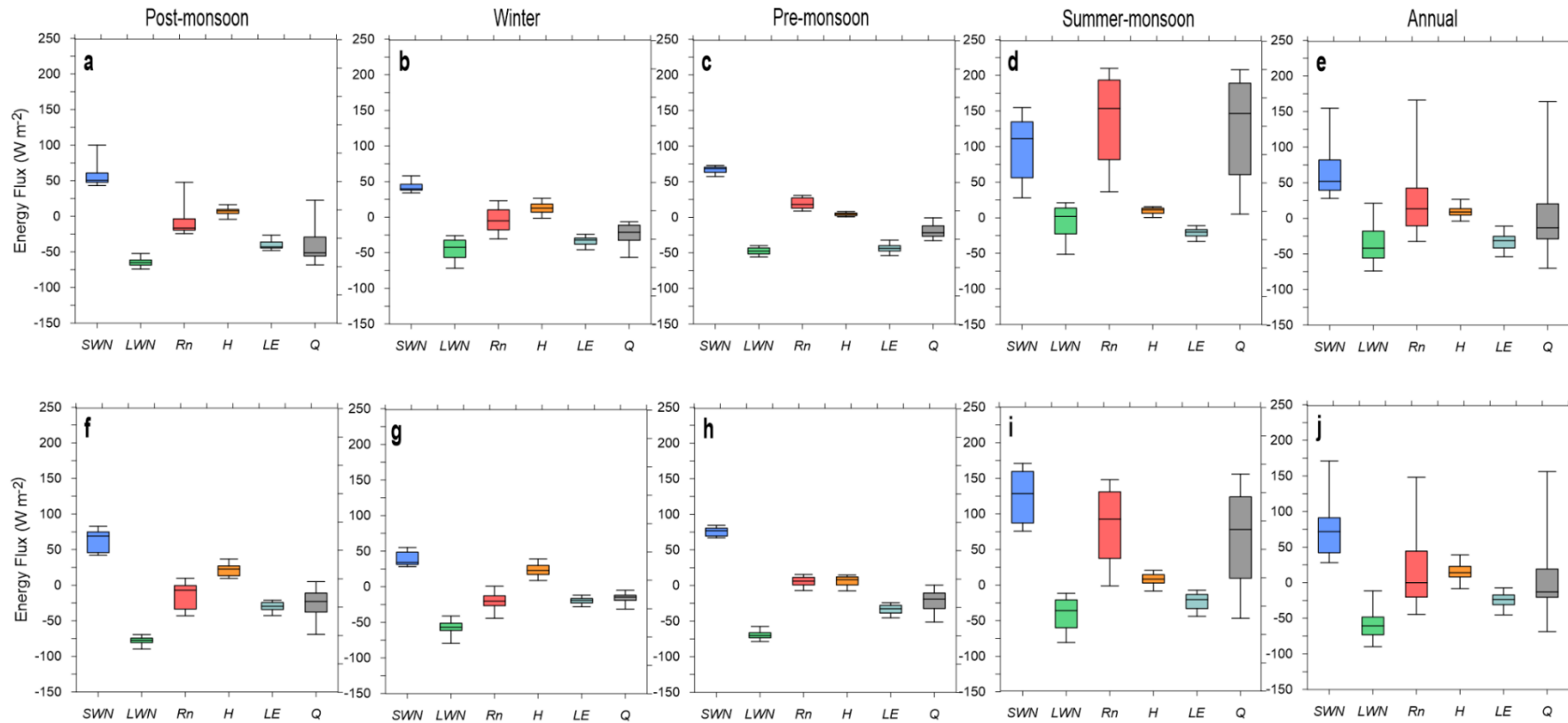


**Figure 4.7:** Box-whisker plots of mean daily SEB components calculated from all available data from 1979-2020 and classified into seasons, post-monsoon, winter, pre-monsoon, and summer-monsoon. The boundaries of each box cover the 25<sup>th</sup> to the 75<sup>th</sup> percentile of each distribution, while the middle line of the box shows the median value. Box-whisker in (a - e) shows the values for DBG and (f - j) CSG, respectively.

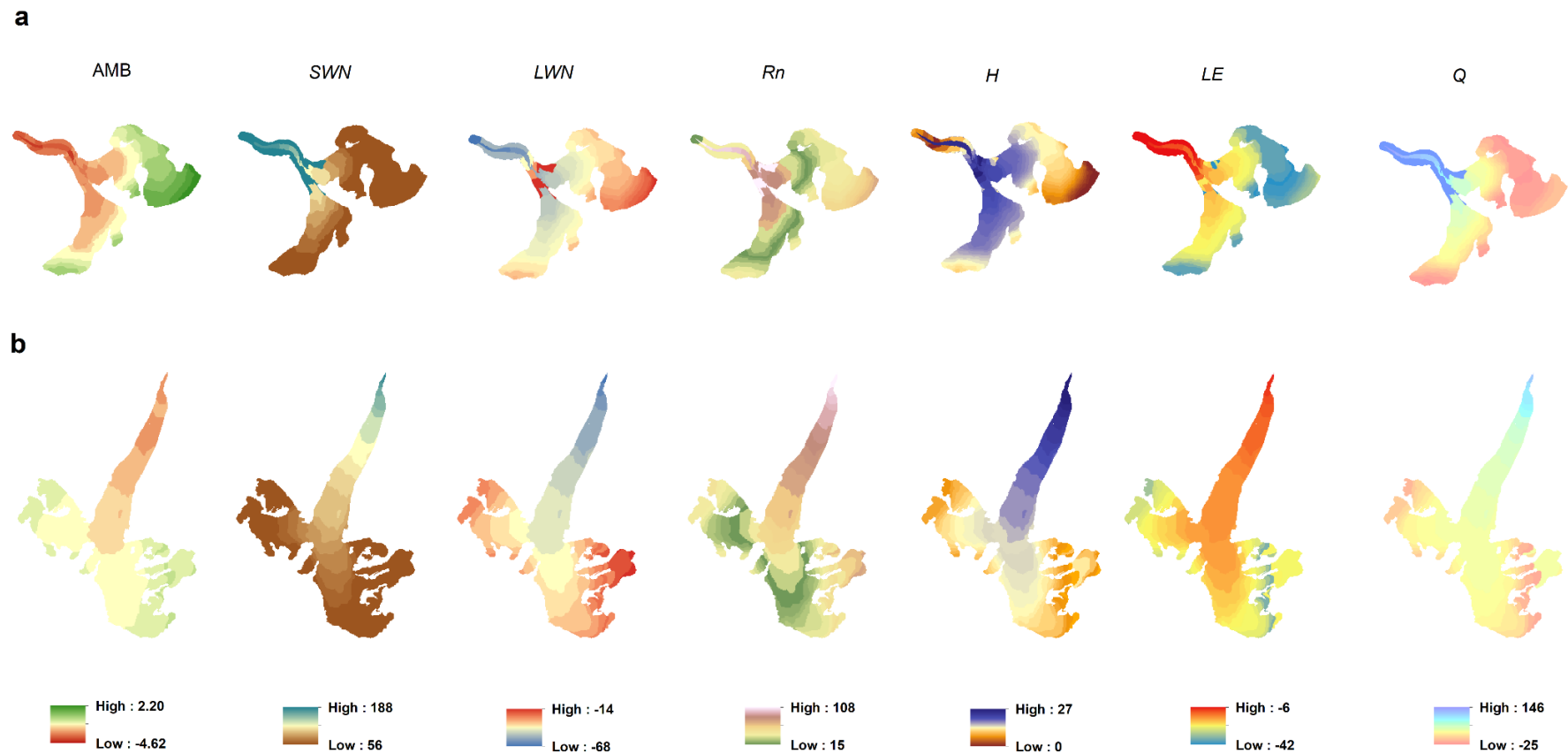


**Figure 4.8:** Distribution of modelled mean altitudinal mass balances and mean SEB components for 1979-2020 period of (a) DBG and (b) CSG, respectively. Glaciers' maps not to scale.

#### 4.4.5 Glacier-wide sublimation

The mean long-term glacier-wide sublimation was computed as  $-1.42$  and  $-0.91$  mm w.e.  $d^{-1}$  over 1979-2020, with a strong spatial and temporal variability, on DBG and CSG, respectively (Fig. 4.8 and Fig. 4.9). Previously, using in-situ AWS data from the middle of the ablation zone (4670 m a.s.l.) on CSG, a point-scale SEB study was performed and a mean sublimation was computed to be  $-0.63$  mm w.e.  $d^{-1}$  in the summer-monsoon, post-monsoon and winter season (Azam et al., 2014b). The mean monthly sublimation was highest in May on DBG ( $-2.03$  mm w.e.  $d^{-1}$ ) and in June ( $-1.53$  mm w.e.  $d^{-1}$ ) on CSG, and sharply decreased over July-August as soon as monsoon arrived over these glaciers (Fig. 4.9). Despite the lowest  $WS$ , highest  $RH$  and  $T_a$  in the summer-monsoon months (Fig. 4.9) reversed the specific humidity gradient. This reversal led to slightly positive values of  $LE$ , at least over the ablation area, in July-August indicating re-sublimation on both the glaciers (section 5.1). This provided the least glacier-wide values of  $LE$  thus the least amounts of sublimation in the summer-monsoon on both the glaciers (Fig. 4.9). The sign reversal of  $LE$  from negative to positive during humid and warmer conditions has also been observed from SEB studies in different mountain ranges including the HK region (Oerlemans, 2000; Wagnon et al., 1999, 2003; Sicart et al., 2005; Azam et al., 2014b; Litt et al., 2015; Stigter et al., 2018). Even though the  $WS$  was highest in winter, the mean monthly glacier-wide sublimations were moderate due to the lowest  $RH$  and  $T_a$  on both the glaciers whereas sublimation was highest during pre-monsoon and post-monsoon months corresponding to moderate  $WS$ ,  $RH$  and  $T_a$  (Fig. 4.9). Similar results were found on CSG at point scale SEB (Azam et al., 2014b).

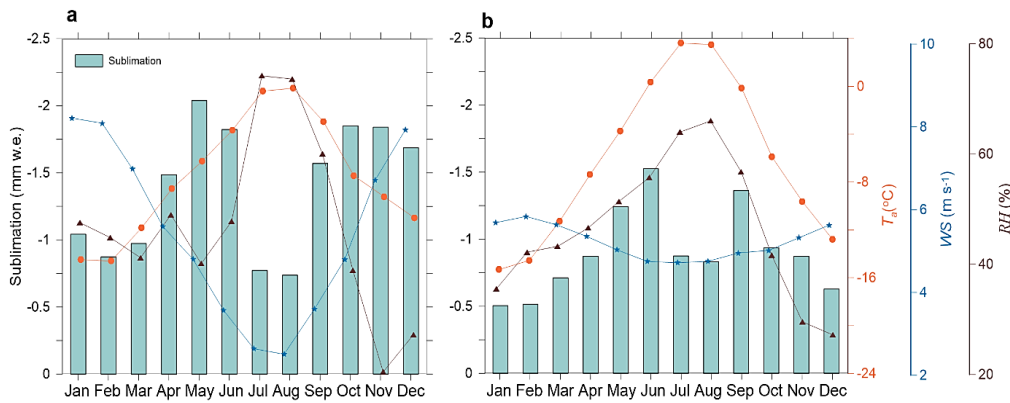


**Figure 4.9:** Monthly mean glacier-wide  $T_a$  (orange dots),  $RH$  (brown triangles),  $WS$  (blue stars), sublimation (blue-green bars) on (a) DBG and (b) CSG.

#### 4.4.6 Relative mass wastage from snow, clean ice and debris-covered ice

Snow, clean ice and debris-covered ice ablation (melt + sublimation) contributed 56%, 27%, and 17% to the total ablation on DBG while on CSG these contributions were 65%, 29% and 6%, respectively (Fig. 4.10). In agreement to highest glacier-wide snow ablation over both the glaciers, previous glacio-hydrological T-index modeling studies also suggested that the snowmelt contribution was maximum on DBG and CSG (Engelhardt et al., 2017; Azam et al., 2019; Azam and Srivastava, 2020). A slightly higher percentage of snow ablation on CSG compared to DBG is probably due to the reason that it gets around 53% of its annual precipitation in winter months that melt out in the summer-monsoon months while DBG receives the maximum of its annual precipitation in the summer-monsoon when  $T_a$  is highest that might result in rainfall on DBG even up to 5100 m a.s.l. (Pratap et al., 2015) (section 4.1). Under similar mass wastage conditions (section 4.2), the percent contribution of melt from debris-covered ice on DBG was three times of CSG because of three folds of debris-covered ice on DBG (~13%) compared to CSG (~4%) (Vincent et al., 2013; Pratap et al., 2015) (Fig. 4.10). These results clearly indicate that even though the melt is reduced over the thick debris-covered areas yet these areas experience significant mass wastage over both the glaciers.

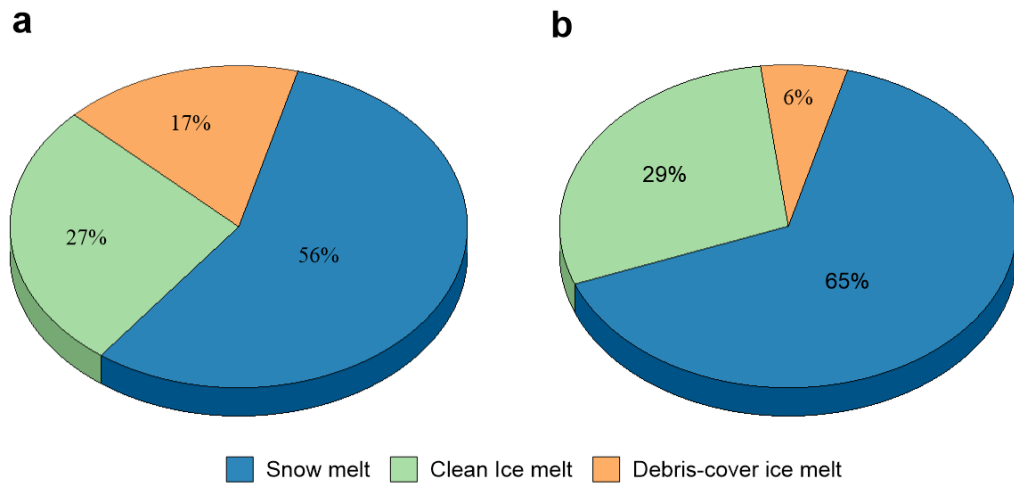


**Figure 4.10:** Relative mass wastage contribution from snow (dark blue color), clean ice (green color), and debris-covered ice (orange color) on (a) DBG and (b) CSG.

## 4.5 Discussion

### 4.5.1 SEB in ablation and accumulation zones

Most of the SEB studies in the HK have been performed at point-scale in the ablation zones (Azam et al., 2018; Litt et al., 2019). However, a few glacier-wide studies suggested that SEB is quite different in the ablation and accumulation zones of glaciers (Sun et al., 2012; Patel et al., 2021). To investigate the SEB in ablation and accumulation zones of DBG and CSG, we estimated the mean annual ablation-wide and accumulation-wide SEBs separately, dividing the ablation and accumulation zones using the mean ELA from the literature (Table 4.1).

Mean monthly *SWN* budgets were similar over ablation zones of both the glaciers: strong mean monthly cycles with highest *SWN* in August during the summer-monsoon and lowest *SWN* in winter, while relatively moderate values in accumulation zone throughout the year except winter when *SWN* were lowest on both the glaciers (Table 4.6, Fig. 4.11). In winter, both the glaciers were completely covered by snow that resulted in higher surface albedo hence similar ablation- and accumulation-wide *SWN* budgets (Table 4.6). Negative *LWN* budgets showed higher loss of energy in the ablation zone compared to

the accumulation zone throughout the year with most negative values in winter on both the glaciers (Table 4.6 and Fig. 4.11), except slightly positive values in July-August on DBG most probably because of highest  $LWI$  due to heavy monsoonal cloud cover (Table 4.4). Mean monthly  $H$  were positive as  $T_a$  was higher than  $T_s$  in the ablation zones of both the glaciers, while negative in the accumulation zones during the summer-monsoon and pre-monsoon (Table 4.6 and Fig. 4.11) as  $T_s$  becomes higher than  $T_a$  on both the glaciers (Table 4.5).  $LE$  was consistently negative in the accumulation zones of both the glaciers suggesting continuous mass loss through sublimation from higher altitudes, however it was slightly positive in the ablation zones over July-August on both the glaciers indicating re-sublimation during the core summer-monsoon (Fig. 4.11).  $Q$  remained negative throughout the year except for the summer-monsoon in the ablation zones and July-August in the accumulation zones because of higher  $SWN$  on both the glaciers. Similar kinds of results have been discussed in other SEB studies on the Himalayan glaciers (Azam et al., 2014b; Litt et al., 2019; Patel et al., 2021).

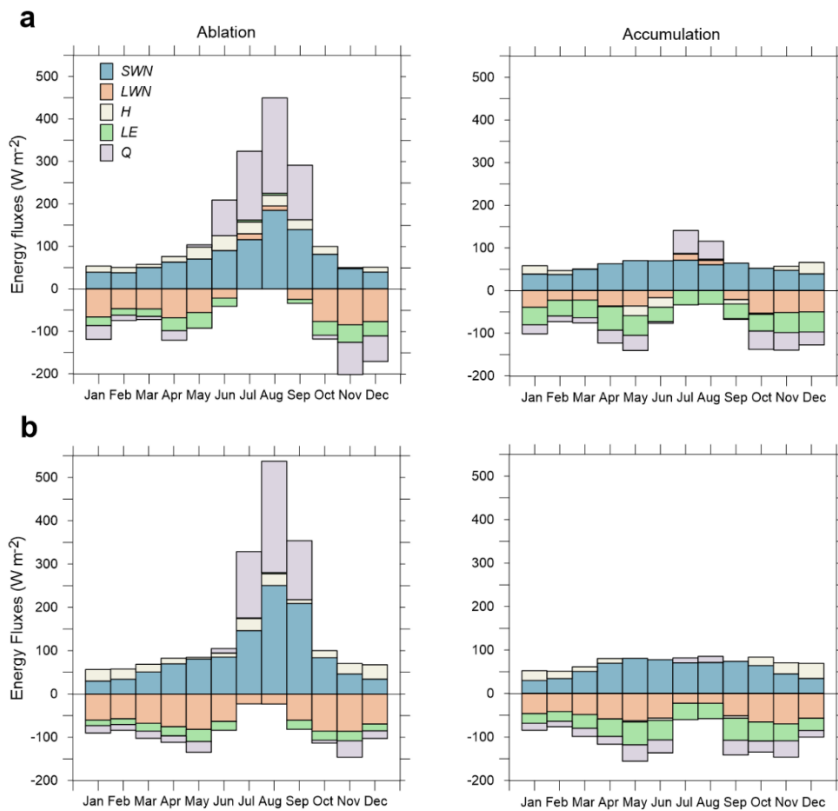


**Figure 4.11:** SEB in ablation and accumulation zones of (a) DBG and (b) CSG.

**Table 4.6:** Mean seasonal and annual SEB components ( $\text{W m}^{-2}$ ) over ablation and accumulation zone of DBG and CSG.

	Variable	Dokriani Bamak Glacier		Chhota Shigri Glacier	
		Ablation	Accumulation	Ablation	Accumulation
Post-monsoon (ON)	<i>SWN</i>	65	50	65	55
	<i>LWN</i>	-81	-52	-86	-68
	<i>H</i>	10	4	20	23
	<i>LE</i>	-37	-43	-21	-41
	<i>Q</i>	-42	-42	-22	-32
Winter (DJFM)	<i>SWN</i>	42	42	37	37
	<i>LWN</i>	-59	-33	-64	-48
	<i>H</i>	11	14	25	21
	<i>LE</i>	-22	-42	-15	-26
	<i>Q</i>	-28	-19	-16	-16
Pre-monsoon (AM)	<i>SWN</i>	67	67	75	75
	<i>LWN</i>	-62	-36	-79	-61
	<i>H</i>	20	-12	8	4
	<i>LE</i>	-33	-51	-24	-46
	<i>Q</i>	-8	-32	-20	-28
Summer- monsoon (JJAS)	<i>SWN</i>	130	67	173	73
	<i>LWN</i>	-6	-3	-43	-38
	<i>H</i>	28	-7	18	-3
	<i>LE</i>	-5	-34	-9	-42
	<i>Q</i>	150	23	139	-10
Annual (mean)	<i>SWN</i>	80	56	93	59
	<i>LWN</i>	-45	-27	-63	-50
	<i>H</i>	18	1	19	11
	<i>LE</i>	-21	-41	-16	-37
	<i>Q</i>	32	-11	34	-18

#### 4.5.2 Major drivers for glacier mass balances

Due to the scarcity of mass balance and meteorological data in the HK, the climatic drivers controlling the mass balances have been poorly discussed (Shea et al., 2015a; Azam et al., 2018). To comprehend the major drivers controlling the glacier-wide seasonal and annual mass balances, the correlation coefficients ( $r$ ) were developed amid annual and seasonal mass balances, bias-corrected mean annual ERA5 data, and surface energy fluxes over 1979-2020 on both the glaciers (Fig. 4.12).

$B_a$  on DBG showed strong positive correlations ( $r = \sim 0.40-0.70$ ) with  $P$  and surface albedo while moderately negative correlations ( $r = \sim 0.40-0.60$ ) with

$SWN$ ,  $R_n$  and  $Q$  (Fig. 4.12). Similarly, CSG also showed good correlations with  $P$  and surface albedo however the negative correlations with  $SWN$ ,  $R_n$  and  $Q$  were stronger ( $r = \sim 0.80$ ) (Fig. 4.12). Due to their undersized role in total SEB (section 4.3),  $H$ ,  $LE$  and  $LWN$  showed insignificant correlations with annual as well as seasonal mass balances on both the glaciers (Fig. 4.12).

$B_a$  and summer mass balances on CSG showed moderate correlations with  $SWI$  while these correlations on DBG were insignificant (Fig. 4.12). This is probably due to heavy monsoonal clouds that reduce the amount of  $SWI$  on DBG hence low mean annual values (Table 4.5). Winter mass balances on DBG showed weak positive correlation ( $r = 0.27$ ) with  $P$  while a stronger positive correlation ( $r = 0.63$ ) was observed on CSG (Fig. 4.12). This is expected as DBG and CSG are summer and winter accumulation-type glaciers, respectively (section 4.1). Further, summer mass balances on both the glaciers showed moderately positive but almost similar correlations ( $r = \sim 0.50$ ) with  $P$  (Fig. 4.12). Despite the fact that CSG receives its major annual precipitation during winter, almost similar correlation between summer mass balances and  $P$  is most probably because of sporadic summer-monsoonal snowfall events on CSG (Azam et al., 2019). A previous study on CSG investigated the critical role of summer-monsoon snowfalls in detail and concluded that these snowfalls often cover the whole or part of the ablation zone during peak melting months and abruptly reduce the  $SWI$  absorption hence control the summer mass balances that further control the  $B_a$  (Azam et al., 2014b).  $T_a$  showed weak and moderate negative correlations with  $B_a$  ( $r = -0.30$ ) and summer ( $r = -0.52$ ) mass balances, respectively on DBG, while moderate negative correlations with  $B_a$  ( $r = -0.44$ ) and summer ( $r = -0.40$ ) mass balances (Fig. 4.12).  $T_a$  was poorly correlated with winter mass balances on both the glaciers (Fig. 4.12). However, as expected,  $T_a$  showed very strong correlations with  $T_s$  and  $LWO$  on both the glaciers (Fig. 4.12).

$B_a$  on DBG and CSG showed moderately strong correlations with winter mass balances ( $r = 0.58$  and  $r = 0.67$ , respectively) while very strong correlations with summer mass balances ( $r = 0.80$ ,  $r = 0.97$ , respectively) (Fig. 4.12). Higher dependency of  $B_a$  on summer mass balances suggests that both

the glaciers have high vulnerability to regional warming hence expected to lose more mass in continuation of warming (Banerjee and Azam, 2016; Kraaijenbrink et al., 2017; Krishnan et al., 2019; Mahto and Mishra, 2019).

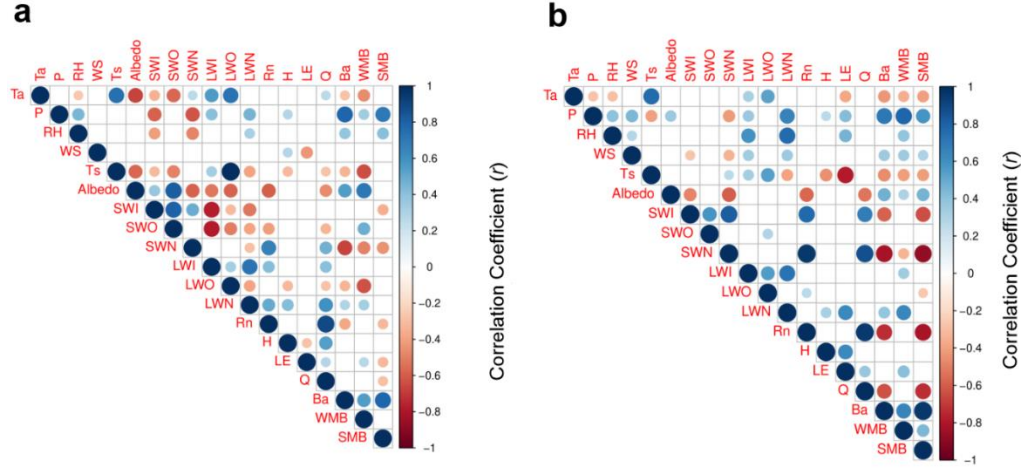


**Figure 4.12:** The panel (a) and (b) shows a graphical representation of correlations with 1% (0.01)  $p$  significance values among the inter-annual variability of mass balance, energy fluxes and its meteorological drivers during 1979-2020 for DBG and CSG, respectively (red color shows negative while blue color shows positive correlation values). WMB and SMB are winter and summer mass balances.

### 4.5.3 Annual glacier-wide mass balance sensitivity

Mass balance sensitivities were computed to understand the glacier's response to the changes in different model input parameters. These sensitivities were computed, one-by-one, by re-running the model with a unique set of each model parameter where  $h_H$  was the highest and  $h_L$  was the lowest value of parameter  $h$ , holding all the other parameters constant. Following Ragettli and others (2013), the  $h_H$  and  $h_L$  were estimated by varying each parameter  $h$  by  $\pm 10\%$  from its calibrated value except for  $T_m$ ,  $T_p$ ,  $T_a$  which were varied by 0.1, 0.1 and 1.0 °C, respectively (Table 4.3). The mass balance sensitivities were estimated for the period 1979-2020 following Oerlemans and others, 1998:

$$\frac{dB_a}{dh} = \frac{B_a(h_H) - B_a(h_L)}{2} \quad (4.25)$$

Where,  $B_a$  is the glacier-wide mass balance averaged over the period 1979-2020.

The estimated  $B_a$  sensitivities on DBG and CSG are given in Table 4.3. The  $B_a$  was most sensitive to  $\alpha_s$ , with the sensitivities of 0.29 and 0.37 m w.e.  $a^{-1}$  on DBG and CSG, respectively (Table 4.3). Previous studies on other glaciers in the Alps and Himalaya also showed the maximum sensitivity of  $B_a$  to  $\alpha_s$  (Klok and Oerlemans, 2004; Johnson and Rupper, 2020; Stigter et al., 2021). The modelled  $B_a$  showed moderate sensitivities to  $T_{LR}$  (DBG = 0.10 m w.e.  $a^{-1}$ ; CSG = 0.12 m w.e.  $a^{-1}$ ). Sensitivities were quite low to  $T_p$ ,  $T_M$ ,  $\alpha_d$ ,  $\alpha_i$  and  $P_G$  for both the glaciers (Table 4.3).

The sensitivity of modelled mean  $B_a$  to  $1^\circ\text{C}$  change in  $T_a$  was higher on DBG ( $-0.50$  m w.e.  $a^{-1}$ ) than CSG ( $-0.30$  m w.e.  $a^{-1}$ ) whereas the sensitivities to 10% change in  $P$  were roughly the same (DBG =  $0.23$  m w.e.  $a^{-1}$ , CSG =  $0.13$  m w.e.  $a^{-1}$ ) (Table 4.3). Higher sensitivity to  $T_a$  on DBG is probably because of different precipitation regimes on both the glaciers. DBG receives its maximum of annual precipitation in the summer-monsoon when  $T_a$  is highest hence more sensitivity to  $T_a$  compared to CSG that receives its major precipitation in winters (Fujita, 2008; Azam et al., 2014a). Using the T-index model, a previous study on CSG computed higher sensitivity ( $-0.52$  m w.e.  $a^{-1}$ ) of mass balance to  $1^\circ\text{C}$  change in  $T_a$  and roughly similar sensitivity ( $0.16$  m w.e.  $a^{-1}$ ) to 10% change in  $P$  (Azam et al., 2014a). Another study on Zhadang Glacier in Tibet showed similar results using an energy balance model with the sensitivity of  $-0.47$  m w.e.  $a^{-1}$  to  $1^\circ\text{C}$  change in  $T_a$  and sensitivity of  $0.14$  m w.e.  $a^{-1}$  to 10% change in  $P$  (Mölg et al., 2012). Our sensitivity results are quite comparable with these studies in the mountain glaciers.

## 4.6 Conclusions

Due to harsh climatic conditions, the long-term in-situ glacio-meteorological observations are sparse in the HK region that impedes an in-depth understanding of glacier-climate relationship. To get around this constraint, we developed a mass-, and energy-balance model, using the long-term ERA5 reanalysis data since 1979, for two climatically diverse glaciers of DBG and CSG where a fairly good amount of in-situ glacio-meteorological data are available from previous studies. The in-situ measurements are used to

calibrate/validate the developed mass-, and energy-balance model for DBG and CSG. The developed model is further used to study the altitudinal patterns of mass balance and surface energy fluxes over both the glaciers.

Both the glaciers experience a warm and moist weather condition with low wind velocity during the summer-monsoon (June-September) and a cold, dry windy condition during winter (December to March). Intermediate weather conditions persist during pre-monsoon (April to May) and post-monsoon (October-November). DBG receives the majority of precipitation (~74%) in the summer-monsoon whereas CSG receives maximum precipitation (~53%) in winter.

DBG and CSG are losing mass at a moderate rate with the mean  $B_a$  of  $-0.27 \pm 0.32$  m w.e.  $a^{-1}$  and  $-0.31 \pm 0.38$  m w.e.  $a^{-1}$ , respectively, over 1979-2021. Though the mean mass wastage on both the glaciers is similar, the annual mass turnover on CSG is almost double compared to DBG. The mean summer and winter mass balances are computed to be  $-0.60 \pm 0.30$  and  $0.32 \pm 0.02$  m w.e.  $a^{-1}$  on DBG and  $-0.79 \pm 0.36$  and  $0.48 \pm 0.02$  m w.e.  $a^{-1}$  on CSG, respectively. Glacier-wide net shortwave radiation has the dominant control over energy balance followed by longwave net radiation, latent heat flux and sensible heat flux on both the glaciers. On the annual scale, both DBG and CSG showed a positive glacier-wide net energy of  $10 \text{ W m}^{-2}$  indicating a mass wastage over 1979-2020. Latent heat flux is always negative suggesting glacier-wide sublimation throughout the year except for peak summer-monsoon when it is slightly positive over ablation zone indicating re-sublimation on both the glaciers.

$B_a$  on DBG and CSG showed moderately strong correlations with winter mass balances ( $r = 0.58$  and  $r = 0.67$ , respectively) while very strong correlations with summer mass balances ( $r = 0.80$ ,  $r = 0.97$ , respectively) suggesting summer as the main mass balance driver season. The sensitivity of modelled mean  $B_a$  to  $1^\circ\text{C}$  change in  $T_a$  is higher on DBG ( $-0.50$  m w.e.  $a^{-1}$ ) than the CSG ( $-0.30$  m w.e.  $a^{-1}$ ) whereas the sensitivities to 10% change in  $P$  are nearly the same (DBG =  $0.23$  m w.e.  $a^{-1}$ , CSG =  $0.13$  m w.e.  $a^{-1}$ ) over 1979-2020. Mass-, and energy-balance model is the most sensitive to snow albedo

followed by temperature lapse rates and least sensitive to the rest of the model parameters on both the glaciers.

The modelled  $B_a$  on both the glaciers show a good agreement with the available mass balances from geodetic, model and in-situ measurements. Further, modelled mass balance series also show near-balanced state over the 1990s on both the glaciers, in line with previously modelled mass balances from T-index model and field measurements.

## **Chapter 5**

# **Glaciohydrological modelling of Dokriani Bamak Glacier**

### **5.1 Introduction**

The Himalayan Mountain range is the origin of several perennial river systems in south Asia such as Indus, Ganga and Brahmaputra and provides a continuous fresh water supply for over 800 million people (Bolch et al., 2019). Current global warming raises serious concerns about the Himalayan river hydrology, specifically with regard to the seasonal impacts of different hydrologic components (glacier melt runoff, snowmelt runoff, and rainfall). Glaciers have been losing mass over the last 5-6 decades (Azam et al., 2018) with a heterogeneous pattern along the Himalayan arc (Brun et al., 2017). This heterogeneous mass wastage indicates that the impact of the changing climate on melt runoff generation depends on the regional climate of glaciers in the Himalaya (Sakai and Fujita, 2017). Therefore, accurate quantification of the snow and glacier melt contributions to river runoff in different parts of the Himalaya is important for future planning in water sensitive sectors, water resources management and flood risk reduction.

In the Himalaya, field-based glacio-hydro-meteorological studies are available for only short periods of time on a few glaciers due to high altitude, rugged terrain and extreme climate of the Himalaya (Azam et al., 2018). Therefore, glacier mass balance-runoff models, which exploit the available field-based data (precipitation, temperature, glacier mass balance, runoff, etc.), provide a good alternative to reconstruct long term glacier mass balance and runoff patterns. Over the last decade, some model studies have been developed focusing on glacier mass balance estimates (Azam et al., 2014a; Shea et al., 2015b; Kumar et al., 2019) and runoff (Racoviteanu et al., 2013; Nepal et al., 2014; Immerzeel et al., 2013; Lutz et al., 2014; Azam et al., 2019; Armstrong et al., 2019) in different parts of the Himalaya. In almost all such studies,

handling the spatial distribution of precipitation was the most difficult task as most of the meteorological stations are located at the bottom of valleys, and are often located on the southern slopes of the Himalayan range. Therefore, the extrapolation of precipitation from these stations to the higher altitudes and over the whole Himalaya is subject to large uncertainties (Immerzeel et al., 2015; Savéan et al., 2015; Azam et al., 2019). Precipitation is the main driver of the hydrological cycle, hence any bias in precipitation amounts will produce strong biases in the hydrologic components. For instance, the significantly imbalanced field-observed water budget reported over the 2001-2005 period in the Dudh Koshi basin (Nepal) was due to a large underestimation of high-altitude precipitation; on the contrary, the modelled water budget was well balanced due to unrealistic overestimation of the glacier melt volume (Savéan et al., 2015). The uncertain precipitation distribution together with difficult access to these remote areas makes it difficult to develop accurate, reliable glacier mass balance-runoff models for the Himalaya.

Various methods of different complexities have been used to understand the runoff composition in the Himalayan region including empirical relationship between runoff and precipitation (Thayyen et al., 2005), chemical-tracer methods (Maurya et al., 2011; Ahluwalia et al., 2013; Rai et al., 2016); ice ablation models (Racoviteanu et al., 2013), hydrograph separation method (Mukhopadhyay and Khan, 2014; 2015), geodetic mass wastage method (Gardner et al., 2013; Brun et al., 2017); water balance approach (Singh and Jain, 2002; Jeelani et al., 2012) and semi-distributed/distributed glacier mass balance-runoff models (Lutz et al., 2014; Savéan et al., 2015; Azam et al., 2019).

In the present study, we developed a temperature-index based mass balance-runoff model to reconstruct the glacier-wide mass balance and runoff for the highly glacierized Dokriani Glacier catchment (Garhwal Himalaya, India) using long-term meteorological reanalysis data from ERA5 between 1979 and 2018. The model was then used to estimate the relative contribution of the different hydrologic components including snow melt, ice melt and rainfall-runoff, and the impact of debris cover on glacier mass balance.

## 5.2 Study Area, climatic settings and previous studies

The Dokriani Glacier catchment, also known as Din Gad Catchment, is located in the upper Ganga Basin in Garhwal region of central Himalaya (Fig. 5.1), with an area of 15.71 km<sup>2</sup> (Fig. 5.2). In the upper reaches, the catchment is bounded by three peaks, Jaonli (6632 m a.s.l.) on the eastern side, Draupadi Ka Danda I (5716 m a.s.l.) on the southern side and Draupadi Ka Danda II (5670 m a.s.l.) on the western side (Fig. 5.1). Dokriani Glacier (30°50' N and 78°50' E) is a valley glacier, ranging from 4050 to 6632 m a.s.l. and an area of 7.03 km<sup>2</sup> (Table 5.1 and Fig. 5.2). In the lower part of the ablation area (4050 to 4900 m a.s.l.), the glacier tongue is covered with debris (0.90 km<sup>2</sup> ~13% of total glacier area) (Fig. 5.2) issued from the steep valley walls, while the middle portion is clean (Fig. 5.1). The glacier currently has a single proglacial stream called Din Gad, and the discharge station (3820 m.a.s.l.) is located on this stream around 1.25 km below the glacier snout (Thayyen et al., 2005).

The climate of the Himalaya is controlled by western disturbances (WDs) and the Indian summer monsoon (ISM) (Gadgil et al., 2003). Western Himalaya is prone to receive a large amount of precipitation from WDs (extratropical low-pressure cyclones) during winter (Dimri et al., 2016), while central and eastern Himalaya receive most of their precipitation from orographic upliftment of ISM during summer (Bookhagen and Burbank, 2006). WDs weaken from west to east, while ISM intensity decreases from east to west along the Himalayan Mountain range (Bookhagen and Burbank, 2006). As Dokriani Glacier receives most of its annual precipitation during the summer season (May to October) (Thayyen et al., 2005; Verma et al., 2018), it is considered a summer-accumulation-type glacier (Maussion et al., 2014). Summer precipitation may fall as rain up to 5000-5100 m a.s.l. on some warm days whereas on some colder days summer snowfalls may also occur over the whole glacier (Pratap et al., 2015). The snowfalls on lower elevations melt quickly due to high summer temperatures and high incoming solar radiation.

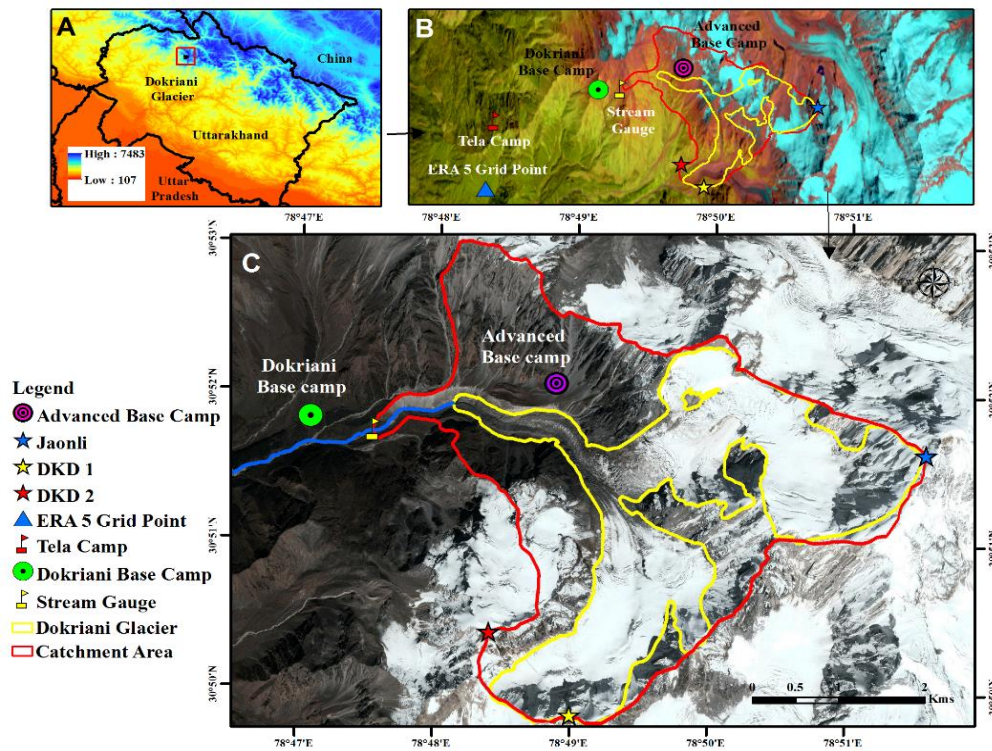


**Figure 5.1:** Location of the study area. (a) panel a show the state boundary of Uttarakhand, (b) locations of Tela camp, base camp and advance base camp, in Dokriani Glacier catchment, and (c) location map of Dokriani Glacier catchment (red outline) and the glacier area (yellow line) on imagery from Google Earth (CNES/Airbus) of 10 July 2017. The locations of surrounding mountain peaks Jaonli, DKD I and II are also shown on the map.

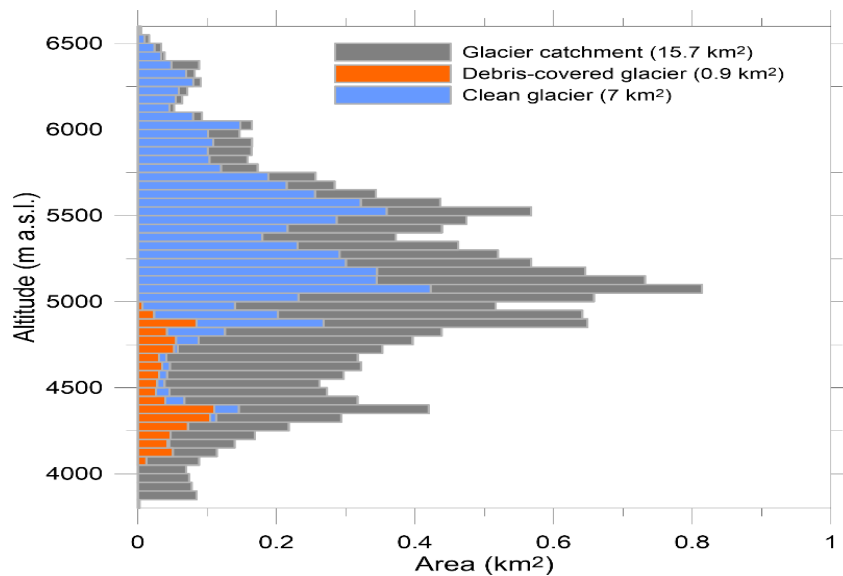


**Figure 5.2:** The hypsography (50-meter altitudinal ranges) for Dokriani Glacier catchment. Symbology: grey, blue and orange bars represent the catchment area, glacier area and debris-covered glacier area. The glacier area-altitude distribution is estimated in the present study using the high-resolution google earth image (CNES/Airbus) on 10 July 2017.

**Table 5.1:** Topographical characteristics of Dokriani Glacier catchment.

<b>Dokriani Catchment characteristics</b>	
Latitude, Longitude	30°50' N, 78°50' E
Catchment area	15.71 km <sup>2</sup>
Maximum altitude	6632 m a.s.l.
Catchment outlet	3820 m a.s.l.
Total Glacierized area	7.35 km <sup>2</sup> (2017)
<b>Dokriani Glacier characteristics</b>	
Glacier area	7.03 km <sup>2</sup> (in 2017)
Debris-covered area	0.94 km <sup>2</sup> (in 2017)
Glacier length	~5 km
Snout position	4050 m a.s.l. (in 2017)
Mean orientation	north-west
Max altitude	6632 m a.s.l.

Dokriani Glacier catchment has been relatively well studied in terms of glacier mass balance (Dobhal et al., 2008), meteorology (Verma et al., 2018; Yadav et al., 2019), hydrology (Singh et al., 2003; Thayyen et al., 2005) and stream sediments (Kumar et al., 2014). The meteorological observations were initiated in the 1990s at Base Camp station (3763 m a.s.l.), but these measurements were only taken during summer months (mid-May to October) and are only available for selected years (1994, 1998-2000) (Thayyen et al., 2005). Year-round meteorological data at Base Camp were acquired using an automatic weather station during 2011-2014 (Verma et al., 2018). The precipitation measurements were done manually using an ordinary rain gauge and cylinder calibrated and prescribed by the Indian Meteorological Department during summer while snow measurements during winter were conducted on a

flat surface using a manual staff gauge and then was melted out to get the water equivalent (Verma et al., 2018). The annual mass balance observations were conducted intermittently over the last decade of 20<sup>th</sup> century (1992-1995; 1996-2000) (Dobhal et al., 2008). Azam et al. (2018) evaluated all the available mass balance series from the Himalaya and categorized them in different categories (Excellent, Good, Fair and Dubious) based on their quality and reliability. Dokriani Glacier mass balance series was kept in 'the fair' category. Daily discharge measurements were performed at the runoff station on Din Gad stream during the summer ablation period (May to October) (Thayyen et al., 2005). Discharge was derived from the rating curve established using the area-velocity method.

## **5.3 Data and methods**

### **5.3.1 Climate data and bias corrections**

Daily temperature and precipitation data from ERA5 was used to reconstruct the glacier-wide mass balance and catchment-wide runoff of the Dokriani Glacier catchment. ERA5 data are available since 1979 at 30 km grid resolution (Climate Data Centre (CDS) <https://cds.climate.copernicus.eu/>). The ERA5 data (daily temperature and precipitation) was extracted for the nearest grid point (30°75'N, 78°75'E; 3590 m a.s.l.; 650 hPa) of the Dokriani Glacier Base Camp (30°51'N, 78°46'E; 3774 m a.s.l.; 635 hPa), where historical data is available from AWS (Fig. 5.1). The whole ERA5 data series was bias-corrected using the mean monthly temperature and precipitation sums available for the 2011-2014 period at the Dokriani Glacier Base Camp (Verma et al., 2018). Raw ERA5 mean monthly temperature showed a strong correlation with field-observed temperature over 2011-2014 ( $R^2 = 0.99$ ;  $y = 1.0447x + 0.0172$ ; where  $y$  = field-observed temperature and  $x$  = raw ERA5 temperature) (Fig. S1). The mean monthly temperature anomalies also showed strong correlation with mean monthly anomalies from raw ERA5 temperature series ( $R^2 = 0.99$ ;  $y = 1.0447x + 3 \times 10^{-16}$ ; where  $y$  = field-observed temperature anomalies and  $x$  = raw ERA5 temperature anomalies) (Fig. S2). The correlation between mean monthly

precipitation from raw ERA5 and field-observed precipitation over 2011-2014 was somewhat poorer ( $R^2 = 0.86$ ;  $y = 0.8187x$ ; where  $y$  = field-observed precipitation and  $x$  = raw ERA5 precipitation) (Fig. S3). The estimated RMSEs for mean monthly temperatures and mean monthly precipitations were 0.47 °C and 67 mm, respectively. Given that we had only mean monthly data over 2011-2014 from the field, we used a regression equation between mean monthly temperature from raw ERA5 and field data over the common period to bias-correct the whole ERA5 temperature series. For precipitation bias correction, the monthly scale factors were used to bias-correct the whole raw ERA5 precipitation series (Table S1).

Fig. 5.3a shows the mean monthly cycles for temperature and precipitation from bias-corrected ERA5 (1979-2018) data as well as from Verma et al. (2018). The mean monthly temperature and precipitation sums from the summer monsoon period (mid-May to October) of 1994, 1998-2000 (Thayyen et al., 2005) are also shown in Fig. 5.3a. The mean monthly cycles for temperature and precipitation from bias-corrected ERA5 showed strong similarities with mean monthly cycles from previous studies. Fig. 5.3b shows bias-corrected annual mean temperature and annual precipitation sums from ERA5 that are used to reconstruct the mass balance and runoff for 1979-2018 period.

The bias-corrected annual mean temperature at the Base Camp was 3.1 °C for 1979-2018 with a maximum and minimum annual mean temperature of 4.3 °C and 1.8 °C for 2016 and 1997, respectively. The mean summer season (May-October) and winter season (November-April) temperatures were 7.4 and -1.2 °C, respectively. July was the hottest month with a mean temperature of 10.1 °C while January was the coldest month with a mean temperature -4.1 °C during 1979-2018. The bias-corrected mean annual precipitation was 1616 mm between 1979 and 2018, with a maximum precipitation of 2113 mm in 2010 and a minimum of 1094 mm in 1987. Dokriani Glacier Base Camp received 77% of its annual precipitation during the summer season (May-October) while winter season (November to April) contributed only 23% to the annual mean precipitation during the 1979-2018 period.

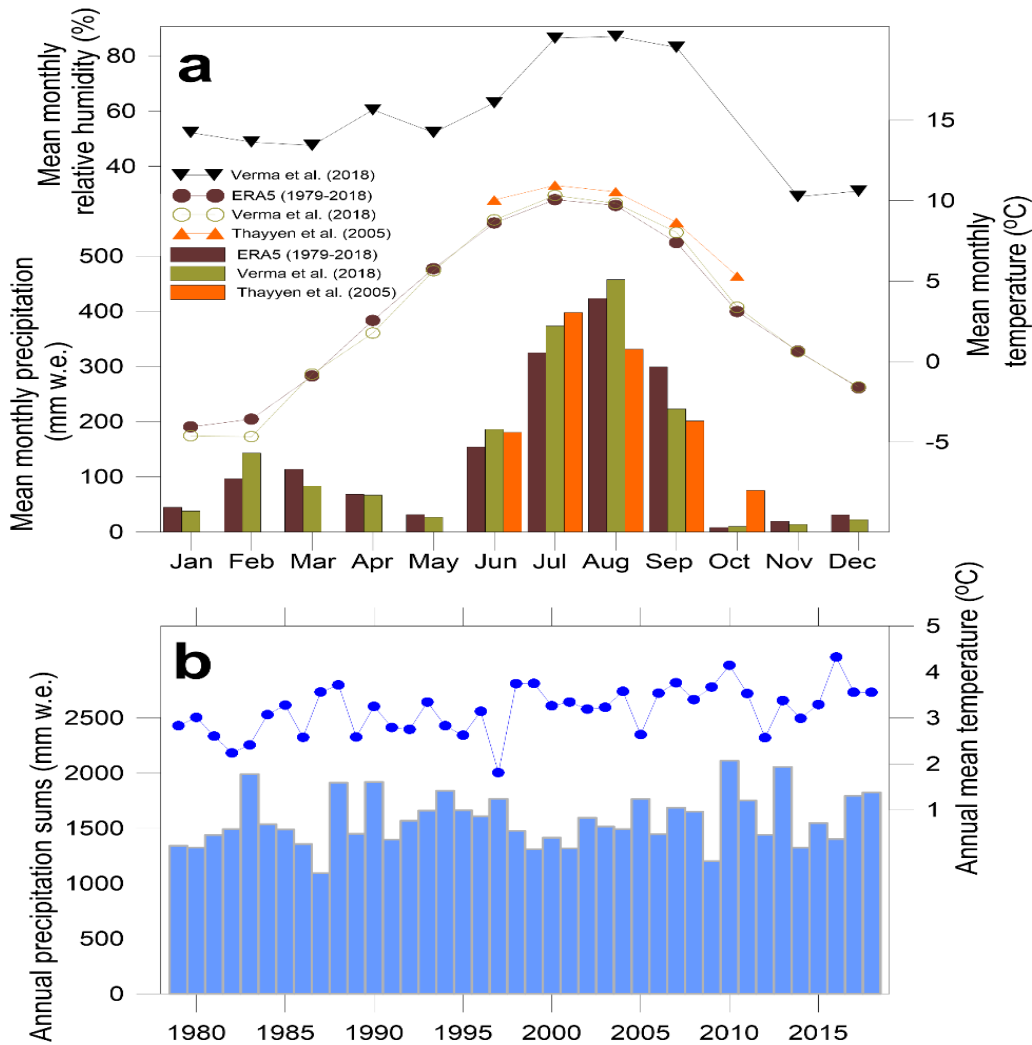


**Figure 5.3:** (a) Mean monthly cycle of temperature and precipitation obtained from daily data from ERA5 bias-corrected series over 1979-2018. Mean monthly cycles of temperature, relative humidity and precipitation observed at Dokriani Glacier base camp from available studies (Thayyen et al., 2005; Verma et al., 2018) are also shown, (b) Series of annual mean temperature (blue dots) and annual precipitation sums (blue bars) from bias-corrected ERA5 data set (1979-2018).

### 5.3.2 Model set-up

The annual glacier-wide mass balance and catchment-wide runoff are simulated applying a glacier mass balance-runoff model that includes an accumulation module, a temperature-index ablation module, and a rain module. The required forcing data for this model are precipitation and temperature from ERA5 at daily

resolution. The precipitation and temperature fields for each 50-m altitudinal range were generated from daily precipitation sums and daily mean temperatures estimated from bias-corrected ERA5 data at the Base Camp, by applying the altitudinal precipitation gradient and temperature lapse rates (Table 5.2 and section 3.3). The model starts on 1st November of a year and calculates glacier mass balance (accumulation and melting) and runoff (snow melt, ice melt, and rainfall-runoff) taking into account the glacier surface state (snow, bare ice or debris) for each altitudinal range of 50 m at daily time-step for a full hydrological year (until 31<sup>st</sup> October of the following year). The model structure is shown in Fig. 5.4.

At a given altitudinal range (glacierized and non-glacierized), the biased-corrected daily precipitation  $P$  (mm w.e. d<sup>-1</sup>) is extrapolated as:

$$P = P_{BC} + P_G \times \Delta H \quad (5.1)$$

Where  $P$  is the extrapolated precipitation at different elevation bands,  $P_{BC}$  is the precipitation at base camp (mm w.e. d<sup>-1</sup>),  $\Delta H$  is the altitudinal difference between base camp and altitudinal band (m) and  $P_G$  is the precipitation gradient (% increase per 1000 meter) (Fig. S4).

The daily snow accumulation  $c$  (mm w.e. d<sup>-1</sup>) at each altitudinal range (glacierized and non-glacierized), is computed by:

$$c = \begin{cases} P: & \text{when } and T \leq T_P \\ 0: & \text{when } and T > T_P \end{cases} \quad (5.2)$$

where  $P$  and  $T$  are daily precipitation (mm) and temperature (°C) respectively extrapolated at each altitudinal range and  $T_P$  is the threshold temperature (°C) for snow-rain.

The daily rainfall  $r$  at a given altitudinal range (glacierized and non-glacierized), is computed by:

$$r = \begin{cases} 0: & \text{when } and T \leq T_P \\ P: & \text{when } and T > T_P \end{cases} \quad (5.3)$$

The computed rainfall and, in general, every computed runoff component mentioned hereafter are assumed to reach the discharge site within the same day.

The temperature-index module relates the amount of melt with positive air temperature sums (positive degree days) and a proportionality factor called degree-day factor ( $DDF$ ). At each altitudinal range, the ablation  $a$  (mm w.e. d<sup>-1</sup>) is computed by:

$$a = \begin{cases} DDF_{S,I,D} \cdot (T - T_M): & \text{when } T > T_M \\ 0: & \text{when } T \leq T_M \end{cases} \quad (5.4)$$

where,  $DDF$  denotes the degree-day factor (mm d<sup>-1</sup> °C<sup>-1</sup>), different for snow ( $S$ ), ice ( $I$ ) and debris-covered ice ( $D$ ) surfaces, and  $T$  is extrapolated daily mean air temperature (°C) at given altitudes and  $T_M$  is the threshold temperature (°C) for melt. The model maintains a dynamic storage of snow during the whole modelling period. Snow is added to the 50-m altitudinal ranges over the whole catchment (glacierized and non-glacierized areas) following equation (2) and is melted as a function of  $DDF$  for snow when  $T > T_M$  at any given altitudinal range (equation 4). If  $T > T_M$  and snow is melted out at a given altitude, then over the glacierized areas, ice is melted as a function of  $DDF$  for debris cover or  $DDF$  for ice, depending on whether the surface is debris-covered ice or clean ice (equation 4).

Total snow melt runoff,  $Q_{snow}$ , over the whole catchment is computed as:

$$Q_{snow} = a_{sg} + a_{sng} \quad (5.5)$$

where,  $a_{sg}$  and  $a_{sng}$  are snow melt over the glacierized area and non-glacierized area, respectively.

Total rainfall runoff,  $Q_{rain}$ , over the whole catchment is computed as:

$$Q_{rain} = r_g + r_{ng} \quad (5.6)$$

where,  $r_g$  and  $r_{ng}$  are rainfall runoff from the glacierized and non-glacierized areas, respectively.

The resulting daily runoff,  $Q$ , at the catchment outlet is computed using the following equation:

$$Q = Q_{snow} + Q_{rain} + Q_{ice} \quad (5.7)$$

where,  $Q$ ,  $Q_{snow}$ ,  $Q_{ice}$ , and  $Q_{rain}$  are total runoff, snow melt runoff (over whole catchment), ice melt runoff (clean ice as well as debris-covered ice) and rainfall runoff (over the whole catchment), respectively.

For the computation of mass balance and runoff components, we used a static glacier surface over the whole modelling period (see section 3.6). Moreover, the sub-surface water fluxes are assumed to be negligible.

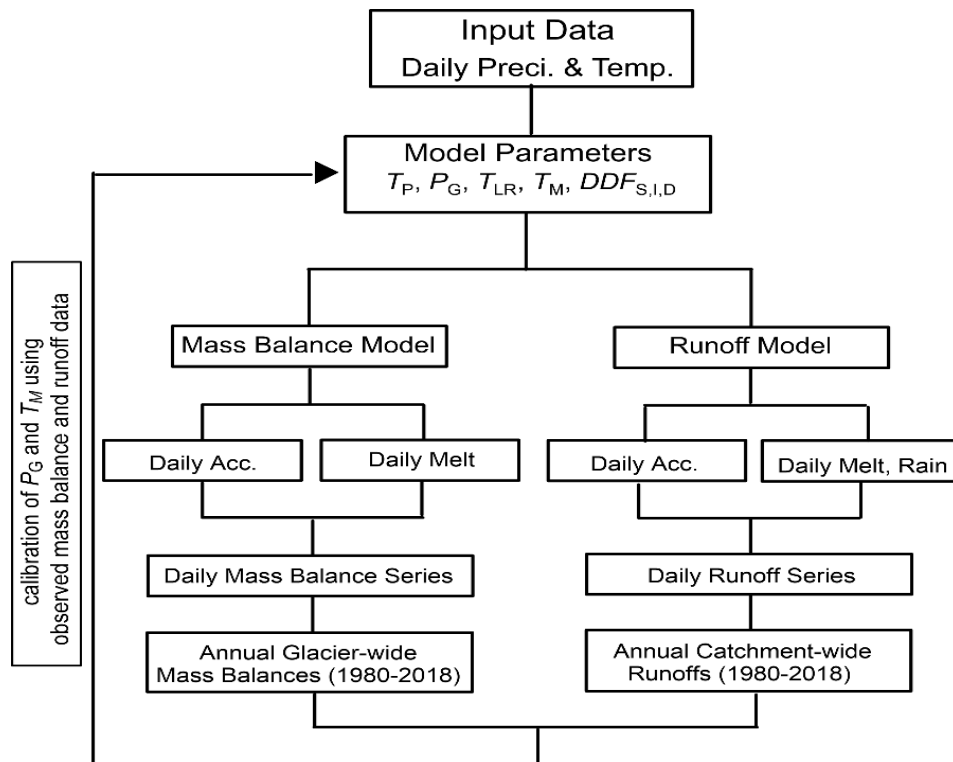


**Figure 5.4:** Glacio-hydrological model structure.  $T_P$ ,  $P_G$ ,  $T_{LR}$ ,  $T_M$ ,  $DDF_{S,I,D}$  are the threshold temperature for snow/rain limit, altitudinal precipitation gradient, temperature lapse rates, threshold temperature for melt, degree day factor ( $DDF$ ) for snow, ice and debris-covered ice, respectively. The details about all input parameters are given in Table 5.2.

### 5.3.3 Model parameters

In glacier mass balance-runoff modelling, air temperature is one of the most important input parameters that controls the snowfall/rain distribution and affects the melting of snow cover and glacier (Shea et al., 2015b). The mean monthly temperature lapse rates ( $T_{LRs}$ ) for Dokriani Glacier catchment had been

estimated using temperatures at Tela Camp (TC, 2540 m a.s.l.) and Base Camp (BC, 3763 m a.s.l.) for the 2002-2004 period (Table 5.2, Thayyen and Dimri, 2018) (Fig. 5.5). Yadav et al. (2019) estimated the mean monthly  $T_{LRs}$  over the 2011-2015 period using three automatic weather stations (AWSs). These AWSs are located at TC, BC and Advance Base Camp (ABC, 4364 m a.s.l.) with aerial distances between TC-BC and BC-ABC of ~10 and ~2.7 km, respectively (Fig. 5.1). The mean monthly  $T_{LRs}$  from these studies clearly indicate seasonal variability with  $T_{LRs}$  being lowest during summer monsoon months and highest during the pre-monsoon season (April-May) (Fig. 5.5). Lower  $T_{LRs}$  during the summer monsoon months have also been observed in other parts of the Himalaya and were attributed to strong monsoonal convective activity that produces an efficient mixing of the lower atmosphere (Azam et al., 2014a; Shea et al., 2015b). The aerial distance between BC and ABC is only ~2.7 km; therefore, the estimated  $T_{LRs}$  may not represent the mean behaviour of temperature distribution over the whole catchment. We calculated the average of mean monthly  $T_{LRs}$  available from the studies of Thayyen and Dimri (2018) and Yadav et al. (2019) (Fig. 5.5; Table S2), and used it in our study for the temperature distribution over the whole Dokriani Glacier catchment. Though meteorological stations at TC (2540 m a.s.l.), BC (3763 m a.s.l.) and ABC (4364 m a.s.l.) cover ~2 km altitudinal range yet the calculated mean  $T_{LRs}$  may not fully represent the  $T_{LRs}$  over the glacier due to possible generation of katabatic winds (Grisogono and Oerlemans, 2002); therefore, we performed a sensitivity test for estimated mean  $T_{LRs}$  (section 5.4).

Singh et al. (2000) computed the degree day factors ( $DDFs$ ) on Dokriani Glacier in May 1997 and June-July 1998 at 4000 m a.s.l. separately for clean ice and fresh snow as well as after spraying some local, natural fine dust cover of around 2 mm uniform thickness on ice and snow surfaces. The mean  $DDFs$  for clean snow and dusted snow had been estimated to be 5.7 and 6.4 mm °C<sup>-1</sup> d<sup>-1</sup>, respectively whereas for clean ice and dusted ice  $DDFs$  were found to be 7.4 and 8.0 mm °C<sup>-1</sup> d<sup>-1</sup>, respectively. Dust and soot progressively accumulate on the glacier surface as summer season progresses (Gertler et al., 2016); therefore, we calculated the mean  $DDFs$  for ice and snow surfaces as 6.1 and

7.7 mm °C<sup>-1</sup> d<sup>-1</sup> by taking the mean of clean and dusted *DDFs* of snow and clean and dusted *DDFs* ice surfaces, respectively (Singh et al., 2000). The difference (1.6 mm °C<sup>-1</sup> d<sup>-1</sup>) in mean *DDFs* of snow and ice surfaces on Dokriani Glacier is much less than the difference (3.3 mm °C<sup>-1</sup> d<sup>-1</sup>) in *DDFs* of snow and ice surfaces estimated on Chhota Shigri Glacier in the western Himalaya (Azam et al., 2014a), and may be attributed to the altitudes, snow properties, solar inclination etc. Furthermore, reduced melt rates over debris-covered ice (37% less than clean-ice) were reported on Dokriani Glacier using stake ablation data over 2009-2013 (Pratap et al., 2015). A total of 16 stakes were installed over debris cover thickness ranging from 2 cm to 40 cm (Pratap et al., 2015); therefore, the estimated mean melt covers the spatial distribution of debris to some extent. We calculated the *DDF* for debris-covered ice as 4.8 mm °C<sup>-1</sup> d<sup>-1</sup> from *DDF* for ice by applying the ratio of melt over debris to melt over clean ice (0.63) from Pratap et al. (2015). Since *DDFs* have high temporal and spatial variations (Zhang et al., 2006) and uncertainties (e.g., Singh et al. 2000), a sensitivity test was conducted for all *DDFs* (section 5.4).

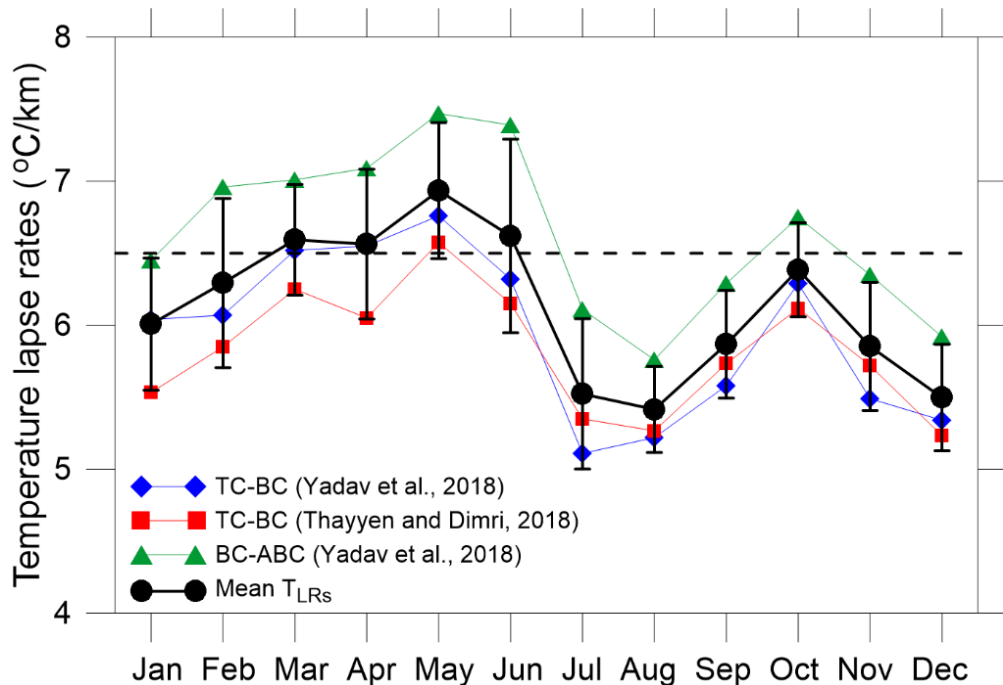


**Figure 5.5:** Monthly temperature lapse rates ( $T_{LRs}$ ) in Dokriani Glacier catchment estimated between Tela Camp (TC, 2540 m a.s.l.), Base Camp (BC, 3763 m a.s.l.) and Advance Base Camp (ABC, 4364 m a.s.l.) from all available

studies. The black dots are the mean monthly *TLRs* estimated from Thayyen and Dimri (2018) and Yadav et al. (2019), error bars show the  $1\sigma$  values (standard deviation). The dotted line shows the standard environmental lapse rate value of  $6.49\text{ }^{\circ}\text{C}/\text{km}$ .

With increasing global warming and as well as local Himalayan warming (Banerjee and Azam, 2016), the elevation where the snow-rain transition occurs shifts to higher elevations, resulting in decreased snow accumulation. The snow-rain threshold temperature is therefore a crucial model parameter in glacier mass balance-runoff modelling. Unfortunately, field studies estimating the snow-rain threshold temperature are not available in the Himalaya. Jennings et al. (2018) computed these snow-rain threshold temperatures for the whole northern hemisphere for different ranges of relative humidity. Dokriani Glacier being in a monsoon-dominated catchment (Yadav et al., 2019), we selected a snow-rain threshold temperature of  $0.7\text{ }^{\circ}\text{C}$  corresponding to 70-80% of relative humidity, at which 90-100% precipitation falls as snow (Jennings et al., 2018).

We expect valley-specific, orographic precipitation in this monsoon-dominated catchment (Immerzeel et al., 2015b). Precipitation distribution with altitude ( $P_G$ ) and threshold temperature for melt ( $T_M$ ) are unknown in this region, therefore used as calibrating parameters for our model (section 5.3.4). The parameter values are given in Table 5.2.

### **5.3.4 Model calibration**

Handling the precipitation distribution with altitude is the biggest challenge in glacier mass balance-runoff modelling and is largely unknown in the Himalaya (Immerzeel et al., 2015; Bolch et al., 2019). Furthermore, glacier mass balance-runoff models are very sensitive to change in  $T_M$ , which is also uncertain (Azam et al., 2019). Some studies suggest that melting may not necessarily start at air temperature even  $>0\text{ }^{\circ}\text{C}$  (Kuhn, 1987; Hock, 2003). Since our model runs at a daily time step, there may be situations when melt occurs during the peak noon hours on sunny days (with temperature several degrees higher than  $0\text{ }^{\circ}\text{C}$ ) and daily mean temperatures are yet sub-zero (Hock, 2003). Therefore, precipitation gradient ( $P_G$ ) and  $T_M$  were chosen as model calibrating parameters, while

keeping all other parameters constant (Table 5.2). In such calibration, and general in model calibration, some equifinality issue (the existence of many parameter sets associated with the same optimal model output) is expected (discussed in details in section 5.4). The  $P_G$  was changed between 0%  $\text{km}^{-1}$  to 100%  $\text{km}^{-1}$ , with a step size of 5% increase; the  $T_M$  for melt was varied from 4 °C to -4 °C with a step size of 0.1 °C. The model was calibrated to minimize concurrently (1) the resulting root-mean-square errors (RMSE) between modelled and measured annual mass balances available from 1993-1995 and 1998-2000, and (2) the RMSE between mean monthly modelled runoffs and field-observed runoffs for summers of 1994 and 1998-2000 (mid-May to October). Though the daily runoff was observed but only monthly runoff data was available for this study (Thayyen et al., 2005). A total of 1701 (21x81) runs were performed. The minimum RMSE of 0.15 m w.e.  $\text{a}^{-1}$  for mass balance (corresponding to RMSE of 2.14  $\text{m}^3 \text{s}^{-1}$  for runoff) was achieved for -0.3 °C of  $T_M$  and for 0% of  $P_G$ , while a minimum RMSE of 0.72  $\text{m}^3 \text{s}^{-1}$  for runoff (corresponding to RMSE of 1.69 m w.e.  $\text{a}^{-1}$  for mass balance) was achieved with -4.0 °C of  $T_M$  and 55% of  $P_G$ . To get the best optimized RMSE values among all 1701 model runs, we plotted the scatter plot between RMSE for mass balance and RMSE for runoff for each combination of  $P_G$  and  $T_M$  (Fig. 5.6). The best optimized RMSE values of 0.28 m w.e  $\text{a}^{-1}$  and 0.79  $\text{m}^3 \text{s}^{-1}$  for mass balance and runoff, respectively were obtained for  $T_M$  of -2.7 °C and an increase in  $P_G$  of 80%  $\text{km}^{-1}$ . The low  $T_M$  of -2.7 °C is in correspondence with the sub-zero temperature of -1.9 °C reported on Chhota Shigri Glacier in the western Himalaya while modelling the melting at a daily time step (Engelhardt et al., 2017). The requirement of sub-zero threshold temperature for melt was also discussed over the western Greenland using a detailed surface energy balance approach and suggested to be as low as -5°C (van den Broeke et al., 2010). In-situ estimated  $P_G$  are almost negligible in the Himalaya and found to have strong spatial distribution due to steep topography and adjoining windward and leeward catchments (Singh and Kumar, 1997). The calibrated  $P_G$  of 22%  $\text{km}^{-1}$  was found in Chhota Shigri catchment (leeward side) (Azam et al., 2019) and 40%  $\text{km}^{-1}$  in Langtang catchment (windward side) (Immerzeel et al., 2012;

Ragettli et al., 2013). Our calibrated  $P_G$  of  $80\% \text{ km}^{-1}$  in the Dokriani catchment (windward side) is higher than these calibrated  $P_G$  but it is acceptable as a few studies suggested that the precipitation amounts over the glacierized regions could be 2-10 times higher than the valley bottom precipitation in the Himalayan topographic settings (Singh and Kumar, 1997; Savéan et al., 2015; Immerzeel et al., 2015; Eeckman et al., 2017).

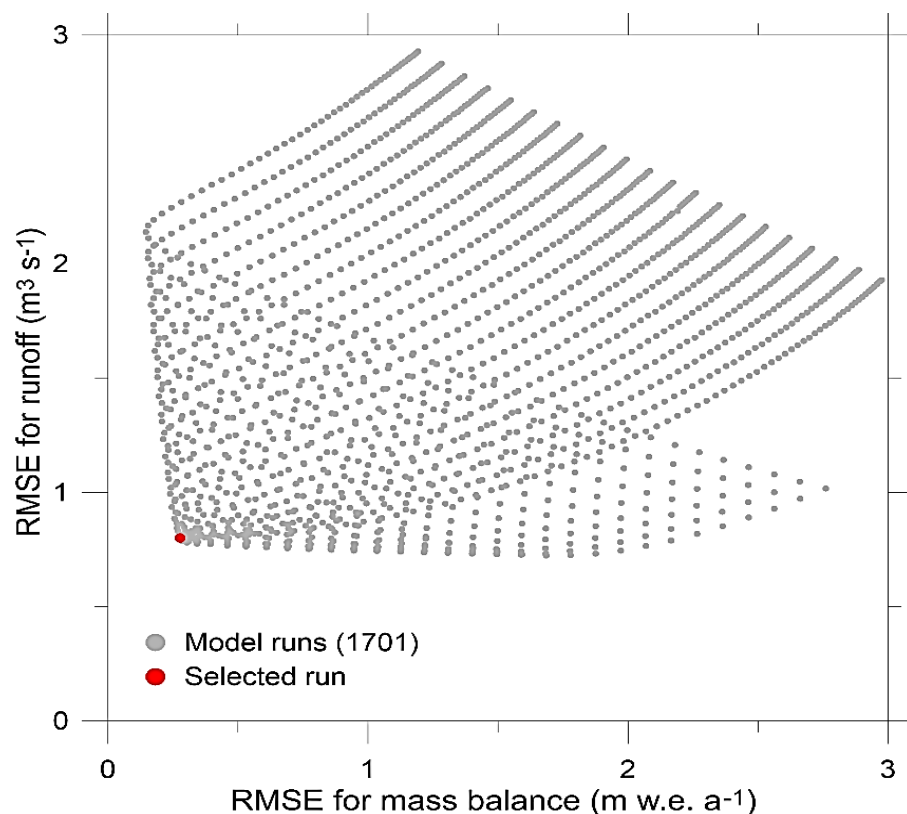


**Figure 5.6:** Scatter plot between mass balances and runoffs RMSEs (root mean square errors) estimated through model calibration (section 3.4). Grey dots show the total model runs and red dot shows the selected model run.

The model can simulate the annual glacier-wide mass balances as well as monthly catchment-wide runoffs fairly well (Fig. 5.7). Compared to the field-observed mass balances, the modelled mass balances are almost the same for 1995 and 2000 years, but were more negative for 1994, 1998 and 1999, and more positive for 1993 (Fig. 5.7a). The uncertainty in observed mass balances was not estimated and assumed to be only  $0.03 \text{ m w.e. a}^{-1}$  (Dobhal et al., 2008), a severe underestimation compared to the uncertainties of  $\pm 0.40 \text{ m w.e. a}^{-1}$  reported on Chhota Shigri Glacier (western Himalaya, India) (Azam et al.,

2012) and  $\pm 0.28 \text{ m w.e. a}^{-1}$  on Mera Glacier (central Himalaya, Nepal) (Wagnon et al., 2013). We consider the differences between modelled and observed mass balances in our study to be in an acceptable range.

Fig. 5.7b shows the modelled mean monthly runoffs against the field-observed mean monthly runoffs. The model showed an underestimation of runoff by 7%. The uncertainty in field measurement is not known (Thayyen et al., 2005), but a recent study of similar runoff measurements, estimated the uncertainty to be about 25% of the total runoff (Eeckman et al., 2017); therefore, we consider the difference (7% underestimation) to be acceptable. However, we would like to stress that the underestimation in runoff (Fig. 5.7b) and slight overestimation of mass balances (Fig. 5.7a) could be due to non-involvement of possible permafrost thaw contribution and sublimation losses, not computed in the present model as well as a biased snow-rain transition or precipitation measurements which cascade to the ERA5.

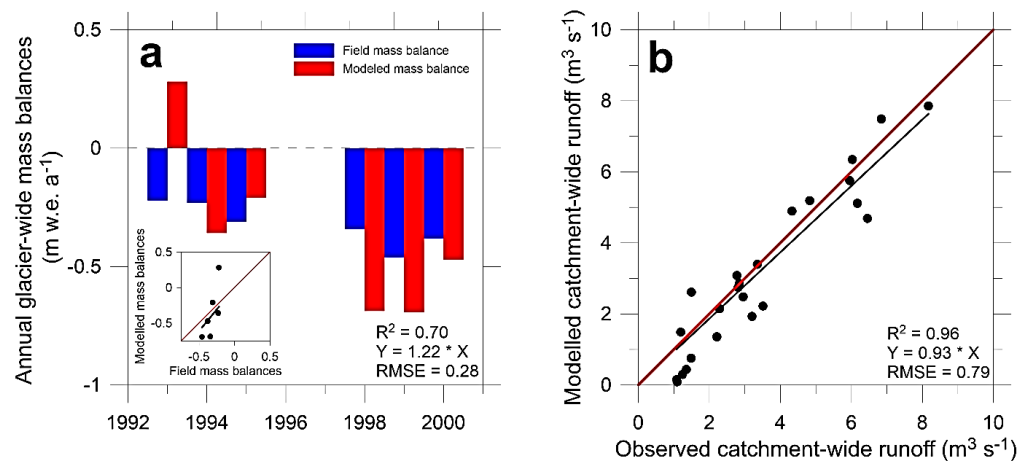


**Figure 5.7:** Model Calibration, (a) the modelled and field-observed mass balances and (b) the modelled and field-observed mean monthly runoffs. The inset in panel (a) shows the correlation between modelled and observed annual mass balances.

### 5.3.5 Model validation

For the model validation, we compared the snow line altitude (SLA) computed from the model with SLA derived from Landsat satellite images of the same days from 1992 to 2017 (Fig. 5.8a). The modelled SLA showed good agreement ( $R^2 = 0.99$ ) with satellite-derived SLA with an overestimation of 1% and an

RMSE of 157 m (Fig. 5.8a). A mismatch has been observed mainly during the late summer period (September-October) when monsoon snowfalls over the higher elevations on the glacier may encounter avalanches or snowdrift bringing snow to lower elevations, which is not included in the model.

After model calibration (section 3.4), modelled SLAs were independently simulated with the calibrated parameters (Table 5.2) at 5m altitudinal ranges. Such modelled SLA represents a single altitude for a specific day while in reality SLA may have several altitudes in different parts of the glacier, mainly depending on the aspect. Given that the model was run at 5 m altitudinal range, the uncertainty in modelled SLAs was assumed to be equal to 10 m. Satellite-derived SLAs were estimated from manual delineation of snow line on the geo-referenced Landsat satellite imageries between 1992 and 2017. SLA is dynamic and marks a divide between the snow-covered and snow-free area on the glacier (Kenzhebaev et al., 2017). Given that Dokriani Glacier is located in the monsoon-dominated region, the availability of satellite images with a clear sky is limited. A total of 28 clear-sky images were selected and SLAs were extracted from Cartosat-1 Digital Elevation Model (DEM, 30 m, 5 May 2005), downloaded from the Bhuvan portal (<https://bhuvan.nrsc.gov.in/>). Uncertainty in SLA is defined and estimated following the protocol of Racoviteanu et al. (2019) in which the accuracy of DEM is used for surface partition, the size of buffer is used for snow lines and the uncertainty in snow and ice area estimates are also taken into consideration. The SLA uncertainty is derived as  $\pm 18.03\text{m}$  from:

$$\Delta SLA = \sqrt{\Delta_{dem}^2 + \Delta_{snowline}^2} \quad (5.8)$$

where  $\Delta_{dem}$  is the vertical error of the Cartosat-1 DEM, taken as  $\pm 9.6$  m based on Singh et al. (2019) and  $\Delta_{snowline}$  is half the pixel size of the Landsat imagery used, i.e.,  $\pm 15\text{m}$  (Racoviteanu et al. 2019).

**Table 5.2:** List of the model parameters, range of parameters used to estimate the uncertainties (section 5.3.6), and mass balance and runoff sensitivity for unit change in each parameter estimated in section 5.5.4.

<b>Model parameter</b>	<b>Value used in model</b>	<b>Range used for uncertainty estimation</b>	<b>Range used for sensitivity test</b>	<b>Mass-balance sensitivity (m w.e. a<sup>-1</sup>)</b>	<b>Runoff sensitivity (m<sup>3</sup> s<sup>-1</sup>)</b>
DDF for debris-covered ice (mm d <sup>-1</sup> °C <sup>-1</sup> )	4.8	4.7 to 5.0	3.8 to 5.8	-0.13	0.03
DDF for ice (mm d <sup>-1</sup> °C <sup>-1</sup> )	7.7	7.4 to 8.0	6.7 to 8.7	-0.13	0.03
DDF for snow (mm d <sup>-1</sup> °C <sup>-1</sup> )	6.1	5.7 to 6.4	5.1 to 7.1	-0.21	0.06
Altitudinal precipitation gradient (calibrated) (% km <sup>-1</sup> ) <sup>#</sup>	80	72 to 88	72 to 88	0.15	0.04
Temperature LRs (°C km <sup>-1</sup> )	T <sub>LRs</sub> <sup>*</sup>	T <sub>LRs</sub> +1σ to T <sub>LRs</sub> -1σ	T <sub>LRs</sub> +1σ to T <sub>LRs</sub> -1σ	0.23	-0.07
Threshold temperature for snow/rain (T <sub>p</sub> ) (°C)	0.7	0.63 to 0.77	-0.3 to +1.7	0.35	-0.11
Threshold temperature for melting (T <sub>M</sub> ) (°C) <sup>#</sup>	-2.7	-3.0 to -2.4	-3.7 to -1.7	0.77	-0.20
Precipitation (10%)	-	-	-10% to +10%	0.24	0.08
Temperature (1 °C)	-	-	T+1 to T-1	-1.11	0.31

<sup>#</sup> calibrated parameters, \* T<sub>LRs</sub> are mean monthly values

A second validation was done using the field-observed mean monthly catchment-wide runoffs available for summer seasons of 1997 (JJAS) and 1998 (JAS) from Singh et al. (2006). This runoff data was collected at the same discharge site as of Thayyen et al. (2005) (section 2). The modelled mean monthly catchment-wide runoffs showed a very strong relationship ( $R^2 = 0.99$ ) with an overestimation of 21% and an RMSE of  $1.11 \text{ m}^3 \text{ s}^{-1}$  (Fig. 5.8b). Nash and Sutcliffe efficiency test (Nash and Sutcliffe, 1970) was also done to check the performance of our model. The calculated efficiency (E) of 0.67 (E = 1, corresponding to a perfect match and E =  $-\infty$ , corresponding to infinite) advocates the good performance of the model.

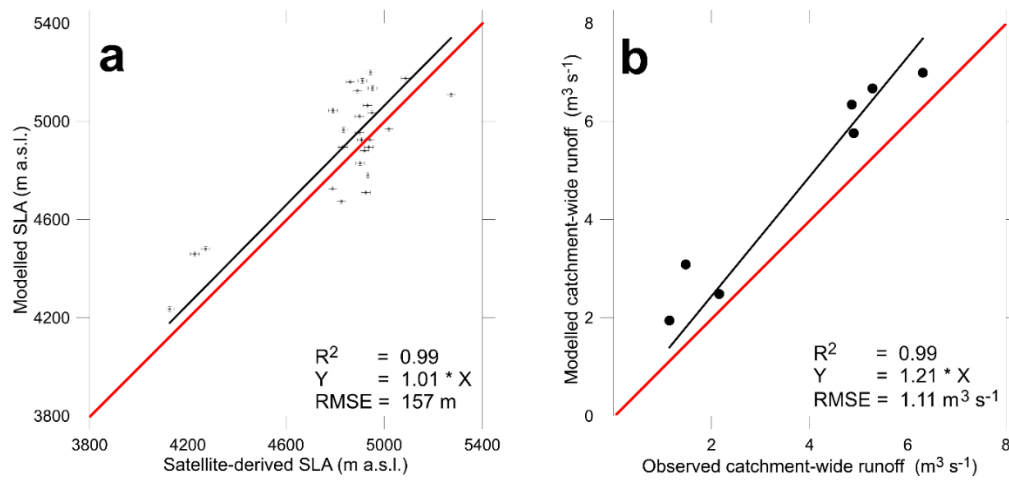


**Figure 5.8:** Validation of modelled snow Line Altitudes (SLAs) with the satellite-derived SLAs for 28 days between 1992 and 2017. The red line indicates a perfect agreement between modelled and satellite-derived SLAs.

### 5.3.6 Model sensitivity and uncertainty estimation

Model sensitivity ( $S$ ) for each parameter was evaluated, one-by-one, by re-running the model with a new set of each parameter (highest parameter value,  $S_H$ , and lowest parameter value,  $S_L$ ), while keeping all the other parameters unchanged (Table 5.2). These sensitivities were estimated by calculating the annual glacier-wide mass balance and catchment-wide runoff averaged over the period 1979–2018 (Oerlemans, 1998) following:

$$\frac{dB_a}{dS} = \frac{B_a(S_H) - B_a(S_L)}{2} \quad (5.9)$$

$$\frac{dQ}{dS} = \frac{Q(S_H) - Q(S_L)}{2} \quad (5.10)$$

where  $B_a$  and  $Q$  are the glacier-wide mass balance and catchment-wide runoff averaged over 1979–2018, using the highest/lowest value of the parameter  $S$  for sensitivity test (Table 5.2). The estimated sensitivities for each model parameter are discussed in section 5.4.

The uncertainty in modelled glacier-wide mass balance and catchment-wide runoff mainly depends on the selected model parameters. This uncertainty in modelled glacier-wide mass balances was assessed by rerunning the model by changing the parameters one by one while keeping all other parameters unchanged (Table 5.2). The lower and upper bound for  $DDF$  for ice (7.4 and 8.0) and snow (5.7 and 6.4) were taken from the field data (Singh et al., 2000) for dusted, clean ice and snow surface, respectively. The range for  $DDF$  for debris-covered ice was estimated following Pratap et al. (2015). Uncertainty in  $T_{LRs}$  was taken as the mean of monthly standard deviations after removing the seasonality in monthly  $T_{LRs}$ . For other parameters ( $P_G$ ,  $T_M$ , and  $T_P$ ) the uncertainties are unknown and therefore these parameters were changed by  $\pm 10\%$  from their original/calibrated values. This is a common practice when plausible ranges for model parameters are unknown to estimate the parametric uncertainty (Anslow et al., 2008; Ragettli et al., 2013; Heynen et al., 2013). The parameter ranges used for uncertainty estimation are given in Table 5.2. The parametric uncertainties in glacier-wide annual, winter and summer mass balances, and catchment-wide runoffs due to each parameter was estimated as their sensitivities using the equations 8 and 9, respectively (Table S3). The total model uncertainty in annual glacier-wide mass balance and catchment-wide runoff was estimated by adding all the parametric uncertainties using error propagation law. The mean uncertainties for glacier-wide mass balance and runoff were estimated to be  $0.37 \text{ m w.e. a}^{-1}$  and  $0.10 \text{ m}^3 \text{ s}^{-1}$ , respectively.

A fixed glacier area has been used for modelling the mass balance and runoff in the present study. The catchment and glacier hypsographies (Fig. 5.2) were extracted manually from high resolution CNES/Airbus data available from

July 2017 using high-resolution Google Earth platform. Dobhal and Mehta (2010) estimated 9.5% area shrinkage between 1962 and 2007, which is equivalent to a very low shrinkage rate of  $0.2\% \text{ a}^{-1}$ ; therefore, the uncertainties due to the fixed-area assumption are assumed to be much lower than already estimated uncertainties and ignored. The fixed-area assumption also induces mass balance uncertainties due to temperature changes resulting from surface elevation changes which is not considered in the model. These uncertainties were estimated on Chhota Shigri Glacier and found to be negligible compared to the total estimated uncertainty in mass balances (Azam et al., 2019) therefore we ignored these uncertainties in the present study. The un-melted snow, stored over steep valley walls outside the glacier at higher elevations (above zero-degree isotherm), falls sporadically on the glacier surface through avalanches. Our model doesn't include the avalanche process hence the avalanche contribution cannot be estimated and ignored in the present study.

Another source of uncertainty could be the ignored sublimation losses in our model. Sublimation and other wind-driven ablation processes can be significant on the Himalayan glaciers, and cannot be resolved in simple temperature-index based models (Wagnon et al., 2013; Litt et al., 2019). Available studies suggest that ablation through sublimation highly depends on regional climate and local meteorology of the glacier (Azam et al., 2018; Litt et al., 2019). For instance, on Puruogangri ice cap in dry climate (north-central Tibetan Plateau), sublimation accounted for 66% of its total mass wastage from 2001 to 2011 (Huintjes et al., 2015a). Monsoon influenced, Zhadang Glacier (south-central Tibetan Plateau) showed 26% losses through sublimation compared to total mass wastage over 2001-2011 (Huintjes et al., 2015b). On Yala Glacier in monsoon-dominated Nepalese Himalaya, sublimation was estimated to be 21% of annual precipitation (Stigter et al., 2018). On Chhota Shigri Glacier in Indian Himalaya, influenced by both ISM and WDs, the sublimation was accounted to be around 2% of total mass loss over 2012-2013 (Azam et al., 2014b). Indeed, estimation of sublimation requires lots of meteorological data not available for Dokriani Glacier and therefore, could not be estimated in the present study. However, Dokriani Glacier being located in a

monsoon-dominated region with mean annual relative humidity around 60% (80% during June to September, Verma et al., 2018), the sublimation losses are expected to be low compared to total mass loss (section 4.1). However, we performed a sensitivity analysis (section 5.4) for sublimation assuming losses equivalent to 20% of annual precipitation (Stigter et al., 2018).

## **5.4 Results**

### **5.4.1 Annual and seasonal glacier-wide mass balances**

Over the modelling period of 1979-2018, annual glacier-wide mass balances were negative for 28 years and positive/balanced for 11 years (Fig. 5.9a; Table S3). The cumulative annual glacier-wide mass balance was  $-9.64 \pm 2.32$  m w.e., which is equivalent to  $-0.25 \pm 0.37$  m w.e.  $a^{-1}$ , showing a moderate mass loss over the last four decades (Table 5.3). The hydrological year 1991/92 showed the maximum mass balance of  $0.38 \pm 0.33$  m w.e. whereas 2015/16 showed the most negative mass balance of  $-0.96 \pm 0.40$  m w.e.

Though annual glacier-wide mass balance is of wide interest and has been estimated in some glacier-monitoring programs in the Himalaya (Azam et al., 2018), it does not provide insights into climate–glacier interactions. Seasonal (winter and summer) glacier-wide mass balances allow better insights to climate-glacier interactions (Ohmura, 2006). In our modelling, the summer glacier-wide mass balances were estimated between 1<sup>st</sup> May to 31<sup>st</sup> October while the winter-glacier wide mass balances were estimated between 1<sup>st</sup> November and 30<sup>th</sup> April of each hydrological year. Modelled seasonal mass balances show large annual variability, with values from  $-1.55$  to  $-0.20$  m w.e.  $a^{-1}$  for summer mass balances and  $0.29$  to  $1.25$  m w.e.  $a^{-1}$  for winter mass balances (Fig. 5.9a; Table S3). The mean summer and winter glacier-wide mass balances were  $-0.97 \pm 0.32$  m w.e. (1979-2018) and  $0.72 \pm 0.05$  m w.e. (1979-2018), respectively (Table 5.3).

### **5.4.2 Equilibrium-line altitude and accumulation area ratio**

The lower ablation area of the glacier (4050-5000 m a.s.l.) is 54% debris covered (the central part is clean while the margins are debris covered) (Fig.

5.1). The annual equilibrium-line altitude (ELA) was estimated using the regression line extracted through the annual altitudinal mass balances of the clean area of the glacier between 5000 and 5500 m a.s.l. (section 5.1). The highest ELA was 5391 m a.s.l., observed for 2015/16 hydrological year, corresponding to the lowest mass balance of  $-0.96$  m w.e., whereas the lowest ELA of 5215 m a.s.l., corresponding to the highest mass balance of  $0.38$  m w.e., was observed for 1991/92 hydrological year (Table S3). The estimated mean annual ELA over 1979-2018 was 5309 m a.s.l. corresponding to annual mean mass loss of  $-0.25$  m w.e. (Table 5.3). The field-observed mean ELA over 1993-1995 and 1998-2000 was 5066 m a.s.l. (Dobhal et al., 2008), which is 248 m lower than the modelled mean annual ELA of 5314 m a.s.l. over the same years. This difference is most probably because of steep glacier topography (an average slope of  $\sim 25$  degree over 4500-5500 m a.s.l. range) that support snowdrift from the accumulation area to the ablation area, a process not considered in the model structure. The modelled mass balances are fairly consistent with observed mass balances (Fig. 5.7a), but the modelled ELAs are higher than the observed ELAs. Such a trend has also been observed on Qiya Glacier, Qilian Mountain Range, China (Wang et al., 2017).

The Accumulation-area ratio (AAR) for each hydrological year between 1979 and 2018 was calculated using the ELA of the corresponding year (Table S3). The mean annual AAR was 46%, corresponding to annual mean mass loss of  $-0.25$  m w.e. over 1979-2018 (Table 5.3). The modelled annual ELA and AAR showed a good correlation with annual glacier-wide mass balance ( $R^2 = 0.82$  and  $0.82$ , respectively) over 1979-2018 (Fig. 5.9b and 5.9c). The ELA for a zero-mass balance ( $ELA_0$ ) was also derived from the regression between glacier-wide mass balances and ELAs over 1979-2018 yielding 5280 m a.s.l. (Fig. 5.9b). Similarly,  $AAR_0$  was 48% for steady-state glacier mass balance (Fig. 5.9c). The estimated  $AAR_0$  on Dokriani Glacier is in close agreement with estimated AAR of 44% for zero mass balance in the western Himalaya (Kulkarni, 1992).

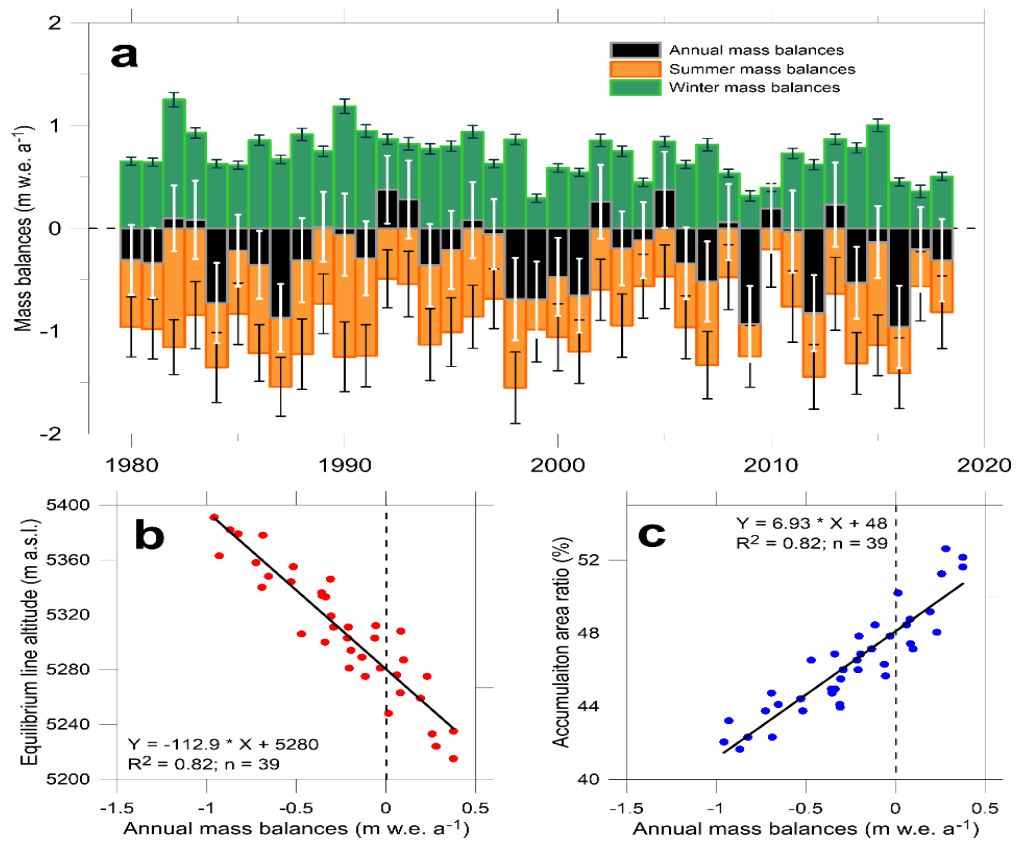


**Figure 5.9:** (a) Annual (black bars), winter (green bars) and summer (orange bars) glacier-wide mass balances for Dokriani Glacier over the modelled period of 1979–2018. The uncertainties on annual, winter and summer glacier-wide mass balances are also shown. The horizontal dotted line represents the zero MB, (b) equilibrium line altitude as a function of annual-glacier wide mass balances, and (c) accumulation area ratio as a function of annual-glacier wide mass balance.

**Table 5.3:** Modelled mean glacier-wide mass balance, equilibrium line altitude (ELA), accumulation area ratio (AAR) and runoff are discussed in section 5.4. The modelled mean mass balance gradients are estimated separately for debris-covered ablation area (<5000 m a.s.l.), clean ablation area (5000-5500 m a.s.l.) and accumulation area (5500-6600 m a.s.l.) (section 5.3.1) Mean Meteorological conditions are calculated from bias-corrected ERA5 dataset available over 1979-2018 and extracted at Base Camp (section 5.3.1).

<b>Dokriani Catchment runoff characteristics (1979-2018)</b>	
Mean annual catchment-wide runoff	$1.56 \pm 0.10 \text{ m}^3 \text{ s}^{-1}$
<b>Dokriani Glacier mass balance and runoff characteristics (1979-2018)</b>	
Mean annual mass balance	$-0.25 \pm 0.37 \text{ m w.e.}$
Cumulative mass balance	$-9.64 \pm 2.32 \text{ m w.e.}$
Mean summer mass balance	$-0.97 \pm 0.32 \text{ m w.e.}$
Mean winter mass balance	$0.72 \pm 0.05 \text{ m w.e.}$
Mean ELA	5309 m a.s.l.
Mean AAR	46% (1979-2018)
Mass balance gradient for debris-covered ablation area	$0.70 \text{ m w.e. (100m)}^{-1}$
Mass balance gradient for clean ice ablation area	$0.91 \text{ m w.e. (100m)}^{-1}$
Mass balance gradient for accumulation area	$0.28 \text{ m w.e. (100m)}^{-1}$
<b>Meteorological characteristics (3763 m a.s.l.)</b>	
Annual temperature	3.1 °C
Summer temperature	7.4 °C
Winter temperature	-1.2 °C
Annual precipitation	1616 mm w.e. (100%)
Summer precipitation	1242 mm w.e. (77%)
Winter precipitation	374 mm w.e. (23%)

### 5.4.3 Annual and seasonal catchment-wide runoff

The computed mean annual catchment-wide runoff was  $1.56 \pm 0.10 \text{ m}^3 \text{ s}^{-1}$  over 1979-2018 showing a large inter-annual variability with the minimum runoff of  $1.32 \pm 0.09 \text{ m}^3 \text{ s}^{-1}$  for the hydrological year 1986-1987 and the maximum runoff of  $1.94 \pm 0.11 \text{ m}^3 \text{ s}^{-1}$  for the hydrological year 1982-1983. The rainfall runoff contributed a maximum of  $44 \pm 2\%$  to total catchment runoff, followed by  $34 \pm 1\%$  from snow melt and  $22 \pm 2\%$  from ice melt between 1979 and 2018.

**Table 5.4:** Mean annual (AMB), summer (SMB) and winter (WMB) glacier-wide mass balances (m w.e. a<sup>-1</sup>) for demarcated periods I (1979-1988), II (1989-1997), III (1998-2006), IV (2007-2018) and for the whole 39-year period over 1979-2018 with their corresponding catchment-wide snow-melt runoff, ice-melt runoff, rainfall runoff, and total runoff. All hydrologic components are in m<sup>3</sup> s<sup>-1</sup>. The values in brackets show the runoff contribution of each hydrologic component in % with respect to total runoff. Mean temperature (°C a<sup>-1</sup>) and precipitation (mm w.e. a<sup>-1</sup>) anomalies are also shown for each period.

<b>Period</b>	<b>AMB</b>	<b>SMB</b>	<b>WMB</b>	<b>Snow melt</b>	<b>Ice melt</b>	<b>Rainfall</b>	<b>Total runoff</b>	<b>T anomaly</b>	<b>P anomaly</b>
1980-1988 (I)	-0.33	-1.12	0.80	0.52 (34)	0.34 (23)	0.66 (43)	1.52 (100)	-0.25	-65
1989-1997 (II)	-0.02	-0.88	0.86	0.56 (36)	0.32 (20)	0.69 (44)	1.57 (100)	-0.34	67
1998-2006 (III)	-0.28	-0.93	0.65	0.53 (36)	0.35 (23)	0.61 (41)	1.48 (100)	0.15	-93
2007-2018 (IV)	-0.33	-0.94	0.62	0.53 (32)	0.37 (23)	0.74 (45)	1.65 (100)	0.34	68
1980-2018	-0.25	-0.97	0.72	0.53 (34)	0.35 (22)	0.68 (44)	1.56 (100)	-	-

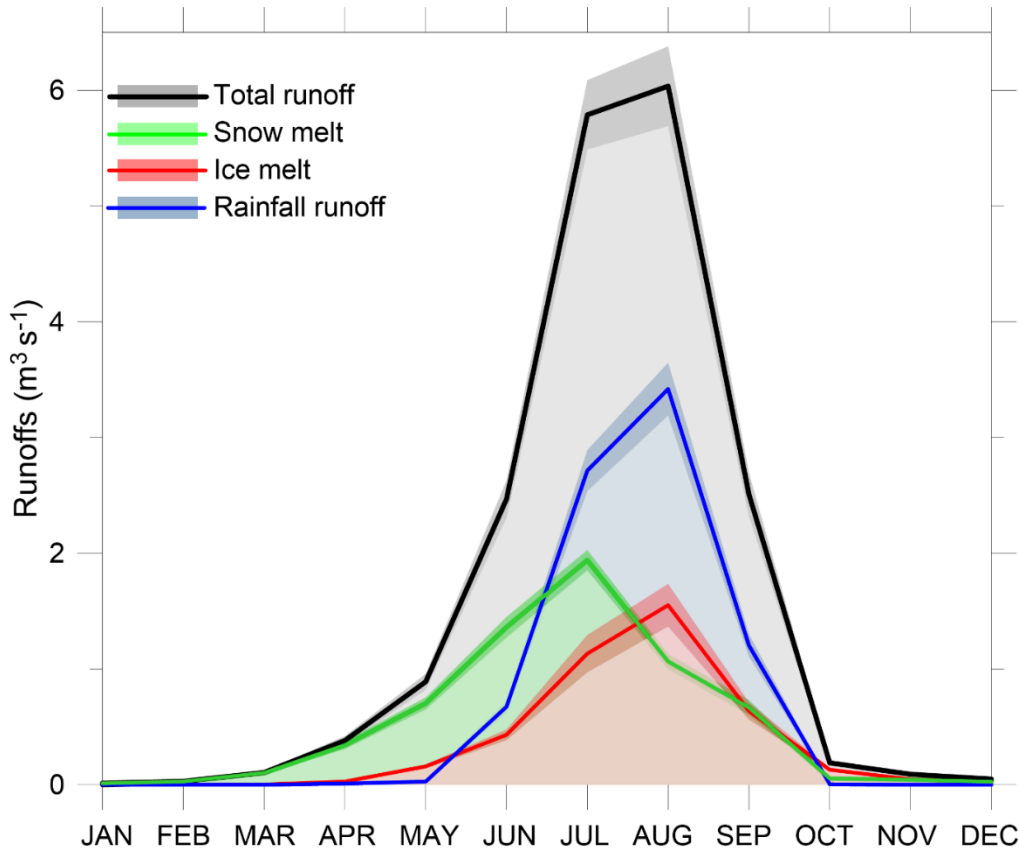


**Figure 5.10:** Mean monthly hydrographs of total runoff and different hydrologic components (snow melt, ice melt, and rainfall-induced runoff) for the whole year. The envelopes on hydrographs represent the parametric uncertainties.

Fig. 5.10 represents the mean annual hydrographs of all modelled hydrologic components at Dokriani Glacier catchment outlet (Fig. 5.1). The catchment-wide runoff ( $2.98 \text{ m}^3 \text{ s}^{-1}$ ) in summer (May to October) makes up almost all annual runoff, winter (November to April) runoff being negligible ( $0.11 \text{ m}^3 \text{ s}^{-1}$ ). Winter snow cover starts melting in March and provides the maximum snow melt of  $1.94 \pm 0.09 \text{ m}^3 \text{ s}^{-1}$  in July before a sharp decrease in snow cover in August due to highest summer temperatures (Fig. 5.3a). The maximum ice melt occurs in August ( $1.55 \pm 0.18 \text{ m}^3 \text{ s}^{-1}$ ,  $\sim 37\%$  of total ice melt) due to the least available snow cover (limited to high altitudes only) and the highest temperatures (Fig. 5.3a). Higher precipitation during monsoon (June to September) (Table 5.3, Fig. 5.3a) result in major rainfall contribution to annual

runoff with a maximum contribution of  $3.42 \pm 0.23 \text{ m}^3 \text{ s}^{-1}$  in August (Fig. 5.10). The catchment-wide runoff production of  $6.04 \pm 0.34 \text{ m}^3 \text{ s}^{-1}$  is highest in August (due to maximum ice melt and rainfall runoff) followed by  $5.79 \pm 0.30 \text{ m}^3 \text{ s}^{-1}$  in July (due to maximum snow melt and higher ice melt and rainfall runoff) (Fig. 5.10). Peaking of catchment-wide runoff generation in July-August has also been observed in other regions of the Himalaya (Lutz et al., 2014; Azam et al., 2019).

The mean melt contribution of 56% (34% snow melt + 22% ice melt) from Dokriani Glacier catchment is less than that of 80% melt contribution (63% snow melt + 17% ice melt) in Chhota Shigri Glacier catchment obtained using the same model (Azam et al., 2019). Given that both the catchments have around 50% glacierized area, the difference in melt contributions can mainly be assigned to different climatic regimes. Dokriani Glacier receives 77% of its annual precipitation from ISM in summer and 23% from WDs in winter; conversely Chhota Shigri Glacier gets 29% of its annual precipitation from ISM in summer and 71% from WDs in winter. These contrasting precipitation regimes provide much higher rainfall contribution in Dokriani Glacier catchment (44% compared to 20% on Chhota Shigri Glacier) and higher snow melt contribution in Chhota Shigri Glacier catchment (63% compared to 34% on Dokriani Glacier) while ice melt contributions are nearly same (22% in Dokriani Glacier versus 17% in Chhota Shigri Glacier).

## **5.5 Discussion**

### **5.5.1 Spatial distribution of debris-cover, altitudinal mass balances and gradients**

The glacier occupies an area of  $1.66 \text{ km}^2$  below 5000 m a.s.l., out of which 54% is debris covered and the rest is clean ice. Debris accumulates toward the steep valley walls and middle flow of the glacier is relatively clean ice (Fig. 5.1). Debris-covered and clean ice areas for each 50m-altitudinal range below 5000 m a.s.l. are shown separately. Mean altitudinal mass balances as well as mass balance (hence ablation) fractions from debris-covered and clean ice parts are

also computed separately for each 50m-altitudinal range (Fig. 5.11). The heterogeneous distribution of debris cover gives high spatial variability in mean altitudinal mass balances below 5000 m a.s.l. (Fig. 5.11). The mean altitudinal mass balance curve shows subdued mass balances over 4150-4350 and 4600-4800 m a.s.l. altitudinal ranges due to the presence of extensive debris cover (96% and 76%, respectively), having lower *DDF* than ice surface (Table 5.2). This insulating effect has been reported on Chhota Shigri Glacier (western Himalaya) using field-based point-scale measurements over the lower ablation area (Wagnon et al., 2007; Azam et al., 2016). Similar attenuated mass balances due to debris cover were also found on some other Himalayan glaciers (Sharma et al., 2016; Shukla and Qadir, 2016; Thompson et al., 2016; Vincent et al., 2016; Sherpa et al., 2017; Shah et al., 2019).

Fig. 5.12 shows the distribution of modelled mean altitudinal mass balances for 1979-2018 over the whole glacier. We estimated the altitudinal mass balance gradients by fitting separate linear regressions on modelled mean annual altitudinal mass balances for debris-covered ablation area (<5000 m a.s.l.), clean ablation area (5000-5500 m a.s.l.) and accumulation area (5500-6600 m a.s.l.) (Fig. 5.11). The mass balance gradients for debris-covered ablation area, clean ablation area and accumulation area were estimated to be 0.70, 0.91 and 0.28 m w.e. (100m)<sup>-1</sup>. The low mass balance gradient in accumulation area is due to little or no melting in the accumulation area hence gradient is mainly controlled by precipitation gradient. The difference in mean altitudinal mass balance gradients over debris-covered and clean ablation areas also suggests that debris cover retards melting on this glacier (Fig. 5.11). Some studies used single value of mass balance gradient and developed melt models at catchment scale (Racoviteanu et al., 2013). Indeed, often the lower ablation area of the Himalayan glaciers is debris covered; therefore, such models can be improved in the future using different mass balance gradients for debris-covered and clean ice surfaces.

The estimated mean mass balance gradients for debris-covered and clean ablation areas of Dokriani Glacier are comparable to those observed in other parts of the Himalayan region (Shea et al., 2015b; Azam et al., 2016;

Sherpa et al., 2017; Sunako et al., 2019) as well as other mid-latitude regions (Rabatel et al., 2005; Zemp et al., 2009; Shea et al., 2013). The mean altitudinal mass balance gradient of  $0.27 \text{ m w.e. (100m)}^{-1}$  was modelled for all glaciers in the Dudh Koshi Basin (central Himalaya) (Shea et al., 2015b). In the same area, using field measurements, Sherpa et al. (2017) estimated the mean altitudinal mass balance gradients of  $0.46$ ,  $0.87$ ,  $1.37$  and  $1.47 \text{ m w.e. (100m)}^{-1}$  on Mera, Naulek, Pokalde and West Changri Nup glaciers. On Trambau Glacier (central Himalaya) the mean altitudinal mass balance gradient was calculated to be  $0.66 \text{ m w.e. (100m)}^{-1}$  (Sunako et al., 2019), while on Chhota Shigri Glacier (western Himalaya) altitudinal mass balance gradients of  $0.68$  and  $0.22 \text{ m w.e. (100m)}^{-1}$  were calculated separately for clean ablation area and accumulation area, respectively (Azam et al., 2016; Mandal et al., 2020). On Stok Glacier (western Himalaya) the mean altitudinal mass balance gradient was  $0.61 \text{ m w.e. (100m)}^{-1}$  (Soheb et al., 2020).

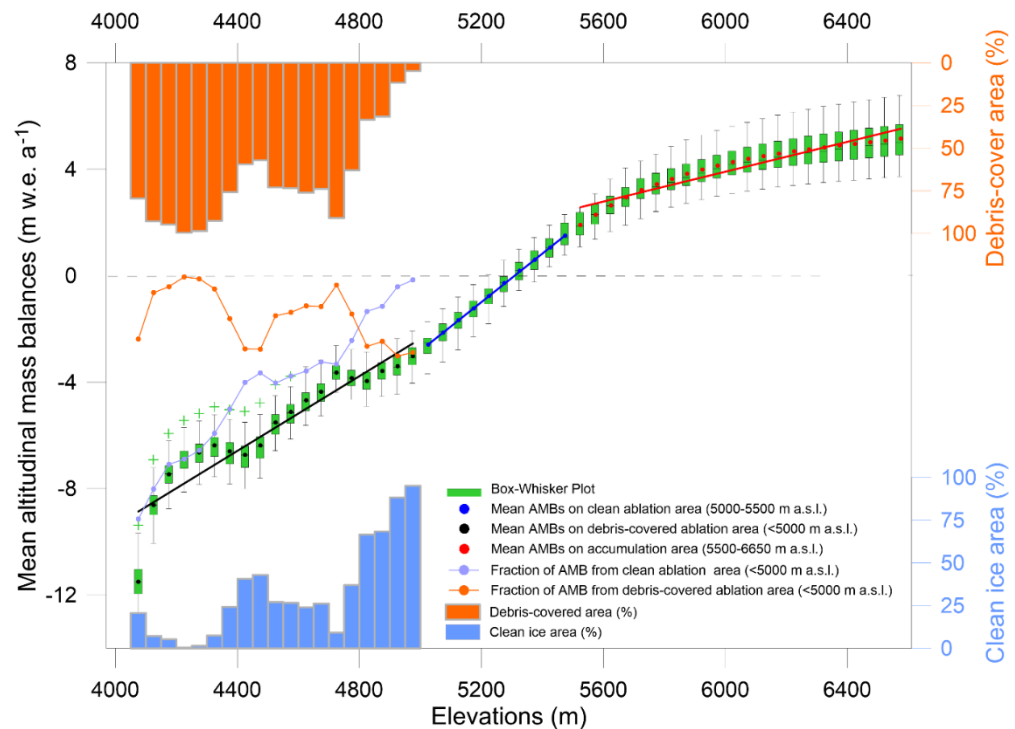


**Figure 5.11:** Box-Whisker plot of modelled mean annual mass balances ( $\text{m w.e. a}^{-1}$ ) calculated for 50m intervals (1979-2018) for Dokriani Glacier. The boundaries of each box indicate the upper and lower quartiles, while the middle line of the box shows the median value. Whisker ends indicate the maximum and minimum values excluding outliers (shown as green plus sign). Orange and

light blue bars represent the fraction of debris-covered and clean ice area for each 50m altitudinal range below 5000 m a.s.l. while orange and light blue dots represent the mass balance fractions from debris-covered and clean ice area from each 50m altitudinal range below 5000 m a.s.l. The mean altitudinal mass balance gradients for debris-covered ablation area (<5000 m a.s.l.), clean ablation area (5000-5500 m a.s.l.) and accumulation area (5500-6600 m a.s.l.) are shown in black, blue and red lines.

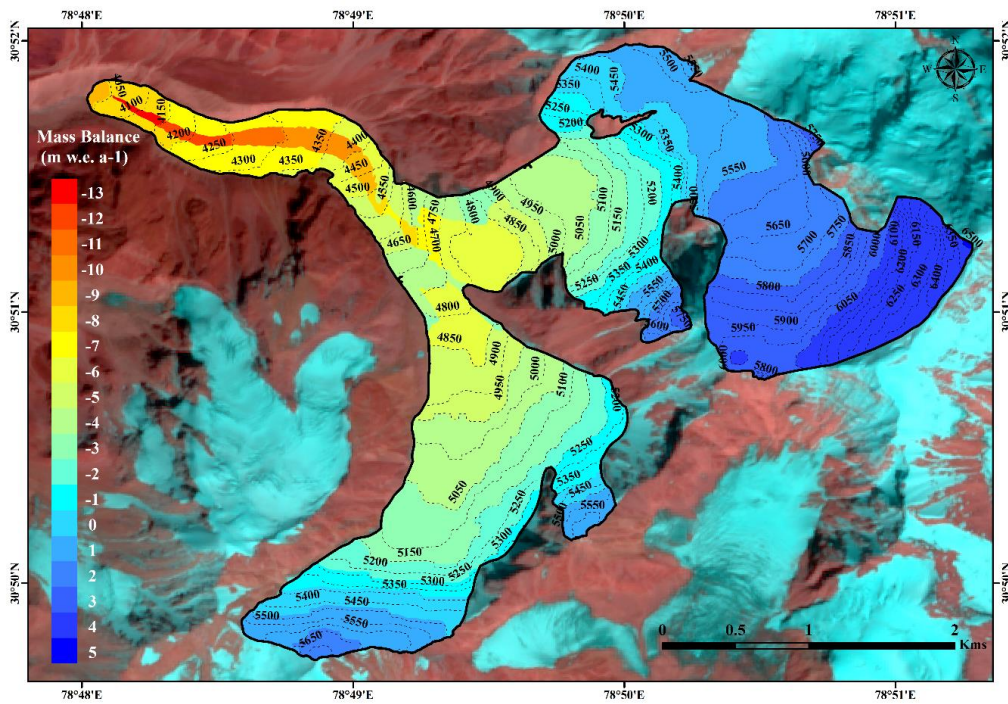


**Figure 5.12:** Distribution of modelled mean altitudinal mass balances for 1979-2018 period over the whole glacier. Dotted lines show the contours at 50 m difference.

### 5.5.2 Decadal mass balances, runoffs and climatic drivers

Over the whole simulation period (1979–2018), the cumulative glacier-wide mass balance of Dokriani Glacier was  $-9.64 \pm 2.32$  m w.e. Four decadal periods (9, 9, 9 and 12 years, respectively) were distinguished arbitrarily according to the glacier mass wastage rates in the modelled mass balance series (Table 5.4). During periods I (1979–88), III (1998–2006), and IV (2007-2018) Dokriani Glacier lost mass at almost similar rates of  $-0.33$ ,  $-0.28$  and  $-0.33$  m w.e.  $a^{-1}$ , respectively, whereas during period II (1989–1997) it remained close to steady-

state conditions, with a mean annual glacier-wide mass balance of  $-0.02 \text{ m w.e. a}^{-1}$ .

Period I (1979–88) and IV (2007–2018) showed similar mass balance conditions ( $-0.33 \text{ m w.e. a}^{-1}$ ) yet both the periods were climatically opposite. Period I experienced negative temperature ( $-0.25 \text{ }^{\circ}\text{C a}^{-1}$ ) and precipitation ( $-65 \text{ mm w.e. a}^{-1}$ ) anomalies while Period IV had positive temperature ( $0.34 \text{ }^{\circ}\text{C a}^{-1}$ ) and precipitation ( $68 \text{ mm w.e. a}^{-1}$ ) anomalies (Table 5.4). The positive temperature and positive precipitation anomalies resulted in the higher mass turn over consequently higher catchment-wide runoff of  $1.65 \text{ m}^3 \text{ s}^{-1}$  over Period IV compared to  $1.52 \text{ m}^3 \text{ s}^{-1}$  over Period I, under the same mass wastage conditions over both periods. The near steady state of Dokriani Glacier over Period II (1989–1997) is in good agreement with the negative temperature anomaly ( $-0.34 \text{ }^{\circ}\text{C a}^{-1}$ ) and positive precipitation anomaly ( $67 \text{ mm w.e. a}^{-1}$ ) that resulted in the least negative summer mass balance ( $-0.88 \text{ m w.e. a}^{-1}$ ) and the highest winter mass balance ( $0.86 \text{ m w.e. a}^{-1}$ ). Further in line, Period II was characterized by the highest snow melt contribution and the smallest ice melt contribution compared to other periods (Table 5.4). Period III (1998–2006) was moderately warm (positive temperature anomaly of  $0.15 \text{ }^{\circ}\text{C a}^{-1}$ ) but the driest (negative precipitation anomaly of  $-93 \text{ mm w.e. a}^{-1}$ ) period and experienced a mass wastage of  $-0.28 \text{ m w.e. a}^{-1}$  corresponding to the higher ice melt runoff, least rainfall runoff and minimum catchment-wide runoff of  $1.48 \text{ m}^3 \text{ s}^{-1}$  (Table 5.4).

### **5.5.3 Near-balanced conditions preceding 2000**

Decadal mass balance trends (section 5.2) suggest a near-balanced state for Dokriani Glacier between 1989 and 1997. Glacier-wide annual mass balance observations over the 1990s are available for sporadic years (1992–1995; 1996–2000) and showed a moderate wastage of  $-0.32 \text{ m w.e. a}^{-1}$  (Dobhal et al., 2008). Our modelled glacier-wide mass balances are in good agreement with these field-observed data and showed an average wastage of  $-0.36 \text{ m w.e. a}^{-1}$  over the same years (Fig. 5.7). Unfortunately, field-observed mass balances are not available from other glaciers in the Himalaya over the 1990s (Azam et al.,

2018). Therefore, we compared the reconstructed mass balance series on Dokriani Glacier with other long-term mass balance reconstructions available from Mera Glacier, central Himalaya (Shea et al., 2015b) and Chhota Shigri Glacier, western Himalaya (Azam et al., 2019). Fig. 5.13 shows the cumulative mass balance curve for Dokriani Glacier along with the Mera and Chhota Shigri glaciers. The near-balanced state on Dokriani Glacier over 1989-1997 with a slight mass wastage of  $-0.02$  m w.e.  $a^{-1}$  is in close agreement with the near-balanced conditions observed on Mera and Chhota Shigri (average mass balances of  $-0.07$  m w.e.  $a^{-1}$  over 1985-2000 and  $0.01$  m w.e.  $a^{-1}$  over 1986-2000, respectively) glaciers. Balanced mass balances on Chhota Shigri Glacier over the 1990s have also been observed through the ice-flux method (Azam et al., 2012) and geodetic mass estimate (Vincent et al., 2013). Given the unavailability of such data and high model uncertainty (section 3.6), we advocate caution while accepting this near-balanced condition over 1989-1997 on Dokriani Glacier. However, the above-mentioned long-term mass balance reconstructions showed an increasing mass wastage after 2000 (Fig. 5.13). The near-balanced conditions preceding 2000 and accelerated wastage after 2000 on these glaciers are in agreement with Maurer et al. (2019). They estimated the geodetic mass balances of 650 glaciers along the whole Himalayan range and found that the mass wastage over 1975-2000 with an average rate of  $-0.22 \pm 0.13$  m w.e.  $a^{-1}$  is almost half that of  $-0.43 \pm 0.14$  m w.e.  $a^{-1}$  mass wastage over 2000-2016. Another study with geodetic mass wastage of  $-0.17 \pm 0.12$  and  $-0.29 \pm 0.19$  m w.e.  $a^{-1}$  over 1968-2006 and 2006-2014 periods, respectively on nearby Gangotri Glacier (Bhattacharya et al., 2016) also confirms the recently accelerated wastage in this region of the Himalaya.

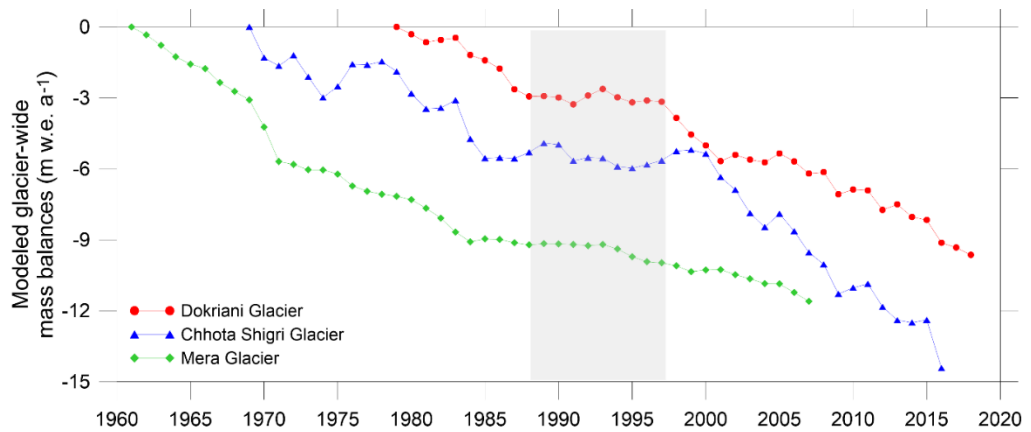


**Figure 5.13:** The cumulative mass balance curves for Mera (central Himalaya, Nepal) over 1961-2007 (Shea et al., 2015b), Chhota Shigri (western Himalaya, India) over 1969-2016 (Azam et al., 2019) and Dokriani glaciers for 1979-2018 (present study). The grey shaded area between 1989-1997 shows the near-balanced state for Dokriani Glacier.

#### 5.5.4 Mass balance and runoff sensitivity

The model sensitivity was the highest to a unit change in  $T_M$  (mass balance sensitivity =  $0.77 \text{ m w.e. a}^{-1}$  and runoff sensitivity =  $-0.20 \text{ m}^3 \text{ s}^{-1}$ ) followed by unit change in  $T_P$  (mass balance sensitivity =  $0.35 \text{ m w.e. a}^{-1}$  and runoff sensitivity =  $-0.11 \text{ m}^3 \text{ s}^{-1}$ ). The model output was the least sensitive for a unit change in  $DDF$  for clean ice (mass balance sensitivity =  $-0.12 \text{ m w.e. a}^{-1}$  and runoff sensitivity =  $0.03 \text{ m}^3 \text{ s}^{-1}$ ).

Models have been used in different glacierized mountain ranges to assess the modelled glacier mass balance and runoff sensitivities to changing climate (Braithwaite and Raper, 2007; Anderson et al., 2010; Mölg et al., 2012; Azam et al., 2019). We also checked the model sensitivities for a unit change in input air temperature and 10% change in precipitation. The sensitivities of modelled glacier-wide mass balance and catchment-wide runoff to temperature were calculated to be  $-1.11 \text{ m w.e. a}^{-1} \text{ } ^\circ\text{C}^{-1}$  and  $0.31 \text{ m}^3 \text{ s}^{-1} \text{ } ^\circ\text{C}^{-1}$ , respectively. The estimated model sensitivity for temperature was almost twofold that of Chhota Shigri Glacier in the western Himalaya (Azam et al., 2014a) as well as glaciers in the Alps (Vincent, 2002). This higher sensitivity of Dokriani Glacier is most probably due to its location in the monsoon-dominated region, receiving 77% of its annual precipitation during the summer season (Table 5.1) and

therefore, highly sensitive for temperature change (Fujita, 2008). A recent study (Wang et al., 2019a) estimated the sensitivities of 45 glaciers in different climatic regimes of High Mountain Asia (HMA) ranging between  $-0.20$  and  $-1.49$  m w.e.  $a^{-1} \text{ } ^\circ\text{C}^{-1}$ .

A similar sensitivity test was performed for precipitation, assuming a  $\pm 10\%$  change. The sensitivities of modelled glacier-wide mass balance and catchment-wide runoff were computed to be  $0.24$  m w.e.  $a^{-1}$  and  $0.08$   $\text{m}^3 \text{ s}^{-1}$ , respectively to a 10% change in precipitation. The model was run several times while changing successive total precipitation to discern the precipitation amount needed to compensate for a  $1$   $^\circ\text{C}$  change in temperature. An increase of 49% in precipitation is required to offset the change in glacier-wide mass balance resulting from a  $1$   $^\circ\text{C}$  increase in temperature. Our results are in good agreement with Braithwaite (2002) and Braithwaite and Raper (2007), who reported a 30-40% increase in precipitation to offset the effects of a  $+1$   $^\circ\text{C}$  temperature change. Besides estimating the model sensitivities for input parameters, we also checked the sensitivity for sublimation losses by reducing input precipitation by 21%, as sublimation losses were computed to be 21% of annual precipitation on Yala Glacier in Nepalese Himalaya (Stigter et al., 2018). The model sensitivity of mass balance and runoff for 21% reduction in input precipitation was estimated to be  $0.26$  m w.e.  $a^{-1}$  and  $0.09$   $\text{m}^3 \text{ s}^{-1}$ , respectively.

### **5.5.5 Model equifinality**

The equifinality issue is found in all hydrological models (Beven and Freer 2001; Beven, 2006). Our model is calibrated using two different data sets (section 5.3.4) and independently validated with satellite-derived snow line altitudes and field runoffs (section 3.5); therefore, we expect limited equifinality issue (Ragetti et al., 2015; Lutz et al., 2016). In order to get an idea about equifinality in our model, we plotted the contour maps for RMSEs between modelled and measured annual mass balances (Fig. 5.14a) and mean monthly modelled and field-observed runoffs (Fig. 5.14b) obtained during calibration process (section 5.3.4). Minimum RMSEs of around  $0.4$  m w.e.  $a^{-1}$  between modelled and measured annual mass balances were found for  $T_M$  of  $0$  to  $-3.0$   $^\circ\text{C}$

and  $P_G$  of 0 to 100%/km, suggesting a large range of model parameters (the blue diagonal band in Fig. 5.14a) for similar mass balance output. However, the minimum observed RMSEs of around  $1 \text{ m}^3 \text{ s}^{-1}$  between modelled and measured runoffs were observed for  $T_M$  of  $-2.0$  to  $-4 \text{ }^\circ\text{C}$  and  $P_G$  of 20 to 90%/km (Fig. 5.14b). These large ranges of  $T_M$  and  $P_G$  for quite similar RMSEs (Fig. 5.14) suggest equifinality in our model output. The use of two different outputs during model calibration is found to control the equifinality to a large extent (section 3.4; Fig. 5.6); yet our calibrated  $T_M$  and  $P_G$  should be considered cautiously before applying to other studies.

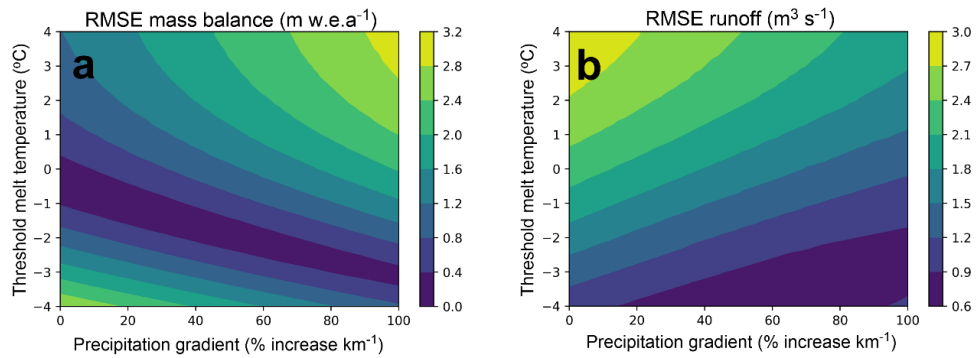


**Figure 5.14:** Contour maps showing the RMSE for mass balance (panel a) and runoff (pane b) for ranges of threshold melt temperature and precipitation gradient used in model calibration (section 3.4).

## 5.6 Conclusions

The snow and glacier melt contribution in the Himalayan rivers is crucial and support large irrigation system and hydropower generation. The available studies are often large scale and used only river runoff at downstream to calibrate their models (Lutz et al., 2014) hence are expected to have large uncertainties in their estimated snow and glacier melt contributions. In this study we exploited extensive field data, available in a remote and highly glacierized catchment of Dokriani Glacier in the central Himalaya, to develop a glacier mass balance-runoff model and provided the detailed understanding of mass balance and runoff behaviour over the last four decades.

The annual glacier-wide mass wastage on Dokriani Glacier was moderate with a mean value of  $-0.25 \pm 0.37 \text{ m w.e. a}^{-1}$  (corresponding to

cumulative mass loss of  $-9.64 \pm 2.32$  m w.e.) over 1979-2018. The corresponding mean winter and summer glacier-wide mass balances were estimated to be  $0.72 \pm 0.05$  and  $-0.97 \pm 0.32$  m w.e.  $a^{-1}$ , respectively over the same period. The mean ELA and AAR were 5309 m a.s.l. and 46%, respectively, and the mean annual catchment-wide runoff was  $1.56 \pm 0.10$   $m^3 s^{-1}$  over 1979-2018. Rainfall contributed the maximum to the total mean annual runoff with  $44 \pm 2\%$  of total runoff, while snow melt and ice melt contributed  $34 \pm 1\%$  and  $22 \pm 2\%$ , respectively over the observed period. Maximum total runoff is produced during summer-monsoon months, peaking in August ( $6.04 \pm 0.34$   $m^3 s^{-1}$ ) corresponding to maximum rainfall runoff, maximum ice melt and high snow melt.

Decadal mass balances suggest that Dokriani Glacier was close to steady-state conditions (annual glacier-wide mass balance of  $-0.02$  m w.e.  $a^{-1}$ ) over period II (1989–1997), whereas other periods I (1979–88), III (1998–2006), and IV (2007-2018) showed moderate mass wastage. Near steady state of Dokriani Glacier was linked with negative temperature anomaly and positive precipitation anomaly over this period which resulted in the least negative summer mass balance ( $-0.88$  m w.e.  $a^{-1}$ ) and highest winter mass balance ( $0.86$  m w.e.  $a^{-1}$ ). The near steady-state conditions over 1989-1997 closely follow the near steady states previously found on Mera Glacier (in the central Himalaya) over 1985-2000 and Chhota Shigri Glacier (in the western Himalaya) over 1986-2000.

The heterogeneous debris-cover distribution over lower ablation area results in high spatial variability in altitudinal mass balance below 5000 m a.s.l. and protects the glacier from higher melting. The altitudinal mass balance gradients for debris-covered ablation area ( $<5000$  m a.s.l.), clean ablation area (5000-5500 m a.s.l.) and accumulation area (5500-6600 m a.s.l.) were 0.70, 0.91 and 0.28 m w.e.  $(100m)^{-1}$ . Mass balance and runoff are most sensitive to the threshold temperature for melt with sensitivities of  $-0.77$  m w.e.  $a^{-1} \text{ } ^\circ C^{-1}$  and  $0.20$   $m^3 s^{-1} \text{ } ^\circ C^{-1}$ , respectively. The model sensitivity tests for input precipitation and temperature suggest that an increase of 49% in precipitation is required to

offset the change in glacier-wide mass balance resulting from a 1 °C increase in temperature.

Hydrological models have to deal with the problem of equifinality. However, due to the model calibration against two field-observed datasets (mass balance and runoff) and independent validation with satellite-derived snow line altitudes and runoffs, we believe the equifinality issue in our model has been limited to a great extent. Nevertheless, we advocate caution when applying our calibrated melt threshold temperature and precipitation gradient to other studies. We also suggest to increase the in-situ glacio-hydro-meteorological monitoring from different climatic regimes to predict the future water evolution at better confidence level.

## Chapter 6

# Glacier mass balance-runoff relationship in Monsoon and Alpine regimes of Himalayan catchments

### 6.1 Introduction

The Himalaya—otherwise known as the Third Pole—contains a large amount of snow, ice and permafrost that are essential water resources to over 1 billion population of Indus, Ganga and Brahmaputra River basins for irrigation, hydropower, industries, and municipal sector (Azam et al., 2021). These basins cover an area of 2.75 million (M) km<sup>2</sup> with Indian sovereignty over most of the area with 1.50 M km<sup>2</sup> followed by Pakistan (0.52 M km<sup>2</sup>), China (0.39 M km<sup>2</sup>), Nepal (0.15 M km<sup>2</sup>), Bangladesh (0.09 M km<sup>2</sup>), Afghanistan (0.07 M km<sup>2</sup>), and Bhutan (0.04 M km<sup>2</sup>). The region hosts some of the largest irrigated areas of the world, with a total irrigated area of 0.58 M km<sup>2</sup> and an installed hydropower capacity of 26432 MW (Azam et al., 2021). Ganga is the most densely-populated basin with the maximum irrigated area, over 0.16 M km<sup>2</sup>.

Glaciers regulate the headwaters of the Himalayan River basins therefore, any glacial change can modify the runoff characteristics from daily to multi-century scales (Lutz et al., 2014) depending on regional climate (Maussion et al., 2014). Daily, seasonal and inter-annual runoff variations are of critical importance at micro-scale for local water supplies and hydropower generation at high altitudes, whereas long-term changes are significant at macro-scale at lower altitudes, mainly for irrigation in the Indo-Gangetic Plains (Biemans et al., 2019; Azam et al., 2021). The percent contribution of glacier runoff to total river runoff depends on the percentage of glacierized area at any given basin outlet; hence the fraction of glacier runoff increases with elevation (Kaser et al., 2010; Azam et al., 2021). The solid to liquid precipitation ratio depends on climatic regimes and is important in any basin (Jennings et al., 2018). Snow can be deposited as seasonal/perennial snow (firn) or glacier ice,

and remains in the basin for a long time, whereas rain, generally, runs off from the basin comparatively faster.

In-situ measurements, and application of remote sensing and models suggest that the Himalayan glaciers have been losing mass, since the 1970s (Azam et al., 2018). However, glacier wastage is heterogeneous along the Himalayan mountain range (Brun et al., 2017; Azam et al., 2018) implying that the climate change impacts on glacier melt runoff production depend on the local/regional climate (Maussion et al., 2014; Sakai and Fujita, 2017). Glacier melt runoff contribution in the Himalaya also has strong seasonality (Immerzeel et al., 2010; Lutz et al., 2014; Azam et al., 2021). It is suggested that the glacier runoff reduces during positive mass balance (MB) years because some water is stored on the glaciers while it increases during negative MB years as some water is released from long-term glacier storage (Hock, 2005).

Over the recent decades, in-situ glacier-wide annual MB observations were started on several glaciers in Bhutan, China, India and Nepal, yet the catchment-wide runoff observations were often overlooked (Azam et al., 2018; 2021). Consequently, the joint in-situ observations of glacier-wide annual MBs and catchment-wide runoffs are not available from recent decade; therefore, the relationship between in-situ glacier-wide annual MBs and catchment-wide runoffs has been discussed for a limited number of glaciers using very sparse and short-term data, mostly from the pre-2000 period (Thayyen and Gergan, 2010).

The MB-runoff relationship is not straightforward as a universal definition of glacier runoff is difficult to frame. In the literature, several definitions have been used depending on the authors' expertise and research objectives. The most commonly used definitions are: (1) Glacier runoff can be thought of as all the water coming out at the glacier terminus whether it is from glacier melt, snow melt, rain or any other source (Radić and Hock, 2014), (2) Glacier runoff generated from the melting of glacier snow, firn and ice (Cogley, 2011), (3) Glacier runoff produced only from glacier firn and ice, with the concept that all other components (snow melt, rain, etc.) would exist in the basin even if the glaciers are gone, (4) Glacier runoff produced due to glacier net

wastage (Kääb et al., 2012; Brun et al., 2017), which can also be termed as glacier-degraded runoff (net water withdrawal from glacier storage at the end of the hydrological year) and do not exist if the glacier MB is balanced or positive (Thayyen and Gergan, 2010). The glacier runoff from definition-1 can directly be measured while the runoff in the other three scenarios can only be indirectly estimated/modelled, bringing in larger uncertainties in data sparse regions (Azam et al., 2021).

In the present study, the long-term relationships between glacier-wide annual MBs and catchment-wide runoffs have been analysed on two reference catchments —Dokriani Bamak Glacier (DBG) and Chhota Shigri Glacier (CSG)— in the Himalaya using the long-term output from a simple glacio-hydrological model since 1950. Further, the available short-term, in-situ glacier MB and runoff data have been exploited to understand the MB-runoff relationship in eight glacierized catchments of the Himalaya. Glacier runoff definition-1 is used in the present study for investigating the MB-runoff relationship. However, it is emphasized that glacier changes, in any case, will influence river runoff, though the perceived impact would vary with the adopted glacier runoff definition.

## **6.2 Climate, study area and existing data**

### **6.2.1 Climate and climatic regimes**

The Himalayan climate is controlled by Indian Summer Monsoon (ISM) and Western Disturbances (WDs) (Maussion et al., 2014). ISM strength decreases westward while WDs weaken eastward along with the Himalayan Mountain range. This spatio-temporal distribution in precipitation and different river runoff composition (Lutz et al., 2014; Azam et al., 2021) along the Himalayan Range provide three major glacio-hydrological regimes: (1) Himalayan catchments, (2) Alpine catchments, and (3) Cold-arid catchments (Thayyen and Gergan, 2010). The Himalayan catchments (central and eastern catchments of the Ganga and Brahmaputra basin) receive their major annual precipitation from ISM during summer months and glacier meltwater contribution to the river

runoff is maximum during the peak-flow period. In these catchments, the glacier ablation period coincides with snow accumulation at high elevations thus, the glaciers of Himalayan catchments are called ‘summer-accumulation type glaciers’ (Maussion et al., 2014). Alpine catchments (winter snow-dominated regions of south of the western Himalaya and Karakoram) receive their major annual precipitation from winter snow falls from the WDs that is released in summer months; therefore, the glaciers in these catchments are called ‘winter-accumulation type glaciers’ (Maussion et al., 2014; Azam et al., 2014a). Cold-arid catchments of the Ladakh (north-west of the western Himalaya, extending from India to Tibet) are extremely dry due to the decrepit reach of ISM and WDs; therefore, glaciers, snow and permafrost melting are the major sources of water in these catchments (Thayyen and Gergan, 2010; Wani et al., 2020).

### **6.2.2 Study area**

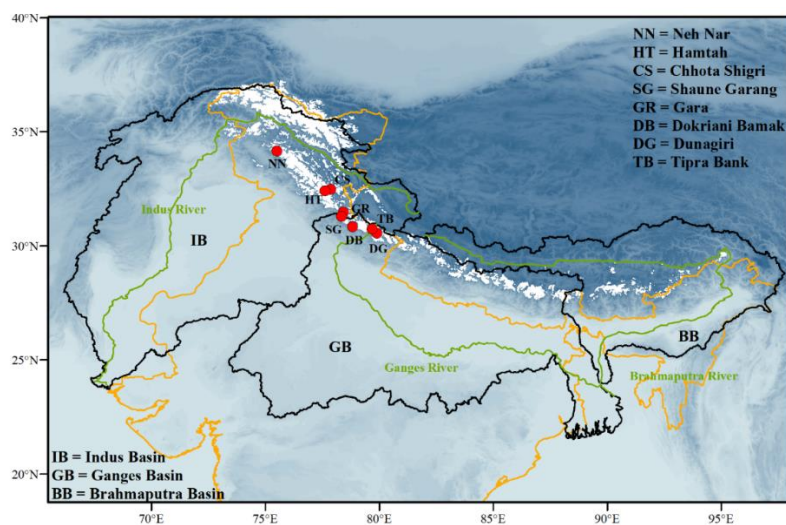
DBG catchment (30°51’ N, 78°49’ E), covering an area of 15.71 km<sup>2</sup>, is located in the upper Ganga basin of the central Himalaya (Garhwal Range, Uttarakhand, India) (Fig. 6.1; Table 6.1). This catchment falls in the ISM-dominated region (Table 6.1). DBG flows over a length of ~6 km and covers an area of 7.03 km<sup>2</sup>, ranging from 4050-6632 m a.s.l. (Table 6.1). Its terminus area (4050-4900 m a.s.l.) is partially debris-covered (0.90 km<sup>2</sup>, ~13% of DBG area) (Fig. 6.2). The proglacial stream released is called ‘Din Gad’ that contributes to the Bhagirathi River of the Ganga River system. DBG catchment is one of the best-studied catchments in the Himalaya for MB, meteorology, and hydrology (Thayyen et al., 2005; Dobhal et al., 2008; Kumar et al., 2014; Pratap et al., 2015; Yadav et al., 2019). The runoff station is located on the proglacial stream around 1.25 km below the glacier terminus (Thayyen et al., 2005).

CSG catchment (32°28’ N, 77°52’ E), covering an area of 34.7 km<sup>2</sup> (3840 m a.s.l.) (Wagnon et al., 2007), is located in the upper Indus basin of the western Himalaya (Lahaul valley, Himachal Pradesh, India) (Fig. 6.1; Table 6.1). This catchment falls in the WDs-dominated region (Table 6.1). CSG flows over a length of ~9 km and covers an area of 15.5 km<sup>2</sup>, ranging from 4070-5850 m a.s.l. (Azam et al., 2016) (Fig. 6.2). This is almost a clean glacier (with only

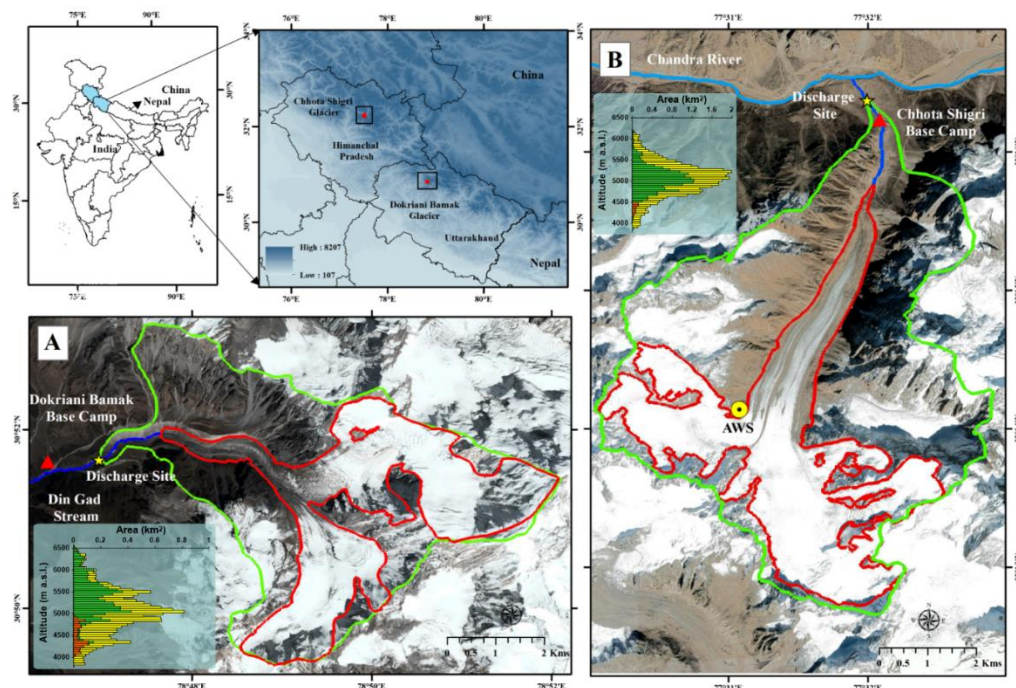
~4% debris cover over its lower tongue; Vincent et al., 2013). The catchment is bounded by a cirque in the south and a peak, Devachan (6263 m a.s.l.), in the east (Fig. 6.2). CSG has extensively been studied for various aspects including MBs, dynamics, ice thickness, energy balance, and hydrology (Wagnon et al., 2007; Azam et al., 2014b; 2016; Ramsankaran et al., 2018; Mandal et al., 2020; Haq et al., 2021). CSG issues a single proglacial stream that drains to the Chandra River, a tributary of the Indus River (Fig. 6.2).

Fig. 6.1 and Table 6.1 present the location and characteristics of eight glacierized catchments (DBG, CSG, Dunagiri, Tipra, Hamtah, Gara, Neh Nar and Shaune Garang) in the Himalaya, respectively where in-situ glacier-wide annual MBs and catchment-wide runoffs are available and discussed in this study (see section 2.3).

All these catchments are from the Indian Himalaya, and are concentrated in the Indus and Ganga basins. The glacierized area varies from 14% to 45% at their runoff sites in different catchments. These catchments are classified as ‘Monsoon catchments’ (ISM-dominated regime) and ‘Alpine catchments’ (WDs-dominated Alpine regime) (Table 6.1). For ISM-dominated catchments, the term ‘Monsoon catchment’ is preferred in this study instead of ‘Himalayan catchment’ as suggested previously (Thayyen and Gergan, 2010) in order to avoid any confusion with the ‘Himalaya’. Further, it is more appropriate to use ‘Monsoon catchment’ for monsoon-dominated catchments. Glacier-wide MB and catchment-wide runoff data are not yet available from the Cold-arid region.



**Figure 6.1:** Location of eight glacierized catchments where glacier-wide MB and catchment-wide runoff measurements are available in the Himalaya (Table 6.1). Glacier cover (white polygons) is from RGIv6 ([https://www.glims.org/RGI/rgi60\\_dl.html](https://www.glims.org/RGI/rgi60_dl.html)). The green lines represent the rivers in different basins.



**Figure 6.2:** Location of Dokriani Bamak Glacier (DBG) (A) and Chhota Shigri Glacier (CSG) (B) catchments in the Himalaya. Red and green polygons show the boundary of glaciers and catchments, respectively and insets show the 50-m hypsometry for debris cover (orange bars), clean glacier (green bars) and total catchment area (yellow bars) in both the catchments.

### 6.2.3 MB and runoff data

During the 1970s and 80s, the Geological Survey of India (GSI) was the primary organisation responsible for collecting the annual glacier-wide MB and catchment-wide runoff data on several catchments in the Indian Himalaya. Fig. 6.1 shows the location of all these catchments where both MB and runoff data are available. In September 1974, GSI conducted the first in-situ annual glacier-wide MB observations on the Gara Glacier (western Himalaya) (Raina et al., 1977). Gradually, GSI expanded the glacier monitoring network in different climatic regimes of the Himalaya. Out of 26 observed glaciers in the Himalaya during different time periods (1-10 years), 11 glaciers have been monitored by

**Table 6.1:** Characteristics of eight glacierized catchments in the Himalaya where glacier-wide annual MB and catchment-wide runoff data are available.

Glacier catchment (Region)	Location	Catchment Area	Glacier Area (km <sup>2</sup> )	Catchment regime	Data availability <sup>#</sup>	References
		(km <sup>2</sup> )	(%)			
1. Dokriani Bamak (DB), Garhwal, Ganga Basin	30°50'N 78°50'E	15.7	7.0 (44.6)	Monsoon	1994, 1998-2000	Dobhal et al. (2008) Thayyen et al. (2005)
2. Chhota Shigri (CS), Lahaul-Spiti, Indus Basin	32°28'N 77°52'E	34.7	15.5 (44.7)	Alpine	2010-2016	Azam et al. (2019) Mandal et al. (2020)
3. Dunagiri (DG), Garhwal, Ganga Basin	30°33'N 79°54'E	17.9	2.6 (14.3)	Monsoon	1985-1990, 1992	GSI, 2001
4. Tipra Bank (TB), Garhwal, Ganga Basin	30°44'N 79°41'E	41.6	15.4 (37.0)	Monsoon	1982-1988	GSI, 2001
5. Hamtah (HT), Lahaul-Spiti, Indus Basin	32°24'N 77°37'E	-	3.2 (-)	Alpine	2001-2008, 2010	GSI, 2001
6. Gara (GR), Baspa Basin, Indus Basin	31°28'N 78°25'E	17.0	5.2 (30.6)	Monsoon	1975-1980, 1982	Raina et al. (1977)
7. Neh Nar (NN), Jhelum Basin, Indus Basin	34°09'N 75°31'E	-	1.3 (-)	Alpine	1978-1981, 1983-1984	GSI, 2001
8. Shaune Garang* (SG), Baspa Basin, Indus Basin	31°17'N 78°20'E	35.5	9.2 (26.0)	Monsoon	1982-1990	GSI, 2001

<sup>#</sup> = data availability period is the common period when both glacier MB and runoff data are available.

\*Shaune Garang Catchment contains 9 glaciers upstream Ratia Thatch outlet, where the runoff measurements were taken.

the GSI (Azam et al., 2018). The annual glacier-wide MB measurements were often taken over September-end to September-end of a consecutive year using the traditional stake/pit method (Østrem and Stanley, 1969). However, the available literature, annual expedition reports or short abstracts, sometimes lack the important details such as distribution of stakes, accumulation methods (pit vs snow/firn coring), snow/firn density measurements, map details, and measurements dates which make it difficult to estimate the uncertainties in MB measurements (Azam et al., 2018).

GSI had generally developed integrated glacier-monitoring programmes and therefore, glacier runoff measurements were also carried out for a few catchments. Runoff measurements were often performed during the core-monsoon period i.e., July to September. The length of the observation period mainly depends on access (roads are sometimes snow covered even up to June-July) and was not always uniform—in some cases, the observations were started in the first or second week of August (GSI, 2001). Runoff sites were developed as close as possible to the glacier terminus. In the case of Neh Nar Glacier, a rectangular weir was erected across the glacier stream (GSI, 2001). In Shaune Garang catchment, the runoff was measured at Ratia Thatch, where the basin area is 35.5 km<sup>2</sup> with 26% glaciated cover (nine glaciers above Ratia Thatch including Shaune Garang). Usually, the runoff was measured by the standard area-velocity method. The stream velocity was measured either with the float method or current meter, and the water levels were continuously measured by using an automatic water level recorder. In turbulent streams, runoffs were measured by using the salt dilution method (GSI, 2001). Hamtah, Neh Nar and Dunagiri glacier catchments were surveyed by GSI, and MB and runoff data are available over 2000-2008, 1978-1984 and 1985-1990 periods, respectively (GSI, 2001). CSG runoff measurements were performed from May through September and were available for 2010-2016 period (Azam et al., 2019). The associated uncertainties in runoff measurements were not estimated in the original sources, hence, not available for this study. However, focusing

on the runoff measurements in similar conditions, the uncertainties can be up to 25% of the measured runoff (Eeckman et al., 2017).

## **6.3 Methods**

### **6.3.1 Climate data and bias correction**

Glacio-hydrological models for the DBG and CSG catchments were forced with long-term daily temperature and precipitation data from bias-corrected ERA5 over 1950-2020 (<https://cds.climate.copernicus.eu/#!/home>). The data were downloaded at the nearest grids and bias-corrected using available in-situ meteorological data for DBG and CSG catchments from previous studies (Verma et al., 2018; Azam et al., 2016; Mandal et al., 2020). For the DBG catchment, the daily temperature was bias-corrected using linear regression equation between raw ERA5 and off-glacier Automatic Weather Station (AWS; 3774 m a.s.l.) mean monthly data, while for precipitation monthly factors were used between raw ERA5 and AWS data (Verma et al., 2018). The details of these bias corrections were given in Azam and Srivastava (2020). For the CSG catchment, a linear regression equation, developed between mean monthly temperature from raw ERA5 and an off-glacier AWS (4863 m a.s.l., Fig. 6.2) data over 2009-2016 (Azam et al., 2016), was applied to bias-correct the ERA5 temperature series, while monthly scale factors were applied to bias-correct the ERA5 precipitation series using precipitation data from an automated rain/snow gauge (Geonor T-200B), installed at CSG base camp (Fig. 6.2) since 2012.

### **6.3.2 Glacio-hydrological model**

Long-term glacier-wide MBs and catchment-wide runoffs on DBG (Monsoon regime) and CSG catchments (Alpine regime) were reconstructed using a simple glacio-hydrological model—including an accumulation module, rain module and a temperature-index melt module— was used at daily temporal resolution. The reconstructions were already performed on DBG catchment over 1979-2018 (Azam and Srivastava, 2020) and CSG catchment over 1969-2016 (Azam et al., 2019) using the same model, and were extended over the 1950-2020 period in the present study. The details about the model can be found

in previous studies (Azam et al., 2014b; Azam et al., 2019; Azam and Srivastava, 2020) however, a brief description of the model is as follows:

The daily snow accumulation ( $S_{acc}$ , mm w.e. d<sup>-1</sup>) is computed at each 50 m elevation range of the catchment (glacierized and non-glacierized) as:

$$S_{acc} = \begin{cases} P: & \text{when } and T \leq T_P \\ 0: & \text{when } and T > T_P \end{cases} \quad (6.1)$$

where  $P$  and  $T$  denote daily precipitation (mm) and temperature (°C), respectively, which are extrapolated at each 50-m elevation range applying the temperature and precipitation gradients, respectively and  $T_P$  is the threshold temperature (°C) for snow-rain.

The daily rainfall ( $r$ , mm w.e. d<sup>-1</sup>) is computed at each 50-m elevation range of the catchment (glacierized and non-glacierized) as:

$$r = \begin{cases} 0: & \text{when } and T \leq T_P \\ P: & \text{when } and T > T_P \end{cases} \quad (6.2)$$

The computed rainfall (and all other computed runoff components mentioned hereafter) are assumed to arrive at the catchment outlet at the end of each day.

The daily melt ( $M$ , mm w.e. d<sup>-1</sup>) from each 50-m elevation range is computed as:

$$M(S, I, D) = \begin{cases} DDF_{S,I,D} \cdot (T - T_M): & \text{when } and T > T_M \\ 0: & \text{when } and T \leq T_M \end{cases} \quad (6.3)$$

where  $DDF$  is the degree-day factor (mm d<sup>-1</sup> °C<sup>-1</sup>) which is different for different surface conditions (snow  $S$ , ice  $I$  and debris-covered ice  $D$ ), and  $T_M$  is the threshold temperature (°C) for melt.

Mean altitudinal MB for each 50-m elevation range ( $b_z$ , m w.e.) is estimated using the accumulation and the ablation terms as:

$$b_z = S_{acc} - M \quad (6.4)$$

Daily glacier-wide MB  $B_a$ , (m w.e.) is calculated using the mean elevation MBs as:

$$B_a = \frac{\sum A_z b_z}{A} \quad (6.5)$$

Where  $A_z$  ( $m^2$ ) and  $b_z$  (m w.e.) are the 50-m elevation glacier area and mean altitudinal MBs, respectively, and  $A$  is the total glacier area ( $m^2$ ). Annual glacier-wide MBs are calculated using daily MBs for the hydrological year from 1 November through 31 October of next the year for DBG (Dobhal et al., 2008) and hydrological year from 1 October through 30 September of the next year for CSG (Wagnon et al., 2007).

The daily catchment-wide snow melt runoff ( $Q_s$ ,  $m^3/s$ ) is computed as:

$$Q_s = m_{sg} + m_{sng} \quad (6.6)$$

where  $m_{sg}$  and  $m_{sng}$  denote snow melt runoff from the glacierized and non-glacierized areas, respectively.

The daily catchment-wide rainfall runoff ( $Q_r$ ,  $m^3/s$ ) is computed as:

$$Q_r = r_g + r_{ng} \quad (6.7)$$

where  $r_g$  and  $r_{ng}$  denote rainfall runoff from the glacierized and non-glacierized areas, respectively.

The daily catchment-wide total runoff ( $Q$ ,  $m^3/s$ ) is computed as:

$$Q = Q_s + Q_r + Q_i \quad (6.8)$$

where,  $Q_s$ ,  $Q_r$ , and  $Q_i$  are the catchment-wide snow melt runoff, rainfall runoff and ice melt runoff (clean and debris-covered ice). The overall structure of model is shown in Fig. 6.3.

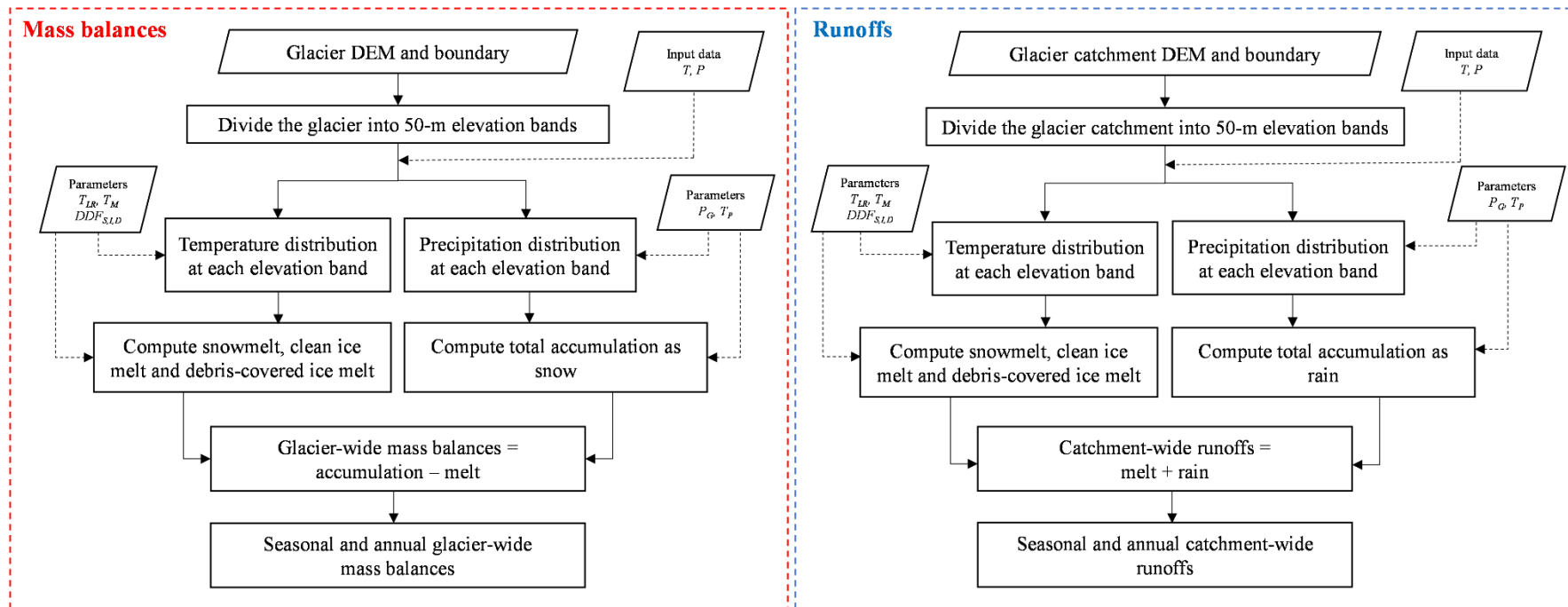


**Figure 6.3:** MB-runoff model structure.  $T, P, T_P, T_{LR}, T_M, P_G$  and  $DDF_{S,I,D}$  are the temperature, precipitation, threshold temperature for snow/rain limit, temperature lapse rates, threshold temperature for melt, altitudinal precipitation gradient and degree day factor (DDF) for snow, ice and debris-covered ice, respectively.

### 6.3.3 Model parameters and extrapolation of climate data

Temperature plays an important role in MB-runoff modelling as it determines the distribution of snowfall/rain over the catchment. Temperature was extrapolated at every 50-m elevation range applying the mean monthly temperature lapse rates ( $T_{LRs}$ ): for DBG catchment estimated in Azam and Srivastava (2020), while for CSG catchment estimated using in-situ temperature data recorded using automatic temperature sensors with solar radiations shields (HOBO, U23-002) at CSG base camp (3850 m a.s.l.) and AWS site (4863 m a.s.l.; Fig. 6.2) over three hydrological years from October 2016 to September 2019.  $T_p$  values of 0.7°C and 1.1°C were used corresponding to 70-80% and 60-70% relative humidity ranges for DBG and CSG, respectively, at which 90 to 100% precipitation was considered as snow (Jennings et al., 2018). The  $DDFs$  for snow, clean ice and debris-cover ice surfaces were adopted from previous studies for both DBG and CSG catchments (Azam et al., 2019; Azam and Srivastava, 2020).

The glacio-hydrological models were found to be highly sensitive to  $T_M$ , an unknown in the Himalayan catchments (Engelhardt et al., 2017; Azam et al., 2019; Azam and Srivastava, 2020). Further, precipitation distribution over the Himalayan region is spatially non-uniform due to valley-specific precipitation gradients ( $P_G$ ) (Sakai et al., 2015; Immerzeel et al., 2015). Hence, in this study, the calibrated values of  $T_M$  and  $P_G$  have been adopted for the DBG catchment from Azam and Srivastava (2020), while for the CSG catchment these parameters were calibrated against the in-situ MB and runoff data (details are mentioned in Table 6.2). Precipitation at every 50-m elevation range was then extrapolated using calibrated  $P_G$  for both the catchments.

The rainfall over the glacier was assumed to contribute directly to the runoff and refreezing of rain water or melt water was assumed negligible. Melt water/rainfall refreezing was ignored as it is insignificant on temperate glaciers. For more details about the parameters, readers are invited to go through previous publications (Azam et al., 2014b; 2019; Azam and Srivastava, 2020).

**Table 6.2:** Details of the model parameters, input data, calibration, and validation. Details can be found in Azam et al. (2014b; 2019) and Azam and Srivastava, (2020).

Glacier	Dokriani Bamak	Chhota Shigri
<b>Modelling period</b>	1950-2020	1950-2020
<b>Daily Input data</b> (temperature and precipitation)	ERA5	ERA5
<b>Model parameters</b>		
DDF for debris-covered ice ( $\text{mm d}^{-1} \text{ }^{\circ}\text{C}^{-1}$ )	4.8 (IS)	3.34 (IS)
DDF for ice ( $\text{mm d}^{-1} \text{ }^{\circ}\text{C}^{-1}$ )	7.7 (IS)	8.63 (IS)
DDF for snow ( $\text{mm d}^{-1} \text{ }^{\circ}\text{C}^{-1}$ )	6.1 (IS)	5.28 (IS)
Altitudinal precipitation gradient ( $\% \text{ km}^{-1}$ )	80 (C)	89 (C)
Temperature LRs ( $^{\circ}\text{C km}^{-1}$ )	Mean monthly (IS)	Mean monthly (IS)
Threshold temperature for snow/rain ( $T_P$ ) ( $^{\circ}\text{C}$ )	0.7 (L)	1.1 (L)
Threshold temperature for melting ( $T_M$ ) ( $^{\circ}\text{C}$ )	-2.7 (C)	-0.7 (C)
<b>Model calibration data</b>	Annual glacier-wide MBs (1993-1995; 1998-2000), Mean monthly runoffs (1994, 1998-2000)	Annual glacier-wide MBs (2003-2012), Mean monthly runoffs (2010-2012)
<b>Model validation data</b>	Snow line altitudes (1992-2017), Monthly runoff data (1997-1998)	Snow line altitudes (1989-2017), Mean monthly runoffs data (2013-2015)

(IS) = In-situ value, (C) = calibrated value and, (L) = literature value

### 6.3.4 Model calibration and validation

The DBG model was forced with meteorological data from ERA5 (<https://cds.climate.copernicus.eu/#!/home>) and calibrated/validated using in-situ data over the recent years (Azam and Srivastava, 2020); therefore, in this study no further calibration and validation were performed. The CSG model was forced with meteorological data from the Indian Meteorological Department station at Bhuntar town (50-km away, other side of the orographic barrier) and calibrated/validated with the available in-situ data (Azam et al., 2019). In this study, ERA5 bias-corrected data was used for MB and runoff reconstructions in the CSG catchment since 1950, hence new calibration and validation processes were performed.

For the model calibration, the  $P_G$  and  $T_M$  parameters were varied over the plausible parameter's limits ( $P_G$  from 0 to 100% km<sup>-1</sup> and  $T_M$  from -4°C to +4°C) in both the catchments. The model run with minimized RMSE (root-mean-square error) between modelled and in-situ annual MBs and monthly runoffs were selected for both the catchments. The selected run showed RMSEs of 0.28 m w.e. a<sup>-1</sup> (1993-1995; 1998-2000) and 0.43 m w.e. a<sup>-1</sup> (2003-2012) between modelled and in-situ MBs and 0.79 10<sup>6</sup> m<sup>3</sup> a<sup>-1</sup> (1994, 1998-2000) and 1.22 10<sup>6</sup> m<sup>3</sup> a<sup>-1</sup> (2010-2012) between modelled and in-situ runoffs for the DBG and CSG catchments, respectively (Fig. 6.4).

The model was validated against the snow line altitudes (SLAs) derived from model and satellite images. The satellite-derived SLAs were obtained for DBG from Azam and Srivastava (2020) and for CSG from Chandrasekharan et al. (2018). The modelled SLAs showed a good agreement with satellite-derived SLAs for both DBG and CSG catchments with RMSEs of 157 and 156 m, respectively (Fig. 6.4).

Another validation was performed using modelled and in-situ monthly runoffs with RMSE of 1.11 10<sup>6</sup> m<sup>3</sup> a<sup>-1</sup> (1997-1998) from Singh et al. (2006) and 1.66 10<sup>6</sup> m<sup>3</sup> a<sup>-1</sup> (2013-2015) from Azam et al. (2019) for DBG and CSG catchments, respectively. Multiple-criteria calibration/validation has been suggested in Azam et al. (2021) for reducing the equifinality problem in the hydrological models. In line, we have used multiple datasets for model calibration (MBs and runoffs) and validation (runoffs and SLAs) in the present study on both the catchments.

To check the model performance, Nash-Sutcliffe efficiency test (Nash and Sutcliffe, 1970) was also performed. This test is described in equation 6.9.

$$E = 1 - \frac{\sum_{i=1}^n (Q_o - Q_m)^2}{\sum_{i=1}^n (Q_m - \bar{Q})^2} \quad (6.9)$$

where,  $E$  is the efficiency of the model.  $Q_o$ , and  $Q_m$  are the in-situ and modelled runoffs, respectively for a particular year, and  $\bar{Q}$  is the mean in-situ runoff during the period of consideration.  $E$  ranges between 1 to  $-\infty$  with  $E = 1$  being the favourable value. Efficiencies of 0.85 and 0.81 between in-situ and

modelled runoff for DBG and CSG catchments, respectively recommend the good performance of the model.

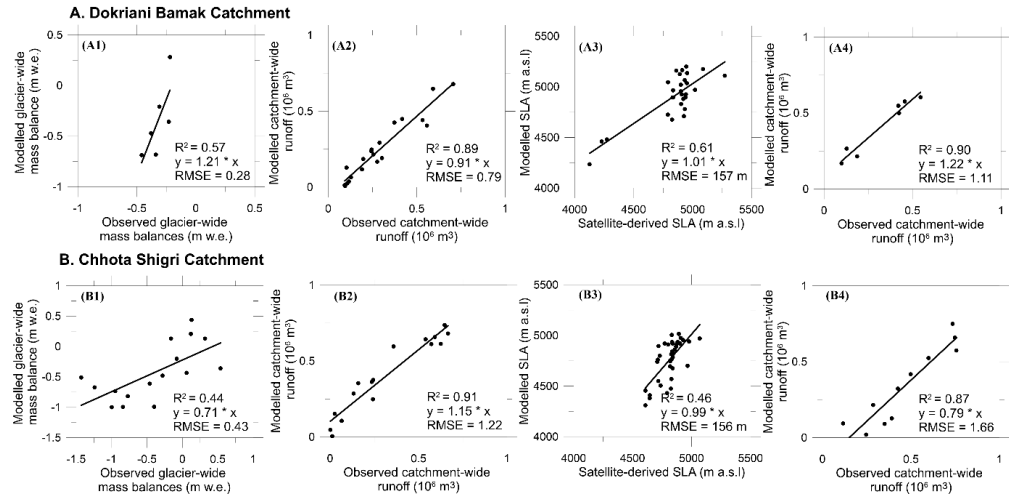


**Figure 6.4:** Model Calibration: Modelled and field-observed glacier-wide mass balances for DBG (A1) and CSG (B1); Modelled and field-observed catchment-wide runoffs for DBG (A2) and CSG (B2) and Model validation: Modelled and satellite derived SLAs for DBG (A3) and CSG (B3) ; Modelled and field-observed catchment-wide runoffs for DBG (A4) and CSG (B4).

### 6.3.5 Uncertainty estimation

To estimate the uncertainties in the reconstructed MBs and runoffs, the model was rerun by changing the input parameters one-by-one —within the plausible ranges, and keeping all other input model parameters as calibrated. The minimum and maximum values of  $DDF$  for ice, snow and debris- covered ice for DBG and CSG catchments were taken from Azam and Srivastava (2020) and Azam et al. (2019), respectively. For  $T_{LRs}$ , the upper and lower uncertainty bounds were estimated as the mean monthly standard deviations, after eliminating the seasonality in monthly  $T_{LRs}$ . The uncertainties in  $P_G$ ,  $T_M$ , and  $T_P$  were unknown. Therefore, to get the upper and lower values, they were changed by +10% and -10%, respectively from their original/calibrated values (Table 6.3). All these parametric uncertainties were added by applying the error propagation law to compute the total uncertainties in MB and runoff. The mean annual uncertainties for MB were estimated to be 0.35 and 0.28 m w.e.  $a^{-1}$  for DBG and CSG catchments, respectively, while the uncertainties for runoff were the same with a value of  $0.01 \cdot 10^6 m^3 a^{-1}$  for both the catchments.  $T_{LR}$  and  $T_M$

contributed maximum uncertainty to MB estimates over DBG catchment while  $DDF_S$  and  $DDF_I$  to CSG catchment (Table 6.3).

The glacier and catchment hypsometries (Fig. 6.2) were manually delineated from CNES/Airbus data (10/07/2017) at Google-Earth platform (Azam and Srivastava, 2020) for DBG catchment and using a Digital Elevation Model developed exploiting Pléiades stereo pair (18/08/2014) (Azam et al., 2016) for CSG catchment. In the present study, static glacier surfaces have been assumed for the MB and runoff reconstructions on both the glaciers. The estimated area shrinkage rates were very low on DBG ( $0.2\% \text{ a}^{-1}$  over 1962-2007; Dobhal and Mehta (2010)) and CSG ( $0.01\% \text{ a}^{-1}$  over 1980-2010; Pandey and Venkataraman (2013)); therefore, the model uncertainties related to the static-area assumption were expected to be much smaller than the already computed uncertainties, hence ignored. In addition to these uncertainties, the static-area assumption also gives uncertainties due to temperature changes at each elevation range resulting from glacier thickness changes, not included in the modelling scheme. A previous study found that these uncertainties were very small compared to total computed uncertainty in MBs on CSG (Azam et al., 2014b), thus also ignored in our study.

Another source of model uncertainty could be from avalanching, snow blowing or snow drift. There are very limited studies/models that involve these processes (Azam et al., 2021). In Langtang catchment ( $360 \text{ km}^2$ , central Himalaya, Nepal), avalanche contribution was 5% to the runoff (Ragettli et al., 2015). DBG and CSG are the benchmark glaciers/catchments that were selected carefully for long-term MB and runoff studies (Wagnon et al., 2007; Dobhal et al., 2008). An ice-flow modelling study investigated the role of avalanches on several glaciers, and reported that DBG and CSG are not receiving significant avalanche accumulation as compared to the annual MB (Laha et al., 2017). Given that both the catchments are relatively less affected by avalanching, we assumed that its role is insignificant (Azam et al., 2019; Azam and Srivastava, 2020).

**Table 6.3:** List of model parameters and uncertainty ranges for DBG and CSG catchments.

Parameters	Dokriani Bamak Glacier				Chhota Shigri Glacier			
	Model value	Uncertainty estimation range	MB uncertainty (m w.e. a <sup>-1</sup> )	Runoff uncertainty (10 <sup>6</sup> m <sup>3</sup> s <sup>-1</sup> )	Model value	Uncertainty estimation range	MB uncertainty (m w.e. a <sup>-1</sup> )	Runoff uncertainty (10 <sup>6</sup> m <sup>3</sup> s <sup>-1</sup> )
Altitudinal precipitation gradient (% km <sup>-1</sup> ) *	80	72 to 88	0.15	0.00	89	80 to 98	0.10	0.00
Temperature Lapse rate (T <sub>LR</sub> ) (°C km <sup>-1</sup> )	T <sub>LR</sub>	T <sub>LR</sub> +1σ to T <sub>LR</sub> -1σ	0.21	0.01	T <sub>LR</sub>	T <sub>LR</sub> +1σ to T <sub>LR</sub> -1σ	0.00	0.00
Threshold temperature for snow/rain (T <sub>P</sub> ) (°C)	0.7	0.63 to 0.77	0.02	0.00	1.1	0.99 to 1.21	0.01	0.00
Threshold temperature for melting (T <sub>M</sub> ) (°C) *	-2.7	-3 to -2.4	0.22	0.00	-0.7	-0.77 to -0.63	0.04	0.00
Degree Day Factor for snow (DDF <sub>S</sub> ) (mm d <sup>-1</sup> °C <sup>-1</sup> )	6.1	5.7 to 6.4	-0.02	0.00	5.28	4.05 to 5.43	-0.20	0.01
Degree Day Factor for ice (DDF <sub>I</sub> ) (mm d <sup>-1</sup> °C <sup>-1</sup> )	7.7	7.4 to 8	-0.03	0.00	8.63	5.13 to 9.08	-0.14	0.01
Degree Day Factor for debris-covered ice (DDF <sub>D</sub> ) (mm d <sup>-1</sup> °C <sup>-1</sup> )	4.8	4.7 to 5	-0.07	0.00	3.34	-	-	-

\*Calibrated parameters

### 6.3.6 Glacier MB-runoff relationship: concept

Glacier MB-runoff relationship can simply be described by the following equation (Cuffey and Paterson, 2010),

$$R_g = A_g[P_g - E_g] - B_a \quad (6.10)$$

where  $R_g$  is annual glacier-wide runoff,  $A_g$  is glacier area,  $P_g$  and  $E_g$  are annual precipitation and evaporation on/from glacier surface, and  $B_a$  is annual glacier-wide MB. Groundwater fluxes and changes of stored water within the glacier are assumed negligible here. For a steady state ( $B_a = 0$ ), glacier-wide runoff corresponding to annual precipitation and evaporation over the glacier can be defined as mass-balanced runoff ( $A_g[P_g - E_g]$ ). In other situations ( $B_a =$  positive or negative), the runoff is therefore, imbalanced runoff. The imbalanced runoff from negative glacier-wide MB ( $B_a < 0$ ) can also be defined as glacier-degraded runoff (Thayyen and Gergan, 2010). If the glacier disappears, the catchment would still release certain runoff ( $A[P - E]$ ), and changes in this runoff would solely depend on the precipitation and evaporation. During negative MB years, in addition to balanced runoff, perennial glacier storage also generates glacier-degraded runoff that results in increased glacier melt runoff; on the other hand, during positive MB years, glacier melt runoff decreases as some snow is accumulated on the glacier (Hock, 2005).

On mountain valley glaciers this MB-runoff relationship (more runoff with more negative MBs) may not always be true because of two major reasons: (1) glacier catchments are not completely glacierized and there would always be some runoff as a result of precipitation and evaporation over non-glacierized parts of the catchment contributing to the total runoff at the glacier terminus, and (2) on the ground, runoff is generally measured downstream of the glacier terminus, further increasing the impact of non-glacierized parts on runoff. Therefore, in the case of mountain valley glaciers, the runoff ( $R$ ) at glacier snout or downstream runoff site can be defined as,

$$R = R_g + R_{ng} = A_g[P_g - E_g] - B_a + A_{ng}[P_{ng} - E_{ng}] \quad (6.11)$$

where  $A_{ng}$ , is the non-glacierized area at glacier catchment outlet and  $R_{ng}$ ,  $P_{ng}$  and  $E_{ng}$  are runoff, precipitation and evaporation from the non-glacierized area, respectively. This is a simplified runoff equation and ignores all the sub-surface water fluxes as well as avalanche, snow blowing and refreezing processes.

## 6.4 Results

### 6.4.1 Glacier-wide MBs and annual mass turn over

The mean modelled annual MBs were  $-0.09 \pm 0.35$  m w.e.  $a^{-1}$  and  $-0.12 \pm 0.28$  m w.e.  $a^{-1}$  with cumulative mass wastage of  $-6.33$  m w.e. and  $-8.61$  m w.e. on DBG and CSG over 1950-2020, respectively. The year 1974/75 and 1950/51 showed maximum annual MBs of  $1.24 \pm 0.32$  m w.e. and  $1.03 \pm 0.20$  m w.e., while the year 2015/16 and 2000/01 showed minimum annual MBs of  $-0.95 \pm 0.40$  m w.e. and  $-1.23 \pm 0.33$  m w.e. for DBG and CSG, respectively (Fig. 6.5).

Summer mass balances (SMBs) have been considered from month May to October and April to September while winter mass balances (SMBs) have been considered from November to April and October to March on DBG and CSG catchments, respectively. Modelled seasonal MBs ranged from 0.29 to 1.48 m w.e.  $a^{-1}$  and 0.45 to 1.73 m w.e.  $a^{-1}$  for winter, and  $-1.68$  to  $-0.12$  w.e.  $a^{-1}$  and  $-1.98$  to  $-0.08$  w.e.  $a^{-1}$  for summer on DBG and CSG, respectively (Fig. 6.4). Though the mean annual wastage was almost same on both the glaciers, the annual mass turnover on DBG was smaller with a value of 1.83 m w.e.  $a^{-1}$  (corresponding to a mean winter and summer MBs of 0.87 and  $-0.96$  m w.e.  $a^{-1}$ , respectively) compared to CSG which had a slightly higher annual mass turnover of 2.04 m w.e.  $a^{-1}$  (corresponding to the mean winter and summer MBs of 0.96 and  $-1.08$  m w.e.  $a^{-1}$ , respectively) (Fig. 6.5). Though the difference in annual mass turnovers on both the glaciers is small but it is statistically different ( $p < 0.005$ ), and might be linked with the climate regimes. DBG, in the Monsoon regime, receives a significant amount of accumulation during the summer-monsoon period that limits the mass wastage during the peak melting season (July-September) (Azam and Srivastava, 2020). CSG, in the Alpine regime,

receives its major accumulation during winter months while summer accumulation was very limited (Mandal et al., 2020) consequently has stronger seasonality of accumulation and ablation that result in a higher mass turnover compared to DBG.

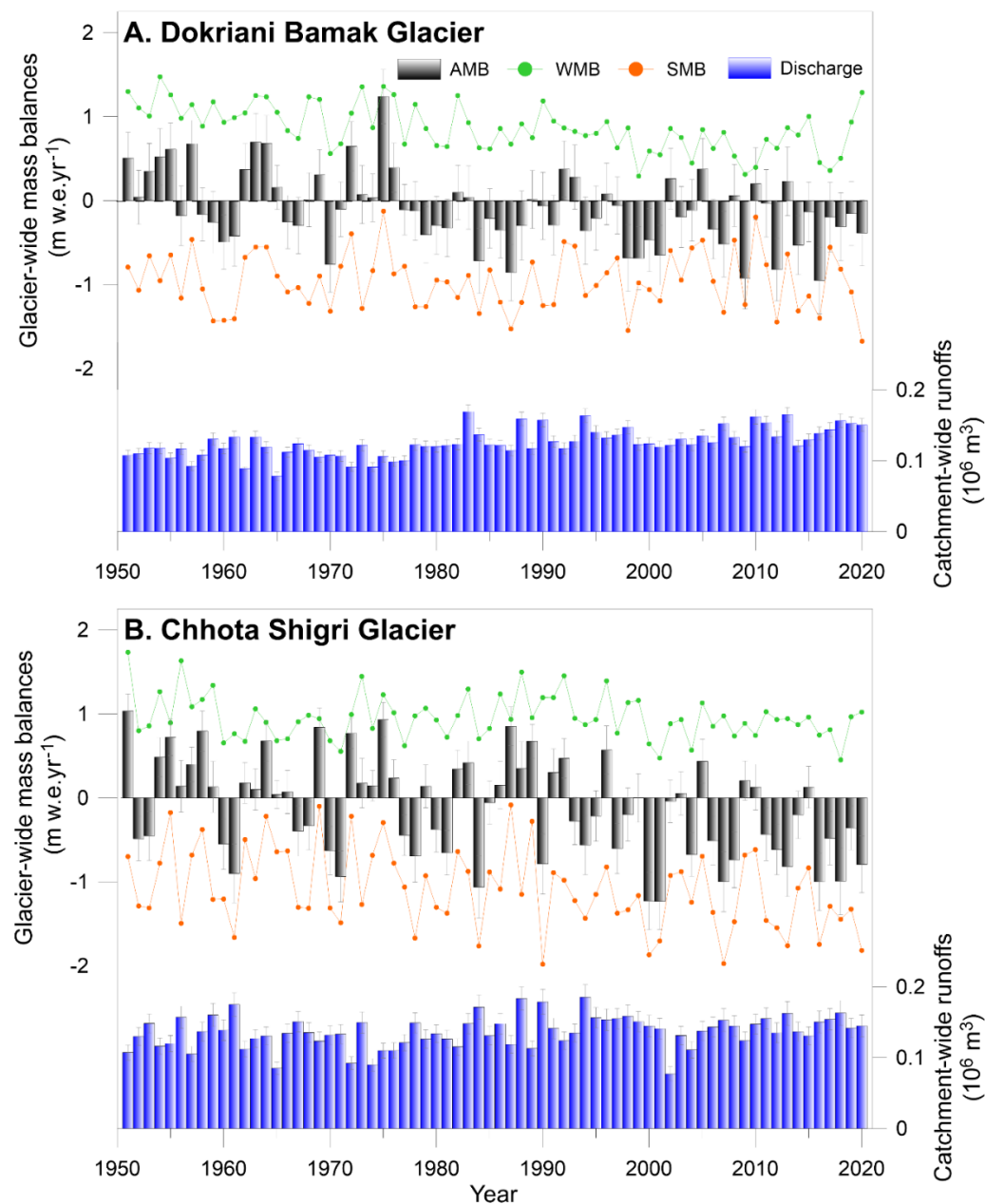


**Figure 6.5:** Annual (black shaded bars), winter (green dots) and summer (orange dots) glacier-wide MBs and annual catchment-wide runoffs on (A) DBG in Monsoon regime and (B) CSG in Alpine regime over 1950-2020. Error bars are showing MBs and runoff uncertainties.

### 6.4.2 Catchment-wide runoffs

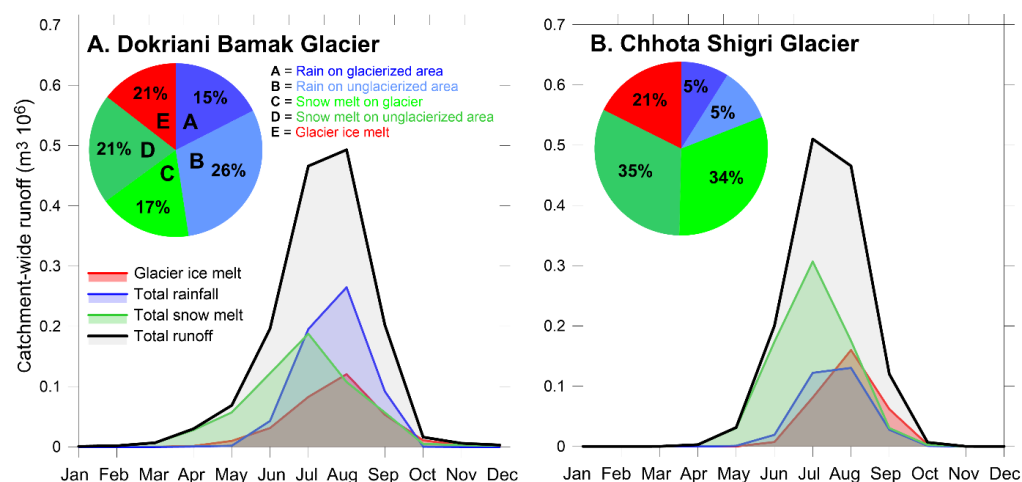
The mean annual catchment-wide runoffs were  $0.13 \pm 0.01 \text{ } 10^6 \text{ m}^3 \text{ a}^{-1}$  and  $0.14 \pm 0.01 \text{ } 10^6 \text{ m}^3 \text{ a}^{-1}$  from DBG and CSG catchments over 1950-2020, respectively (Fig. 6.6). The year 2012/13 and 1993/94 showed maximum annual runoffs of  $0.17 \pm 0.01 \text{ } 10^6 \text{ m}^3$  and  $0.19 \pm 0.02 \text{ m w.e.}$ , while the year 1964/65 and 2000/01 showed similar minimum annual runoffs of  $0.08 \pm 0.01 \text{ } 10^6 \text{ m}^3$  for DBG and CSG, respectively (Fig. 6.6).

Fig. 6.6 shows the mean monthly evolution of glacier-melt, snow-melt, rainfall and total runoffs at both the catchments. Runoffs in the winter months (October to March/April) were negligible in both the catchments. Runoff generation started in March with the inception of snow melt in the DBG catchment and in April in the CSG catchment (Fig. 6.6). Both catchments received rainfall runoff over May-October and glacier-ice melt over June-October. Snow-melt runoff peaked in July, while August experienced the maximum glacier-ice melt and maximum rainfall runoff that resulted in maximum total catchment-wide runoff in August in both the catchments (Fig. 6.6). The glacier-ice melt contribution was almost same with 21% to the total catchment-wide runoff in both DBG and CSG catchments. However, snow melt and rainfall runoff contributions were quite different. DBG catchment generated 41% of rainfall runoff (15% from glacierized and 26% from un-glacierized area) and 38% of snow-melt runoff (17% from glacierized and 21% from un-glacierized area). Conversely, CSG catchment produced only 10% of rainfall runoff (5% from glacierized and 5% from un-glacierized area) and 69% of snow melt runoff (34% from glacier snow melt and 35% from snow melt from un-glacierized area). Thus, the total runoff was dominated by rainfall in the DBG catchment and snow melt in the CSG catchment (Fig. 6.6), in accordance with Monsoon and Alpine regimes, respectively.

### 6.4.3 Glacier-wide MB and catchment-wide runoff patterns

Over the last two-five decades, several studies have modelled the glacier MBs and runoffs at the glacier to basin scales in the Himalaya (Azam et al., 2018; 2021). Present reconstructed glacier-wide MB and catchment-wide runoff in

DBG and CSG catchments since 1950 are the longest known reconstructions in the Himalaya, and allow this study to investigate the MB and runoff patterns over the last seven decades. Three periods were arbitrarily defined in the present study: Period I (1950-1975), Period II (1976-2000) and Period III (2001-2020) (Table 6.4). For each period, the glacier-wide MBs and catchment-wide runoffs were estimated using annual data.



**Figure 6.6:** Mean monthly hydrographs of total runoff and different hydrologic components (snow melt, ice melt and rainfall runoff) for (A) DBG and (B) CSG catchment. Pie charts in inset show the rain on glacierized area, rain on unglacierized area, snow melt on glacier, snow melt on unglacierized area and glacier ice melt.

**Table 6.4:** Annual and seasonal glacier-wide MBs (m w.e. a<sup>-1</sup>) for periods I (1951-1975), II (1976-2000) and III (2001-2020) with their corresponding total catchment-wide runoffs (10<sup>6</sup> m<sup>3</sup> a<sup>-1</sup>).

Period	Dokriani Bamak Glacier				Chhota Shigri Glacier			
	AMB*	SMB <sup>@</sup>	WMB <sup>#</sup>	Runoff	AMB	SMB	WMB	Runoff
1951-1975 (I)	0.16	-0.91	1.07	0.11	0.12	-0.87	0.99	0.13
1976-2000 (II)	-0.21	-1.03	0.82	0.13	-0.11	-1.12	1.02	0.14
2001-2020 (III)	-0.26	-0.94	0.68	0.14	-0.45	-1.29	0.85	0.14
1951-2020	-0.09	-0.96	0.87	0.13	-0.12	-1.08	0.96	0.14

\*AMB = Annual MB, <sup>@</sup>SMB = summer MB and <sup>#</sup>WMB = winter MB.

Period I (1950-1975) showed positive MBs on both DBG (0.16 m w.e. a<sup>-1</sup>) and CSG (0.12 m w.e. a<sup>-1</sup>) corresponding to lowest summer MBs on both the glaciers and, highest and moderate winter MBs on DBG and CSG, respectively (Table 6.4). Period II (1976-2000) experienced moderate mass loss

( $-0.21 \text{ m w.e. a}^{-1}$ ) with the highest summer and moderate winter MBs on DBG, and close-to-balance MB on CSG ( $-0.11 \text{ m w.e. a}^{-1}$ ) with moderate summer and highest winter MBs (Table 6.3). Period III (2001-2020) showed the highest mass wastage on both DBG ( $-0.26 \text{ m w.e. a}^{-1}$ ) and CSG ( $-0.45 \text{ m w.e. a}^{-1}$ ) corresponding to moderate and highest summer MBs, and lowest winter MBs on both the glaciers, respectively (Table 6.4). In agreement with increasing mass loss over the three selected periods, catchment-wide runoffs also increased systematically from 0.11 to  $0.14 \cdot 10^6 \text{ m}^3 \text{ a}^{-1}$  in DBG and 0.13 to  $0.14 \cdot 10^6 \text{ m}^3 \text{ a}^{-1}$  in CSG catchment (Table 6.4).

On DBG, the MB over Period I was statistically different than Period II ( $p = 0.001$ ) and III ( $p = 0.001$ ), while the MBs over Period II and III were statistically similar ( $p = 0.33$ ). Conversely, on CSG, the MBs over Period I and II were statistically similar ( $p = 0.08$ ), and the MBs over Period I and III ( $p = 0.001$ ) and Period II and III ( $p = 0.02$ ) were statistically different. The runoffs over Period I, II and III were statistically different on DBG ( $p < 0.05$ ), while runoff over Period I was statistically different than Period II ( $p = 0.01$ ) and Period III ( $p = 0.04$ ), and period II and III were statistically same ( $p = 0.27$ ) on CSG. Though the arbitrarily selected periods were not always statistically different for MBs and runoffs, but provide a simplified analysis of the 70 years MB and runoff series, and an inter-comparison of DBG and CSG as well as other studies (mostly focusing on pre- and post-2000 periods).

The glacier-wide MB records (in-situ, reconstructed or geodetic) are often available post-1975 with very limited knowledge of glacier behaviour before 1975 (Azam et al., 2018). Previously, a possible close-to-balance state was proposed over the 1990s on both DBG and CSG as well as on Mera Glacier (central Himalaya, Nepal) (Shea et al., 2015b; Azam and Srivastava, 2020). During Period II (1976-2000), the reconstructed moderate and close-to-balance MB wastage on DBG and CSG, respectively is in agreement with the suggested short-term, steady-state over the 1990s. However, with the present 7-decade long reconstruction, it is clear that both the glaciers gained some mass during Period I (1951-1975). The accelerated mass wastage over Period III (2001-2020) observed on DBG and CSG are also in agreement with several remote

sensing as well as modelling studies that suggest a rapid post-2000 mass wastage (Bhattacharya et al., 2016; Maurer et al., 2019; Mandal et al., 2020). Though, present study, together with other studies, suggest a slightly positive MB period (1950-1975), a near-steady state (1976-2000) and an accelerated wastage (post-2020) on DBG and CSG, yet, given the large uncertainties in our study as well as other studies compared here (Shea et al., 2015b; Bhattacharya et al., 2016; Maurer et al., 2019; Azam and Srivastava, 2020) these inferred MB states should be viewed with caution.

## **6.5 Discussion**

### **6.5.1 Glacier MB-runoff relationship in Himalaya: short-term historical data**

In DBG catchment, the MB-runoff relationship was discussed using four years (1994, 1998-2000) of observed annual MBs and mean daily summer runoffs (Fig. 6.7A), and it was surmised that higher catchment-wide runoffs were associated with less negative glacier-wide MBs while lower runoffs with higher negative MBs (Thayyen and Gergan, 2010). Though based on very limited data, this relationship “higher catchment-wide runoff with lower negative or positive MBs and vice versa” was thought to be a characteristic of the ‘Monsoon catchment regime’ where monsoon coincides with peak glacier melt runoff. This idea was further propagated by some other studies (Singh et al., 2016; Kumar et al., 2016).

All possible in-situ data from the literature (Table 6.1) has been collected, and carefully investigated for the MB-runoff relationship on eight glacierized catchments in the Himalaya (Fig. 6.7). DBG, Gara, Neh Nar and Hamtah catchments showed higher runoff at catchment outlets with less negative glacier-wide MBs. Conversely, Tipra Bank, Dunagiri and CSG showed higher runoff with more negative MBs. Shaune Garang catchment showed no relationship between glacier-wide MBs and catchment-wide runoffs (Fig. 6.7B). At the outlet of Shaune Garang Glacier catchment (Alpine catchment regime), the runoff comes from 9 glaciers including Shaune Garang

(Table 6.1) that is compared with the annual MBs of Shaune Garang Glacier. Indeed, in the same climatic settings, the MB behaviour of neighbouring glaciers may be different depending on the local topography and debris cover (Sherpa et al., 2017). Therefore, the comparison of catchment-wide runoff (including runoff from 9 glaciers) with annual glacier-wide MBs of Shaune Garang Glacier is questionable.

Further, Neh Nar and Hamtah glaciers, in the Alpine catchment regime, showed higher runoff with less negative MBs, while Tipra Bank and Dunagiri glaciers, in the Monsoon catchment regime, showed higher runoff with more negative MBs (Fig. 6.7). These examples cannot be explained with the previous explanation of the ‘Monsoon catchment regime’ based on the DBG catchment (Thayyen and Gergan, 2010). As already discussed, (section 2.3), the uncertainties in MBs and runoff measurements are mostly unknown. Strong negative MB ( $-1.43 \text{ m w. e. yr}^{-1}$  during 2000–2012) on Hamtah Glacier was three-times more negative than the estimated geodetic MB ( $-0.45 \pm 0.16 \text{ m w. e. yr}^{-1}$ ; 1999–2011) (Vincent et al., 2013). CSG MB series was the only series which was systematically corrected for area changes and validated against the geodetic MB (Azam et al., 2016). In fact, except for CSG catchment (Alpine catchment regime), the MB-runoff relationships were very weak and insignificant in all other catchments (Fig. 6.7). Such insignificant relationships together with unknown uncertainties in the measurements, make it very difficult to interpret the MB-runoff relationship in the Himalaya using the available short-term, in-situ runoff and MB data. Glaciohydrological models, calibrated using short-term in-situ observations, provide an alternative to understand the long-term MB-runoff relationship. However, the length of in-situ observations plays a critical role for the model calibration; therefore, in-situ measurements should be continued for a long time on a few selected glacierized catchments in the Himalaya (Azam, 2021).

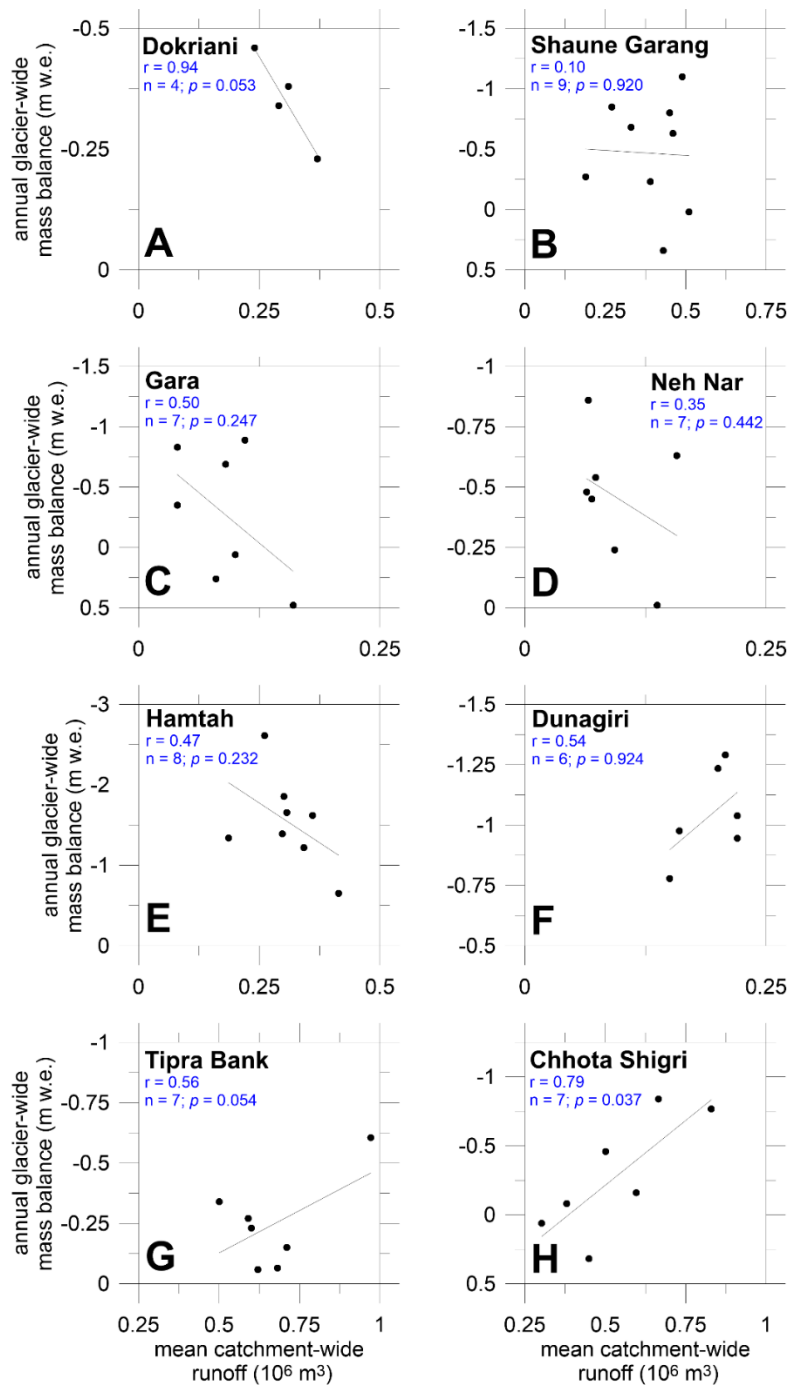


**Figure 6.7:** Relationship between annual glacier-wide MB and mean daily summer runoff at catchment outlet (Table 6.1) for eight glaciers' catchments in the Himalaya. DBG, Shaune Garang, Gara, Neh Nar and Hamtah glaciers (panels A-E) showed higher catchment-wide runoff associated with less negative glacier-wide MBs while Tipra Bank, Dunagiri and CSG (F-H) showed higher catchment-wide runoff with more negative glacier-wide MBs. However, the MB-runoff relationship is significant only on CSG ( $p < 0.05$ ). 'A' stands for alpine and 'M' stands for monsoon catchment regime.

### **6.5.2 Glacier MB-runoff relationship in studied reference catchments: long-term modelled data**

The long-term relationship between MB and runoff was investigated using the modelled annual MB and runoff data (section 4.1 and 4.2). DBG catchment in the Monsoon regime showed a weak but significant correlation ( $r = 0.30$ ;  $p < 0.02$ ) with increasing catchment-wide runoffs corresponding to more negative MBs and vice versa (Fig. 6.8A). The correlation was average in the CSG catchment ( $r = 0.47$ ;  $p < 0.001$ ) (Fig. 6.8B). Unlike, associated challenges with in-situ observations of the runoff (section 5.1), model output also permits to estimate the glacier-wide runoff. The correlations between annual glacier-wide MB and annual glacier-wide runoff on DBG ( $r = 0.53$ ;  $p < 0.001$ ) and CSG ( $r = 0.75$ ;  $p < 0.001$ ) were stronger compared to catchment-wide runoffs (Fig. 6.8). Stronger relationships —with increasing catchment-wide runoffs corresponding to more negative MBs and vice versa— of annual glacier-wide MBs with glacier-wide runoffs compared to catchment-wide runoffs are expected as modelled glacier-wide runoff does not involve the non-glacierized runoff (Fig. 6.8), which is often rainfall or snow melt that has no contribution in the modelled MB. In line, another long-term, model-based study on 6 glaciers of Nuuk region of the Greenland ice sheet (Alpine regime) also showed higher annual glacier-wide runoff accompanying more negative MBs during 1960–2012 (Van As et al., 2014; Singh et al., 2016).

Though the glacierized areas are the same in DBG (44.6%) and CSG (44.7%) catchments (Table 6.1), the weaker MB-runoff relationships in the DBG catchment compared to CSG catchment is probably linked to their climatic regimes. To further investigate the MB-runoff relationship and to understand the functioning of both the catchments, the inter-relationships among MBs (annual, winter and summer), runoffs (glacierized, non-glacierized and catchment-wide) and climatic parameters (annual, winter and summer temperatures and precipitations) were investigated by developing the correlation matrix (Fig. 6.9).

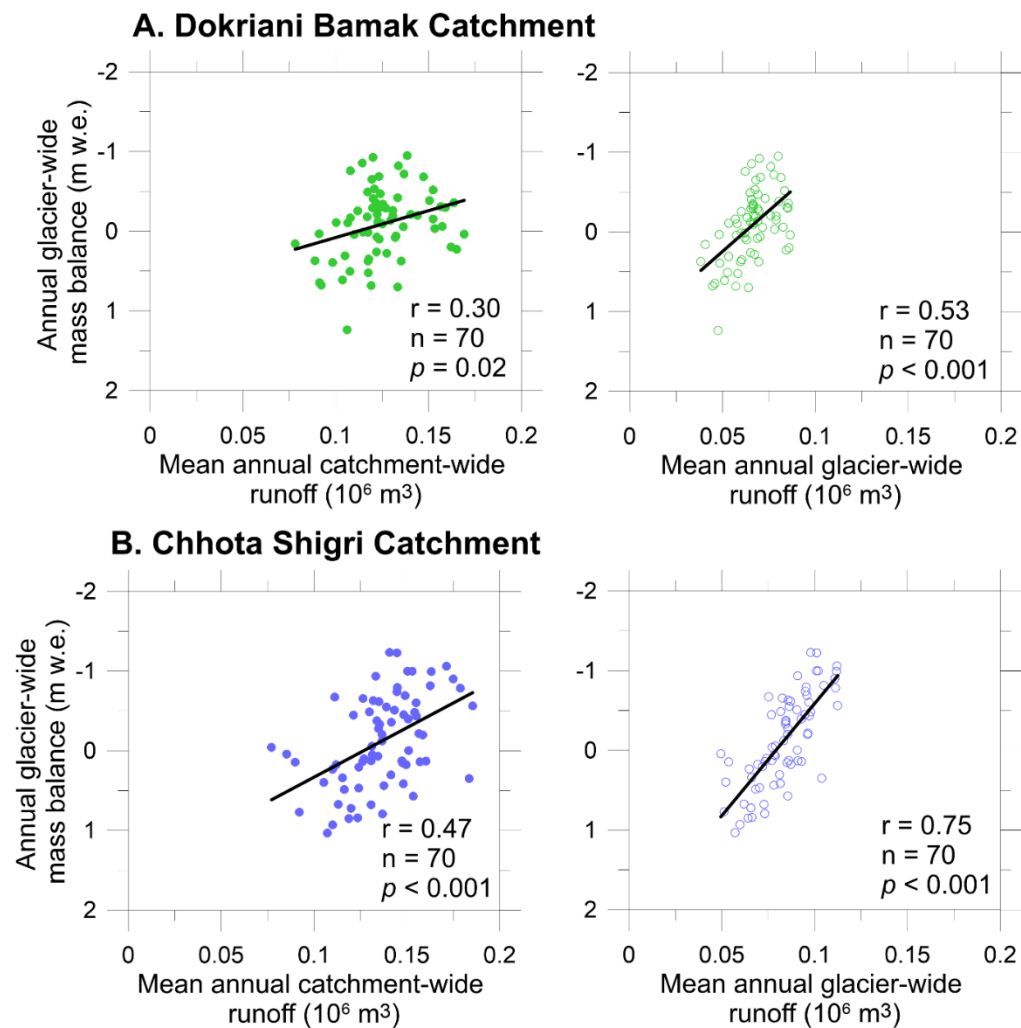


**Figure 6.8:** Relationship between annual glacier-wide MB and annual mean glacier-wide runoff for DBG (A) and SCG (B) catchments.

As expected, annual and seasonal MBs showed negative correlations with the annual and seasonal temperatures in both the catchments; conversely, catchment-wide runoffs showed positive correlations with seasonal and annual temperatures (Fig. 6.9). Annual MBs on DBG showed moderate correlation with winter precipitation ( $r = 0.64$ ) but no significant relationship was found with summer precipitation, while annual MBs on CSG showed moderate correlations with winter ( $r = 0.60$ ) as well as summer ( $r = 0.61$ ) precipitations. On the other hand, catchment-wide runoff in DBG showed weak correlation ( $r = -0.24$ ) with winter precipitation and strong correlation ( $r = 0.85$ ) with summer precipitation, while in CSG catchment, runoff showed no significant correlation

with summer or winter precipitations (Fig. 6.9). This analysis (Fig. 6.8 and 6.9) clearly indicates that the hydrology of the DBG catchment is mainly controlled by the summer precipitation while hydrology in the CSG catchment is mainly controlled by the glacier-wide annual MBs.

The different control of hydrology is because of the different precipitation regimes in both the catchments. DBG, in the Monsoon catchment regime, receives monsoonal rainfall and snowfalls (that often melt quickly due to high summer temperature) that make up a significant runoff contribution; therefore, the catchment hydrology is mainly controlled by the summer precipitation. Conversely, CSG, in the Alpine catchment regime, receives most of the precipitation through snowfall during winter months that contributes to the glacier MB, and then during summer months glacier melt (snow and ice) is generated that contributes to the catchment runoff hence providing a strong relationship between glacier MB and catchment runoff.

Contrasting to the previously suggested MB-runoff relationship in the Monsoon catchment regime (Thayyen and Gergan, 2010), present analysis, based on long-term data, shows that the catchment-wide runoff increases with more negative MBs and vice versa, in agreement with the concept of Hock (2005). However, in line with Thayyen and Gergan (2010), the analysis also suggests that the hydrology of the DBG in the Monsoon catchment regime is mainly controlled by the summer precipitation.

In the CSG catchment, higher annual and seasonal temperatures were negatively correlated with annual and seasonal precipitations, respectively. This is probably due to the moisture holding capacity of the air parcel at higher temperature (Hornberger et al., 2014). In line, the winter temperature was negatively correlated with winter precipitation the DBG catchment, while annual and summer temperatures showed positive correlations with annual and summer precipitations (Fig. 6.9). We could not find any concrete reason for these positive correlations but these may be linked with monsoon dynamics, which is not yet clearly understood (Duan et al., 2004; Mishra, 2015).

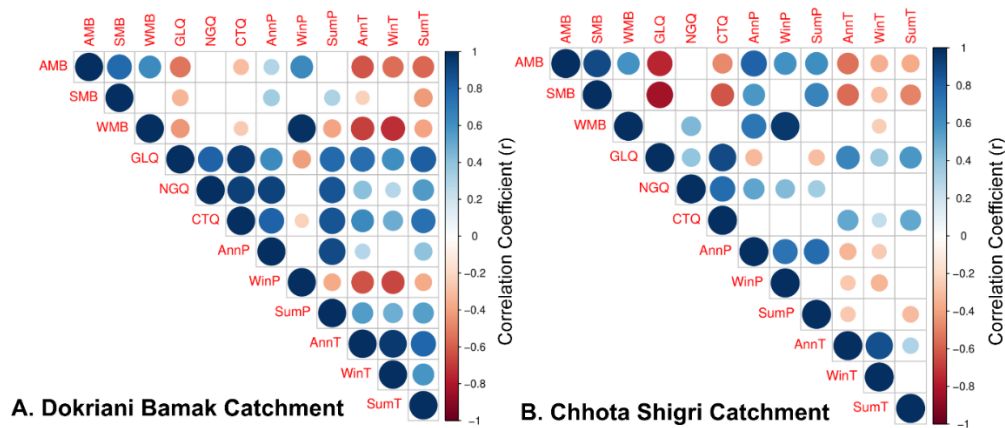


**Figure 6.9:** Correlation matrix for DBG (A) and CSG (B) catchments. Large circles correspond to strong correlations while smaller circles represent weaker correlations. The color scale indicates the sort of correlation (1 denotes completely positive correlation, dark blue, and  $-1$  denotes completely negative correlation, dark red). Only significant correlations are shown ( $P < 0.05$ ). AMB, SMB and WMB = Annual, summer and winter glacier-wide MBs; GLO, NGQ and CTQ = Glacier runoff, non-glacier runoff and catchment runoff; AnnP, WinP and SumP = Annual, winter and summer precipitation sums, and AnnT, WinT and SumT = Annual, winter and summer mean temperatures.

### 6.5.3 Glacier buffer system: glacier-degraded runoff

Glaciers and snow cover act as an important buffer system for downstream rivers by storing snow during accumulation periods whereas producing glacier/snow melt in ablation periods. In order to understand the relative importance of the glacier buffer system in the Monsoon and Alpine catchment regimes of the Himalaya, the glacier-degraded runoffs from DBG and CSG catchments are computed using the modelled annual MB data (Thayyen and Gergan, 2010) (Fig. 6.10). Indeed, the glacier-degraded runoff contribution to catchment runoff is zero for balanced or positive MB years (section 5.2).

Runoff from non-glacierized regions in both the catchments is strongly and moderately correlated with annual precipitation of DBG ( $r = 0.93$ ) and CSG ( $r = 0.52$ ) catchments, respectively and therefore, during dry years non-glacierized runoff drastically reduced (Fig. 6.9). In such dry years, the corresponding negative annual MBs on both the glaciers provided additional glacier-degraded runoff to the catchment stream (Fig. 6.10). For highly negative MB years, glacier-degraded runoff can be quite high. For instance, glacier-

degraded runoffs were as high as 13% (2015/16) and 38% (1999/2000 and 2000/2001) of total catchment-wide runoff on DBG and CSG catchments, respectively (Fig. 6.10). However, the mean annual glacier-degraded runoff was 3% (for negative MB years = 6%) and 10% (for negative MB years = 17%) of total catchment-wide runoff at DBG and CSG catchments over 1951-2020, respectively. Almost three-fold higher contribution of glacier-degraded runoff in the CSG catchment compared to DBG catchment confirms the control of glacier-wide MBs on CSG catchment hydrology, and suggests that the glacier buffer system is more important in the Alpine catchment regime compared to the Monsoon catchment regime, where precipitation mainly controls the catchment-wide runoff (section 5.2). Further, more glacier-degraded runoff from CSG compared to DBG, with almost similar mean annual MBs (section 4.1), again suggests the high mass turn over on CSG compared to DBG (section 4.1).

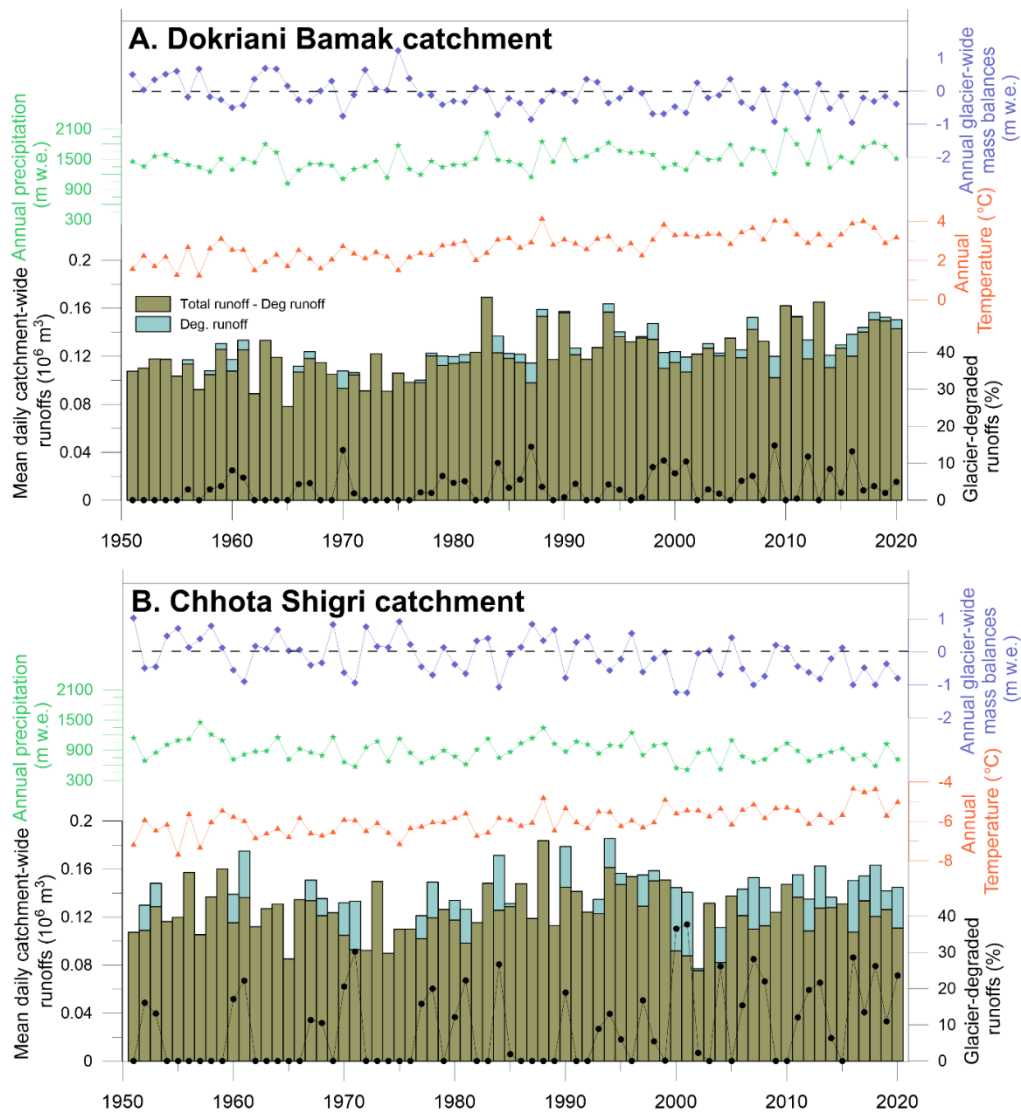


**Figure 6.10:** Relationship between annual glacier-wide MB and mean daily catchment-wide runoffs on Dokriani (DBG) (A) and Chhota Shigri (CSG) (B) catchments. Glacier-degraded runoff % contribution to total catchment-wide runoff is also shown.

### 6.5.4 Hydrological years: daily mean glacier-wide MBs and catchment-wide runoffs

The hydrological year for glacier MB is thought to be starting from the end of summer when the glacier-wide MB is normally close to balance. Following the previous studies (Dobhal et al., 2008; Wagon et al., 2007), the glacier-wide MBs and runoffs in this study were computed for the hydrological year from 1 November to 31 October for the following year on DBG and hydrological year from 1 October to 30 September of the following year on CSG (section 3.2). In

this section, the suitability of aforesaid hydrological years on both the glaciers is discussed. Fig. 6.11 shows the daily mean glacier-wide MBs and catchment-wide runoffs for DBG and CSG for all Julian days (starting from 1 October to 30 September of the next year) estimated from modelled daily MB and runoff data over 1950-2020.

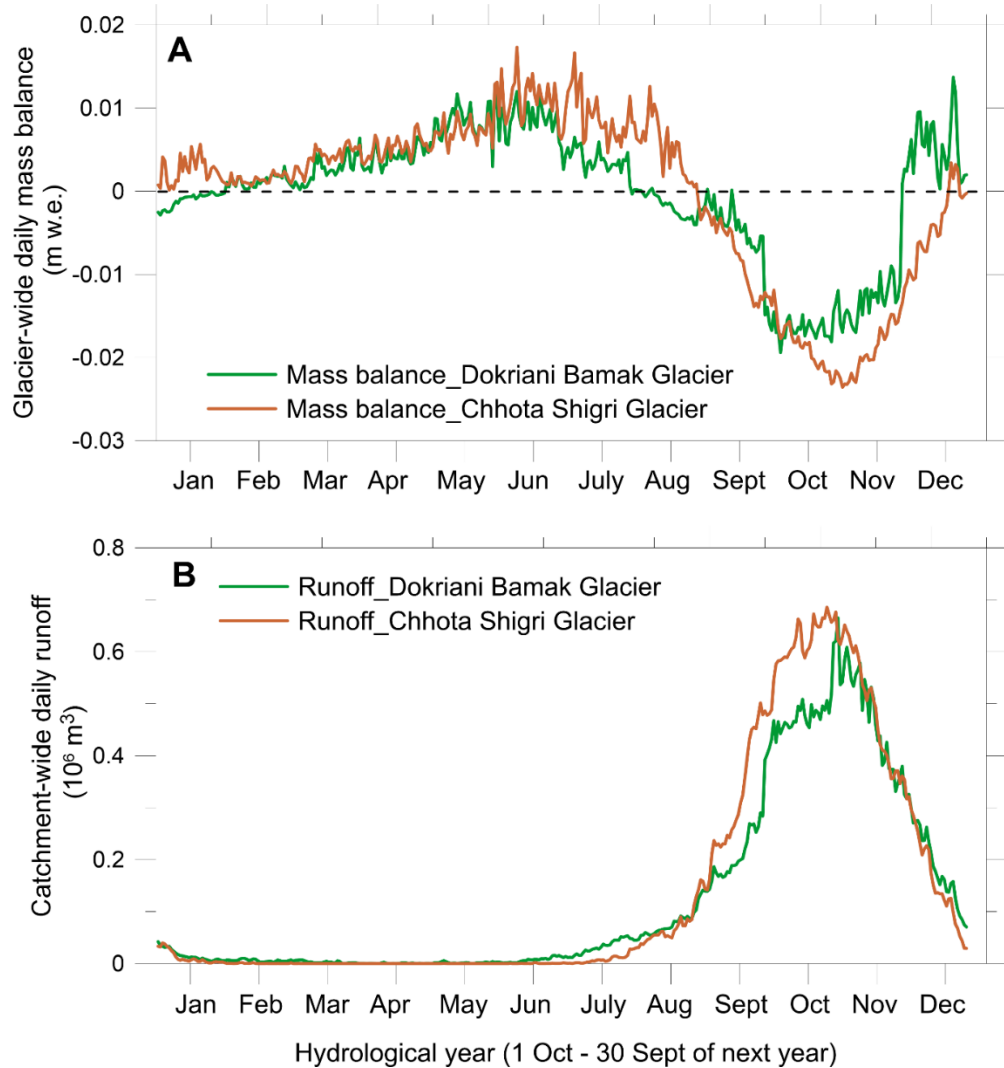


**Figure 6.11:** Panel (A) shows glacier-wide daily mass balances and (B) shows catchment-wide daily runoffs for Dokriani (DBG) and Chhota Shigri (CSG). Hydrological year is defined between 1<sup>st</sup> October to 30 September of next year.

On both DBG and CSG, the daily mean glacier-wide MBs are positive during winter months (October to March) and start decreasing over pre-monsoon (April-May) and become negative during summer-monsoon months (June-September). The transition from positive to negative daily mean MBs

takes place in the month of May on DBG and in June on CSG (Fig. 6.11). On CSG, in accordance with the Alpine regime (winter-accumulation type glacier), the daily mean glacier-wide MBs showed a clear pattern of accumulation (1 October to 31 May) and ablation (1 June to 30 September), justifying the selection of hydrological year from 1 October to 30 September. While on DBG, daily mean glacier-wide MBs subdued as soon as the monsoon arrives in June—that probably provided snow accumulation at high altitudes and rain at lower altitudes with the concurrence of melt season hence reduced daily mean MBs at glacier-wide scale. With the progression of the monsoon, in September when the temperatures are low hence low melting, the daily mean glacier-wide MBs even become positive. However, as soon as the monsoon retreats, the daily mean glacier-wide MBs again become slightly negative in the month of October. Further in November, the temperature is very low and the glacier experiences positive daily MBs. The daily mean glacier-wide MBs pattern on DBG confirms the selection of hydrological year from 1 November to 31 October.

The daily mean catchment-wide runoff hydrographs in both the catchments indicate negligible runoff in winter months from October to mid-April, while almost all runoff is produced in the summer months from mid-April to end-September with a peak in early August (Fig. 6.11). The hydrographs in both the catchments show a sharp rising limb with the progression of the summer season. However, the rising limb of DBG hydrograph is subdued at the arrival of monsoon around the end of June and again shows a sharp rise from mid-August to end-August before an abrupt decrease in September (Fig. 6.11). Though, the runoff commencing dates are different (from mid-April in DBG catchment and from May in CSG catchment), both the catchments show a simultaneous reduction in runoff in September. The reduction in runoff at the arrival of monsoon around end of June followed by a sharp rise in runoff from mid-August in the DBG catchment is probably because of monsoonal snow falls that accumulate in June-July and then due to highest temperatures of August produces strong melt runoff hence a sharp rise. The present study, based on a temperature-index melt model, cannot investigate the physical process

explaining the impact of monsoonal snow falls on runoff generation. However, previous studies, using surface energy balance models, suggested that these summer-monsoon snowfall events increase the glacier surface albedo hence reducing the energy available at glacier surface for melting in the peak ablation period and control the melt production (Fujita, 2008; Mölg et al., 2014; Azam et al., 2014a).

## 6.6 Conclusions

Understanding of the MB-runoff relationship is weak in the Himalaya due to limited in-situ glacier MBs and runoffs measurements. A simplified glacio-hydrological model is used to reconstruct the long-term MBs and runoffs on two small glacierized catchments of DBG and CSG, having similar glacier cover. DBG falls in the Monsoon regime while CSG is in the Alpine regime of the Himalaya. The modelled MBs and runoffs data since 1950 are used to understand the MB patterns as well as MB-runoff relationships in both the catchments.

Over the last seven decades, DBG and CSG show similar, limited mass wastage with mean annual glacier-wide MB of  $-0.09 \pm 0.35$  m w.e.  $a^{-1}$  and  $-0.12 \pm 0.28$  m w.e.  $a^{-1}$ , respectively. Both the glaciers show positive MBs over 1950-1975 and moderate mass loss over 1976-2000, followed by an accelerated mass wastage post-2000. Though the MBs are similar, the mass turn over on CSG is slightly higher than DBG. The mean catchment-wide runoffs are also almost similar  $0.13 \pm 0.01$   $10^6$   $m^3$   $a^{-1}$  and  $0.14 \pm 0.01$   $10^6$   $m^3$   $a^{-1}$  from DBG and CSG catchments, respectively over 1950-2020. The catchment-wide runoff is dominated by rainfall in the DBG catchment and snow melt in the CSG catchment in accordance with Monsoon and Alpine regimes, respectively.

Short-term historical MB and runoff data, available from eight glacierized catchments, do not show any significant MB-runoff relationship except for CSG catchment. Such insignificant relationships and associated unknown uncertainties in in-situ measurements do not allow interpretation of the MB-runoff relationship in the Himalaya using short-term in-situ data. The long-term modelled MB and runoff data on both DBG and CSG catchments

suggests that the higher catchment-wide runoffs correspond to more negative MBs, and *vice versa*, in agreement to Hock (2005). This is in contrast to the previously suggested MB-runoff relationship, based on very limited in-situ data, on DBG (Thayyen and Gergan, 2010). Present long-term analysis suggests that the hydrology of the DBG catchment is mainly dominated by the summer precipitation, while in CSG catchment, it is mainly controlled by the glacier-wide annual MBs. The MB-runoff relationship being different with the adopted glacier runoff definition suggests that the relationship depends on the relative amount of glacierized and non-glacierized runoffs in a catchment. However, it is also stressed that any change in glacier MB will influence the river runoff irrespective of the adopted glacier runoff definition.

The mean annual glacier-degraded runoffs are 3% and 10% of total catchment-wide runoff at DBG and CSG catchments, respectively over 1951-2020. In dry years, the corresponding negative annual MBs on both the glaciers provided additional glacier-degraded runoff to the catchment stream. Higher glacier-degraded runoff in the CSG catchment compared to DBG catchment confirms the control of glacier-wide MBs on catchment hydrology and also suggests that the glacier buffer system is more critical in the Alpine catchment regime compared to the Monsoon catchment regime, where precipitation mainly controls the catchment-wide runoff. The mean daily glacier-wide MB series also confirms the hydrological years used on both the glaciers for in-situ MB measurements.

## Chapter 7

### Conclusions and scope of future work

#### 7.1 Conclusions

Glaciers and snow provide seasonally delayed meltwater. A rapidly expanding literature, mainly the application of glaciohydrological models, has investigated the contribution of meltwater from glaciers and snow to river runoff, impacts of climate change on melt runoff, and future runoff evolution. Several major gaps that existed a decade ago have been partly but incompletely filled—the mapping of glaciers, their surface flow speeds, the shrinking areas and surface downwasting (in some places, growth), and evolution of glacial lakes. In the Indus basin, river runoff is dominated by meltwater because a majority of precipitation comes as snow during winter months. Conversely, in the Ganges and Brahmaputra basins, river runoff is dominated by direct monsoonal rainfall, while melt contributions are relatively small but highly variable from one watershed to the next and can be a very large fraction of flow near the glaciers. Therefore, meltwater has far greater hydrological significance in the Indus basin than the Ganges and Brahmaputra basins. In the Indus basin, generally, glacier melt dominated in the Karakoram while snow melt contributed more than glacier melt to the annual runoffs in the western Himalaya. The melt contribution to river runoff generally depends on the percent of glacierized cover in a basin, yet relative contributions of different runoff components differ largely for the same catchments from different studies, highlighting the discrepancies in the available runoff estimates—a major gap in consensus understanding. The research gaps that are generally overlooked and can yield large uncertainties in glacio-hydrological modelling include glacier area/volume, precipitation distribution, permafrost, sublimation, BC-dust, debris cover over the glaciers, glacier dynamics. The flawed glacier area/volume and precipitation distribution inputs and absence of important processes of sublimation, permafrost thaw, BC/dust-induced melt, debris-cover impact and glacier dynamics in glacio-hydrological modelling produce

inaccurate runoff contributions and hinders projecting reliable future water evolution including total volumes and seasonality in the HK region. Furthermore, improvements can be made in mapping glacial lake growth, lake bathymetry observations, debris-covered glaciers' margins and debris thicknesses, area changes, downwasting rates, and other glacier dynamics that affect water supplies. Existing models ignore many of these parameters and are not fully adequate for quantifying relative uncertainties in the modelled runoff. This stresses the need for an integrated framework including variables involving all these gaps to investigate the relative magnitudes of all identified/discussed uncertainties.

Due to harsh climatic conditions, long-term in-situ glaciological observations are sparse in the Himalaya that hindering an in-depth understanding of the glacier-runoff-climate relationship. The present study investigated the long-term dimensional, mass balance and runoff changes on two climatically diverse glaciers of Dokriani Bamak (central Himalaya) and Chhota Shigri (western Himalaya), where a good amount of in-situ glacio-meteorological data are available from previous studies. The objectives of the study were achieved by exploiting a combination of satellite data, T-index, and SEB models.

T-index modelling was performed over the last seven decades on Dokriani Bamak and Chhota Shigri glaciers to reconstruct the longest mass balance series in the HK using the ERA-reanalysis data. Both the glaciers showed almost similar and limited mass wastage since 1950. Decadal mass balances showed a positive mass balance state over 1950-1980s, slight mass wastage over 1990s, and an accelerated mass wastage post-2000. The results revealed a significant impact of mass balance on satellite data-derived deglaciation and retreat of both the glaciers. The deglaciation and retreat rates were negligible upto 1990 when the glaciers were in almost balanced condition. However, post-2000 period, particularly during 2011-2020, the mass balances became more negative and both Dokriani Bamak and Chhota Shigri glaciers experienced accelerated deglaciation and retreat. The observations also revealed that the impact of mass balance is manifested through dimensional changes on

or within the decadal time-scale. Further, though the mass wastage patterns were similar on both the glaciers, Chhota Shigri Glacier showed consistently lower terminus retreat than the Dokriani Bamak Glacier because of the topographic settings of its snout. The combined effect of shading and thick debris cover resulted in lower terminus retreat of the Chhota Shigri Glacier than Dokriani Bamak Glacier where the snout area is widely open and having a big supraglacial stream. The negative mass balance regime post-2000 period also led to significant reduction in glacier velocity on both the glaciers which, in turn, likely influence the debris growth rates and epi-glacial morphology.

A mass-, and energy-balance model was also developed using the long-term ERA5 reanalysis data since 1979 for Dokriani Bamak and Chhota Shigri glaciers. The in-situ measurements are used to calibrate/validate the developed mass-, and energy-balance model for both the glaciers. The developed model is further used to study the altitudinal patterns of mass balance and surface energy fluxes over both the glaciers. Both the glaciers are losing mass at a moderate rate over 1979-2021. Glacier-wide net shortwave radiation has the dominant control over energy balance followed by longwave net radiation, latent heat flux and sensible heat flux on both the glaciers. Latent heat flux is always negative suggesting glacier-wide sublimation throughout the year except for peak summer-monsoon when it is slightly positive over ablation zone indicating re-sublimation on both the glaciers. Mass-, and energy-balance model is the most sensitive to snow albedo on both the glaciers.

A glacier T-index glaciohydrological model was developed and applied on Dokriani Bamak Glacier catchment for the detailed understanding of mass balance and runoff behaviour since 1979. A similar study was performed on Chhota Shigri Glacier catchment previously (Azam et al., 2019) hence the model was not applied on Chhota Shigri Glacier in the present study. Modelled mass balance on Dokriani Bamak Glacier was moderate over 1979–2018. The heterogeneous debris-cover distribution over lower ablation area (< 5000 m a.s.l.) retards melting and protects the glacier. Rainfall contributed the maximum to the total mean annual runoff in Dokriani Bamak Glacier

catchment. Maximum total runoff is produced during summer-monsoon months, peaking in August corresponding to maximum rainfall runoff, maximum ice melt and high snow melt. Mass balance and runoff are most sensitive to the threshold temperature for melt.

Understanding of the mass balance-runoff relationship is weak in the Himalaya due to limited in-situ glacier mass balance and runoffs measurements. To investigate it, the developed T-index glaciohydrological model is used to reconstruct the long-term mass balances and runoffs on the Dokriani Bamak and Chhota Shigri glacier catchments. The modelled mass balances and runoffs data since 1950 are used to understand the mass balance patterns as well as mass balance-runoff relationships. Both the glaciers show positive mass balances over 1950-1975 and moderate mass loss over 1976-2000, followed by an accelerated mass wastage post-2000. The mean catchment-wide runoffs are also almost similar for both the catchments over 1950-2020. Short-term historical mass balance and runoff data, available from eight glacierized catchments, do not show any significant mass balance-runoff relationship except for Chhota Shigri Glacier catchment. Such insignificant relationships and associated unknown uncertainties in in-situ measurements do not allow interpretation of the mass balance-runoff relationship in the Himalaya using short-term in-situ data. The long-term modelled mass balance and runoff data on both catchments suggest that the higher catchment-wide runoffs correspond to more negative mass balances, and *vice versa*, in agreement to Hock et al. (2005). This contrasts with the previously suggested mass balance-runoff relationship, based on very limited in-situ data, on Dokriani Bamak catchment (Thayyen and Gergan, 2010). Present long-term analysis suggests that the hydrology of the Dokriani Bamak catchment is mainly dominated by the summer precipitation, while in Chhota Shigri catchment, it is mainly controlled by the glacier-wide annual mass balances.

## **7.2 Future scope of work**

The present research work first presents a review of the status of the glaciohydrological studies in the HK and then is mainly devoted to understand

the functioning of two glacierized catchments from different climatic regimes of the Himalaya. These catchment-scale investigations present the dimensional changes, SEB drivers, and mass balance and runoff patterns in Dokrani Bamak and Chhota Shigri glaciers over the last seven decades. Though the detailed glaciohydrological review and analysis on two selected catchments brought several insights about the issues, gaps and functioning of glacierized catchments in the HK, yet, a lot many challenges exist in the field of glaciohydrological modelling of the HK cryosphere. Thus, the following could be the possible future works.

- Future hydrological modelling, including the glacier dynamics, in Dokrani Bamak and Chhota Shigri glacier catchments is required to understand the future runoff patterns in these reference catchments.
- Like this study, more integrated catchment-wide glaciohydrological studies should be developed for other reference catchments from different climatic regimes along with the HK, where some in-situ data is available.
- Most of the SEB studies are available at a point-scale in the ablation area that provides the physical processes for glacier/snow melt. The present work highlights a significant mass loss through sublimation on the selected glaciers that is supported by the detailed review presented in this study. Spatially-designed, dedicated AWSs may be installed in an accumulation area where sublimation amounts are expected to be higher, to understand the sublimation losses. Sublimation estimation through SEB models requires lots of data hence simplified models, parameterizing the sublimation as a function of temperature and wind speed, may be developed that can further be incorporated in large-scale glaciohydrological models.
- Precipitation distribution probably brings the largest uncertainty in the glaciohydrological model output in the HK. Some dedicated studies aiming to understand the spatial distribution of precipitation in different basins should be developed. A first step could be to deploy some pairs

of automatic precipitation gauges at the valley bottom and mountain ridges above glaciers. The generated data can also be used to calibrate the gridded/satellite precipitations.

- Comparison projects for glacier area and volumes should be developed. Studies focusing on permafrost thaw, BC/dust-induced melt, debris-cover impact and glacier dynamics may be developed first at the catchment scale and then at the regional scale. Such advancements would lead to better project with the accurate contribution of different runoff components, future river runoff volumes and their seasonality shift. Prospective solutions for rapid progress may come from satellite remote sensing data, including InSAR, GRACE, high-resolution DEMs and in-situ geophysical surveys.
- Finally, an integrated, interdisciplinary approach is sorely needed to understand the sensitivities of the natural ecosystem and wildlands biodiversity to coupled climate, glacier, and hydrological change.

## REFERENCES

- Acharya, A. and Kayastha, R.B., 2019. Mass and energy balance estimation of Yala glacier (2011–2017), Langtang valley, Nepal. *Water*, 11(1), p.6.
- Ahluwalia, R.S., Rai, S.P., Jain, S.K., Kumar, B. and Dobhal, D.P., 2013. Assessment of snowmelt runoff modelling and isotope analysis: a case study from the western Himalaya, India. *Annals of glaciology*, 54(62), pp.299-304.
- Andermann, C., Longuevergne, L., Bonnet, S., Crave, A., Davy, P. and Gloaguen, R., 2012. Impact of transient groundwater storage on the discharge of Himalayan rivers. *Nature geoscience*, 5(2), pp.127-132.
- Anderson, B., Mackintosh, A., Stumm, D., George, L., Kerr, T., Winter-Billington, A. and Fitzsimons, S., 2010. Climate sensitivity of a high-precipitation glacier in New Zealand. *Journal of Glaciology*, 56(195), pp.114-128.
- Anslow, F.S., Hostetler, S., Bidlake, W.R. and Clark, P.U., 2008. Distributed energy balance modeling of South Cascade Glacier, Washington and assessment of model uncertainty. *Journal of Geophysical Research: Earth Surface*, 113(F2).
- Armstrong, R.L., Rittger, K., Brodzik, M.J., Racoviteanu, A., Barrett, A.P., Khalsa, S.J.S., Raup, B., Hill, A.F., Khan, A.L., Wilson, A.M. and Kayastha, R.B., 2019. Runoff from glacier ice and seasonal snow in High Asia: separating melt water sources in river flow. *Regional Environmental Change*, 19(5), pp.1249-1261.
- Azam, M.F. and Srivastava, S., 2020. Mass balance and runoff modelling of partially debris-covered Dokriani Glacier in monsoon-dominated Himalaya using ERA5 data since 1979. *Journal of Hydrology*, 590, p.125432.
- Azam, M.F., Kargel, J.S., Shea, J.M., Nepal, S., Haritashya, U.K., Srivastava, S., Maussion, F., Qazi, N., Chevallier, P., Dimri, A.P. and Kulkarni,

- A.V., 2021. Glaciohydrology of the Himalaya-Karakoram. Science.
- Azam, M.F., Ramanathan, A.L., Wagnon, P., Vincent, C., Linda, A., Berthier, E., Sharma, P., Mandal, A., Angchuk, T., Singh, V.B. and Pottakkal, J.G., 2016. Meteorological conditions, seasonal and annual mass balances of Chhota Shigri Glacier, western Himalaya, India. *Annals of Glaciology*, 57(71), pp.328-338.
- Azam, M.F., Wagnon, P., Berthier, E., Vincent, C., Fujita, K. and Kargel, J.S., 2018. Review of the status and mass changes of Himalayan-Karakoram glaciers. *Journal of Glaciology*, 64(243), pp.61-74.
- Azam, M.F., Wagnon, P., Ramanathan, A., Vincent, C., Sharma, P., Arnaud, Y., Linda, A., Pottakkal, J.G., Chevallier, P., Singh, V.B. and Berthier, E., 2012. From balance to imbalance: a shift in the dynamic behaviour of Chhota Shigri glacier, western Himalaya, India. *Journal of Glaciology*, 58(208), pp.315-324.
- Azam, M.F., Wagnon, P., Vincent, C., Ramanathan, A., Linda, A. and Singh, V.B., 2014b. Reconstruction of the annual mass balance of Chhota Shigri glacier, Western Himalaya, India, since 1969. *Annals of Glaciology*, 55(66), pp.69-80.
- Azam, M.F., Wagnon, P., Vincent, C., Ramanathan, A.L., Favier, V., Mandal, A. and Pottakkal, J.G., 2014a. Processes governing the mass balance of Chhota Shigri Glacier (western Himalaya, India) assessed by point-scale surface energy balance measurements. *The Cryosphere*, 8(6), pp.2195-2217.
- Azam, M.F., Wagnon, P., Vincent, C., Ramanathan, A.L., Kumar, N., Srivastava, S., Pottakkal, J.G. and Chevallier, P., 2019. Snow and ice melt contributions in a highly glacierized catchment of Chhota Shigri Glacier (India) over the last five decades. *Journal of Hydrology*, 574, pp.760-773.
- Bahuguna, I.M., Rathore, B.P., Brahmabhatt, R., Sharma, M., Dhar, S., Randhawa, S.S., Kumar, K., Romshoo, S., Shah, R.D., Ganjoo, R.K. and

- Ajai, 2014. Are the Himalayan glaciers retreating?. *Current science*, pp.1008-1013.
- Bajracharya, S.R. and Shrestha, B.R., 2011. The status of glaciers in the Hindu Kush-Himalayan region. International Centre for Integrated Mountain Development (ICIMOD).
- Bandyopadhyay, D., Singh, G. and Kulkarni, A.V., 2019. Spatial distribution of decadal ice-thickness change and glacier stored water loss in the Upper Ganga basin, India during 2000–2014. *Scientific reports*, 9(1), pp.1-9.
- Banerjee, A. and Azam, M.F., 2016. Temperature reconstruction from glacier length fluctuations in the Himalaya. *Annals of Glaciology*, 57(71), pp.189-198.
- Banerjee, A. and Shankar, R., 2013. On the response of Himalayan glaciers to climate change. *Journal of Glaciology*, 59(215), pp.480-490.
- Banerjee, A., 2017. Brief communication: Thinning of debris-covered and debris-free glaciers in a warming climate. *The Cryosphere*, 11(1), pp.133-138.
- Banerjee, A., Patil, D. and Jadhav, A., 2020. Possible biases in scaling-based estimates of glacier change: a case study in the Himalaya. *The Cryosphere*, 14(9), pp.3235-3247.
- Basnett, S., Kulkarni, A.V. and Bolch, T., 2013. The influence of debris cover and glacial lakes on the recession of glaciers in Sikkim Himalaya, India. *Journal of Glaciology*, 59(218), pp.1035-1046.
- Benn, D.I. and Evans, D.J.A., 2010. *Glaciers and Glaciation*. Hodder Education. London, UK, 802.
- Bergström, S., 1976. Development and application of a conceptual runoff model for Scandinavian catchments.
- Berthier, É. and Brun, F., 2019. Karakoram geodetic glacier mass balances between 2008 and 2016: persistence of the anomaly and influence of a large rock avalanche on Siachen Glacier. *Journal of Glaciology*, 65(251), pp.494-507.

- Berthier, E., Arnaud, Y., Kumar, R., Ahmad, S., Wagnon, P. and Chevallier, P., 2007. Remote sensing estimates of glacier mass balances in the Himachal Pradesh (Western Himalaya, India). *Remote Sensing of Environment*, 108(3), pp.327-338.
- Beven, K. and Freer, J., 2001. Equifinality, data assimilation, and uncertainty estimation in mechanistic modelling of complex environmental systems using the GLUE methodology. *Journal of hydrology*, 249(1-4), pp.11-29.
- Beven, K., 2006. A manifesto for the equifinality thesis. *Journal of hydrology*, 320(1-2), pp.18-36.
- Bhambri, R. and Bolch, T., 2009. Glacier mapping: a review with special reference to the Indian Himalayas. *Progress in Physical Geography*, 33(5), pp.672-704.
- Bhambri, R., Bolch, T., Chaujar, R.K. and Kulshreshtha, S.C., 2011. Glacier changes in the Garhwal Himalaya, India, from 1968 to 2006 based on remote sensing. *Journal of Glaciology*, 57(203), pp.543-556.
- Bhambri, R., Watson, C.S., Hewitt, K., Haritashya, U.K., Kargel, J.S., Shahi, A.P., Chand, P., Kumar, A., Verma, A. and Govil, H., 2020. The hazardous 2017–2019 surge and river damming by Shispare Glacier, Karakoram. *Scientific reports*, 10(1), pp.1-14.
- Bhattacharya, A., Bolch, T., Mukherjee, K., Pieczonka, T., Kropáček, J.A.N. and Buchroithner, M.F., 2016. Overall recession and mass budget of Gangotri Glacier, Garhwal Himalayas, from 1965 to 2015 using remote sensing data. *Journal of Glaciology*, 62(236), pp.1115-1133
- Bhutiyan, M.R., Kale, V.S. and Pawar, N.J., 2010. Climate change and the precipitation variations in the northwestern Himalaya: 1866–2006. *International Journal of Climatology: A Journal of the Royal Meteorological Society*, 30(4), pp.535-548.
- Biemans, H., Siderius, C., Lutz, A.F., Nepal, S., Ahmad, B., Hassan, T., von Bloh, W., Wijngaard, R.R., Wester, P., Shrestha, A.B. and Immerzeel,

- W.W., 2019. Importance of snow and glacier meltwater for agriculture on the Indo-Gangetic Plain. *Nature Sustainability*, 2(7), pp.594-601.
- Biskaborn, B.K., Smith, S.L., Noetzli, J., Matthes, H., Vieira, G., Streletskiy, D.A., Schoeneich, P., Romanovsky, V.E., Lewkowicz, A.G., Abramov, A. and Allard, M., 2019. Permafrost is warming at a global scale, *Nature Communications*, 10, 264.
- Bocchiola, D., Diolaiuti, G., Soncini, A., Mihalcea, C., D'agata, C., Mayer, C., Lambrecht, A., Rosso, R. and Smiraglia, C., 2011. Prediction of future hydrological regimes in poorly gauged high altitude basins: the case study of the upper Indus, Pakistan. *Hydrology and Earth System Sciences*, 15(7), pp.2059-2075.
- Bøggild, C.E., Knudby, C.J., Knudsen, M.B. and Starzer, W., 1999. Snowmelt and runoff modelling of an Arctic hydrological basin in west Greenland. *Hydrological Processes*, 13(12-13), pp.1989-2002.
- Bolch, T., Buchroithner, M., Pieczonka, T. and Kunert, A., 2008. Planimetric and volumetric glacier changes in the Khumbu Himal, Nepal, since 1962 using Corona, Landsat TM and ASTER data. *Journal of Glaciology*, 54(187), pp.592-600.
- Bolch, T., Kulkarni, A., Kääh, A., Huggel, C., Paul, F., Cogley, J.G., Frey, H., Kargel, J.S., Fujita, K., Scheel, M. and Bajracharya, S., 2012. The state and fate of Himalayan glaciers. *Science*, 336(6079), pp.310-314.
- Bolch, T., Pieczonka, T. and Benn, D.I., 2011. Multi-decadal mass loss of glaciers in the Everest area (Nepal Himalaya) derived from stereo imagery. *The Cryosphere*, 5(2), pp.349-358.
- Bolch, T., Pieczonka, T., Mukherjee, K. and Shea, J., 2017. Brief communication: Glaciers in the Hunza catchment (Karakoram) have been nearly in balance since the 1970s. *The Cryosphere*, 11(1), pp.531-539. doi:10.5194/tc-11-531-2017
- Bolch, T., Shea, J.M., Liu, S., Azam, F.M., Gao, Y., Gruber, S., Immerzeel, W.W., Kulkarni, A., Li, H., Tahir, A.A. and Zhang, G., 2019. Status and

- change of the cryosphere in the extended Hindu Kush Himalaya region. In *The Hindu Kush Himalaya Assessment* (pp. 209-255). Springer, Cham.
- Bolch, T., Yao, T., Kang, S., Buchroithner, M.F., Scherer, D., Maussion, F., Huintjes, E. and Schneider, C., 2010. A glacier inventory for the western Nyainqentanglha Range and the Nam Co Basin, Tibet, and glacier changes 1976–2009. *The Cryosphere*, 4(3), pp.419-433.
- Bookhagen, B. and Burbank, D.W., 2006. Topography, relief, and TRMM-derived rainfall variations along the Himalaya. *Geophysical Research Letters*, 33(8).
- Bookhagen, B. and Burbank, D.W., 2010. Toward a complete Himalayan hydrological budget: Spatiotemporal distribution of snowmelt and rainfall and their impact on river discharge. *Journal of Geophysical Research: Earth Surface*, 115(F3).
- Boori, M.S., Vozenilek, V. and Balzter, H., 2014. Satellite datasets and their scaling factor for land surface temperature. *J Geol Geosci*, 3, pp.01-02.
- Boral, S. and Sen, I.S., 2020. Tracing ‘Third Pole’ ice meltwater contribution to the Himalayan rivers using oxygen and hydrogen isotopes. *Geochem. Perspect. Lett*, 13, pp.48-53.
- Brahmbhatt, R.M., Bahuguna, I.M., Rathore, B.P., Kulkarni, A.V., Shah, R.D., Rajawat, A.S. and Kargel, J.S., 2017. Significance of glaciomorphological factors in glacier retreat: a case study of part of Chenab basin, Himalaya. *Journal of Mountain Science*, 14(1), pp.128-141.
- Braithwaite, R.J. and Raper, S.C., 2007. Glaciological conditions in seven contrasting regions estimated with the degree-day model. *Annals of Glaciology*, 46, pp.297-302.
- Braithwaite, R.J., 2002. Glacier mass balance: the first 50 years of international monitoring. *Progress in Physical Geography*, 26(1), pp.76-95.
- Braithwaite, R.J., Raper, S.C. and Chutko, K., 2006. Accumulation at the equilibrium-line altitude of glaciers inferred from a degree-day model

- and tested against field observations. *Annals of Glaciology*, 43, pp.329-334.
- Brock, B.W. and Arnold, N.S., 2000. A spreadsheet-based (Microsoft Excel) point surface energy balance model for glacier and snow melt studies. *Earth Surface Processes and Landforms*, 25(6), pp.649-658.
- Brown, M.E., Racoviteanu, A.E., Tarboton, D.G., Gupta, A.S., Nigro, J., Policelli, F., Habib, S., Tokay, M., Shrestha, M.S., Bajracharya, S. and Hummel, P., 2014. An integrated modeling system for estimating glacier and snow melt driven streamflow from remote sensing and earth system data products in the Himalayas. *Journal of Hydrology*, 519, pp.1859-1869.
- Brun, F., Berthier, E., Wagnon, P., Kääb, A. and Treichler, D., 2017. A spatially resolved estimate of High Mountain Asia glacier mass balances from 2000 to 2016. *Nature geoscience*, 10(9), pp.668-673.
- Brun, F., Dumont, M., Wagnon, P., Berthier, E., Azam, M.F., Shea, J.M., Sirguey, P., Rabatel, A. and Ramanathan, A., 2015. Seasonal changes in surface albedo of Himalayan glaciers from MODIS data and links with the annual mass balance. *The Cryosphere*, 9(1), pp.341-355.
- Burns, P. and Nolin, A., 2014. Using atmospherically-corrected Landsat imagery to measure glacier area change in the Cordillera Blanca, Peru from 1987 to 2010. *Remote Sensing of Environment*, 140, pp.165-178.
- Chand, P. and Sharma, M.C., 2015. Glacier changes in the Ravi basin, North-Western Himalaya (India) during the last four decades (1971–2010/13). *Global and Planetary Change*, 135, pp.133-147.
- Chandrasekharan, A., Ramsankaran, R.A.A.J., Pandit, A. and Rabatel, A., 2018. Quantification of annual glacier surface mass balance for the Chhota Shigri Glacier, Western Himalayas, India using an Equilibrium-Line Altitude (ELA) based approach. *International Journal of Remote Sensing*, 39(23), pp.9092-9112.

- Cogley, J.G., 2011. Present and future states of Himalaya and Karakoram glaciers. *Annals of Glaciology*, 52(59), pp.69-73.
- Cogley, J.G., 2016. Glacier shrinkage across High Mountain Asia. *Annals of Glaciology*, 57(71), pp.41-49.
- Collier, E., Mölg, T., Maussion, F., Scherer, D., Mayer, C. and Bush, A.B.G., 2013. High-resolution interactive modelling of the mountain glacier–atmosphere interface: an application over the Karakoram. *The Cryosphere*, 7(3), pp.779-795.
- Copernicus Climate Change Service Climate Data Store, 2017. Copernicus Climate Change Service (C3 S) (2017): ERA5: Fifth generation of ECMWF atmospheric reanalyses of the global climate. date of access. <https://cds.climate.copernicus.eu/cdsapp#!/home>.
- Cuffey, K.M. and Paterson, W.S.B., 2010. *The physics of glaciers*. Academic Press.
- Das, S. and Sharma, M.C., 2019. Glacier changes between 1971 and 2016 in the Jankar Chhu Watershed, Lahaul Himalaya, India. *Journal of Glaciology*, 65(249), pp.13-28.
- Dashora, A., Lohani, B. and Malik, J.N., 2007. A repository of earth resource information–CORONA satellite programme. *Current Science*, pp.926-932.
- Datt, P., Srivastava, P.K., Negi, P.S. and Satyawali, P.K., 2008. Surface energy balance of seasonal snow cover for snow-melt estimation in NW Himalaya. *Journal of earth system science*, 117(5), pp.567-573.
- de Kok, R.J., Tuinenburg, O.A., Bonekamp, P.N. and Immerzeel, W.W., 2018. Irrigation as a potential driver for anomalous glacier behavior in High Mountain Asia. *Geophysical research letters*, 45(4), pp.2047-2054.
- Dehecq, A., Gourmelen, N., Gardner, A.S., Brun, F., Goldberg, D., Nienow, P.W., Berthier, E., Vincent, C., Wagnon, P. and Trouvé, E., 2019. Twenty-first century glacier slowdown driven by mass loss in High Mountain Asia. *Nature Geoscience*, 12(1), pp.22-27.

- Denby, B. and Greuell, W., 2000. The use of bulk and profile methods for determining surface heat fluxes in the presence of glacier winds. *Journal of Glaciology*, 46(154), pp.445-452.
- Devkota, L.P. and Gyawali, D.R., 2015. Impacts of climate change on hydrological regime and water resources management of the Koshi River Basin, Nepal. *Journal of Hydrology: Regional Studies*, 4, pp.502-515.
- Dimri, A.P. and Dash, S.K., 2012. Wintertime climatic trends in the western Himalayas. *Climatic Change*, 111(3), pp.775-800.
- Dimri, A.P., 2004. Impact of horizontal model resolution and orography on the simulation of a western disturbance and its associated precipitation. *Meteorological Applications*, 11(2), pp.115-127.
- Dimri, A.P., Niyogi, D., Barros, A.P., Ridley, J., Mohanty, U.C., Yasunari, T. and Sikka, D.R., 2015. Western disturbances: a review. *Reviews of Geophysics*, 53(2), pp.225-246.
- Dimri, A.P., Yasunari, T., Kotlia, B.S., Mohanty, U.C. and Sikka, D.R., 2016. Indian winter monsoon: Present and past. *Earth-science reviews*, 163, pp.297-322.
- Dobhal, D.P. and Mehta, M., 2010. Surface morphology, elevation changes and terminus retreat of Dokriani Glacier, Garhwal Himalaya: implication for climate change. *Himalayan Geology*, 31(1), pp.71-78.
- Dobhal, D.P., Gergan, J.T. and Thayyen, R.J., 2004. Recession and morphogeometrical changes of Dokriani glacier (1962-1995) Garhwal Himalaya, India. *CURRENT SCIENCE-BANGALORE-*, 86(5), pp.692-696.
- Dobhal, D.P., Gergan, J.T. and Thayyen, R.J., 2008. Mass balance studies of the Dokriani Glacier from to, Garhwal Himalaya, India. *Bulletin of glaciological research*, 25, pp.9-17.

- Dobhal, D.P., Pratap, B., Bhambri, R. and Mehta, M., 2021. Mass balance and morphological changes of Dokriani Glacier (1992–2013), Garhwal Himalaya, India. *Quaternary Science Advances*, p.100033.
- Doblas-Reyes, F.J., Sorensson, A.A., Almazroui, M., Dosio, A., Gutowski, W.J., Haarsma, R., Hamdi, R., Hewitson, B., Kwon, W.T., Lamptey, B.L. and Maraun, D., 2021. Linking global to regional climate change.
- Dong, B., Wilcox, L.J., Highwood, E.J. and Sutton, R.T., 2019. Impacts of recent decadal changes in Asian aerosols on the East Asian summer monsoon: Roles of aerosol–radiation and aerosol–cloud interactions. *Climate Dynamics*, 53(5), pp.3235-3256.
- Duan, K., Yao, T. and Thompson, L.G., 2004. Low-frequency of southern Asian monsoon variability using a 295-year record from the Dasuopu ice core in the central Himalayas. *Geophysical Research Letters*, 31(16).
- Eeckman, J., Chevallier, P., Boone, A., Neppel, L., Rouw, A.D., Delclaux, F. and Koirala, D., 2017. Providing a non-deterministic representation of spatial variability of precipitation in the Everest region. *Hydrology and Earth System Sciences*, 21(9), pp.4879-4893.
- Eeckman, J., Nepal, S., Chevallier, P., Camensuli, G., Delclaux, F., Boone, A. and De Rouw, A., 2019. Comparing the ISBA and J2000 approaches for surface flows modelling at the local scale in the Everest region. *Journal of Hydrology*, 569, pp.705-719.
- Engelhardt, M., Ramanathan, A.L., Eidhammer, T., Kumar, P., Landgren, O., Mandal, A. and Rasmussen, R.O.Y., 2017. Modelling 60 years of glacier mass balance and runoff for Chhota Shigri Glacier, Western Himalaya, Northern India. *Journal of Glaciology*, 63(240), pp.618-628.
- Farinotti, D., Immerzeel, W.W., De Kok, R.J., Quincey, D.J. and Dehecq, A., 2020. Manifestations and mechanisms of the Karakoram glacier Anomaly, *Nat. Geosci.*, 13, 8–16.
- Favier, V., Wagnon, P., Chazarin, J.P., Maisincho, L. and Coudrain, A., 2004. One-year measurements of surface heat budget on the ablation zone of

- Antizana Glacier 15, Ecuadorian Andes. *Journal of Geophysical Research: Atmospheres*, 109(D18).
- Fowler, H.J. and Archer, D.R., 2005. Hydro-climatological variability in the Upper Indus Basin and implications for water resources. *Regional Hydrological Impacts of Climatic Change: Impact Assessment and Decision Making*.
- Frenierre, J.L. and Mark, B.G., 2014. A review of methods for estimating the contribution of glacial meltwater to total watershed discharge. *Progress in Physical Geography*, 38(2), pp.173-200.
- Frey, H., Machguth, H., Huss, M., Huggel, C., Bajracharya, S., Bolch, T., Kulkarni, A., Linsbauer, A., Salzmann, N. and Stoffel, M., 2014. Estimating the volume of glaciers in the Himalayan–Karakoram region using different methods. *The Cryosphere*, 8(6), pp.2313-2333.
- Fujita, K. and Ageta, Y., 2000. Effect of summer accumulation on glacier mass balance on the Tibetan Plateau revealed by mass-balance model. *Journal of Glaciology*, 46(153), pp.244-252.
- Fujita, K. and Sakai, A., 2014. Modelling runoff from a Himalayan debris-covered glacier. *Hydrology and Earth System Sciences*, 18(7), pp.2679-2694.
- Fujita, K., 2008. Effect of precipitation seasonality on climatic sensitivity of glacier mass balance. *Earth and Planetary Science Letters*, 276(1-2), pp.14-19.
- Fujita, K., Sakai, A., Takenaka, S., Nuimura, T., Surazakov, A.B., Sawagaki, T. and Yamanokuchi, T., 2013. Potential flood volume of Himalayan glacial lakes. *Natural Hazards and Earth System Sciences*, 13(7), pp.1827-1839.
- Fujita, K., Takeuchi, N., Nikitin, S.A., Surazakov, A.B., Okamoto, S., Aizen, V.B. and Kubota, J., 2011. Favorable climatic regime for maintaining the present-day geometry of the Gregoriev Glacier, Inner Tien Shan. *The Cryosphere*, 5(3), pp.539-549.

- Gadgil, S., Vinayachandran, P.N. and Francis, P.A., 2003. Droughts of the Indian summer monsoon: Role of clouds over the Indian Ocean. *Current Science*, pp.1713-1719.
- Gantayat, P., Kulkarni, A.V., Srinivasan, J. and Schmeits, M.J., 2017. Numerical modelling of past retreat and future evolution of Chhota Shigri glacier in Western Indian Himalaya. *Annals of Glaciology*, 58(75pt2), pp.136-144.
- Gardelle, J., Berthier, E. and Arnaud, Y., 2012. Slight mass gain of Karakoram glaciers in the early twenty-first century. *Nature geoscience*, 5(5), pp.322-325.
- Gardelle, J., Berthier, E., Arnaud, Y. and Kääb, A., 2013. Region-wide glacier mass balances over the Pamir-Karakoram-Himalaya during 1999–2011. *The Cryosphere*, 7(4), pp.1263-1286.
- Gardner, A.S., Moholdt, G., Cogley, J.G., Wouters, B. and Arendt, A.A., Wahr, J., Berthier E. Hock R, Pfeffer WT, Kaser G, Ligtenberg SRM, Bolch T, Sharp MJ, Hagen JO, van den Broeke MR, Paul F (2013) A Reconciled Estimate of Glacier Contributions to Sea Level Rise: 2003 to 2009. *Science*, 340, pp.6134.
- Garg, P.K., Garg, S., Yousuf, B., Shukla, A., Kumar, V. and Mehta, M., 2021b. Stagnation of the Pensilungpa glacier, western Himalaya, India: causes and implications. *Journal of Glaciology*, pp.1-15.
- Garg, P.K., Shukla, A. and Jasrotia, A.S., 2017b. Influence of topography on glacier changes in the central Himalaya, India. *Global and Planetary change*, 155, pp.196-212.
- Garg, P.K., Shukla, A., and Jasrotia, A.S., 2017, July. An integrated field and remote sensing based approach for estimating influence of debris thickness on glacier surface elevation changes. In 2017 IEEE International Geoscience and Remote Sensing Symposium (IGARSS) (pp. 2840-2843). IEEE.

- Garg, P.K., Shukla, A., Tiwari, R.K. and Jasrotia, A.S., 2017a. Assessing the status of glaciers in part of the Chandra basin, Himachal Himalaya: a multiparametric approach. *Geomorphology*, 284, pp.99-114.
- Garg, P.K., Yadav, J.S., Rai, S.K. and Shukla, A., 2021a. Mass balance and morphological evolution of the Dokriani Glacier, central Himalaya, India during 1999–2014. *Geoscience Frontiers*, 13(1), p.101290.
- Garg, S., Shukla, A., Mehta, M., Kumar, V., and Shukla, U.K., 2019. On geomorphic manifestations and glaciation history of the Kangriz glacier, western Himalaya. *Himal. Geol*, 40(2), pp.115-127.
- Gascoin, S., Kinnard, C., Ponce, R., Lhermitte, S., MacDonell, S. and Rabatel, A., 2011. Glacier contribution to streamflow in two headwaters of the Huasco River, Dry Andes of Chile. *The Cryosphere*, 5(4), pp.1099-1113.
- Gertler, C.G., Puppala, S.P., Panday, A., Stumm, D. and Shea, J., 2016. Black carbon and the Himalayan cryosphere: A review. *Atmospheric environment*, 125, pp.404-417.
- Ginot, P., Dumont, M., Lim, S., Patris, N., Taupin, J.D., Wagnon, P., Gilbert, A., Arnaud, Y., Marinoni, A., Bonasoni, P. and Laj, P., 2014. A 10 year record of black carbon and dust from a Mera Peak ice core (Nepal): variability and potential impact on melting of Himalayan glaciers. *The Cryosphere*, 8(4), pp.1479-1496.
- Godwin-Austen, H.H., 1864. On the glaciers of the Mustakh Range. *The Journal of the Royal Geographical Society of London*, 34, pp.19-56.
- Granshaw, F.D. and Fountain, A.G., 2006. Glacier change (1958–1998) in the north Cascades national park complex, Washington, USA. *Journal of Glaciology*, 52(177), pp.251-256.
- Grisogono, B. and Oerlemans, J., 2002. Justifying the WKB approximation in pure katabatic flows. *Tellus A: Dynamic Meteorology and Oceanography*, 54(5), pp.453-462.

- Gruber, S., 2012. Derivation and analysis of a high-resolution estimate of global permafrost zonation. *The Cryosphere*, 6(1), pp.221-233.
- Gruber, S., Fleiner, R., Guegan, E., Panday, P., Schmid, M.O., Stumm, D., Wester, P., Zhang, Y. and Zhao, L., 2017. Inferring permafrost and permafrost thaw in the mountains of the Hindu Kush Himalaya region. *The Cryosphere*, 11(1), pp.81-99.
- Hagg, W., Hoelzle, M., Wagner, S. and Klose, Z., 2011. Estimation of future glaciation and runoff in the Tanimas basin, Eastern Pamirs. *Hydrology and Earth System Sciences Discussions*, 8(1), pp.1507-1540.
- Hall, D.K., Bayr, K.J., Schöner, W., Bindschadler, R.A. and Chien, J.Y., 2003. Consideration of the errors inherent in mapping historical glacier positions in Austria from the ground and space (1893–2001). *Remote Sensing of Environment*, 86(4), pp.566-577.
- Haq, M.A., Azam, M.F. and Vincent, C., 2021. Efficiency of artificial neural networks for glacier ice-thickness estimation: A case study in western Himalaya, India. *Journal of Glaciology*, pp.1-14.
- Hay, J.E. and Fitzharris, B.B., 1988. A comparison of the energy-balance and bulk-aerodynamic approaches for estimating glacier melt. *Journal of Glaciology*, 34(117), pp.145-153.
- Heid, T. and Kääb, A., 2012. Evaluation of existing image matching methods for deriving glacier surface displacements globally from optical satellite imagery. *Remote Sensing of Environment*, 118, pp.339-355.
- Hersch, R., 1993. The velocity-area method. *Flow measurement and instrumentation*, 4(1): 7-10.
- Hewitt, K., 2005. The Karakoram anomaly? Glacier expansion and the ‘elevation effect,’ Karakoram Himalaya. *Mountain Research and Development*, 25(4), pp.332-340.
- Heynen, M., Pellicciotti, F. and Carenzo, M., 2013. Parameter sensitivity of a distributed enhanced temperature-index melt model. *Annals of glaciology*, 54(63), pp.311-321.

- Hock, R., 2003. Temperature index melt modelling in mountain areas. *Journal of hydrology*, 282(1-4), pp.104-115.
- Hock, R., 2005. Glacier melt: a review of processes and their modelling. *Progress in physical geography*, 29(3), pp.362-391.
- Hock, R., Rasul, G., Adler, C., Cáceres, B., Gruber, S., Hirabayashi, Y., Jackson, M., Kääb, A., Kang, S., Kutuzov, S. and Milner, A., 2019. High mountain areas Supplementary Material. IPCC Special Report on the Ocean and Cryosphere in a Changing Climate.
- Hornberger, G.M., Wiberg, P.L., Raffensperger, J.P. and D'Odorico, P., 2014. *Elements of physical hydrology*. JHU Press.
- Huintjes, E., Neckel, N., Hochschild, V. and Schneider, C., 2015. Surface energy and mass balance at Purogangri ice cap, central Tibetan Plateau, 2001–2011. *Journal of Glaciology*, 61(230), pp.1048-1060.
- Huss, M. and Hock, R., 2018. Global-scale hydrological response to future glacier mass loss. *Nature Climate Change*, 8(2), pp.135-140.
- Huss, M., 2013. Density assumptions for converting geodetic glacier volume change to mass change. *The Cryosphere*, 7(3), pp.877-887.
- Huss, M., Farinotti, D., Bauder, A. and Funk, M., 2008. Modelling runoff from highly glacierized alpine drainage basins in a changing climate. *Hydrological processes*, 22(19), pp.3888-3902.
- Huss, M., Jouvett, G., Farinotti, D. and Bauder, A., 2010. Future high-mountain hydrology: a new parameterization of glacier retreat. *Hydrology and Earth System Sciences*, 14(5), pp.815-829.
- Immerzeel, W.W., Droogers, P., De Jong, S.M. and Bierkens, M.F.P., 2009. Large-scale monitoring of snow covers and runoff simulation in Himalayan river basins using remote sensing. *Remote sensing of Environment*, 113(1), pp.40-49.
- Immerzeel, W.W., Lutz, A.F., Andrade, M., Bahl, A., Biemans, H., Bolch, T., Hyde, S., Brumby, S., Davies, B.J., Elmore, A.C. and Emmer, A., 2020. Importance and vulnerability of the world's water towers. *Nature*,

577(7790), pp.364-369.

- Immerzeel, W.W., Pellicciotti, F. and Bierkens, M.F.P., 2013. Rising river flows throughout the twenty-first century in two Himalayan glacierized watersheds. *Nature geoscience*, 6(9), pp.742-745.
- Immerzeel, W.W., Van Beek, L.P. and Bierkens, M.F., 2010. Climate change will affect the Asian water towers. *Science*, 328(5984), pp.1382-1385.
- Immerzeel, W.W., Van Beek, L.P.H., Konz, M., Shrestha, A.B. and Bierkens, M.F.P., 2012. Hydrological response to climate change in a glacierized catchment in the Himalayas. *Climatic change*, 110(3), pp.721-736.
- Immerzeel, W.W., Wanders, N., Lutz, A.F., Shea, J.M. and Bierkens, M.F.P., 2015. Reconciling high-altitude precipitation in the upper Indus basin with glacier mass balances and runoff. *Hydrology and Earth System Sciences*, 19(11), pp.4673-4687.
- Jacobi, H.W., Lim, S., Ménégoz, M., Ginot, P., Laj, P., Bonasoni, P., Stocchi, P., Marinoni, A. and Arnaud, Y., 2015. Black carbon in snow in the upper Himalayan Khumbu Valley, Nepal: observations and modeling of the impact on snow albedo, melting, and radiative forcing. *Cryosphere Discussions*, 8(5).
- Jeelani, G., Feddema, J.J., van der Veen, C.J. and Stearns, L., 2012. Role of snow and glacier melt in controlling river hydrology in Liddar watershed (western Himalaya) under current and future climate. *Water Resources Research*, 48(12).
- Jennings, K.S., Winchell, T.S., Livneh, B. and Molotch, N.P., 2018. Spatial variation of the rain–snow temperature threshold across the Northern Hemisphere. *Nature communications*, 9(1), pp.1-9.
- Jóhannesson, T., Raymond, C. and Waddington, E.D., 1989. Time–scale for adjustment of glaciers to changes in mass balance. *Journal of Glaciology*, 35(121), pp.355-369.
- Johnson, E. and Rupper, S., 2020. An examination of physical processes that trigger the albedo-feedback on glacier surfaces and implications for

- regional glacier mass balance across High Mountain Asia. *Frontiers in Earth Science*, 8, p.129.
- Kääb, A., Berthier, E., Nuth, C., Gardelle, J. and Arnaud, Y., 2012. Contrasting patterns of early twenty-first-century glacier mass change in the Himalayas. *Nature*, 488(7412), pp.495-498.
- Kääb, A., Treichler, D., Nuth, C. and Berthier, E., 2015. Brief Communication: Contending estimates of 2003–2008 glacier mass balance over the Pamir–Karakoram–Himalaya. *The Cryosphere*, 9(2), pp.557-564.
- Kaser, G., Fountain, A., Jansson, P., Heucke, E. and Knaus, M., 2003. A manual for monitoring the mass balance of mountain glaciers (Vol. 137). Paris: Unesco.
- Kaser, G., Großhauser, M. and Marzeion, B., 2010. Contribution potential of glaciers to water availability in different climate regimes. *Proceedings of the National Academy of Sciences*, 107(47), pp.20223-20227.
- Kayastha, R.B., Ohata, T. and Ageta, Y., 1999. Application of a mass-balance model to a Himalayan glacier. *Journal of Glaciology*, 45(151), pp.559-567.
- Kayastha, R.B., Steiner, N., Kayastha, R., Mishra, S.K. and McDonald, K., 2020. Comparative study of hydrology and icemelt in three Nepal river basins using the Glacio-Hydrological Degree-Day Model (GDM) and observations from the Advanced Scatterometer (ASCAT). *Frontiers in Earth Science*, 7, p.354.
- Kenzhebaev, R., Barandun, M., Kronenberg, M., Chen, Y., Usabaliev, R. and Hoelzle, M., 2017. Mass balance observations and reconstruction for Batysh Sook Glacier, Tien Shan, from 2004 to 2016. *Cold Regions Science and Technology*, 135, pp.76-89.
- Khan, A., Richards, K.S., Parker, G.T., McRobie, A. and Mukhopadhyay, B., 2014. How large is the Upper Indus Basin? The pitfalls of auto-delineation using DEMs. *Journal of Hydrology*, 509, pp.442-453.

- Khan, M.Q.I., Venkataratnam, L., Rao, B.R.M., Rao, D.P. and Subrahmanyam, C., 2001. International classification and codification of watersheds and river basins. *Journal of Water Resources Planning and Management*, 127(5), pp.306-315.
- Klok, E.J. and Oerlemans, J., 2004. Modelled climate sensitivity of the mass balance of Morteratschgletscher and its dependence on albedo parameterization. *International Journal of Climatology: A Journal of the Royal Meteorological Society*, 24(2), pp.231-245.
- Konz, M. and Seibert, J., 2010. On the value of glacier mass balances for hydrological model calibration. *Journal of hydrology*, 385(1-4), pp.238-246.
- Kraaijenbrink, P.D., Bierkens, M.F.P., Lutz, A.F. and Immerzeel, W.W., 2017. Impact of a global temperature rise of 1.5 degrees Celsius on Asia's glaciers. *Nature*, 549(7671), pp.257-260.
- Kraaijenbrink, P.D., Shea, J.M., Litt, M., Steiner, J.F., Treichler, D., Koch, I. and Immerzeel, W.W., 2018. Mapping surface temperatures on a debris-covered glacier with an unmanned aerial vehicle. *Frontiers in Earth Science*, 6, p.64.
- Krishnan, R., Shrestha, A.B., Ren, G., Rajbhandari, R., Saeed, S., Sanjay, J., Syed, M.A., Vellore, R., Xu, Y., You, Q. and Ren, Y., 2019. Unravelling climate change in the Hindu Kush Himalaya: rapid warming in the mountains and increasing extremes. In *The Hindu Kush Himalaya Assessment* (pp. 57-97). Springer, Cham.
- Kuhn, M., 1987. Micro-meteorological conditions for snow melt. *Journal of glaciology*, 33(113), pp.24-26.
- Kulkarni, A.V. and Karyakarte, Y., 2014. Observed changes in Himalayan glaciers. *Current Science*, pp.237-244.
- Kulkarni, A.V., 1992. Mass balance of Himalayan glaciers using AAR and ELA methods. *Journal of Glaciology*, 38(128), pp.101-104.

- Kulkarni, A.V., Bahuguna, I.M., Rathore, B.P., Singh, S.K., Randhawa, S.S., Sood, R.K. and Dhar, S., 2007. Glacial retreat in Himalaya using Indian remote sensing satellite data. *Current science*, pp.69-74.
- Kulkarni, A.V., Rathore, B.P., Singh, S.K. and Bahuguna, I.M., 2011. Understanding changes in the Himalayan cryosphere using remote sensing techniques. *International journal of remote sensing*, 32(3), pp.601-615.
- Kulkarni, A.V., Shirsat, T.S., Kulkarni, A., Negi, H.S., Bahuguna, I.M. and Thamban, M., 2021. State of Himalayan cryosphere and implications for water security. *Water Security*, 14, p.100101.
- Kumar, A., Negi, H.S. and Kumar, K., 2020. Long-term mass balance modelling (1986–2018) and climate sensitivity of Siachen Glacier, East Karakoram. *Environmental monitoring and assessment*, 192(6), pp.1-16.
- Kumar, A., Negi, H.S. and Kumar, K., 2021. Long-term (~ 40 years) mass balance appraisal and response of the Patsio glacier, in the Great Himalayan region towards climate change. *Journal of Earth System Science*, 130(1), pp.1-12.
- Kumar, A., Verma, A., Dobhal, D. P., Mehta, M., Kesarwani, K., 2014. Climatic control on extreme sediment transfer from Dokriani Glacier during monsoon, Garhwal Himalaya (India). *J. Earth Syst. Sci.* 123(1), 109-120.
- Kumar, P., Saharwardi, M.S., Banerjee, A., Azam, M.F., Dubey, A.K. and Murtugudde, R., 2019. Snowfall variability dictates glacier mass balance variability in Himalaya-Karakoram. *Scientific reports*, 9(1), pp.1-9.
- Kumar, R., Singh, S., Kumar, R., Singh, A., Bhardwaj, A., Sam, L., Randhawa, S.S. and Gupta, A., 2016. Development of a glacio-hydrological model for discharge and mass balance reconstruction. *Water Resour. Manag.* 30(10), 3475-3492.

- Kumar, V., Singh, P. and Singh, V., 2007. Snow and glacier melt contribution in the Beas River at Pandoh dam, Himachal Pradesh, India. *Hydrological sciences journal*, 52(2), pp.376-388.
- Laha, S., Kumari, R., Singh, S., Mishra, A., Sharma, T., Banerjee, A., Nainwal, H.C. and Shankar, R., 2017. Evaluating the contribution of avalanching to the mass balance of Himalayan glaciers. *Annals of Glaciology*, 58(75pt2), pp.110-118.
- Litt, M., Shea, J., Wagnon, P., Steiner, J., Koch, I., Stigter, E. and Immerzeel, W., 2019. Glacier ablation and temperature indexed melt models in the Nepalese Himalaya. *Scientific reports*, 9(1), pp.1-13.
- Litt, M., Sicart, J.E. and Helgason, W., 2015. A study of turbulent fluxes and their measurement errors for different wind regimes over the tropical Zongo Glacier (16° S) during the dry season. *Atmospheric Measurement Techniques*, 8(8), pp.3229-3250.
- Liu, W., Zhang, D., Qin, X., van den Broeke, M.R., Jiang, Y., Yang, D. and Ding, M., 2021. Monsoon Clouds Control the Summer Surface Energy Balance on East Rongbuk Glacier (6,523 m Above Sea Level), the Northern of Mt. Qomolangma (Everest). *Journal of Geophysical Research: Atmospheres*, 126(8), p.e2020JD033998.
- Lutz, A.F., Immerzeel, W.W., Kraaijenbrink, P.D., Shrestha, A.B. and Bierkens, M.F., 2016. Climate change impacts on the upper Indus hydrology: sources, shifts and extremes. *PloS one*, 11(11), p.e0165630.
- Lutz, A.F., Immerzeel, W.W., Shrestha, A.B. and Bierkens, M.F.P., 2014. Consistent increase in High Asia's runoff due to increasing glacier melt and precipitation. *Nature Climate Change*, 4(7), pp.587-592.
- Mahto SS and Mishra V (2019) Does ERA-5 outperform other reanalysis products for hydrologic applications in India? *Journal of Geophysical Research: Atmospheres*, 124(16), pp.9423-9441.
- Managave, S., Shimla, P., Yadav, R.R., Ramesh, R. and Balakrishnan, S., 2020. Contrasting centennial-scale climate variability in High Mountain Asia

- revealed by a tree-ring oxygen isotope record from Lahaul-Spiti. *Geophysical Research Letters*, 47(4), p.e2019GL086170.
- Managave, S.R. and Ramesh, R., 2012. Isotope dendroclimatology: A review with a special emphasis on tropics. *Handbook of Environmental Isotope Geochemistry*, pp.811-833.
- Mandal, A., Ramanathan, A., Azam, M.F., Angchuk, T., Soheb, M., Kumar, N., Pottakkal, J.G., Vatsal, S., Mishra, S. and Singh, V.B., 2020. Understanding the interrelationships among mass balance, meteorology, discharge and surface velocity on Chhota Shigri Glacier over 2002–2019 using in situ measurements. *Journal of Glaciology*, 66(259), pp.727-741.
- Mark, B.G. and Seltzer, G.O., 2003. Tropical glacier meltwater contribution to stream discharge: a case study in the Cordillera Blanca, Peru. *Journal of glaciology*, 49(165), pp.271-281.
- Martinec, J., Rango, A. and Roberts, R., 1995. *The Snowmelt-Runoff Model (SRM) User's Manual (Version 3.2)*. USDA Hydrology Laboratory. Agricultural Research Service, Beltsville, Maryland.
- Matthews, T., Perry, L.B., Koch, I., Aryal, D., Khadka, A., Shrestha, D., Abernathy, K., Elmore, A.C., Seimon, A., Tait, A. and Elvin, S., 2020. Going to extremes: installing the world's highest weather stations on Mount Everest. *Bulletin of the American Meteorological Society*, 101(11), pp.E1870-E1890.
- Maurer, J.M., Schaefer, J.M., Rupper, S. and Corley, A., 2019. Acceleration of ice loss across the Himalayas over the past 40 years. *Science advances*, 5(6), p.eaav7266.
- Maurya, A.S., Shah, M., Deshpande, R.D., Bhardwaj, R.M., Prasad, A. and Gupta, S.K., 2011. Hydrograph separation and precipitation source identification using stable water isotopes and conductivity: River Ganga at Himalayan foothills. *Hydrological Processes*, 25(10), pp.1521-1530.
- Maussion, F., Scherer, D., Mölg, T., Collier, E., Curio, J. and Finkelnburg, R.,

2014. Precipitation seasonality and variability over the Tibetan Plateau as resolved by the High Asia Reanalysis. *Journal of Climate*, 27(5), pp.1910-1927.
- Mehta, M., Dobhal, D.P., Pratap, B., Majeed, Z., Gupta, A.K. and Srivastava, P., 2014. Late quaternary glacial advances in the tons river valley, Garhwal Himalaya, India and regional synchronicity. *The Holocene*, 24(10), pp.1336-1350.
- Mihalcea, C., Mayer, C., Diolaiuti, G., D'agata, C., Smiraglia, C., Lambrecht, A., Vuillermoz, E. and Tartari, G., 2008. Spatial distribution of debris thickness and melting from remote-sensing and meteorological data, at debris-covered Baltoro glacier, Karakoram, Pakistan. *Annals of Glaciology*, 48, pp.49-57.
- Mimeau, L., Esteves, M., Zin, I., Jacobi, H.W., Brun, F., Wagnon, P., Koirala, D. and Arnaud, Y., 2019. Quantification of different flow components in a high-altitude glacierized catchment (Dudh Koshi, Himalaya): some cryospheric-related issues. *Hydrology and Earth System Sciences*, 23(9), pp.3969-3996.
- Mir, R.A., Jain, S.K., Jain, S.K., Thayyen, R.J. and Saraf, A.K., 2017. Assessment of recent glacier changes and its controlling factors from 1976 to 2011 in Baspa basin, western Himalaya. *Arctic, Antarctic, and Alpine Research*, 49(4), pp.621-647.
- Mishra, V., 2015. Climatic uncertainty in Himalayan water towers. *Journal of Geophysical Research: Atmospheres*, 120(7), pp.2689-2705.
- Misra, A., Kumar, A., Bhambri, R., Haritashya, U.K., Verma, A., Dobhal, D.P., Gupta, A.K., Gupta, G. and Upadhyay, R., 2020. Topographic and climatic influence on seasonal snow cover: Implications for the hydrology of ungauged Himalayan basins, India. *Journal of Hydrology*, 585, p.124716.

- Mölg, T., Maussion, F. and Scherer, D., 2014. Mid-latitude westerlies as a driver of glacier variability in monsoonal High Asia. *Nature Climate Change*, 4(1), pp.68-73.
- Mölg, T., Maussion, F., Yang, W. and Scherer, D., 2012. The footprint of Asian monsoon dynamics in the mass and energy balance of a Tibetan glacier. *The Cryosphere*, 6(6), pp.1445-1461.
- Mukherjee, K., Bhattacharya, A., Pieczonka, T., Ghosh, S. and Bolch, T., 2018. Glacier mass budget and climate reanalysis data indicate a climatic shift around 2000 in Lahaul-Spiti, western Himalaya. *Climatic change*, 148(1), pp.219-233.
- Mukhopadhyay, B. and Khan, A., 2014. Rising river flows and glacial mass balance in central Karakoram. *Journal of Hydrology*, 513, pp.192-203.
- Mukhopadhyay, B. and Khan, A., 2015. A reevaluation of the snowmelt and glacial melt in river flows within Upper Indus Basin and its significance in a changing climate. *Journal of Hydrology*, 527, pp.119-132.
- Nainwal, H.C., Banerjee, A., Shankar, R., Semwal, P. and Sharma, T., 2016. Shrinkage of Satopanth and Bhagirath Kharak glaciers, India, from 1936 to 2013. *Annals of glaciology*, 57(71), pp.131-139.
- Nash, J.E. and Sutcliffe, J.V., 1970. River flow forecasting through conceptual models part I—A discussion of principles. *Journal of hydrology*, 10(3), pp.282-290.
- Nepal, S. and Shrestha, A.B., 2015. Impact of climate change on the hydrological regime of the Indus, Ganges and Brahmaputra river basins: a review of the literature. *International Journal of Water Resources Development*, 31(2), pp.201-218.
- Nepal, S., Krause, P., Flügel, W.A., Fink, M. and Fischer, C., 2014. Understanding the hydrological system dynamics of a glaciated alpine catchment in the Himalayan region using the J2000 hydrological model. *Hydrological Processes*, 28(3), pp.1329-1344.
- Nuimura, T., Fujita, K., Yamaguchi, S. and Sharma, R.R., 2012. Elevation

- changes of glaciers revealed by multitemporal digital elevation models calibrated by GPS survey in the Khumbu region, Nepal Himalaya, 1992-2008. *Journal of Glaciology*, 58(210), pp.648-656.
- Oerlemans, J. and Knap, W.H., 1998. A 1-year record of global radiation and albedo in the ablation zone of Morteratschgletscher, Switzerland. *Journal of Glaciology*, 44(147), pp.231-238.
- Oerlemans, J., 1992. Climate sensitivity of glaciers in southern Norway: application of an energy-balance model to Nigardsbreen, Hellstugubreen and Alfortbreen. *Journal of Glaciology*, 38(129), pp.223-232.
- Oerlemans, J., 2000. Analysis of a 3-year meteorological record from the ablation zone of Morteratschgletscher, Switzerland: energy and mass balance. *Journal of Glaciology*, 46(155), pp.571-579.
- Oerlemans, J., 2001. *Glaciers and climate change*. CRC Press.
- Oerlemans, J., 2005. Extracting a climate signal from 169 glacier records. *Science*, 308(5722), pp.675-677.
- Oerlemans, J., Anderson, B., Hubbard, A., Huybrechts, P., Johannesson, T., Knap, W.H., Schmeits, M., Stroeven, A.P., Van de Wal, R.S.W., Wallinga, J. and Zuo, Z., 1998. Modelling the response of glaciers to climate warming. *Climate dynamics*, 14(4), pp.267-274.
- Ohmura, A., 2006. Changes in mountain glaciers and ice caps during the 20th century. *Annals of Glaciology*, 43, pp.361-368.
- Østrem, G. and Brugman, M., 1966. *Glacier mass balance measurements*. Department of Mines and Technical Surveys, Glaciology Section.
- Østrem, G. and Brugman, M., 1991. *Glacier mass-balance measurements: a manual for field and office work*, vol. 4 of NHRI Science Report. National Hydrological Research Institute, Saskatoon.
- Østrem, G. and Brugman, M., 1966. *Glacier mass balance measurements*. Department of Mines and Technical Surveys, Glaciology Section..

- Palazzi, E., Von Hardenberg, J. and Provenzale, A., 2013. Precipitation in the Hindu-Kush Karakoram Himalaya: observations and future scenarios. *Journal of Geophysical Research: Atmospheres*, 118(1), pp.85-100.
- Pandey, P. and Venkataraman, G., 2013. Changes in the glaciers of Chandra–Bhaga basin, Himachal Himalaya, India, between 1980 and 2010 measured using remote sensing. *International Journal of Remote Sensing*, 34(15), pp.5584-5597.
- Patel, A., Goswami, A., Dharpure, J.K., Thamban, M., Sharma, P., Kulkarni, A.V. and Oulkar, S., 2021. Estimation of mass and energy balance of glaciers using a distributed energy balance model over the Chandra river basin (Western Himalaya). *Hydrological Processes*, 35(2), p.e14058.
- Patel, L.K., Sharma, P., Laluraj, C.M., Thamban, M., Singh, A. and Ravindra, R., 2017. A geospatial analysis of Samudra Tapu and Gepang Gath glacial lakes in the Chandra Basin, Western Himalaya. *Natural Hazards*, 86(3), pp.1275-1290.
- Pellicciotti, F., Buergi, C., Immerzeel, W.W., Konz, M. and Shrestha, A.B., 2012. Challenges and uncertainties in hydrological modeling of remote Hindu Kush–Karakoram–Himalayan (HKH) basins: suggestions for calibration strategies. *Mountain Research and Development*, 32(1), pp.39-50. doi:10.1659/MRD-JOURNAL-D-11-00092.1
- Pellicciotti, F., Helbing, J., Rivera, A., Favier, V., Corripio, J., Araos, J., Sicart, J.E. and Carenzo, M., 2008. A study of the energy balance and melt regime on Juncal Norte Glacier, semi-arid Andes of central Chile, using melt models of different complexity. *Hydrological Processes*, 22(19), pp.3980-3997.
- Pratap, B., Dobhal, D.P., Mehta, M. and Bhambri, R., 2015. Influence of debris cover and altitude on glacier surface melting: a case study on Dokriani Glacier, central Himalaya, India. *Annals of Glaciology*, 56(70), pp.9-16.

- Pritchard, H.D., 2019. Asia's shrinking glaciers protect large populations from drought stress. *Nature*, 569(7758), pp.649-654.
- Quick, M.C. and Pipes, A.U.B.C., 1977. UBC WATERSHED MODEL/Le modèle du bassin versant UCB. *Hydrological Sciences Journal*, 22(1), pp.153-161.
- Rabatel, A., Dedieu, J.P. and Vincent, C., 2005. Using remote-sensing data to determine equilibrium-line altitude and mass-balance time series: validation on three French glaciers, 1994–2002. *Journal of glaciology*, 51(175), pp.539-546.
- Racoviteanu, A.E., Armstrong, R. and Williams, M.W., 2013. Evaluation of an ice ablation model to estimate the contribution of melting glacier ice to annual discharge in the Nepal Himalaya. *Water Resources Research*, 49(9), pp.5117-5133.
- Racoviteanu, A.E., Arnaud, Y., Williams, M.W. and Manley, W.F., 2015. Spatial patterns in glacier characteristics and area changes from 1962 to 2006 in the Kanchenjunga–Sikkim area, eastern Himalaya. *The Cryosphere*, 9(2), pp.505-523.
- Racoviteanu, A.E., Paul, F., Raup, B., Khalsa, S.J.S. and Armstrong, R., 2009. Challenges and recommendations in mapping of glacier parameters from space: results of the 2008 Global Land Ice Measurements from Space (GLIMS) workshop, Boulder, Colorado, USA. *Annals of Glaciology*, 50(53), pp.53-69.
- Racoviteanu, A.E., Rittger, K. and Armstrong, R., 2019. An automated approach for estimating snowline altitudes in the Karakoram and eastern Himalaya from remote sensing. *Frontiers in Earth Science*, 7, p.220.
- Radić, V. and Hock, R., 2014. Glaciers in the Earth's hydrological cycle: assessments of glacier mass and runoff changes on global and regional scales. *Surveys in Geophysics*, 35(3), pp.813-837.
- Ragetti, S., Pellicciotti, F., Bordoy, R. and Immerzeel, W.W., 2013. Sources of uncertainty in modeling the glaciohydrological response of a Karakoram

- watershed to climate change. *Water Resources Research*, 49(9), pp.6048-6066.
- Ragettli, S., Pellicciotti, F., Immerzeel, W.W., Miles, E.S., Petersen, L., Heynen, M., Shea, J.M., Stumm, D., Joshi, S. and Shrestha, A., 2015. Unraveling the hydrology of a Himalayan catchment through integration of high resolution in situ data and remote sensing with an advanced simulation model. *Advances in Water Resources*, 78, pp.94-111.
- Rai, S.P., Thayyen, R.J., Purushothaman, P. and Kumar, B., 2016. Isotopic characteristics of cryospheric waters in parts of Western Himalayas, India. *Environmental Earth Sciences*, 75(7), pp.600.
- Raina, V.K., Kaul, M.K. and Singh, S., 1977. Mass-balance studies of Gara Glacier. *Journal of Glaciology*, 18(80), pp.415-423.
- Ramsankaran, R.A.A.J., Pandit, A. and Azam, M.F., 2018. Spatially distributed ice-thickness modelling for Chhota Shigri Glacier in western Himalayas, India. *International Journal of Remote Sensing*, 39(10), pp.3320-3343.
- Rashid, I. and Majeed, U., 2020. Retreat and geodetic mass changes of Zemu Glacier, Sikkim Himalaya, India, between 1931 and 2018. *Regional Environmental Change*, 20(4), pp.1-13.
- Rasmussen, R., Baker, B., Kochendorfer, J., Meyers, T., Landolt, S., Fischer, A.P., Black, J., Thériault, J.M., Kucera, P., Gochis, D. and Smith, C., 2012. How well are we measuring snow: The NOAA/FAA/NCAR winter precipitation test bed. *Bulletin of the American Meteorological Society*, 93(6), pp.811-829.
- Rees, H.G. and Collins, D.N., 2006. Regional differences in response of flow in glacier-fed Himalayan rivers to climatic warming. *Hydrological Processes: An International Journal*, 20(10), pp.2157-2169.
- Remya, S.N., Kulkarni, A.V., Hassan Syed, T. and Nainwal, H.C., 2020. Glacier mass loss in the Alaknanda basin, Garhwal Himalaya on a decadal scale. *Geocarto International*, pp.1-19.

- Reznichenko, N., Davies, T., Shulmeister, J. and McSaveney, M., 2010. Effects of debris on ice-surface melting rates: an experimental study. *Journal of Glaciology*, 56(197), pp.384-394.
- RGI Consortium, 2017. Randolph glacier inventory—a dataset of global glacier outlines: version 6.0. Global Land Ice Measurements from Space, Colorado, USA, Tech. Rep.
- Rounce, D.R., Hock, R. and Shean, D.E., 2020a. Glacier mass change in High Mountain Asia through 2100 using the open-source python glacier evolution model (PyGEM). *Frontiers in Earth Science*, 7, p.331.
- Rounce, D.R., Khurana, T., Short, M.B., Hock, R., Shean, D.E. and Brinkerhoff, D.J., 2020b. Quantifying parameter uncertainty in a large-scale glacier evolution model using Bayesian inference: application to High Mountain Asia. *Journal of Glaciology*, 66(256), pp.175-187.
- Rounce, D.R., Quincey, D.J. and McKinney, D.C., 2015. Debris-covered glacier energy balance model for Imja–Lhotse Shar Glacier in the Everest region of Nepal. *The Cryosphere*, 9(6), pp.2295-2310.
- Sahu, R. and Gupta, R.D., 2019. Spatiotemporal variation in surface velocity in Chandra basin glacier between 1999 and 2017 using Landsat-7 and Landsat-8 imagery. *Geocarto International*, pp.1-21.
- Sakai, A. and Fujita, K., 2017. Contrasting glacier responses to recent climate change in high-mountain Asia. *Scientific reports*, 7(1), pp.1-8.
- Sakai, A., Nuimura, T., Fujita, K., Takenaka, S., Nagai, H. and Lamsal, D., 2015. Climate regime of Asian glaciers revealed by GAMDAM glacier inventory. *The Cryosphere*, 9(3), pp.865-880.
- Salerno, F., Buraschi, E., Bruccoleri, G., Tartari, G. and Smiraglia, C., 2008. Glacier surface-area changes in Sagarmatha national park, Nepal, in the second half of the 20th century, by comparison of historical maps. *Journal of Glaciology*, 54(187), pp.738-752.
- Savéan, M., Delclaux, F., Chevallier, P., Wagnon, P., Gongga-Saholiariliva, N., Sharma, R., Neppel, L. and Arnaud, Y., 2015. Water budget on the Dudh

- Koshi River (Nepal): uncertainties on precipitation. *Journal of Hydrology*, 531, pp.850-862.
- Schaner, N., Voisin, N., Nijssen, B. and Lettenmaier, D.P., 2012. The contribution of glacier melt to streamflow. *Environmental Research Letters*, 7(3), pp.034029.
- Schauwecker, S., Rohrer, M., Huggel, C., Kulkarni, A., Ramanathan, A.L., Salzmann, N., Stoffel, M. and Brock, B., 2015. Remotely sensed debris thickness mapping of Bara Shigri glacier, Indian Himalaya. *Journal of Glaciology*, 61(228), pp.675-688.
- Scherler, D., Bookhagen, B. and Strecker, M.R., 2011. Spatially variable response of Himalayan glaciers to climate change affected by debris cover. *Nature geoscience*, 4(3), pp.156-159.
- Schiemann, R., Lüthi, D., Vidale, P.L. and Schär, C., 2008. The precipitation climate of central Asia—Intercomparison of observational and numerical data sources in a remote semiarid region. *International Journal of Climatology: A Journal of the Royal Meteorological Society*, 28(3), pp.295-314.
- Schmidt, S. and Nüsser, M., 2012. Changes of high altitude glaciers from 1969 to 2010 in the Trans-Himalayan Kang Yatze Massif, Ladakh, northwest India. *Arctic, Antarctic, and Alpine Research*, 44(1), pp.107-121.
- Scott, C.A., Zhang, F., Mukherji, A., Immerzeel, W., Mustafa, D. and Bharati, L., 2019. Water in The Hindu kush himalaya. In *The Hindu Kush Himalaya Assessment* (pp. 257-299). Springer, Cham.
- Shah, S.S., Banerjee, A., Nainwal, H.C. and Shankar, R., 2019. Estimation of the total sub-debris ablation from point-scale ablation data on a debris-covered glacier. *Journal of Glaciology*, 65(253), pp.759-769.
- Sharma, P., Patel, L.K., Ravindra, R., Singh, A., Mahalinganathan, K. and Thamban, M., 2016. Role of debris cover to control specific ablation of adjoining Batal and Sutri Dhaka glaciers in Chandra Basin (Himachal Pradesh) during peak ablation season. *Journal of Earth System*

- Science, 125(3), pp.459-473.
- Shea, J.M., Immerzeel, W.W., Wagnon, P., Vincent, C. and Bajracharya, S., 2015b. Modelling glacier change in the Everest region, Nepal Himalaya. *The Cryosphere*, 9(3), pp.1105-1128.
- Shea, J.M., Menounos, B., Moore, R.D. and Tennant, C., 2013. An approach to derive regional snow lines and glacier mass change from MODIS imagery, western North America. *The Cryosphere*, 7(2), pp.667-680.
- Shea, J.M., Wagnon, P., Immerzeel, W.W., Biron, R., Brun, F. and Pellicciotti, F., 2015a. A comparative high-altitude meteorological analysis from three catchments in the Nepalese Himalaya. *International journal of water resources development*, 31(2), pp.174-200.
- Shean, D.E., Bhushan, S., Montesano, P., Rounce, D.R., Arendt, A. and Osmanoglu, B., 2020. A systematic, regional assessment of high mountain Asia glacier mass balance. *Frontiers in Earth Science*, 7, pp.363.
- Sherpa, S.F., Wagnon, P., Brun, F., Berthier, E., Vincent, C., Lejeune, Y., Arnaud, Y., Kayastha, R.B. and Sinisalo, A., 2017. Contrasted surface mass balances of debris-free glaciers observed between the southern and the inner parts of the Everest region (2007–15). *Journal of Glaciology*, 63(240), pp.637-651.
- Shrestha, A.B., Agrawal, N.K., Alfthan, B., Bajracharya, S.R., Maréchal, J. and Oort, B.V., 2015. The Himalayan Climate and Water Atlas: impact of climate change on water resources in five of Asia's major river basins. *The Himalayan Climate and Water Atlas: impact of climate change on water resources in five of Asia's major river basins*.
- Shroder, J.F., Bishop, M.P., Copland, L. and Sloan, V.F., 2000. Debris-covered glaciers and rock glaciers in the Nanga Parbat Himalaya, Pakistan. *Geografiska Annaler: Series A, Physical Geography*, 82(1), pp.17-31.

- Shukla, A. and Garg, P.K., 2020. Spatio-temporal trends in the surface ice velocities of the central Himalayan glaciers, India. *Global and Planetary Change*, 190, pp.103187.
- Shukla, A. and Qadir, J., 2016. Differential response of glaciers with varying debris cover extent: evidence from changing glacier parameters. *International Journal of Remote Sensing*, 37(11), pp.2453-2479.
- Shukla, A., Garg, S., Mehta, M., Kumar, V. and Shukla, U.K., 2020. Temporal inventory of glaciers in the Suru sub-basin, western Himalaya: impacts of regional climate variability. *Earth System Science Data*, 12(2), pp.1245-1265.
- Sicart, J.E., Wagnon, P. and Ribstein, P., 2005. Atmospheric controls of the heat balance of Zongo Glacier (16 S, Bolivia). *Journal of Geophysical Research: Atmospheres*, 110(D12).
- Singh P, Kumar N., 1997. Effect of orography on precipitation in the western Himalayan region. *Journal of Hydrology* 199: 183–206.
- Singh, M.K., Gupta, R.D. and Ganju, A., 2019. Extraction of high resolution DEM from Cartosat-1 stereo imagery using rational math model and its accuracy assessment for a part of snow covered NW-Himalaya. *Journal of Remote Sensing & GIS*, 4(2), pp.23-34.
- Singh, N., Shekhar, M., Singh, J., Gupta, A.K., Bräuning, A., Mayr, C. and Singhal, M., 2021. Central Himalayan tree-ring isotopes reveal increasing regional heterogeneity and enhancement in ice mass loss since the 1960s. *The Cryosphere*, 15(1), pp.95-112.
- Singh, N., Singhal, M., Chhikara, S., Karakoti, I., Chauhan, P. and Dobhal, D.P., 2020. Radiation and energy balance dynamics over a rapidly receding glacier in the central Himalaya. *International Journal of Climatology*, 40(1), pp.400-420.
- Singh, P. and Jain, S.K., 2002. Snow and glacier melt in the Satluj River at Bhakra Dam in the western Himalayan region. *Hydrological sciences*

- journal, 47(1), pp.93-106.
- Singh, P., Arora, M. and Goel, N.K., 2006. Effect of climate change on runoff of a glacierized Himalayan basin. *Hydrological Processes: An International Journal*, 20(9), pp.1979-1992.
- Singh, P., Jain, S.K. and Kumar, N., 1997. Estimation of snow and glacier-melt contribution to the Chenab River, Western Himalaya. *Mountain Research and Development*, pp.49-56.
- Singh, P., Kumar, N. and Arora, M., 2000. Degree-day factors for snow and ice for Dokriani Glacier, Garhwal Himalayas. *Journal of Hydrology*, 235(1-2), pp.1-11.
- Singh, P., Ramasatri, K.S., Kumar, N. and Bhatnagar, N.K., 2003. Suspended sediment transport from the Dokriani Glacier in the Garhwal Himalayas. *Hydrology Research*, 34(3), pp.221-244.
- Singh, S., Kumar, R. and Dimri, A.P., 2018. Mass balance status of Indian Himalayan Glaciers: A brief review. *Frontiers in Environmental Science*, 6, p.30.
- Singh, S., Kumar, R., Bhardwaj, A., Sam, L., Shekhar, M., Singh, A., Kumar, R. and Gupta, A., 2016. Changing climate and glacio-hydrology in Indian Himalayan Region: a review. *Wiley Interdisciplinary Reviews: Climate Change*, 7(3), pp.393-410.
- Soheb M, Ramanathan A, Angchuk T, Mandal A, Kumar N, Lotus S ,2020. Mass-balance observation, reconstruction and sensitivity of Stok glacier, Ladakh region, India, between 1978 and 2019. *Journal of Glaciology*, pp.1–16.
- Soncini, A., Bocchiola, D., Confortola, G., Bianchi, A., Rosso, R., Mayer, C., Lambrecht, A., Palazzi, E., Smiraglia, C. and Diolaiuti, G., 2015. Future hydrological regimes in the upper indus basin: A case study from a high-altitude glacierized catchment. *Journal of Hydrometeorology*, 16(1), pp.306-326.

- Srivastava, D., 2001. *Glaciology of Indian Himalayas: a bilingual contribution in 150 years of Geological Survey of India*. Geological Survey of India Special Publication, 63, p.213.
- Steiner, J.F., Kraaijenbrink, P.D. and Immerzeel, W.W., 2021. Distributed melt on a debris-covered glacier: field observations and melt modelling on the Lirung Glacier in the Himalaya. *Frontiers in Earth Science*, 9, p.567.
- Steiner, J.F., Litt, M., Stigter, E.E., Shea, J., Bierkens, M.F. and Immerzeel, W.W., 2018. The importance of turbulent fluxes in the surface energy balance of a debris-covered glacier in the Himalayas. *Frontiers in Earth Science*, 6, p.144.
- Stewart, R.L., Westoby, M., Pellicciotti, F., Rowan, A., Swift, D., Brock, B. and Woodward, J., 2021. Using climate reanalysis data in conjunction with multi-temporal satellite thermal imagery to derive supraglacial debris thickness changes from energy-balance modelling. *Journal of Glaciology*, 67(262), pp.366-384.
- Stigter, E.E., Litt, M., Steiner, J.F., Bonekamp, P.N., Shea, J.M., Bierkens, M.F. and Immerzeel, W.W., 2018. The importance of snow sublimation on a Himalayan glacier. *Frontiers in Earth Science*, 6, p.108
- Stigter, E.E., Steiner, J.F., Koch, I., Saloranta, T.M., Kirkham, J.D. and Immerzeel, W.W., 2021. Energy and mass balance dynamics of the seasonal snowpack at two high-altitude sites in the Himalaya. *Cold Regions Science and Technology*, 183, pp.103233.
- Stokes, C.R., Popovnin, V., Aleynikov, A., Gurney, S.D. and Shahgedanova, M., 2007. Recent glacier retreat in the Caucasus Mountains, Russia, and associated increase in supraglacial debris cover and supra-/proglacial lake development. *Annals of Glaciology*, 46, pp.195-203.
- Sun, W., Qin, X., Ren, J., Yang, X., Zhang, T., Liu, Y., Cui, X. and Du, W., 2012. The surface energy budget in the accumulation zone of the Laohugou Glacier No. 12 in the western Qilian Mountains, China, in

- summer 2009. *Arctic, Antarctic, and Alpine Research*, 44(3), pp.296-305.
- Sunako, S., Fujita, K., Sakai, A. and Kayastha, R.B., 2019. Mass balance of Trambau Glacier, Rolwaling region, Nepal Himalaya: in-situ observations, long-term reconstruction and mass-balance sensitivity. *Journal of Glaciology*, 65(252), pp.605-616.
- Survey of India (2005) National map policy. <http://www.surveyofindia.gov.in/tenders/nationalmappolicy/nationalmappolicy.pdf>
- Suzuki, R., Fujita, K. and Ageta, Y., 2007. Spatial distribution of thermal properties on debris-covered glaciers in the Himalayas derived from ADTER data. *Bulletin of Glaciological Research*, 24, pp.13-22.
- Tahir, A.A., Adamowski, J.F., Chevallier, P., Haq, A.U. and Terzago, S., 2016. Comparative assessment of spatiotemporal snow cover changes and hydrological behavior of the Gilgit, Astore and Hunza River basins (Hindukush–Karakoram–Himalaya region, Pakistan). *Meteorology and Atmospheric Physics*, 128(6), pp.793-811.
- Tahir, A.A., Chevallier, P., Arnaud, Y., Neppel, L. and Ahmad, B., 2011. Modeling snowmelt-runoff under climate scenarios in the Hunza River basin, Karakoram Range, Northern Pakistan. *Journal of hydrology*, 409(1-2), pp.104-117.
- Tangborn, W.V., 1984. Prediction of glacier derived runoff for hydroelectric development. *Geografiska Annaler: Series A, Physical Geography*, 66(3), pp.257-265.
- Tawde, S.A., Kulkarni, A.V. and Bala, G., 2017. An estimate of glacier mass balance for the Chandra basin, western Himalaya, for the period 1984–2012. *Annals of Glaciology*, 58(75pt2), pp.99-109.
- Terink, W., Lutz, A.F., Simons, G.W.H., Immerzeel, W.W. and Droogers, P., 2015. SPHY v2. 0: Spatial processes in Hydrology. *Geoscientific Model Development*, 8(7), pp.2009-2034.

- Thakuri, S., Salerno, F., Smiraglia, C., Bolch, T., D'Agata, C., Viviano, G. and Tartari, G., 2014. Tracing glacier changes since the 1960s on the south slope of Mt. Everest (central Southern Himalaya) using optical satellite imagery. *The Cryosphere*, 8(4), pp.1297-1315.
- Thayyen, R.J. and Dimri, A.P., 2018. Slope environmental lapse rate (SELR) of temperature in the monsoon regime of the western Himalaya. *Frontiers in Environmental Science*, 6, pp.42.
- Thayyen, R.J. and Gergan, J.T., 2010. Role of glaciers in watershed hydrology: a preliminary study of a "Himalayan catchment". *The Cryosphere*, 4(1), pp.115-128.
- Thayyen, R.J., Gergan, J.T. and Dobhal, D.P., 2005. Monsoonal control on glacier discharge and hydrograph characteristics, a case study of Dokriani Glacier, Garhwal Himalaya, India. *Journal of hydrology*, 306(1-4), pp.37-49.
- Thompson, S., Benn, D.I., Mertes, J. and Luckman, A., 2016. Stagnation and mass loss on a Himalayan debris-covered glacier: processes, patterns and rates. *Journal of Glaciology*, 62(233), pp.467-485.
- Tiwari, R.K., Gupta, R.P. and Arora, M.K., 2014. Estimation of surface ice velocity of Chhota-Shigri glacier using sub-pixel ASTER image correlation. *Current Science*, pp.853-859.
- Van As, D., Andersen, M.L., Petersen, D., Fettweis, X., Van Angelen, J.H., Lenaerts, J.T., Van Den Broeke, M.R., Lea, J.M., Bøggild, C.E., Ahlstrøm, A.P. and Steffen, K., 2014. Increasing meltwater discharge from the Nuuk region of the Greenland ice sheet and implications for mass balance (1960–2012). *Journal of Glaciology*, 60(220), pp.314-322.
- Van den Broeke, M., Bus, C., Ettema, J. and Smeets, P., 2010. Temperature thresholds for degree-day modelling of Greenland ice sheet melt rates. *Geophysical Research Letters*, 37(18).
- Verbunt, M., Gurtz, J., Jasper, K., Lang, H., Warmerdam, P. and Zappa, M., 2003. The hydrological role of snow and glaciers in alpine river basins

- and their distributed modeling. *Journal of hydrology*, 282(1-4), pp.36-55.
- Verma, A., Kumar, A., Gupta, A.K., Tiwari, S.K., Bhambri, R. and Naithani, S., 2018. Hydroclimatic significance of stable isotopes in precipitation from glaciers of Garhwal Himalaya, Upper Ganga Basin (UGB), India. *Hydrological processes*, 32(12), pp.1874-1893.
- Vijay, S. and Braun, M., 2016. Elevation change rates of glaciers in the Lahaul-Spiti (Western Himalaya, India) during 2000–2012 and 2012–2013. *Remote Sensing*, 8(12), pp.1038.
- Vijay, S. and Braun, M., 2018. Early 21st century spatially detailed elevation changes of Jammu and Kashmir glaciers (Karakoram–Himalaya). *Global and Planetary Change*, 165, pp.137-146.
- Vincent, C., 2002. Influence of climate change over the 20th century on four French glacier mass balances. *Journal of Geophysical Research: Atmospheres*, 107(D19), pp.ACL-4.
- Vincent, C., Kappenberger, G., Valla, F., Bauder, A., Funk, M. and Le Meur, E., 2004. Ice ablation as evidence of climate change in the Alps over the 20th century. *Journal of Geophysical Research: Atmospheres*, 109(D10).
- Vincent, C., Ramanathan, A., Wagnon, P., Dobhal, D.P., Linda, A., Berthier, E., Sharma, P., Arnaud, Y., Azam, M.F., Jose, P.G. and Gardelle, J., 2013. Balanced conditions or slight mass gain of glaciers in the Lahaul and Spiti region (northern India, Himalaya) during the nineties preceded recent mass loss. *The Cryosphere*, 7(2), pp.569-582.
- Vincent, C., Soruco, A., Azam, M.F., Basantes-Serrano, R., Jackson, M., Kjølmoen, B., Thibert, E., Wagnon, P., Six, D., Rabatel, A. and Ramanathan, A., 2018. A nonlinear statistical model for extracting a climatic signal from glacier mass balance measurements. *Journal of Geophysical Research: Earth Surface*, 123(9), pp.2228-2242.
- Vincent, C., Wagnon, P., Shea, J.M., Immerzeel, W.W., Kraaijenbrink, P., Shrestha, D., Soruco, A., Arnaud, Y., Brun, F., Berthier, E. and Sherpa,

- S.F., 2016. Reduced melt on debris-covered glaciers: investigations from Changri Nup Glacier, Nepal. *The Cryosphere*, 10(4), pp.1845-1858.
- Wagnon, P., Brun, F., Khadka, A., Berthier, E., Shrestha, D., Vincent, C., Arnaud, Y., Six, D., Dehecq, A., Ménégoz, M. and Jomelli, V., 2021. Reanalysing the 2007–19 glaciological mass-balance series of Mera Glacier, Nepal, Central Himalaya, using geodetic mass balance. *Journal of Glaciology*, 67(261), pp.117-125.
- Wagnon, P., Linda, A., Arnaud, Y., Kumar, R., Sharma, P., Vincent, C., Pottakkal, J.G., Berthier, E., Ramanathan, A., Hasnain, S.I. and Chevallier, P., 2007. Four years of mass balance on Chhota Shigri Glacier, Himachal Pradesh, India, a new benchmark glacier in the western Himalaya. *Journal of Glaciology*, 53(183), pp.603-611.
- Wagnon, P., Ribstein, P., Kaser, G. and Berton, P., 1999. Energy balance and runoff seasonality of a Bolivian glacier. *Global and planetary change*, 22(1-4), pp.49-58.
- Zemp, M., 2008. Global glacier changes: facts and figures. UNEP/Earthprint.
- Wagnon, P., Sicart, J.E., Berthier, E. and Chazarin, J.P., 2003. Wintertime high-altitude surface energy balance of a Bolivian glacier, Illimani, 6340 m above sea level. *Journal of Geophysical Research: Atmospheres*, 108(D6).
- Wagnon, P., Vincent, C., Arnaud, Y., Berthier, E., Vuillermoz, E., Gruber, S., Ménégoz, M., Gilbert, A., Dumont, M., Shea, J.M. and Stumm, D., 2013. Seasonal and annual mass balances of Mera and Pokalde glaciers (Nepal Himalaya) since 2007. *The Cryosphere*, 7(6), pp.1769-1786.
- Wang, C., Wang, Z., Kong, Y., Zhang, F., Yang, K. and Zhang, T., 2019b. Most of the northern hemisphere permafrost remains under climate change. *Scientific reports*, 9(1), pp.1-10.

- Wang, R., Liu, S., Shangguan, D., Radić, V. and Zhang, Y., 2019a. Spatial heterogeneity in glacier mass-balance sensitivity across High Mountain Asia. *Water*, 11(4), pp.776.
- Wang, S., Yao, T., Tian, L. and Pu, J., 2017. Glacier mass variation and its effect on surface runoff in the Beida River catchment during 1957–2013. *Journal of Glaciology*, 63(239), pp.523-534.
- Wani, J.M., Thayyen, R.J., Gruber, S., Ojha, C.S.P. and Stumm, D., 2020. Single-year thermal regime and inferred permafrost occurrence in the upper Gangass catchment of the cold-arid Himalaya, Ladakh, India. *Science of the Total Environment*, 703, pp.134631.
- Weng, Q., Lu, D. and Schubring, J., 2004. Estimation of land surface temperature–vegetation abundance relationship for urban heat island studies. *Remote sensing of Environment*, 89(4), pp.467-483.
- Yadav, J.S., Misra, A., Dobhal, D.P., Yadav, R.B.S. and Upadhyay, R., 2021. Snow cover mapping, topographic controls and integration of meteorological data sets in Din-Gad Basin, Central Himalaya. *Quaternary International*, 575, pp.160-177.
- Yadav, J.S., Pratap, B., Gupta, A.K., Dobhal, D.P., Yadav, R.B.S. and Tiwari, S.K., 2019. Spatio-temporal variability of near-surface air temperature in the Dokriani glacier catchment (DGC), central Himalaya. *Theoretical and Applied Climatology*, 136(3), pp.1513-1532.
- Zemp, M. and Marzeion, B., 2021. Dwindling Relevance of Large Volcanic Eruptions for Global Glacier Changes in the Anthropocene. *Geophysical Research Letters*, 48(14), p.e2021GL092964.
- Zemp, M., Frey, H., Gärtner-Roer, I., Nussbaumer, S.U., Hoelzle, M., Paul, F., Haeberli, W., Denzinger, F., Ahlstrøm, A.P., Anderson, B. and Bajracharya, S., 2015. Historically unprecedented global glacier decline in the early 21st century. *Journal of glaciology*, 61(228), pp.745-762.
- Zemp, M., Hoelzle, M. and Haeberli, W., 2009. Six decades of glacier mass-balance observations: a review of the worldwide monitoring

- network. *Annals of Glaciology*, 50(50), pp.101-111.
- Zemp, M., Huss, M., Thibert, E., Eckert, N., McNabb, R., Huber, J., Barandun, M., Machguth, H., Nussbaumer, S.U., Gärtner-Roer, I. and Thomson, L., 2019. Global glacier mass changes and their contributions to sea-level rise from 1961 to 2016. *Nature*, 568(7752), pp.382-386.
- Zemp, M., Paul, F., Hoelzle, M. and Haeberli, W., 2008. Glacier fluctuations in the European Alps, 1850–2000. *Darkening Peaks Glacier Retreat Sci. Soc.*
- Zemp, M., Thibert, E., Huss, M., Stumm, D., Rolstad Denby, C., Nuth, C., Nussbaumer, S.U., Moholdt, G., Mercer, A., Mayer, C. and Joerg, P.C., 2013. Reanalysing glacier mass balance measurement series. *The Cryosphere*, 7(4), pp.1227-1245.
- Zhang, Y., Fujita, K., Liu, S., Liu, Q. and Nuimura, T., 2011. Distribution of debris thickness and its effect on ice melt at Hailuoguo glacier, southeastern Tibetan Plateau, using in situ surveys and ASTER imagery. *Journal of Glaciology*, 57(206), pp.1147-1157.
- Zhang, Y., Liu, S. and Ding, Y., 2006. Spatial variation of degree-day factors on the observed glaciers in western China. *ACTA GEOGRAPHICA SINICA-CHINESE EDITION*-, 61(1), pp.89.
- Zhu, M., Yang, W., Yao, T., Tian, L., Thompson, L.G. and Zhao, H., 2021. The Influence of Key Climate Variables on Mass Balance of Naimona'nyi Glacier on a North-Facing Slope in the Western Himalayas. *Journal of Geophysical Research: Atmospheres*, 126(7), p.e2020JD033956.